



HAL
open science

Characterization and modelling of the anisotropic behaviour of high-strength aluminium alloy

Marion Fourmeau

► **To cite this version:**

Marion Fourmeau. Characterization and modelling of the anisotropic behaviour of high-strength aluminium alloy. Mechanics of materials [physics.class-ph]. Norwegian University of Science and Technology; École Normale Supérieure de Cachan, 2014. English. NNT: . tel-01488723

HAL Id: tel-01488723

<https://theses.hal.science/tel-01488723>

Submitted on 22 Mar 2017

HAL is a multi-disciplinary open access archive for the deposit and dissemination of scientific research documents, whether they are published or not. The documents may come from teaching and research institutions in France or abroad, or from public or private research centers.

L'archive ouverte pluridisciplinaire **HAL**, est destinée au dépôt et à la diffusion de documents scientifiques de niveau recherche, publiés ou non, émanant des établissements d'enseignement et de recherche français ou étrangers, des laboratoires publics ou privés.

**THESE DE DOCTORAT
DE L'ECOLE NORMALE SUPERIEURE DE CACHAN**

Présentée par

Marion Fourmeau

**pour obtenir le grade de
DOCTEUR DE L'ECOLE NORMALE SUPERIEURE DE CACHAN**

Domaine :
MECANIQUE- GENIE MECANIQUE – GENIE CIVIL

Sujet de la thèse :

**Caractérisation et modélisation du comportement anisotrope
d'alliage d'aluminium à haute résistance**

Thèse présentée et soutenue à Trondheim le 31 janvier 2014 devant le jury composé de :

Aase G. Reyes	Professeur, NTNU Trondheim	Présidente
Thomas Pardoën	Professeur, Université Catholique de Louvain	Rapporteur
John Botsis	Professeur, Ecole Polytechnique Fédérale de Lausanne	Rapporteur

Preface

This thesis is submitted to the Norwegian University of Science and Technology (NTNU) as part of the degree *Philosophiae Doctor*, and to the École Normale Supérieure de Cachan for obtainment of the title of *Docteur de l'École Normale Supérieure de Cachan*. This was done in the framework of a cotutelle agreement between the two institutions. The work was carried out at the Department of Structural Engineering at NTNU under the supervision of Professor Tore Børvik and Professor Odd Sture Hopperstad and at Laboratoire de Mécanique et Technologie at ENS-Cachan under the supervision of Professor Ahmed Benallal. The research was performed within the Fracture and Crack Propagation program at CRI-SIMLab, Center for Research-based Innovation, financially supported by the Norwegian Research Council (NFR).

Abstract

The purpose of the present study is to describe and characterize the anisotropic flow and fracture behaviour of a high-strength aluminium alloy. To this end, 20 mm thick plates of AA7075-T651 aluminium alloy have been tested. Different specimen geometries were used to investigate various stress states. Each specimen was machined in different directions of the plate to enlighten the anisotropy of the material. For all tests, the plastic flow exhibited a slight anisotropy while the failure strain and failure modes showed a very important dependence to the loading direction.

A microstructure analysis of the virgin material was performed by scanning electron microscope (SEM) and electron back-scatter diffraction to identify its texture, grain shape and particle distribution. A transmission electronic microscope analysis gave information of the precipitate free zones and their composition.

Tensile tests were performed on smooth axisymmetric specimens under uniaxial tension. Tensile tests were also conducted on notched axisymmetric specimens of notch radii $R=2.0$ mm and $R=0.8$ mm to obtain higher stress triaxiality states. Shear tests were performed on butterfly specimens and compression tests were performed on cylindrical specimens. Fracture surface analyses were carried out by SEM to identify the failure modes, supported by the microstructure analysis.

Based on the plastic anisotropy observed experimentally, the Yld2004-18p anisotropic yield function proposed by Barlat et al. (2005) was chosen to model the elasto-plastic behaviour of the AA7075-T651 alloy. The plastic parameters were calibrated using seven in-plane uniaxial tensile tests, a compression test in the normal direction of the plate and a shear test in the rolling direction. Numerical simulations of all the experimental tests were performed using the anisotropic elasto-plastic model. Predicted stress-strain curves were in very good agreement with the experimental curves for all tests including the tensile tests on notched specimens, which were not used in the calibration of the model. The overestimation of predicted stress level, generally observed (e.g. by Wilson, 2002) with notched specimens and isotropic pressure independent yield function, was significantly decreased when taking into

account anisotropy. The stress and strain states on elements where failure is experimentally observed were evaluated. The establishment of a failure locus (relation between failure strain and stress triaxiality) was also discussed.

Analytical approaches were used to gain some insight of the failure process. First, the void growth approach proposed by Rice and Tracey (1969) was extended to an anisotropic matrix. Then, the usual localization criterion (Rice, 1976) was developed with various constitutive characteristics to account for the shape of the yield function, non-associative plastic flow, large deformations and thermo-mechanical couplings.

For industrial applications, a phenomenological failure criterion based on “plastic work”, called the anisotropic extended Cockcroft-Latham (AECL), was proposed. The criterion was calibrated using the seven uniaxial in-plane tensile tests and the shear test performed in the rolling direction. Numerical simulations of all tests were, once again, performed accounting for plastic anisotropy. A parameter study was carried out to enlighten the influence of parameters such as the plastic anisotropy and the failure anisotropy. The predicted failure strain and failure modes were not accurate enough to give predictive capability to this failure criterion in all material tests.

Finally, this anisotropic failure criterion was also used in numerical simulations of some impact tests on AA7075-T651 plates with ogival and blunt projectiles. A thermoelasto-thermoviscoplastic model with anisotropic yielding was used and as for the material tests, a parameter study was performed. Ballistic limits were predicted and compared with the experimental results obtained by Børvik et al. (2010). It was found that the anisotropy of plastic flow and failure had almost no influence at very high impact velocities, while it had a substantial effect at impact velocities close to the ballistic limit. The introduced anisotropy was not found to improve the ballistic limit prediction for all cases, and also other parameters (e.g. yield shape, temperature coefficients and contact algorithms) have a prominent influence on the predicted ballistic limit. However, supported by experimental observations of non-axisymmetric failure modes (Pedersen et al., 2011), both the plastic anisotropy and the failure anisotropy are believed to be important ingredient of the constitutive model.

Résumé

L'objectif de l'étude est d'analyser les effets de l'anisotropie sur le comportement et la rupture d'alliages d'aluminium haute-performance. Pour ce faire, le cas d'étude choisi est l'alliage AA7075-T651 fourni en tôles de 20 mm d'épaisseur obtenues par laminage. Des éprouvettes de géométries différentes sont utilisées pour soumettre le matériau à divers états de contraintes. Chaque type d'éprouvette est usiné dans différentes directions de la tôle afin de révéler l'anisotropie du matériau. La faible texture cristallographique de l'alliage engendre une légère anisotropie de l'écoulement plastique. L'anisotropie de la rupture en traction uniaxiale (déformation à rupture et mode de rupture) est, quant à elle, très prononcée.

Une analyse de la microstructure du matériau vierge est effectuée à des échelles différentes. La morphologie des grains et la répartition des particules de l'alliage sont obtenue par microscopie optique. Des observations au microscope électronique à balayage (MEB) et par EBSD permettent d'identifier l'orientation des grains et d'en déduire la texture du matériau. Enfin, une analyse par microscope électronique à transmission offre des images le long des joints de grains, montrant l'absence de précipités (PFZ) et permettant d'évaluer leur composition.

Des éprouvettes axisymétriques cylindriques sont utilisées pour soumettre le matériau à de la traction uniaxiale. Ces éprouvettes sont usinées dans sept directions du plan de la tôle de 0° à 90° ainsi que dans l'épaisseur de la tôle (éprouvettes miniatures). Des éprouvettes axisymétriques avec rayon d'entailles $R=2.0$ mm et $R=0.8$ mm sont usinées dans le plan de la tôle à 0°, 45° et 90° et utilisées pour atteindre des triaxialités plus élevées. Des essais de cisaillement sont réalisés à l'aide d'éprouvettes papillon usinées dans le plan de la tôle à 0°, 45° et 90°. Pour finir, des essais de compression uniaxiale sont effectués sur des éprouvettes cylindriques usinées dans le plan de la tôle à 0°, 45° et 90° et dans son épaisseur. Le temps, la force et le déplacement de la machine

sont enregistrés afin de tracer les courbes de contrainte-déformation. Certains essais tels que les essais de cisaillement sont réalisés munis d'une caméra. La corrélation d'image est alors utilisée pour identifier les champs de déplacement et en déduire les déformations locales, qui sont des données importantes lors d'essais inhomogènes. Tous les faciès de ruptures sont observés au MEB et l'étude de microstructure réalisée en amont permet d'identifier les modes de rupture.

Pour représenter l'anisotropie de la plasticité observée expérimentalement, la surface de charge anisotrope proposée par Barlat et al. (2005) pour modéliser le comportement elasto-plastique de l'alliage AA7075-T651 a été utilisé. Les paramètres du modèle sont calibrés à partir des sept essais de traction uniaxiale effectués dans le plan de la tôle, du test de compression effectué dans l'épaisseur de la tôle et du test de cisaillement effectué dans la direction de laminage. Les simulations numériques de tous les essais expérimentaux sont réalisées avec le modèle elasto-plastique ainsi calibré. Les courbes de contraintes-déformations simulées sont en accord avec les courbes expérimentales pour tous les essais, y compris les essais sur éprouvettes entaillées n'ayant pas été utilisés pour calibrer le modèle. On s'aperçoit notamment que la surestimation du niveau de contrainte, généralement observée pour ces derniers tests, est atténuée par la prise en compte de l'anisotropie de la plasticité. Les états locaux de contrainte et déformation des éléments situés aux lieux de rupture obtenue expérimentalement sont extraits et permettent d'expliquer les observations précédentes. Ces états locaux pouvant être particulièrement inhomogènes amènent à se poser la question de la pertinence d'une unique relation entre déformation à rupture et triaxialité de contrainte.

Plusieurs approches analytiques sont ensuite évaluées dans l'espoir de modéliser la rupture de notre alliage. L'analyse de croissance de cavité proposée par Rice et Tracey (1969) est ici développée pour un modèle de plasticité anisotrope. Cette analyse révèle que le principal effet du modèle anisotrope se limite à la définition anisotrope du taux de déformation plastique et de la triaxialité. Ensuite, la théorie de la localisation (Rice, 1976) est développée pour différents modèles constitutifs établis dans un cadre thermodynamique. L'influence de la forme de la surface de charge, celle de la non-associativité de l'écoulement plastique, celle de la prise en compte des larges déformations ainsi que celle de conditions de chargement adiabatiques sont évaluées. Ces développements analytiques ne mènent pas à un critère de rupture directement utilisable pour le cas d'étude qu'est l'alliage AA7075-T651, mais apporte une vue

d'ensemble sur les théories existantes, leurs qualités prédictives et les limites de leur champs d'application.

Pour les applications industrielles, un critère de rupture phénoménologique dénommé AECL (Cockcroft-Latham enrichi et anisotrope) a été développé pour rendre compte de l'anisotropie. Ce critère, basé sur une variable d'endommagement liée au travail plastique, non-couplée pour cette étude, est calibré à partir des sept essais de traction uniaxiale effectués dans le plan de la tôle et du test de cisaillement effectué dans la direction de laminage. À nouveau, les simulations numériques de tous les essais expérimentaux sont réalisées avec le modèle elasto-plastique anisotrope et le critère de rupture anisotrope ainsi calibré. Une étude est réalisée pour mettre en lumière les influences respectives de l'anisotropie de la plasticité et celle de l'endommagement. Les déformations à rupture et modes de ruptures obtenus numériquement ne sont pas assez précis pour qualifier le critère AECL de prédictif. Cependant, les résultats obtenus pour les tests ayant servis à calibrer le modèle sont corrects en termes de déformation à rupture, et une extension du domaine de calibration est envisageable. Dans tous les cas, ce critère de rupture AECL associé à une technique d'érosion des éléments n'est pas capable de prédire les modes de rupture. Il est d'ailleurs objecté qu'un raffinement du maillage est une condition sine qua none de prédiction des modes de rupture.

Finalement, ce critère de rupture AECL est utilisé pour les simulations d'impact de tôle par des projectiles à extrémité ogive et tronquée. Un modèle thermoelasto-thermovisocoplastique avec surface de charge anisotrope est utilisé et la même étude paramétrique que pour les tests sur éprouvettes simples est réalisée. Les limites balistique sont évaluées et comparées aux limites obtenues expérimentalement par Børvik et al. (2010). L'anisotropie de l'écoulement plastique et du critère de rupture n'ont qu'une très faible d'influence pour les vitesses d'impact élevées. Par contre, pour les vitesses d'impact proche de la limite balistique, l'anisotropie peut modifier la prédiction numérique de façon non-négligeable. Les résultats obtenus ne sont pas systématiquement améliorés avec l'anisotropie. Néanmoins, l'anisotropie est un ingrédient important du modèle puisqu'il est le seul capable de reproduire les modes de ruptures non-axisymétrique observés par Pedersen et al. (2011). L'anisotropie mérite donc, au même titre que d'autres paramètres influents (forme de la surface de charge, coefficients thermiques ou algorithme de contact), d'être prise en compte lors du choix de modèle constitutif.

Les conclusions de cette étude sont enrichies d'une étude préliminaire réalisée dans le cadre d'un projet plus large de modélisation des PFZs. Un modèle numérique de

grain et de joint de grain avec une couche unique d'éléments 3D est simulé. Les modèles de plasticité attribués à l'intérieur des grains et aux PFZs diffèrent afin de reproduire qualitativement la localisation des déformations aux joints de grains.

Publications related to the thesis

Fourmeau, M., Benallal, A., Børvik, T., Hopperstad, O.S., 2010. Modes d'endommagement et de rupture pour quelques alliages ductiles. Colloque National MECAMAT.

Fourmeau, M., Børvik, T., Benallal, A., Hopperstad, O.S., 2011. Computation of the fracture behaviour of a high-strength aluminium alloy at low stress triaxialities. CFRAC - International Conference on Computational Modeling of Fracture and Failure of Materials and Structures.

Fourmeau, M., Børvik, T., Benallal, A., Lademo, O.G., Hopperstad, O.S., 2011. On the plastic anisotropy of an aluminium alloy and its influence on constrained multiaxial flow. International Journal of Plasticity 27 (12), 2005-2025. Special issue in honor of Nobutada Ohno.

Fourmeau, M., Børvik, T., Benallal, A., Hopperstad, O.S., 2011. Failure at low triaxialities. Workshop on Microstructural effects on damage, fracture and crashworthiness in high performance automotive material.

Fourmeau, M., Børvik, T., Benallal, A., Hopperstad, O.S., 2011. Fracture of aluminium alloy AA7075-T651. 3rd International Conference on Impact Loading of Lightweight Structures.

Hopperstad, O.S., Børvik, T., Fourmeau, M., Benallal, A., 2012. Anisotropic fracture of quasi-brittle aluminium alloy. ICTAM - 23rd International Congress of Theoretical and Applied Mechanics.

Fourmeau, M., Børvik, T., Benallal, A., Hopperstad, O.S., 2012. Anisotropic failure of aluminium alloy AA7075-T651. ESMC – 8th European Solid Mechanics Conference.

Fourmeau, M., Børvik, T., Benallal, A., Hopperstad, O.S., 2013. Anisotropic failure modes of high-strength aluminium alloy under various stress states. International Journal of Plasticity 48, 34-53.

Acknowledgements

I would like to acknowledge the precious members of the Franco-Norwegian Philarmecanic Orchestra, who I was privileged to play with:

Conductor (Tore Børvik): gather the better of every one to create an impacting harmony

Solo violin (Odd Sture Hopperstad): the noble instrument, which lightness arises from great virtuosity

Solo cello (Ahmed Benallal): which sound diffusion bifurcates to localize in ear and create remarkable gradients of emotions

Violins (Simlab-team): all together, promising a sunny-friday hyttatur

Violas (Simlab friends flying to Sintef): the “small-big sisters” of violins

Cellos (Lmt-team): which rich melodies are resourcing, up to exhausting

Double basses (Raka Bumedijsen, Trond Auestad, Tore Wisth, Hans I. Lange): laughing backstage, but essential to the orchestra balance

Piccolo (Calin Marioara, Patrick Aïmediou): a uniquely high tessitura opening towards invisible sounds

Flute (Stephane Dumoulin): which crystal sound and technicity are widely-appreciated

Clarinet (Vegard Martinsen, Ida M. Larsen): neighbouring and laughing with (at) the oboe

Bassoon (Ketill Olav Pedersen): the “grand-father”, quite-strength of the woods

Horn (Odd-Geir Lademo): a majestic presence expressed through endless and remarkable solos

Trumpet (Rodrigue Desmorat): an explosive and inspiring classic, recognizable from far away

Percussion (Torodd Berstad, David Morin): which stability and accuracy relieve the orchestra

Harp (Egil Fagerholt): giving a full picture with only one chord

Triangle (Alexandre Kane): contrary to common idea, has the most important resonance effect

Administration (KT, LMT-Cachan): organizing rehearsals and concerts as well as world tours

Financial founding (Norwegian Research council): providing furniture, sounds and light systems

Content

Preface	i
Abstract.....	iii
Résumé	v
Publications related to the thesis	ix
Acknowledgements	xi
Content	xiii
Notations	xvii
Chapter 1. Introduction	1
1.1 Background.....	1
1.2 Plastic anisotropy towards failure.....	2
1.3 Failure mechanisms	4
1.4 Structural simulations	6
1.5 Objectives and scope	8
1.6 Invariants of the stress tensor.....	9
Chapter 2. The AA7075-T651 aluminium alloy.....	11
2.1 Introduction.....	11
2.2 Optical microscope analysis	11
2.3 Scanning electron microscope (SEM) analysis	12
2.4 Transmission electron microscope (TEM) analysis.....	14
Chapter 3. Experimental study.....	19
3.1 Introduction.....	19
3.2 Tensile tests on smooth axisymmetric specimens (uniaxial tension)	21
3.3 Tensile tests on notched axisymmetric specimens (multiaxial tension).....	26

3.4	Compression tests on cylindrical specimens (uniaxial compression)	28
3.5	Shear tests on butterfly specimens	32
3.6	Fracture surfaces and strain ratios	36
Chapter 4. Anisotropic plasticity model		41
4.1	Introduction	41
4.2	Constitutive model	41
4.3	Identification of the Yld2004-18p material constants	44
4.3.1	The shape parameter m	44
4.3.2	The anisotropy parameters	44
4.4	Numerical procedures and finite element models	48
Chapter 5. Numerical analysis		51
5.1	Introduction	51
5.2	Macroscopic stress-strain curves	51
5.2.1	Isotropic version of Yld2004-18p	52
5.2.2	Anisotropic version of Yld2004-18p	54
5.2.3	Influence of plastic anisotropy	56
5.3	Local stress and strain along fracture surface	59
5.4	Conclusions	64
Chapter 6. Analytical considerations		67
6.1	Introduction	67
6.2	Void growth approach for anisotropic materials	67
6.2.1	Rice and Tracey analysis	68
6.2.2	Extension of the Rice and Tracey analysis for anisotropic matrix behaviour	72
6.2.3	Conclusions	73
6.3	Localization criteria	74
6.3.1	General constitutive framework	74
6.3.2	Localization analysis for a homogeneous material	78
6.3.3	Some applications	81
6.3.4	Conclusions	87

Chapter 7.	Anisotropic failure criterion	89
7.1	Introduction.....	89
7.2	Extended Cockcroft–Latham (ECL) criterion	89
7.3	Anisotropic extended Cockcroft–Latham (AECL) criterion	91
7.4	Quasi-static tests at different stress triaxialities.....	94
7.4.1	Numerical aspects.....	95
7.4.2	Analysis of results	96
Chapter 8.	Structural impact of AA7075-T651 plates	105
8.1	Introduction.....	105
8.2	Experimental and numerical results from Børvik et al. (2010)	105
8.3	Anisotropic thermoelastic-thermoviscoplastic constitutive relations.....	110
8.4	Numerical results and discussion.....	112
8.4.1	Ballistic limit curves and velocities.....	113
8.4.2	Anisotropy versus isotropy.....	114
8.4.3	Sensitivity study	116
8.5	Conclusions.....	119
Chapter 9.	Conclusions and further work	121
9.1	Conclusions.....	121
9.2	Further work	126
	References	131
	Appendix	141
A.	Elastic 4 th order tensor and related.....	141
B.	Thermodynamic framework	143
C.	Localization condition with infinitesimal strains - solutions.....	145
D.	Localization condition with finite strains – formulation and solutions	150
E.	Localization condition with adiabatic conditions - formulation	155
F.	Particular yield functions	156

Notations

The notations used in the manuscript are summed up in the table below. The variables with no denomination and the notations used in the Appendix are not reported for the sake of lightness.

x	scalar
\underline{x}, x_i	1 st order tensor (vector) and components $i \in \{1, 2, 3\}$
\mathbf{x}, x_{ij}, x_k	2 nd order tensor, components $(i, j) \in \{1, 2, 3\}$ and principal values $k \in \{I, II, III\}$
\mathbf{X}, X_{ijkl}	4 th order tensor and components $(i, j, k, l) \in \{1, 2, 3\}$
$\cdot, :, \otimes$	Simple, double contracted and dyadic product between tensors
$\text{diag}(\)$	diagonal matrix
$\text{tr}(\)$	trace of a matrix
RD	rolling direction of the plate (also denoted 0° direction)
TD	transverse direction of the plate (also denoted 90° direction)
ND	normal direction of the plate (also denoted thickness direction)
LS, TS	longitudinal and transverse direction of the specimen
EBSD	electron back-scatter diffraction
SEM	scanning electron microscope
TEM	transmission electron microscope
EDS	energy dispersive spectroscopy
PFZ	precipitate free zone
GB	grain boundary
HAGB	high angle grain boundary
LAGB	low angle grain boundary
l_{G-n}, l_{PFZ}	average length of a grain in the n direction and of a PFZ
GT	generalized tension
GS	generalized shear
GC	generalized compression
CT	uniaxial compression test
ST	shear test
UT	uniaxial tensile test
NT2.0	tensile test on notched specimen of notch radius $R = 2.0$ mm
NT0.8	tensile test on notched specimen of notch radius $R = 0.8$ mm
σ	stress tensor
\mathbf{s}	deviatoric stress tensor

\mathbf{I}	2 nd order identity tensor
I_1	first invariant of the stress tensor
J_2	second invariant of the deviatoric stress tensor
J_3	third invariant of the deviatoric stress tensor
σ_H	hydrostatic stress
σ_{eq}	von Mises equivalent stress
ξ	normalized third stress invariant
θ_L	Lode angle
μ_L	Lode parameter
σ^*	stress triaxiality ratio
σ	Cauchy stress obtained experimentally
ε	logarithmic longitudinal strain obtained experimentally
$\boldsymbol{\varepsilon}$	strain tensor
$\boldsymbol{\varepsilon}^e$	elastic strain tensor
E	Young's modulus
E'	apparent Young's modulus
ν	Poisson ratio
μ	shear modulus
K	bulk modulus
ρ	density
E_t	elasto-plastic tangent modulus
a, R	geometrical parameters of the notched specimens
h_0, D_0	initial height and diameter of the cylindrical specimens
F	reaction force measured by the machine
L_0, D_0, A_0, V_0	initial length, diameter, area, and volume of a specimen
L, D_n, A, V	current length, diameter in the n direction, area and volume of a specimen
DIC	digital image correlation
ε_{eff}	effective strain obtained experimentally
ε_f	effective strain at failure obtained experimentally
α	in-plane direction of a specimen
R_α	strain ratio in the α direction
$\dot{\varepsilon}_n^p$	current plastic strain rate in the n direction
r_α	flow stress ratio in the α direction
R_{biax}	strain ratio for compression tests in the ND
r_{biax}	flow stress ratio for compression tests in the ND
σ_C	yield stress under uniaxial compression in the ND
$\hat{\boldsymbol{\sigma}}, \dot{\hat{\boldsymbol{\sigma}}}$	corotational stress tensor and corotational rate-of-stress tensor
$\mathbf{R}, \mathbf{F}, \mathbf{U}$	rotation, deformation gradient and right stretch 2 nd order tensors
\mathbf{d}	rate-of-deformation tensor (symmetric part of the velocity gradient)
$\hat{\mathbf{d}}$	corotational rate-of-deformation tensor
$\hat{\mathbf{d}}^e, \hat{\mathbf{d}}^p$	elastic and plastic part of $\hat{\mathbf{d}}$
$\hat{\mathbf{C}}_{el}$	4 th order elastic tensor

f	yield function
$\bar{\sigma}$	equivalent stress defined by a chosen yield function
$\dot{\lambda}$	plastic multiplier
$\dot{\bar{p}}$	equivalent plastic strain rate (conjugate of $\bar{\sigma}$)
\bar{p}	accumulated plastic strain associated to $\dot{\bar{p}}$
\bar{p}_f	accumulated plastic strain at failure
Yld2004-18p	anisotropic non-quadratic yield function from Barlat et al. (2005)
ϕ	Yld2004-18p potential
m	yield shape parameter
$\hat{\mathbf{C}}', \hat{\mathbf{C}}'', c'_{ij}, c''_{ij}$	4 th order tensors and components from the Yld2004-18p function $(i, j) \in \{1..6\}$
\mathbf{T}	deviatoric transformation 4 th order tensor
κ	plastic hardening law
σ_0	yield stress under uniaxial tension in RD
Q, C	Voce hardening law coefficients
σ_{PFZ0}	yield stress inside the PFZ
Q_{PFZ}, C_{PFZ}	Voce hardening law coefficients for the PFZ
$\hat{\mathbf{C}}_{el}^T, \mathbf{E}^T, \boldsymbol{\kappa}^T$	thermo-visco versions of $\hat{\mathbf{C}}_{el}, \mathbf{E}, \boldsymbol{\kappa}$
γ_f	friction coefficient between a AA7075-T651 specimen and steel platens
h_e	mesh size
RT	Rice and Tracey
R_0, \dot{R}_0	initial void radius and average void growth rate
$(\underline{\mathbf{e}}_R, \underline{\mathbf{e}}_\theta, \underline{\mathbf{e}}_\phi)$	spherical coordinate system associated to the spherical coordinates (R, θ, ϕ)
$d\Omega$	solid angle
$(\mathbf{S}, \boldsymbol{\Sigma}, \dot{\mathbf{E}})$	value of $(\mathbf{s}, \boldsymbol{\sigma}, \dot{\boldsymbol{\varepsilon}})$ tensors at infinity
Q_e, Q_i	external and internal power
V, V_m, V_v	total, matrix and void volume
S_∞, S_v	surface of matrix at infinity and surface of the void
$\dot{\mathbf{u}}, \dot{\mathbf{u}}^D, \dot{\mathbf{u}}^E$	total, radial and non-radial velocity field
D, E	amplitude of radial and non-radial velocity fields
Σ_H, Σ_{eq}	hydrostatic and equivalent stress at infinity
\dot{p}, \dot{P}	equivalent plastic strain rate (conjugate of σ_{eq}) and value at infinity
\dot{E}_{RR}	radial component of the tensor $\dot{\mathbf{E}}$
μ_{RT}	third invariant of the strain rate tensor
\mathbf{M}	Hill matrix composed of F, G, H, L, M, N parameters
h, x^h	Hill parameter in RT and Hill version of any variable x
LC	localization condition
x^i, x^a, x^j	isothermal, adiabatic and Jaumann formulation versions of any variable x
$\mathbf{L}, \mathbf{E}, \mathbf{H}$	4 th order tangant modulus, elastic modulus and elasto-plastic modulus
ψ	thermo-mechanical potential
F	plastic flow potential
s	entropy

T	temperature
α^{th}	thermal dilatation coefficient
c^{th}	specific heat
(ζ_i, Z_i)	inelastic internal variables and associated driving forces
ω	spin tensor: anti-symmetric part of the velocity gradient
h	hardening modulus
\underline{n}	normal vector to the band
\underline{g}	intensity of the discontinuity vector
h_k, h_{ij}	hardening modulus solutions of the LC $(i, j, k) \in \{1, 2, 3\}$
h_c	critical hardening modulus
T_m, T_r	melting and reference temperature
CL	Cockcroft-Latham failure criterion
IT	integral Tresca failure criterion
(A)ECL	(anisotropic) extended Cockcroft-Latham failure criterion
D, D_C	damage variable and critical damage
S_0, s_0	damage evolution parameters
ϕ	weighing parameter of the damage evolution
\mathbf{P}, P_i	anisotropy diagonal matrix for the damage evolution and components $i \in \{1..6\}$
$s_A, s_{\sigma A}$	anisotropy coefficients of the damage evolution
W_C	critical plastic work
$W_{C\sigma}, W_{Cshear}$	W_C under uniaxial tension and shear in RD
v_i, v_r	impact and residual velocity of a projectile
v_{bl}	ballistic limit of a target
a, p	Recht-Ipson law coefficients
β^{th}	Taylor-Quinney coefficient
RVE	representative volume element
L_G, L_{PFZ}	length of a grain and PFZ in the numerical model
A_{G-PFZ}	numerical ratio between grain and PFZ length
a_{G-PFZ}	experimental ratio between grain and PFZ length

The Voigt notation used to transform the stress and strain tensors into vectors (LSTC, 2007) is

$$\boldsymbol{\sigma} = \begin{bmatrix} \sigma_{xx} & \sigma_{xy} & \sigma_{zx} \\ & \sigma_{yy} & \sigma_{yz} \\ sym & & \sigma_{zz} \end{bmatrix} \Rightarrow \boldsymbol{\sigma} = \begin{bmatrix} \sigma_{xx} \\ \sigma_{yy} \\ \sigma_{zz} \\ \sigma_{xy} \\ \sigma_{yz} \\ \sigma_{zx} \end{bmatrix}, \quad \boldsymbol{\varepsilon} = \begin{bmatrix} \varepsilon_{xx} & \varepsilon_{xy} & \varepsilon_{zx} \\ & \varepsilon_{yy} & \varepsilon_{yz} \\ sym & & \varepsilon_{zz} \end{bmatrix} \Rightarrow \boldsymbol{\varepsilon} = \begin{bmatrix} \varepsilon_{xx} \\ \varepsilon_{yy} \\ \varepsilon_{zz} \\ 2\varepsilon_{xy} \\ 2\varepsilon_{yz} \\ 2\varepsilon_{zx} \end{bmatrix} \quad (1)$$

Also, a linear transformation applied to this 1st order tensor in Voigt notation is a 6×6 matrix and corresponds to a 4th order tensor applied to a symmetric 2nd order tensor with usual notations.

Chapter 1. Introduction

1.1 Background

Context

For the last decades, components made of high-strength aluminium alloys have been increasingly used by the industry. For such alloys, the modelling of fracture has become important as the strength is obtained at the expense of ductility. These components are obtained after various manufacturing operations, e.g. extrusion and rolling processes, which impose extremely large deformations to the material. These operations may lead to strongly anisotropic properties, which cannot always be neglected if one wishes to correctly represent the mechanical behaviour of the processed material. On the one hand, the yielding is often anisotropic when texture exists, i.e. there is a preferential crystallographic orientation of the grains. This anisotropic yielding can have an influence on the plastic flow and therefore on the stress state. On the other hand, the failure process, resulting in a failure mode and a strain at failure, can also be anisotropic. The plastic anisotropy is believed to have an influence on the failure through the resulting stress state and through the deformation incompatibilities between grains. Also, the anisotropic distribution of microstructural features (such as particles and grain boundaries for instance) is believed to play a role in the failure process. For industrial applications, a quantification of the influence of these multiple anisotropies is helpful to ensure relevant and efficient modelling. Depending on the purpose, different modelling scales or approaches might be necessary to exhibit correctly these anisotropies.

AA7075-T651 aluminium alloy

This thesis focuses on the high-strength aluminium alloy AA7075-T651 in the form of 20 mm thick plates. This alloy was developed by the Japanese company Sumitomo metal, in 1936. In the later 40's the Imperial Japanese Navy started to use this alloy in the Mitsubishi A6M Zero fighter's air frame. Then, the AA7075 was sold under various trade names such as Zircal, Ergal

and Fortal Constructal (www.wikipedia.com). Due to its high strength-to-density ratio, this alloy is often used in transport applications such as automotive or aviation industries, but also in civil and military protection systems (Pedersen et al., 2011). However, the AA7075-T651 alloy has low resistance to corrosion, which limit the applications to non-corrosive environments. Depending on the application, the loading conditions seen by the alloy are from quasi-static (10^{-3} s^{-1}) to impact loading (10^6 s^{-1}), and the stress triaxiality state varies from negative (compressive) to highly positive (multiaxial tension). These various loadings will be investigated in the following of the thesis. **Chapter 2** presents the microstructural study performed by scanning electron microscope and transmission electron microscope on the AA7075-T651 in order to identify its texture, grain morphology and grain boundary characteristics.

1.2 Plastic anisotropy towards failure

Plastic anisotropy

Since metallic materials are often provided as extruded or rolled plates, the deformation-induced plastic anisotropy is an important aspect of their material behaviour. Due to their crystallographic texture, the yielding behaviour of such materials depends on the loading direction. The plastic behaviour of a metallic material is usually described through a yield surface in stress space, the associative flow rule and an isotropic hardening law. Since the pioneering work of Hill (1948), a tremendous effort has been made during the last two decades to improve the modelling of anisotropy in macroscopic models (Hill, 1987, 1990; Van Houtte et al., 1989; Arminjon and Bacroix, 1991; Barlat and Chung, 1993; Karafillis and Boyce, 1993; Arminjon et al., 1994; Barlat et al., 2003; Bron and Besson, 2004; Van Houtte and Van Bael, 2004; Choi et al., 2006; Leacock, 2006; Aretz et al., 2007; Hu, 2007; Kim et al., 2007; Monchiet et al., 2008; Soare and Barlat, 2010). The modelling of plastic anisotropy is still a difficult task for macroscopic models and particularly for complex multiaxial paths. The use of crystal plasticity theories can help in this direction, but their use is restricted by computational limitations and the observation that they do not predict the flow stress and the plastic flow simultaneously, as shown for instance in Darrieulat and Montheillet (2003) and Lopes et al. (2003).

Hydrostatic stress influence

Most theories of plasticity assume that the hydrostatic pressure has no or very limited effect on the strain hardening of metals and metallic alloys. Another common assumption in these theories is plastic incompressibility. Since the beginning of the eighties, Richmond and Spitzig

(1980), Brownrigg et al. (1983), Spitzig and Richmond (1984) and Brünig (1999) reported pressure dependence of the flow stress for metals such as steel and aluminium. The effect of this observation is an increase in flow stress of metals with hydrostatic pressure. In these studies (despite the claimed dependence of the flow stress on the hydrostatic pressure), the plastic dilatancy is considered negligible and not related to the normality rule. Even though the effect of hydrostatic pressure was not directly studied, Freed and Sandor (1985) observed plastic volume change in uniaxial tension of the aluminium alloy AA7075-T651. They found elastic and plastic volume changes of similar magnitude and suggested plastic anisotropy to be the prime cause of this plastic compressibility.

Modelling of the AA7075-T651 plastic anisotropy

The objective of **Chapter 3** and **Chapter 4** of this thesis is to analyse in detail the effects of anisotropy on the mechanical behaviour and constrained plastic flow for the high-strength aluminium alloy AA7075-T651. In these chapters, only its effects on the yielding behaviour of the alloy are considered. Though some works (see e.g. Stoughton and Yoon, 2009; Rousselier, 2010) have studied the effect of anisotropy on strain hardening of aluminium alloys, elastic behaviour and strain hardening are here assumed isotropic. The hardening parameters are identified from tensile tests in the rolling direction of the plate. The yield surface is represented by the linear transformation-based yield function Yld2004-18p proposed by Barlat et al. (2005), and a corotational formulation (Belytschko et al., 2000) is adopted to simplify the formulation of plastic anisotropy. The stress measure is defined with respect to the un-rotated configuration and expressed in the rectangular Cartesian coordinate system corresponding to the principal axes of anisotropy of the material. This formulation was successfully used by e.g. Grytten et al. (2008) to model the plastic behaviour of the aluminium alloy AA5083-H116. The defined yield function together with the associative flow rule presumes pressure insensitivity. In this thesis, the yield criterion is identified through tension tests on smooth tensile specimens with longitudinal axes aligned at different directions with respect to the rolling direction of the plate and compression test in the thickness direction of the plate. Both the directional yield stresses and the ratios of transverse to thickness plastic strain increments are measured and used to identify the coefficients of the yield function. The shear test performed in the rolling direction is also used to enhance the calibration by using a trial and error method. The model is then applied in non-linear finite element simulations to reproduce the plastic behaviour of different type of specimens (notched axisymmetric specimens, butterfly shear specimens and cylindrical specimens for compression tests) cut from different material directions. It will be shown that the effects of anisotropy must be taken into account for a good representation of the mechanical behaviour of the alloy at various stress states.

Plasticity towards failure

In addition to anisotropic yielding (Hill, 1948; Barlat et al., 2005; Rousselier et al., 2012), some alloys also show anisotropic failure (e.g. Chen et al., 2009; Holmen et al., 2013). The stress triaxiality and the strain intensity are usually considered the most important factors that control the initiation of fracture. Therefore, the deformation and loading histories are important to correctly predict failure. In that context, using an appropriate anisotropic model for aluminium alloys is an essential step to enable a proper description of the damage leading to anisotropic fracture. In **Chapter 5**, based on the experimental and numerical work presented in Chapter 3 and Chapter 4, the effect of the anisotropy on the effective strain to failure is evaluated taking into account the stress triaxiality and the direction of loading. These effects are then discussed.

1.3 Failure mechanisms

The variety of fracture mechanisms for aluminium alloys have been investigated for more than four decades, and fracture maps were presented by Teirlinck et al. (1988). In this part, only the mechanisms observed in the failure of the aluminium alloy AA7075-T651 are introduced.

Void growth at high stress triaxialities

At high stress triaxiality, voids can nucleate around particles or materials defects, then grow and coalesce to lead to final ductile failure. The growth mechanism was first described analytically for an infinite perfectly plastic isotropic medium containing either a cylindrical void by McClintock (1968) or a spherical void by Rice and Tracey (1969). These studies revealed that the growth of a void is controlled by the stress triaxiality factor and the plastic strain intensity. Later, Gurson (1977) derived an expression for the yield locus of an isotropic medium containing a spherical void. Since these pioneering works, the description of the void growth mechanism has been enriched in many different ways, as outlined in a recent review by Lecarme et al. (2011). Criteria describing nucleation and coalescence of voids were included in the Gurson model by Chu and Needleman (1980) and Tvergaard and Needleman (1984), leading to the well-known GTN model. Hahn and Rosenfield (1975) pointed out that two populations of particles of different magnitude are involved in the fracture process at different levels. Void growth occurs around large constituent particles, while localization leading to coalescence is facilitated by void growth around smaller dispersoids. The void shape effect was further introduced in the Gurson model by Gologanu et al. (1993–1994a). In parallel, the distribution of spherical voids in an isotropic matrix has been numerically investigated by Gologanu et al. (1994b), showing that an anisotropic distribution could influence the

coalescence process. More recently, Pardoan and Hutchinson (2000) proposed to couple this model with the Thomason criterion (Thomason, 1990) for void coalescence. Yerra et al. (2010) numerically described the fracture inside a grain using a crystal plasticity material model around a spherical void. Inclusion of the anisotropy in the Gurson approach was studied by Benzerga and Besson (2001), while Monchiet et al. (2008) analysed the role of anisotropy both on the yield behaviour and the growth of voids. The first part of **Chapter 6** presents the analytical solution of Rice and Tracey (1969) and quantifies the influence of an anisotropic plastic model on the rate of void growth. In addition, these developments point out the assumptions necessary to obtain the well-known exponential triaxiality dependence of the void growth, in particular the influence of the third invariant, often omitted for its assumed small effect. However, despite extensive developments, the theory only considers the void growth mechanism, which is not the only one occurring in metallic materials.

Modelling of failure at lower stress triaxialities

At lower and negative stress triaxiality states or shear dominated loadings, fracture often occurs by shear localization. Efforts have been made to reproduce experimental observations under such conditions. These models are often empirical, since the physics of the underlying fracture process is not clearly identified. For instance, Khan and Liu (2012) proposed a new empirical failure criterion based on the relationship between the hydrostatic pressure and the magnitude of the stress vector and obtained better results than with other well-established criteria, such as the maximum shear stress criterion (Stoughton and Yoon, 2011), the von Mises criterion (J_2 -based) and the Xue-Wierzbicki criterion (Wierzbicki et al., 2005). Based on experimental tests at low stress triaxialities, Bao and Wierzbicki (2004) observed that the strain to failure drops at stress triaxialities close to zero. They proposed to distinguish between void growth, which is predominant at high stress triaxialities, and shear fracture, which dominates at low stress triaxialities. Barsoum and Faleskog (2007) have shown experimentally the influence of the third invariant of the deviatoric stress tensor on ductile failure, while Nahshon and Hutchinson (2008) introduced the third invariant in the Gurson model to reproduce the shear dominated failure mode observed at low stress triaxiality states. To introduce the influence of the third invariant, Bai and Wierzbicki (2010) proposed a modified Mohr-Coulomb fracture criterion formulated in the space of stress triaxiality, Lode angle and equivalent plastic strain. Dunand and Mohr (2011) showed the capabilities of such models to predict fracture of an aluminium alloy over a large range of stress triaxialities and values of the Lode parameter. Gruben et al. (2012) proposed an extension of the Cockcroft-Latham (ECL) failure criterion and analysed the influence of the third invariant captured by this criterion. In a similar way as done for anisotropic yielding, Luo et al. (2012) proposed an anisotropic damage evolution based on a linear transformation of the plastic strain-rate tensor. The six parameters can be calibrated

using the same tests as those for calibration of the anisotropic yield function. **Chapter 7** presents the combination of this anisotropic linear transformation with the uncoupled ECL failure criterion called the anisotropic extended Cockcroft-Latham criterion (AECL). This criterion is then calibrated for the AA7075-T651 alloy and its predictive capability is evaluated using the tests presented in Chapter 3.

Localization analysis

A phenomenological model was developed by Benallal et al. (2008) to predict the localization of strains along an inclined band and its propagation for the aluminium alloy AA5083 exhibiting the Portevin-Le Chatelier effect. A usual approach to model localization of strains is to envisage a bifurcation in the material model. When a ductile metal is deformed into the plastic range, a localized zone of deformation sometimes appears in the form of a narrow band in highly stressed regions, not only at low stress triaxiality states. A typical example is the tensile failure of a sheet material by the so-called process of localized necking. The non-uniform deformation within the band generally leads to ductile fracture by various mechanisms. In the context of ductile fracture, the mechanisms of growth and coalescence of voids presented earlier are often advocated (see e.g. Rice and Tracey, 1969). However, it is not always clear whether the localization occurs because of the progressive softening of the material due to void growth (see e.g. Gurson, 1977) or because some other instability of the plastic flow process first occurs (see e.g. Rice, 1976). Rudnicki and Rice (1975) and Rice (1976) formulated the analytical condition for the localization of strains along a band in a previously homogeneous solid. **Chapter 6** presents, in addition to the Rice and Tracey analysis, the condition of localization for various elasto-plastic material models (following a thermodynamic framework) and evaluates its capability to predict physical observations.

1.4 Structural simulations

Ballistic application

For a material such as the AA7075-T651 aluminium alloy, exhibiting various failure modes and significant anisotropy, one must keep in mind the computational cost/efficiency constraint imposed by the industrial context. Indeed, plastic anisotropy modelling brings an additional experimental cost compared with isotropy, and physically-based failure criteria are computationally demanding. Due to a large number of elements necessary for structural simulations, such as ballistic impact, the CPU time can increase dramatically even with simple material models (Børvik et al., 2010). Therefore, the contribution of the previously presented models to the validity of numerical prediction must be evaluated. **Chapter 8** presents the

numerical simulations of ballistic impact against the AA7075-T651 plate with blunt and ogival projectiles. Both the anisotropic plasticity model (presented in Chapter 4) and the anisotropic failure criterion (presented in Chapter 7) are used. The predictive capability of the anisotropic model is evaluated and the influence of anisotropy is quantified.

Microstructure modelling

Experimental observations tend to show that microstructural features (not only voids) can play an important role in the failure process. None of the previous failure modelling approaches is capable of taking this information into account. Based on tensile tests performed in the three orthotropic directions of a rolled AA7075-T651 aluminium plate and fracture surface observations, Jordon et al. (2009) quantified the influence of two different size-order particle populations (constituent and dispersoids) on the damage process and their anisotropic characteristics. They proposed a continuum-based damage model enriched by internal variables related to the two populations of particles. Hahn and Rosenfield (1975) observed that under certain loading conditions, failure can be partly intergranular. Børvik et al. (2010) and Pedersen et al. (2011) also observed a competition between intragranular and intergranular fracture due to the existence of precipitate free zones (PFZs) along the grain boundaries. This was modelled numerically by Pardoen et al. (2003). Based on microscopic observations of the failure surface presented in Chapter 3 for the AA7075-T651 alloy, it seems that the grain morphology and inclusions (seen to be very anisotropic in Chapter 2) may also play a role in the anisotropy of failure. A numerical model of the microstructure coupled with damage models enabled Steglich et al. (2008) to represent the anisotropic ductile fracture of an aluminium alloy. Together with the conclusions, **Chapter 9** presents some preliminary results of the modelling of anisotropic grains and grain boundaries, in order to capture the localization of strains inside the PFZ.

1.5 Objectives and scope

The main objective of the study is to understand and model the anisotropy of flow and failure exhibited by high-strength aluminium alloys obtained by rolling or extrusion processes. To this end, the aluminium alloy AA7075-T651 is exclusively studied and different steps were followed:

- *Experimental campaign under quasi-static loading conditions*: several specimens were loaded until fracture to exhibit the influence of stress triaxiality on the failure strain and failure modes. Several directions were also investigated to determine the anisotropic behaviour. Microscopic observations of failed specimens enabled to identify the physical features of the failure process.
- *Anisotropic plasticity*: an anisotropic yield function was calibrated using uniaxial tension and shear tests, and numerical simulations of all tests were performed to capture the local stresses and strains at fracture.
- *Anisotropic fracture*: several theories were investigated and their capability to predict the experimental observations was evaluated. A phenomenological failure criterion was proposed, calibrated and evaluated through numerical simulations of quasi-static tests and ballistic impact experiments.

The study was limited to the AA7075-T651 alloy. All material tests were performed under quasi-static loading conditions even though ballistic numerical simulations were performed. It is believed that a good understanding of the failure mechanisms under quasi-static loading conditions is the starting point of further investigations at higher velocities (Børvik et al., 2010; Pedersen et al., 2011). Temperature effects were not studied in this thesis, but thermal parameters (used in the localization analysis and in the ballistic impact simulations) were taken from previous studies. The coupling between temperature and strain-rate effects is obviously an issue to be pursued.

1.6 Invariants of the stress tensor

Some variables and notations that are extensively used in this thesis are defined in the following. The stress invariants are given as

$$\begin{cases} I_1 = \text{tr}(\boldsymbol{\sigma}), & \sigma_H = \frac{I_1}{3} \\ J_2 = \frac{1}{2} \mathbf{s} : \mathbf{s}, & \sigma_{eq} = \sqrt{3J_2} = \sqrt{\frac{3}{2}} \mathbf{s} : \mathbf{s} \\ J_3 = \det(\mathbf{s}), & \xi = \frac{9}{2\sqrt{3}} \frac{J_3}{J_2^{3/2}} = \frac{27}{2} \frac{\det(\mathbf{s})}{\sigma_{eq}^3}, \quad \sin(3\theta_L) = -\xi \end{cases} \quad (2)$$

where I_1 is the first invariant of the stress tensor $\boldsymbol{\sigma}$, while J_2 and J_3 are the second and third invariants of the deviatoric stress tensor $\mathbf{s} = \boldsymbol{\sigma} - \sigma_H \mathbf{I}$, with \mathbf{I} the 2nd order identity tensor. σ_H is the hydrostatic stress, while σ_{eq} is the von Mises equivalent stress. Also, ξ is the normalized third stress invariant and θ_L is the Lode angle. In addition, the Lode parameter μ_L is introduced as the normalized location of the second principal ordered deviatoric stress s_{II} with respect to the first and third principal ordered deviatoric stresses s_I and s_{III} , i.e.

$$\mu_L = \frac{3s_{II}}{s_I - s_{III}} = \sqrt{3} \tan \theta_L, \quad \theta_L = \arctan\left(\frac{\mu_L}{\sqrt{3}}\right) \quad (3)$$

Figure 1.1 illustrates the definitions of the Lode parameter μ_L and the Lode angle θ_L , while Table 1.1 gives values of ξ , θ_L and μ_L for some particular loading conditions.

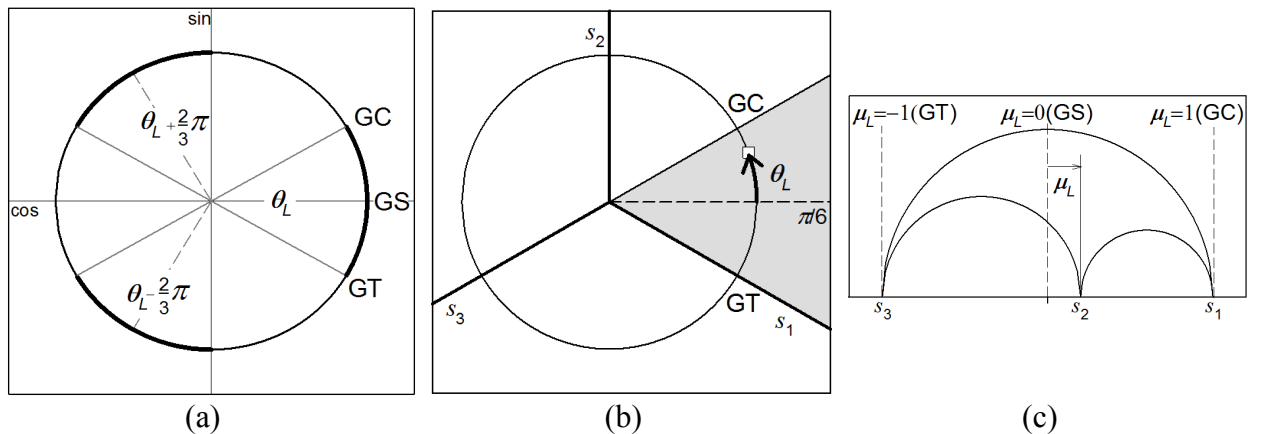


Figure 1.1. Lode angle domain (a) in a trigonometric circle and (b) in the principal deviatoric stress plane. (c) Lode parameter in the Mohr circle representation of the deviatoric stresses. Specific loadings such as generalized tension, shear and compression are specified as (GT), (GS) and (GC), respectively.

Table 1.1. Normalized third invariant, Lode angle and Lode parameter for specific loadings

Stress state	s_I, s_{II}, s_{III}	ξ	θ_L	μ_L
Generalized tension (GT)	$s_I \geq s_{II} = s_{III}$	1	$-\pi/6$	-1
Generalized shear (GS)	$2s_{II} = s_I + s_{III}$	0	0	0
Generalized compression (GC)	$s_I = s_{II} \geq s_{III}$	-1	$\pi/6$	1

A particular and convenient property of the Lode angle is that the deviatoric stress tensor \mathbf{s} can be written with principal ordered values in the principal frame, i.e.

$$\mathbf{s} = \frac{2}{3} \sigma_{eq} \begin{bmatrix} \sin\left(\theta_L + \frac{2\pi}{3}\right) & 0 & 0 \\ 0 & \sin(\theta_L) & 0 \\ 0 & 0 & \sin\left(\theta_L - \frac{2\pi}{3}\right) \end{bmatrix} \quad (4)$$

Thus, a yield function expressed in terms of principal deviatoric stresses can be easily transformed to a function of the equivalent stress σ_{eq} and the Lode angle θ_L .

Chapter 2. The AA7075-T651 aluminium alloy

2.1 Introduction

In this chapter, the microstructure of the AA7075-T651 aluminium alloy is studied at different scales. First, an optical microscope is used to disclose the grain morphology and the distribution of large particles. Second, a scanning electron microscope (SEM) and electron back-scatter diffraction (EBSD) technique are used to determine the texture of the alloy. Third, a transmission electron microscope (TEM) is used to analyse the grain boundaries at the nanometre scale.

2.2 Optical microscope analysis

The studied material is the AA7075 aluminium alloy in temper T651. The nominal chemical composition is given in Table 2.1. This high-strength aluminium alloy has nominal yield and tensile strengths in the rolling direction of 505 MPa and 570 MPa, respectively (based on data from the supplier). All material specimens presented in this study were manufactured from a 20 mm thick rolled plate. Temper T651 implies that the alloy is slightly stretched and aged to peak strength. The grain structure of the as-received AA7075-T651 plate is shown in Figure 2.1 (a) as tri-planar optical micrographs along the three orthogonal directions of the rolled plate, i.e. the rolling direction (RD), the transverse direction (TD) and the normal direction (ND).

The bulk of the AA7075-T651 alloy has a complex microstructure with different classes of particles. Coherent precipitates containing Mg and Zn, the so-called η' -phase, appear during the artificial age hardening of temper T6. The element Cu can also enter in the η' -phase composition (see Marioara et al., 2013). These precipitates are at the nanoscopic scale and densely distributed inside the grains. They contribute to the hardening of the material by preventing the dislocation movements (Park and Ardell, 1988). According to Andreatta et

al. (2003a, 2003b), 7xxx alloys also contain dispersoids of different size ($0.05\text{--}0.15\ \mu\text{m}$) and composition (Al_3Ti , Al_6Mn , Al_3Zr , $\text{Al}_{12}\text{Mg}_2\text{Cr}$, $\text{Al}_{20}\text{Cu}_2\text{Mn}_3$), acting as barriers that limit the recrystallization during tempering. This explains the non-recrystallized grain structure of the AA7075-T651 alloy with flat and elongated grains in the rolling plane of the plate. Large iron-based intermetallic inclusions (at micrometre scale), such as $\text{Al}_6(\text{Fe},\text{Mn})$, Al_3Fe , $\text{Al}(\text{Fe},\text{Mn},\text{Si})$ and $\text{Al}_7\text{Cu}_2\text{Fe}$ (or silicon-based such as Mg_2Si) are preferentially distributed along the rolling direction (RD), as quantified by Jordon et al. (2009) and illustrated in Figure 2.1 (b). This is made possible since they are formed before the rolling operations. The distribution of inclusions is of interest since they can play a major role in the fracture process.

Table 2.1. Nominal chemical composition (in wt%) of the AA7075-T651 aluminium alloy.

Al	Zn	Mg	Cu	Cr	Fe	Ti	Si	Mn	Others
Balance	5.7	2.4	1.3	0.19	0.19	0.08	0.06	0.04	0.15

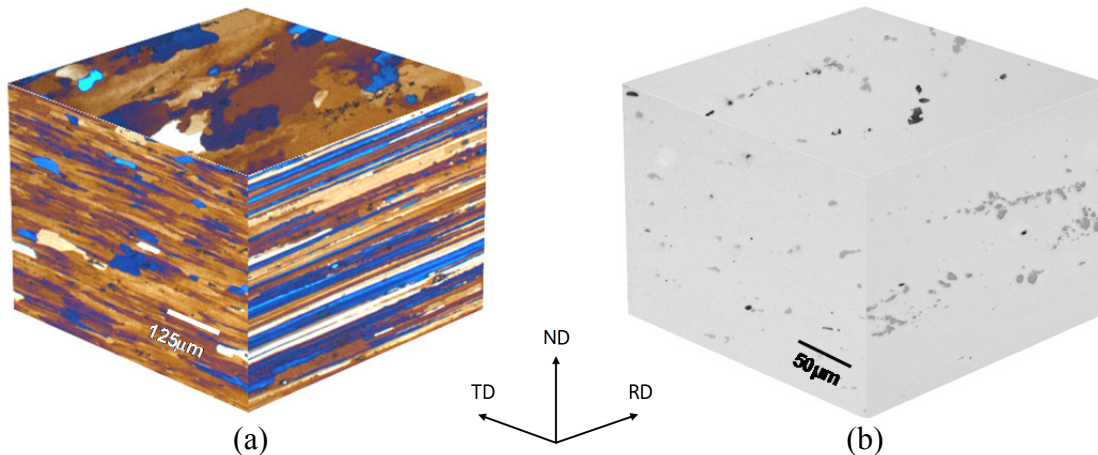


Figure 2.1. Tri-planar optical micrographs showing (a) the grain structure and (b) the distribution of inclusions for the AA7075-T651 aluminium alloy (Børvik et al., 2010).

2.3 Scanning electron microscope (SEM) analysis

The rolling process implies a crystallographic texture and leads to anisotropic characteristics (Børvik et al., 2010). The texture of the plates of AA7075-T651 was determined using the electron back-scatter diffraction (EBSD) technique in a scanning electron microscope (SEM). The scans presented in Figure 2.2 exhibit the crystallographic orientations of the alloy in the three different orthotropic planes. The black spots correspond to inclusions and no orientation is associated to them. These scans were also used to determine the average grain size in the principal directions of the plate ($l_{G-RD} = 138\ \mu\text{m}$ along RD, $l_{G-TD} = 62\ \mu\text{m}$ along TD and $l_{G-ND} = 11\ \mu\text{m}$ along ND). In average, the grains are more than 10 times longer than thick, so the grain boundaries and inclusions are 10 times more densely distributed in the normal

direction (ND) than along the rolling direction (RD) of the plate. The pole figures of the AA7075-T651 alloy presented in Figure 2.3 show that the texture is rather weak (maximum intensity of 2.596). The anisotropy of the shape of the grains and distribution of inclusions is then more important than the crystallographic texture. These are important observations in order to understand the effect of the anisotropy of the plastic flow and fracture in this particular aluminium alloy.

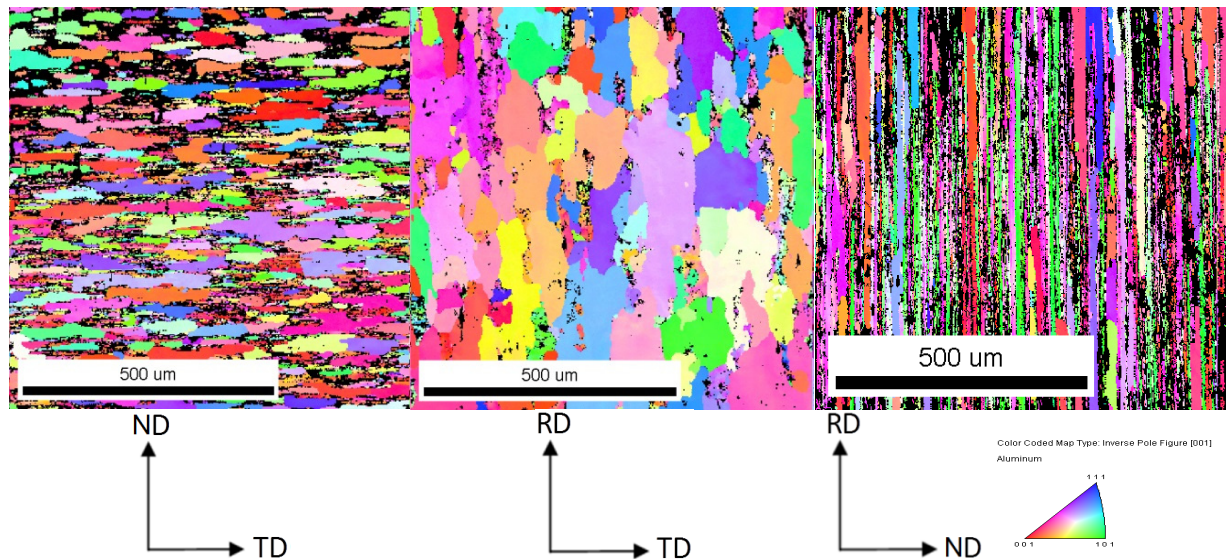


Figure 2.2. Scans giving grains and orientations in the orthotropic planes of the AA7075-T651 plates.

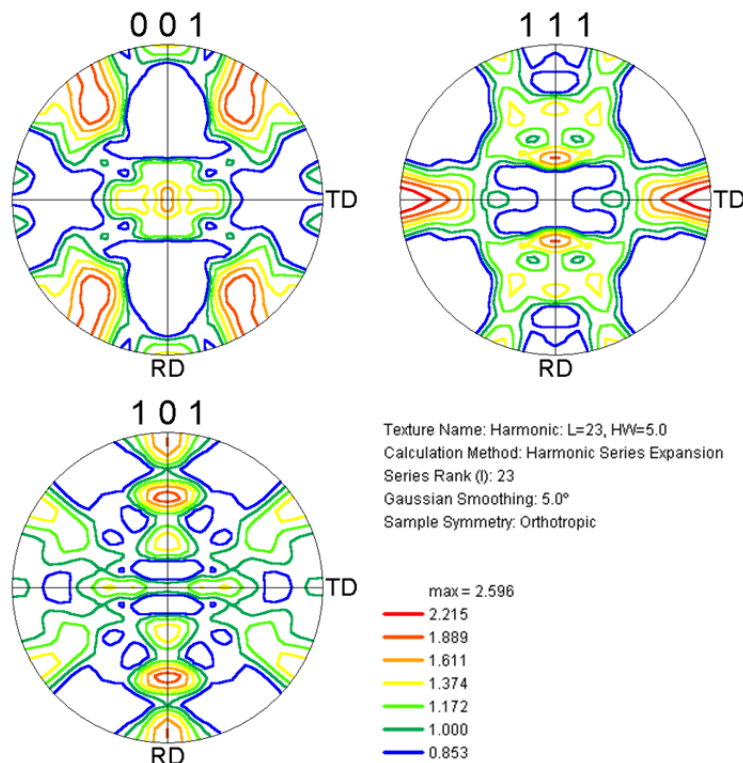


Figure 2.3. Pole figures of the AA7075-T651 plates.

2.4 Transmission electron microscope (TEM) analysis

Another very important microstructural characteristic of the 7xxx (and 6xxx) series of aluminium alloys is the presence of precipitate free zones (PFZs) at nanometre scale created during the quenching operation of the heat treatment and generally located around the grain boundaries (GBs). These zones are generally softer than the matrix hardened by precipitates. Experiments indicate that plastic strain can be highly localized inside these zones and can therefore lead to premature failure of such materials (Dumont et al., 2003). The PFZs are engendered by two closely related phenomena:

- the local depletion of vacancies which inhibits the formation of fine dispersion of precipitates
- the local solute depletion initiated by heterogeneous precipitation of phases at the GBs

These two phenomena require atom mobility and occur therefore during the thermal treatment of the alloy. The cooling rate of the quenching operation influences the width of the PFZs (Deschamps et al., 2009). For instance, a fast cooling inhibits the migration of vacancy and solute toward the GBs and therefore prevents the PFZs from growing.

A transmission electron microscope (TEM) study was performed by Calin Marioara (SINTEF Materials and Technology) on the AA7075-T651 alloy to reveal some of the features of the microstructure. Figure 2.4 (a) is taken in the plane of the plate and shows that grains are elongated and dispersoids are aligned in the rolling direction (RD). Figure 2.4 (b)–(d) shows the hardening precipitates inside the grains and the presence of PFZs along the GBs. In average, these PFZs are wider in the case of high angle grain boundaries HAGB ($l_{PFZ-H} \approx 40$ nm) than for low angle grain boundaries LAGB ($l_{PFZ-L} \approx 20$ nm). The GBs are defined as LAGB (HAGB) when the disorientation between the two neighbouring grains is $\leq 10^\circ$ ($\geq 15^\circ$) (see Verhoeven, 1975). A fortiori, sub-grains within the same grain are separated by a LAGB since they have nearly the same orientation (within a few degrees). The misfit in the orientation of two grains is accommodated by perturbations in the atomic packing. In the case of HAGBs, these perturbations become severely disordered and promote the vacancy and solute migration more than the LAGBs. The PFZ formation is then facilitated around the HAGBs. It is also observed that the LAGBs contains a higher amount of GB precipitates. In the case of 7xxx alloys, the precipitates that form at the GBs (Mg-Zn(-Cu)) need a certain degree of coherency with the matrix in order to form and grow. This cannot be achieved if the adjacent grains have large misorientations. The orientations $\langle 110 \rangle$ and $\langle 112 \rangle$ stipulated on the TEM pictures correspond to the zone axis (orientation) of the respective grains along the viewing direction.

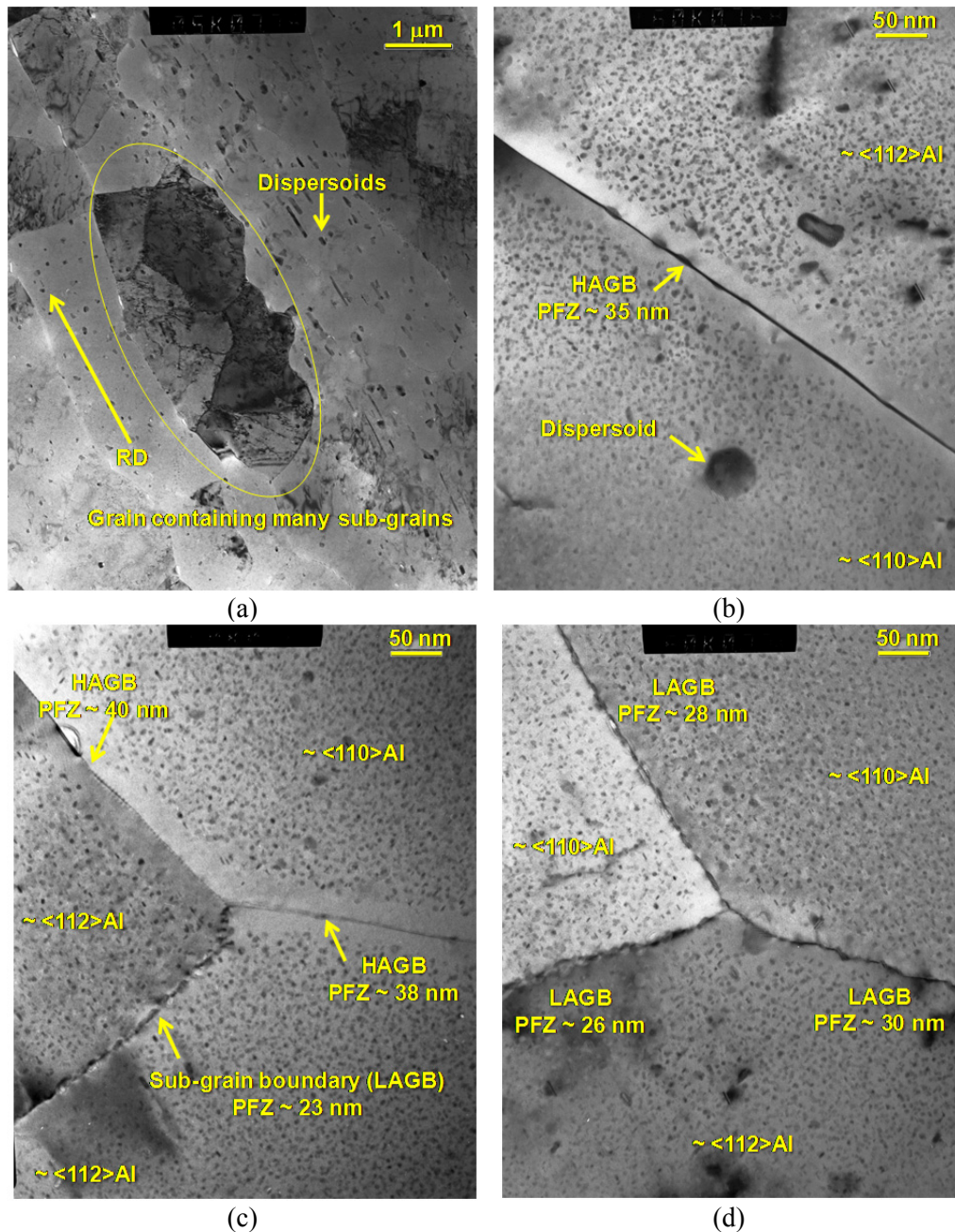


Figure 2.4. TEM pictures of the AA7075-T651 alloy (bright field CM30 operated at 150 kV).

An energy dispersive X-ray spectroscopy (EDS) analysis was performed in parallel to the TEM analysis and gave information about the chemical composition of the microstructural features. Figure 2.5 gives the maps of several alloying elements on a given scanned area. The upper-left picture in Figure 2.5 presents the scanned area and depicts a PFZ along a GB, fine precipitates in the adjacent grains, two large precipitates formed at the GB (3-4) and a large precipitate in the bulk (1) that was formed on a dispersoid (2). The five other maps given in Figure 2.5 are the spatial distribution of different alloying elements (Zn, Mg, Cu, Cr, Fe) within the area.

The following observations can be drawn from the maps

- The fine precipitates contain Zn and Mg, as expected. Based on Marlaud et al. (2010), Cu may enter the composition of the precipitates as well, but to a level below the detection limit.
- The large precipitates (1), (3) and (4) also have a Zn-Mg(-Cu) composition.
- Cr is present in the dispersoid (2) on which particle (1) is nucleated, and in another dispersoid on which particle (3) is nucleated. The alloying element Cr does not play a role in the grain/GB composition.
- Mg, Cu and to a lower extent Zn are present along the GB as thin continuous films. Figure 2.4 (b) exhibits a black GB due to layered precipitates, in contrast to the grey aluminium grain.
- Cu is also spread in solid solution inside the rest of the matrix.
- Fe has no preferential location, indicating that this element is not associated with precipitation and mostly left in solid solution. This is also the case for the elements Mn, Ti and Si, which maps are not presented here.

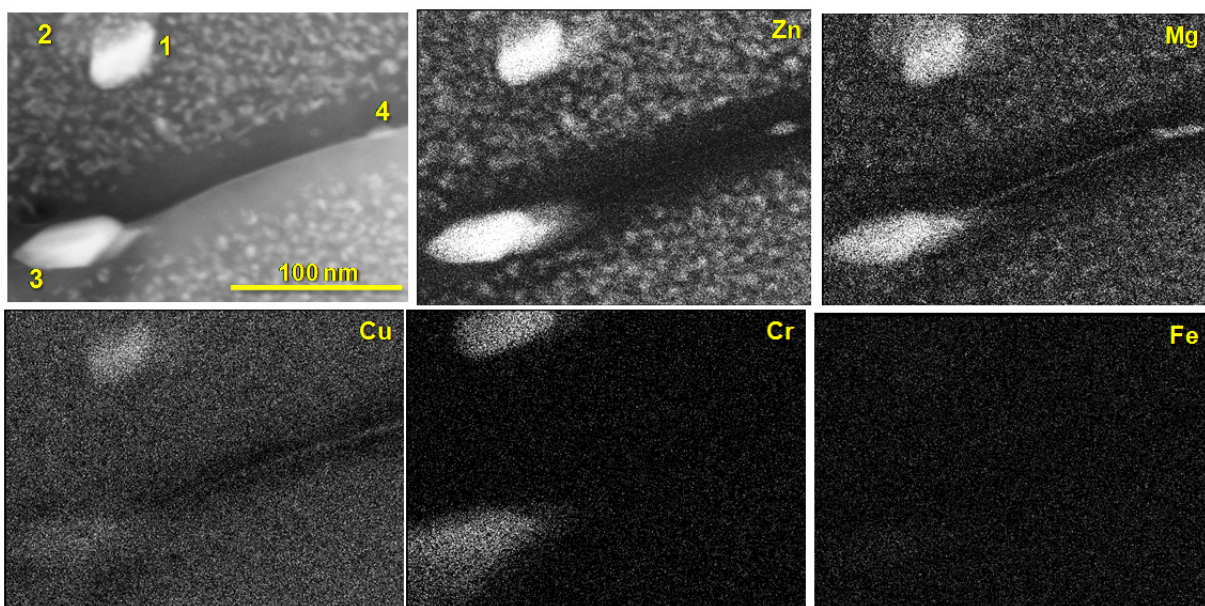
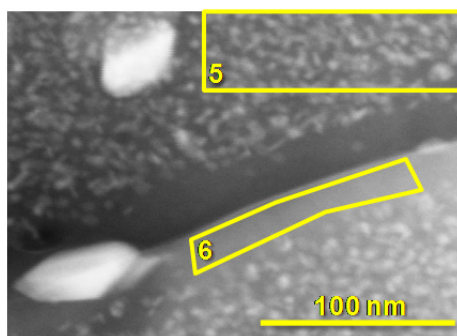


Figure 2.5. TEM image and x-ray maps for five different elements (Zn, Mg, Cu, Cr, Fe) of the AA7075-T651 alloy (Annular Dark Field Scanning TEM mode using a Jeol 2010F microscope operated at 200kV).

Figure 2.6 gives a more accurate description of the alloying content across the whole scanned area (i.e. the whole picture), inside the grain (bulk) (5) and inside the PFZ (6). These data confirm the observations made in Figure 2.5 and give the following additional information:

- Zn and Mg have slightly lower values in the bulk than in the alloy composition. This confirms the presence of a low volume fraction of large MgZn(Cu) precipitates (like (1) and (3) in Figure 2.5 nucleated on dispersoids), in addition to a much higher volume fraction of small MgZn(Cu) hardening precipitates.
- Zn, Mg and possibly Cu are depleted in the PFZ area, most probably due to the formation of MgZn(Cu) GB precipitates that use this solute.
- Compared with the bulk (5), the Zn content in the PFZ (6) is lower by a factor of 5, whereas the Mg and Cu content is only lower by a factor of 2 or less. This suggests that the PFZs contain alloying elements (except Zn) in solid solution even though it is free from precipitates.
- Cr is strongly depleted in the bulk (5) and PFZ (6), indicating that most of it is absorbed into dispersoids. However, its (low) value is similar in bulk and PFZ. This observation and the next one indicate that the formation of PFZs is a vacancy driven process. Consequently, the composition of a certain element in the PFZs should be equal to its composition in the nearby bulk. The exceptions are Zn, Mg and perhaps Cu, as mentioned above, because GB precipitates contain these elements and therefore they become depleted in the neighbouring PFZ.
- Fe, Mn, Ti and Si have similar values in all areas and close to their respective nominal compositions, indicating that these elements do not have a strong association with precipitation and therefore most of them are left in solid solution.
- Cu has unrealistically high values in all areas. This might be an artefact due to the presence of an oxide layer on the sample's surface, as a consequence of the sample preparation.



Element	Nominal	Picture	5:bulk	6:FZ
Zn	5.70	4.56	4.79	1.16
Mg	2.40	2.05	1.97	0.99
Cu	1.30	2.98	3.09	2.11
Fe	0.19	0.28	0.26	0.23
Cr	0.19	0.23	0.04	0.07
Ti	0.08	0.10	0.06	0.07
Si	0.06	0.12	0.11	0.08
Mn	0.04	0.04	0.02	0.04

Figure 2.6. STEM image and alloying content (in wt%) in different areas for the picture.

This analysis suggests that the PFZs, although often considered as pure aluminium zones inside a stronger matrix, contain non-negligible amount of alloying elements in solid solution. The behaviour of the PFZs could then differ from pure aluminium, in terms of plastic hardening for instance. These observations are both important and helpful for the modelling of the microstructure.

Chapter 3. Experimental study

3.1 Introduction

In this chapter, the various material tests performed during the project are presented. The effects of both stress triaxiality and loading direction on the plastic and fracture behaviour of the AA7075-T651 alloy are investigated. The stress triaxiality is defined as the ratio

$$\sigma^* = \frac{I_1}{3\sqrt{3J_2}} = \frac{\sigma_H}{\sigma_{eq}} \quad (5)$$

where I_1 is the first invariant of the stress tensor $\boldsymbol{\sigma}$, J_2 is the second invariant of the deviatoric stress tensor \mathbf{s} , σ_H is the hydrostatic stress and σ_{eq} is the von Mises equivalent stress. All these variables are defined in Chapter 1.6. Different specimen geometries were chosen to define a wide range of stress triaxiality states. The different geometries displayed in Figure 3.1 are designed to give initial stress triaxiality states according to Eq.(5) of $-1/3$ for the pure compression tests on cylindrical specimens, 0 for the shear tests on butterfly specimens, $1/3$ for the tensile tests on smooth axisymmetric specimens and higher than $1/3$ for the tensile tests on notched axisymmetric specimens (of notch root radius $R=2\text{mm}$ and $R=0.8\text{mm}$). Bridgman (1952) gave a theoretical expression for the maximum stress triaxiality in the centre of an axisymmetric tensile specimen after necking as

$$\sigma^* = \frac{1}{3} + \ln\left(1 + \frac{a}{2R}\right) \quad (6)$$

where a is the radius of the specimen at minimum cross section and R is the curvature radius of the neck. When the radius $R = \infty$, i.e. the specimen is smooth, the stress triaxiality takes the value of $\sigma^* = 1/3$. It should be kept in mind that this expression is based on several assumptions, such as isotropy, the von Mises yield function, homogeneous strains over the

cross section of the neck and a circular cross section throughout the test (Dieter, 1988), which are not fulfilled in our study. Even so, Eq.(6) will be used here to give an estimate of the initial stress triaxiality in the notched specimens. The notched specimens are usually used to investigate the influence of the stress state on the fracture strain, whereas the butterfly specimens allow for an approximate shear stress field. In addition, specimens were sampled in several orientations of the plate to evaluate the anisotropic properties of the material. Figure 3.1 presents the specimen geometries for the tensile tests (smooth specimens in (a)-(b) and notched specimens in (c)), the compression tests on cylinders of aspect ratio unity in (d) and the shear tests on butterfly specimen in (e).

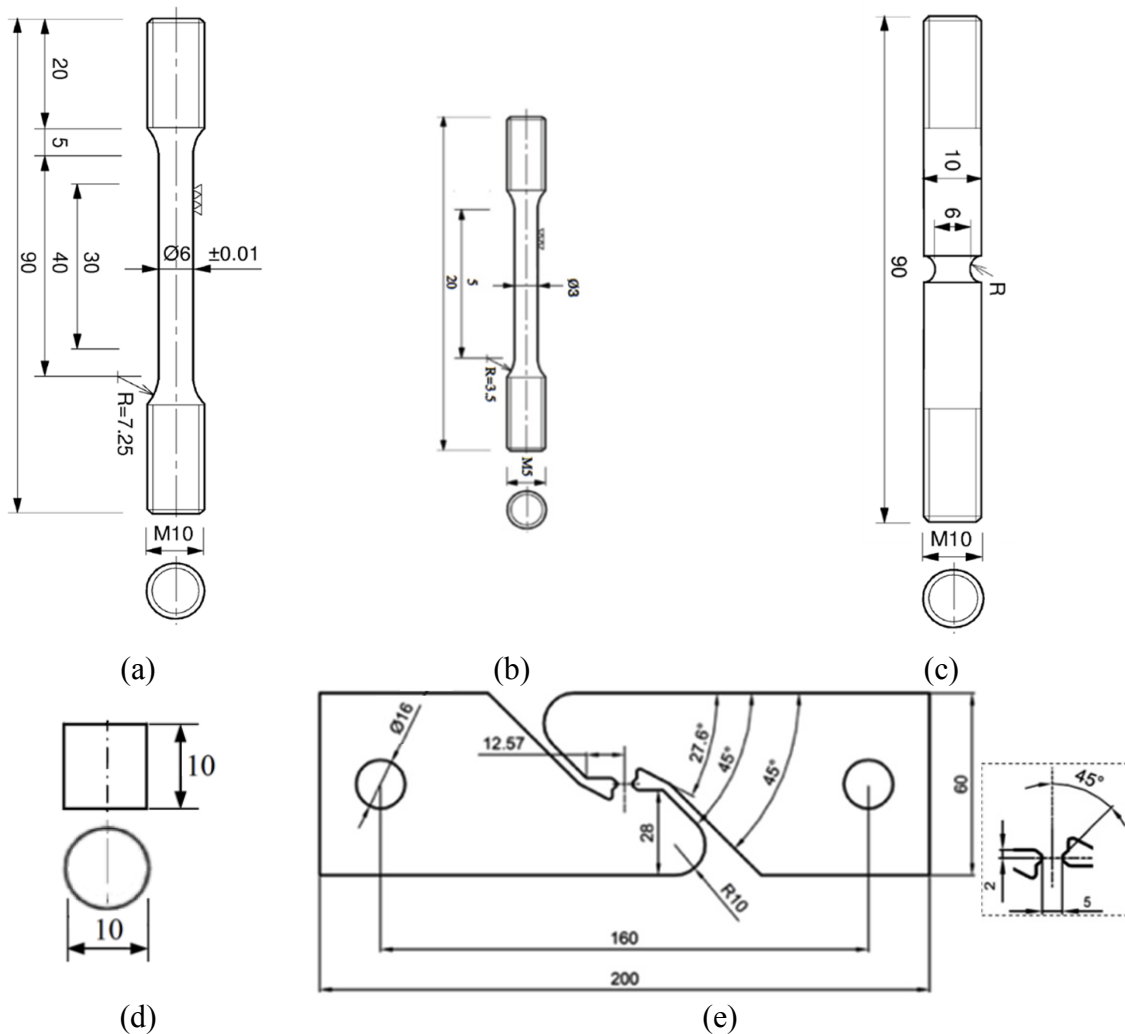


Figure 3.1. Specimen geometries for the material tests: smooth axisymmetric specimen for tensile tests (a) in-plane of the plate and (b) in ND, (c) notched axisymmetric specimen for tensile tests, (d) cylinders with $h_0/D_0=1$ for compression tests and (e) butterfly specimens for shear tests.

The tests were performed using various universal testing machines at room temperature and nominal strain-rates at the order of 10^{-3} s^{-1} (i.e. quasi-static loading conditions). Time,

force and displacement were continuously measured during all tests until fracture of the specimens. Table 3.1 sums up the number of duplicate tests performed on the AA7075-T651 alloy in each direction and for each specimen. For each type of test the following is presented:

- the experimental procedure and specimen geometry
- the post treatment of force and displacement measured from the machines
- the failure strain for all directions
- the failure mode for all directions (and in some cases micrographs)

Table 3.1. Experimental campaign with number of tests performed on the AA7075-T651 alloy.

Specimen	Initial stress state	σ^*	Direction of loading (°)							
			0	15	30	45	60	75	90	ND
Smooth axisymmetric	Uniaxial tension	1/3	5	2	2	3	2	2	3	6
Notched axisymmetric $R = 2.0\text{mm}$	Multiaxial tension	0.89	2	-	-	2	-	-	2	-
Notched axisymmetric $R = 0.8\text{mm}$	Multiaxial tension	1.39	2	-	-	2	-	-	2	-
Cylinder $h/D=1$	Uniaxial compression	-1/3	5	-	-	5	-	-	5	3
Cylinder $h/D=1.5$	Uniaxial compression	-1/3	2	-	-	2	-	-	2	-
Butterfly	Shear	0	6	-	-	7	-	-	6	-

3.2 Tensile tests on smooth axisymmetric specimens (uniaxial tension)

Tensile tests were carried on axisymmetric smooth tensile specimens with a cross-section diameter of 6mm and a gauge length of about 30mm (Figure 3.1 (a)) to study uniaxial tension stress triaxiality states. The tensile axis was oriented at 0°, 15°, 30°, 45°, 60°, 75° and 90° with respect to the rolling direction (RD) of the plate. Additional tests were performed in the normal direction (ND) of the plate on miniature smooth specimens especially designed for plates of 20mm thickness (Figure 3.1 (b)). During testing, the diameter at minimum cross section of the specimen was continuously measured until fracture. This was made possible using a purpose-built measuring rig with two perpendicular lasers that accurately measured the specimen diameter. The lasers were installed on a mobile frame to ensure that the diameters always were measured at the minimum cross section. Each laser projected a beam with dimension $13 \times 0.1\text{mm}^2$ towards the detector on the opposite side of the specimen. Thus, the two orthogonal lasers created a box of laser light of $13 \times 13 \times 0.1\text{mm}^3$ around the minimum cross section of the sample. As the specimen was deformed, the continuous change in diameters was observed by the detectors. This dual-axis micrometre was made up of a high-speed, contactless AEROEL XLS13XY laser gauge with 1 μm resolution. During elongation, the sample

was scanned at a frequency of 1200Hz and the measured data was transferred by the built-in electronics to the remote computer via fast Ethernet. The diameters were measured in the normal direction (ND) of the plate and in the transverse direction of the specimen (TS), denoted D_{ND} and D_{TS} , respectively. For the specimens loaded in the normal direction (ND), the diameters were measured in the rolling direction (RD) and in the transverse direction (TD) of the plate, denoted D_{RD} and D_{TD} , respectively.

The stress-strain curves for the duplicate tensile tests on smooth axisymmetric specimens are presented in Figure 3.2 in terms of Cauchy stress versus logarithmic axial strain averaged over the minimum cross section of the specimen. The Cauchy stress is directly computed from the measurements as

$$\sigma = \frac{F}{A} = \frac{4F}{\pi D_{ND} D_{TS}} \quad (7)$$

where F is the force measured by the load cell in the machine and $A = \frac{\pi}{4} D_{ND} D_{TS}$ is the current elliptical area of the specimen. The logarithmic longitudinal strain is computed from the diameter measurements, assuming plastic incompressibility. The elastic volumetric dilatation is

$$\frac{V}{V_0} = \frac{LD_{ND}D_{TS}}{L_0D_0^2} = \text{tr}(\boldsymbol{\varepsilon}^e) + 1 \quad \text{where} \quad \text{tr}(\boldsymbol{\varepsilon}^e) = \frac{1-2\nu}{E} \sigma \quad (8)$$

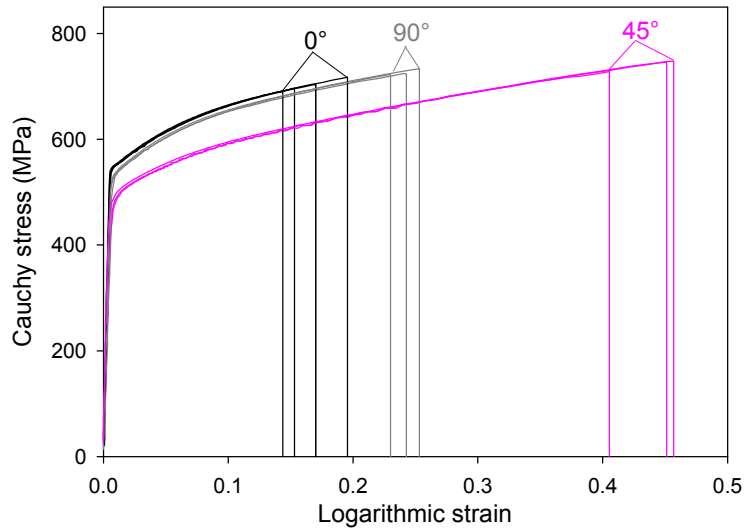
where $\boldsymbol{\varepsilon}^e$ is the elastic strain tensor, E and ν are the elastic parameters, V_0 , L_0 and D_0 are the initial volume, length and diameter of the specimen, and V and L are the current volume and length of the specimen. The logarithmic longitudinal strain is then defined as

$$\varepsilon = \ln\left(\frac{L}{L_0}\right) = \ln\left(\frac{D_0^2}{D_{ND}D_{TS}} \left(1 + \frac{1-2\nu}{E} \sigma\right)\right) \quad (9)$$

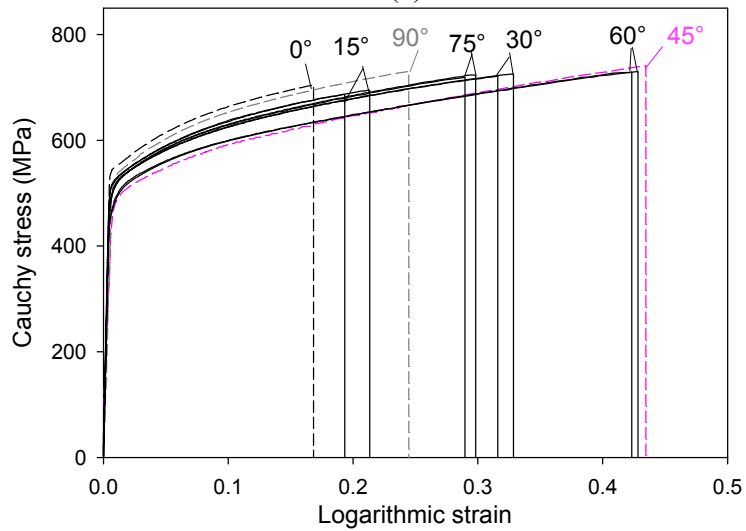
By neglecting the elastic contribution, the total strain reduces to

$$\varepsilon = \ln\left(\frac{L}{L_0}\right) = \ln\left(\frac{A_0}{A}\right) = \ln\left(\frac{D_0^2}{D_{ND}D_{TS}}\right) \quad (10)$$

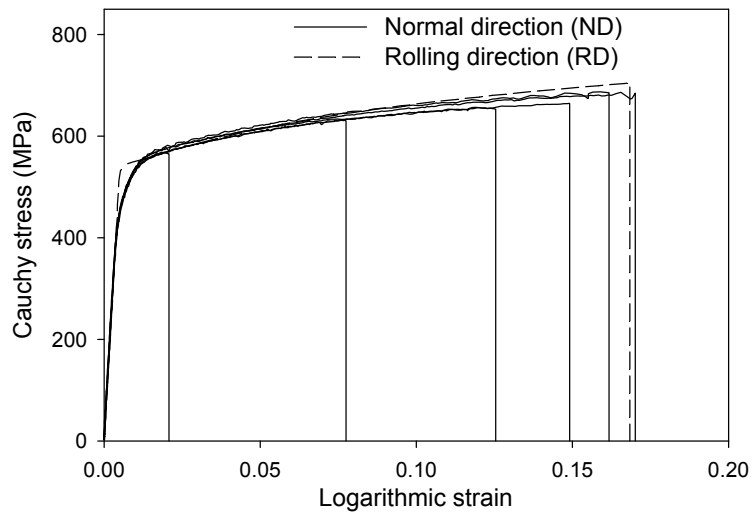
In our case, since plastic deformations are large, neglecting the elastic contribution seems reasonable. However, it should be noted that this assumption makes the ‘‘apparent stiffness’’ differ from the nominal Young’s modulus of aluminium ($E = 70$ GPa): on the Cauchy stress versus logarithmic strain curve calculated with Eq.(7) and Eq.(10), the apparent elastic modulus is $E' = E/(2\nu) = 117$ GPa, where $\nu = 0.3$ is the nominal Poisson ratio.



(a)



(b)



(c)

Figure 3.2. Cauchy stress versus logarithmic strain for tensile tests on smooth specimens in the (a) 0°, 45° and 90°, (b) 15°, 30°, 60° and 75° in-plane directions and (c) in ND.

The yield limit and the strain hardening show good repeatability in each direction, but a significant anisotropy on the flow stress is exhibited. Figure 3.2 (a) and (b) reveal that the strength level is almost identical and highest at 0° and 90° , while it is lowest at 45° and 60° . It is further similar at 15° , 30° and 75° and lies between the two above-mentioned limits. The stress-strain curves for the tests in the normal direction (ND), presented in Figure 3.2 (c), and in the rolling direction (RD) are found to be similar; except around the yielding point, where the yielding is more gradual for the specimens loaded in ND. A more remarkable difference is the large scatter in the strain to failure observed for the uniaxial tension tests in ND. An explanation for this scatter, based on the microstructure of the material, is presented later in this chapter.

Since the elastic part of the strain is negligible compared with the total strain, this study will consider that the plastic strain at failure ε_f^p is approximately equal to the total strain at failure given in Eq.(10) and will be denoted ε_f . Figure 3.3 illustrates the anisotropy of fracture by showing the average failure strain (and the associated range of values) versus the direction of loading for the tensile tests (in the in-plane directions $\alpha \in [0^\circ; 90^\circ]$ and in the normal direction (ND) of the plate). For tensile loading in the normal direction (ND), the failure strain is low and the scatter is considerable.

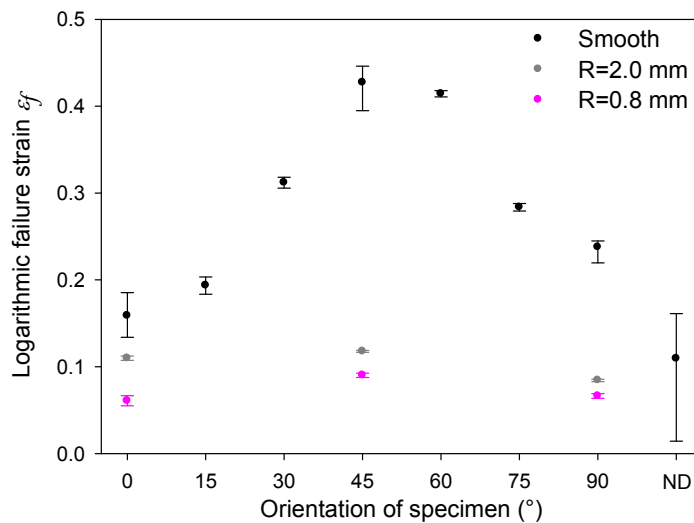


Figure 3.3. Average experimental failure strain versus specimen orientation for tensile tests on smooth and notched specimens. The error bars represent the range of failure strains between duplicate tests.

The different fracture modes obtained during the uniaxial tensile tests are presented in Figure 3.4. For the tests showing the lowest failure strains (i.e. those performed in the 0° and 90° in-plane directions), fracture occurred along a shear band oriented at approximately 45° with respect to the loading direction. The resulting surface is flat, smooth and crosses the whole specimen width. On the contrary, for tests showing the largest failure strains (tests

performed in the 45° and 60° directions), the fracture surface tends to a cup-and-cone shape. For the loading directions showing intermediate failure strains (15°, 30° and 75°), fracture occurred along disrupted shear bands. Thus, for the same initial stress triaxiality state (1/3), the fracture modes differ significantly with the direction of loading.

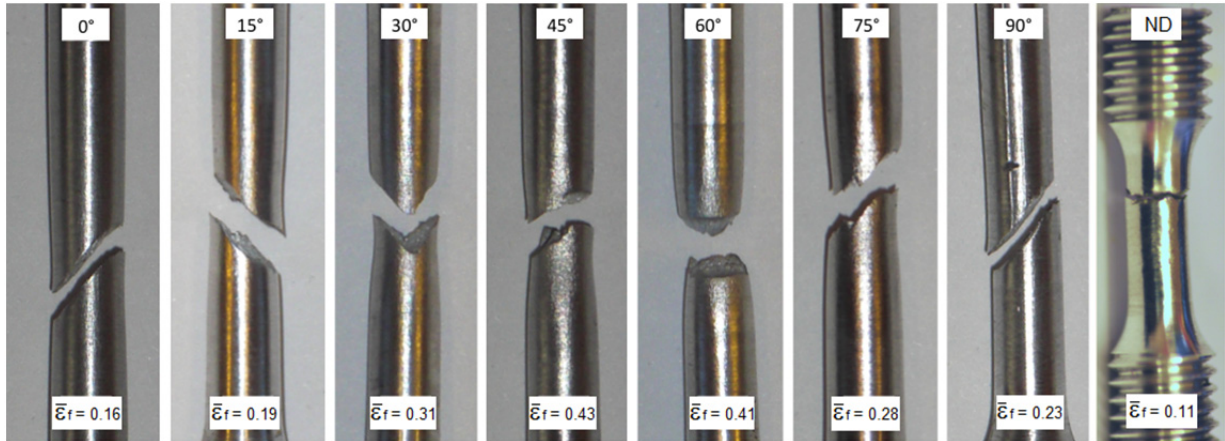


Figure 3.4. Failure modes observed with the smooth specimens in different directions. The label at the top and bottom give the orientation and the average fracture strain, respectively.

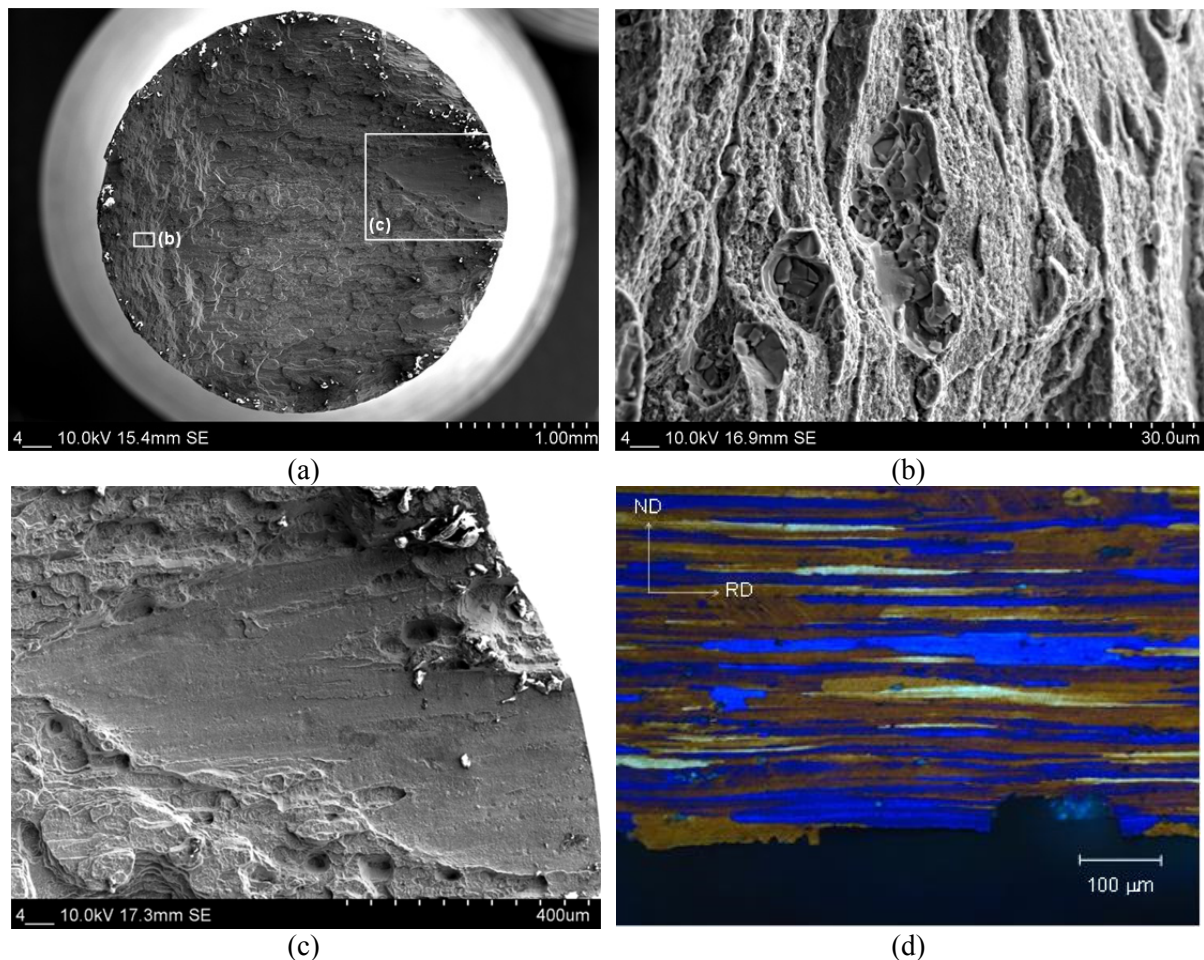


Figure 3.5. Micrographs of the fracture surface of a tensile test on a smooth specimen in ND: (a)-(c) views at different magnifications and (d) mid-section at the fracture location.

In addition, most fracture surfaces obtained from the tensile tests in the normal direction (ND) were orthogonal to the specimen axis, and revealed intergranular fracture. Figure 3.5 presents SEM micrographs of the fracture surface of the specimen loaded in the normal direction (ND) which exhibited the lowest failure strain (see also Figure 3.2 (c)). As visible on Figure 3.5 (b), plastic deformation and void growth around constituent particles seem involved in the failure process. However, a zoom on what seems like a flat area (Figure 3.5 (c)) reveals that fracture occurred along a large grain boundary. The high-magnification micrograph of the longitudinal mid-section presented in Figure 3.5 (d) confirms this statement. These observations indicate delamination of the material along grain boundaries at low plastic strains, as already suggested by Pedersen et al.(2011). Since the cross section of these specimens is only 3mm in diameter, it contains just a few grains, which explains the scatter in failure strain observed between duplicate tests in this direction.

3.3 Tensile tests on notched axisymmetric specimens (multiaxial tension)

Notched axisymmetric specimens, used to obtain initial stress triaxialities higher than with smooth specimens, were sampled in the 0° , 45° and 90° directions with respect to RD (Figure 3.1 (c)). Two different notch root radii were studied, $R=2.0$ mm and $R=0.8$ mm, giving initial stress triaxialities of 0.89 and 1.39, respectively, according to Eq.(6). The same experimental set-up and data analysis as for the tensile tests on smooth specimen were used.

Figure 3.6 (a) and Figure 3.6 (b) show Cauchy stress versus logarithmic strain curves for the notched axisymmetric specimens loaded in the 0° , 45° and 90° in-plane directions, and for two different notch root radii $R=2.0$ mm and $R=0.8$ mm, respectively. The Cauchy stress (averaged over the cross section) and the logarithmic strain are computed following Eq.(7) and Eq.(10) for all duplicate tests. The introduction of a notch in the tensile test specimen increases the stress level and significantly reduces the ductility compared to the behaviour under uniaxial tensile stress states. This is due to the positive hydrostatic stress induced by the notch, which facilitates the growth of voids. Also, following Eq.(6), the stress triaxiality increases with decreasing radius and so does the stress level. Regarding the anisotropy, the introduction of a notch reduces the difference between the stress levels in different directions (Fourmeau et al., 2011). The strain to failure is also less sensitive to the direction of loading than for the smooth specimens. The effect of anisotropy is thus reduced by increasing the multiaxiality of the stress state. This is illustrated in Figure 3.6 (c), where representative true stress-strain curves are presented for all tensile geometries in three different directions. The curves are stopped at the average failure strain found between duplicate tests.

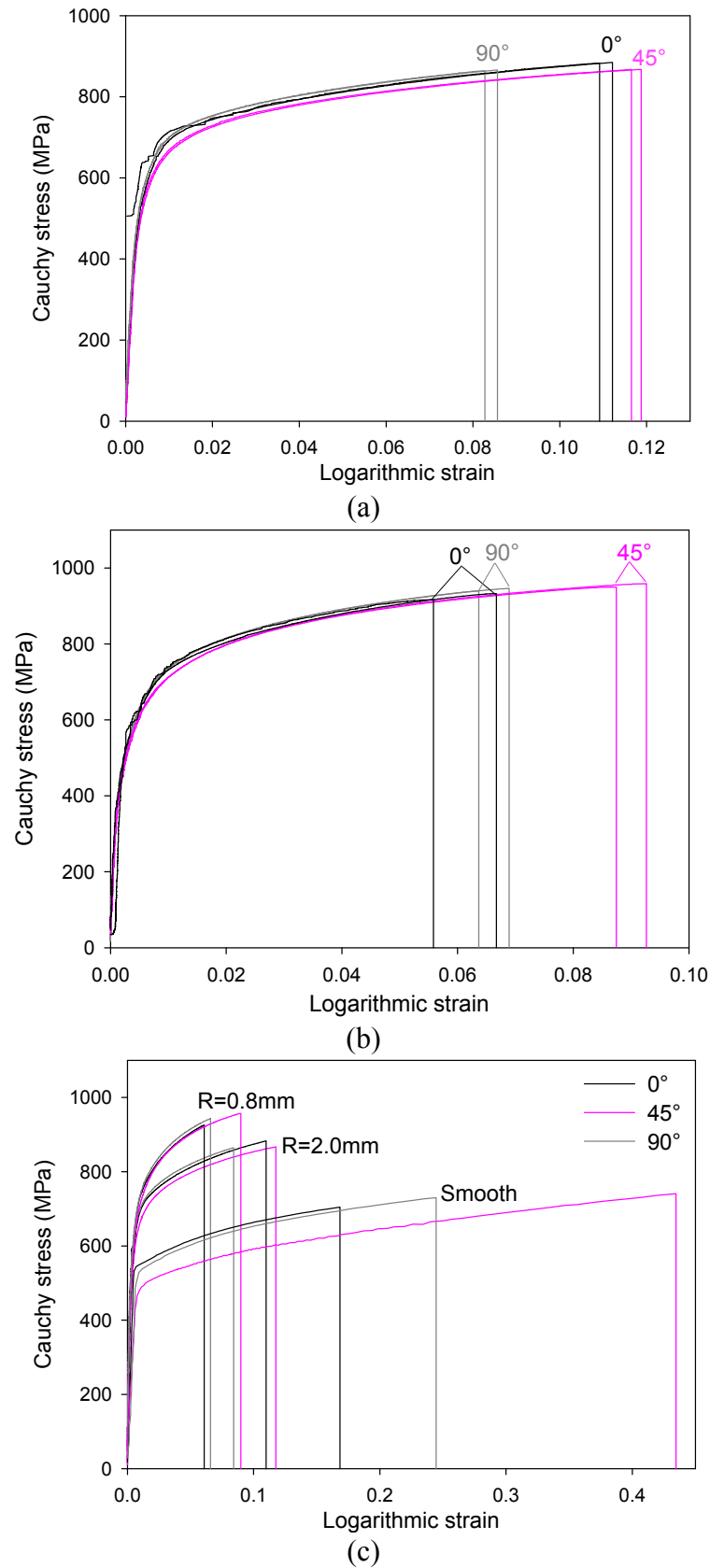


Figure 3.6. Cauchy stress versus logarithmic strain for the tensile tests on notched specimens with (a) $R=2.0\text{ mm}$ and (b) $R=0.8\text{ mm}$ in the 0° , 45° and 90° in-plane directions. (c) Representative curves for all specimens in the 0° , 45° and 90° in-plane directions plotted up to the average failure strains.

The experimental failure strains for tensile tests on notched specimens are computed in the same manner as for uniaxial tensile tests and are depicted in Figure 3.3. The strain to failure is also found less sensitive to the direction of loading than for the smooth specimens. The failure modes are illustrated in Figure 3.7. As pointed out by Børvik et al. (2010), the notched specimens exhibit a cup-and-cone fracture mode and, in addition, the increased stress triaxiality caused by the notch leads to secondary cracks in the plane of the plate. The secondary cracks follow the boundaries of the flat and elongated grains, and are observed in the specimens with the smallest notch radius in Figure 3.7 (a) where the stress triaxiality is highest. It should be noted that in contrast to smooth specimens exhibiting various failure modes, the failure mode for notched specimens is constrained by the notch geometry and remains rather similar for all loading directions.

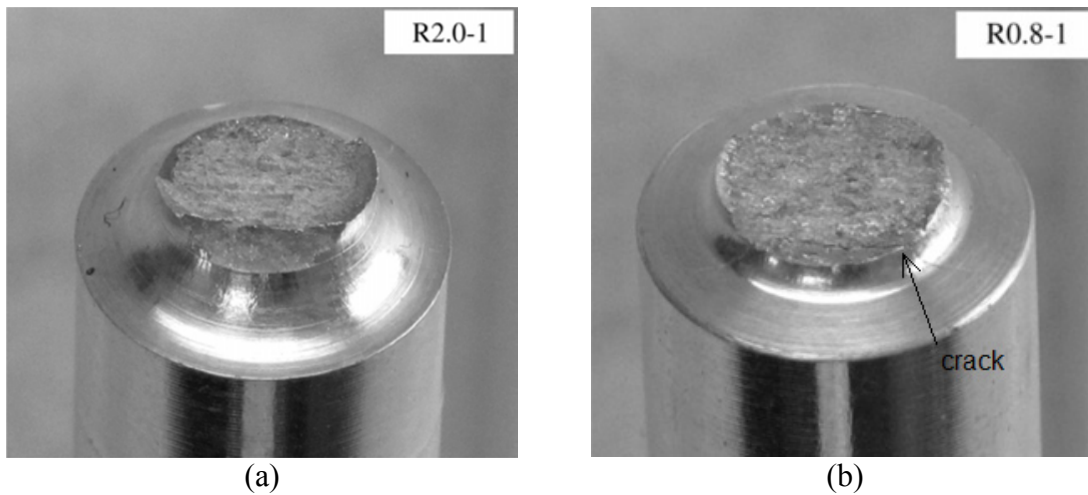


Figure 3.7. Failure modes observed for the tensile tests on notched specimens with (a) $R=2.0$ mm and (b) $R=0.8$ mm in the rolling direction (RD) (Børvik et al., 2010).

3.4 Compression tests on cylindrical specimens (uniaxial compression)

For negative stress triaxialities, compression tests were performed on cylindrical specimens with diameter $D_0=10$ mm and height $h_0=10$ mm (see Figure 3.1 (d)) and $h_0=15$ mm. The specimen axes were oriented at 0° , 45° and 90° with respect to RD. In addition, compression tests on specimens with loading axes along the normal direction (ND) of the plate were conducted with $h_0=10$ mm only. The specimens were compressed between two hardened steel platens, and a graphite paste was used to lubricate the surfaces to minimize the effect of friction (Børvik et al., 2010). Five tests were performed on specimens from each of the in-plane directions, while three tests were performed on specimens sampled in the normal direction (ND). The two first tests using the in-plane specimens and all tests in the short transverse

direction were carried out using an extensometer attached to the platens to measure the overall deformation of the specimen. A fine grained speckle pattern was spray painted on the remaining specimens in the in-plane directions, and a Prosilica GC2450 digital camera equipped with a 28–105mm Nikon lens was used to record images during loading at a framing rate of 10Hz. The image series were post-processed using an in-house 2D digital image correlation (DIC) code (Fagerholt et al., 2010), providing displacement and strain fields of the observed specimen surface. The image series were then analysed to give the displacement of the platen on top of the specimen. This measure is more accurate than the displacement measured by the machine, and comparable to the displacement obtained with an extensometer. Additional tests were carried out on cubic specimens of size $h_0 = 10\text{mm}$. These specimens were designed to get straight-forward DIC analysis of the strain fields. Unfortunately, the corner effect associated with friction engendered more scatter in the force level and the displacement to failure. It was therefore chosen not to present these results.

The Cauchy stress versus logarithmic strain curves from the compression tests in the 0° , 45° and 90° in-plane directions and in the normal direction (ND) of the plate are presented in Figure 3.8. The global values of the Cauchy stress and logarithmic strain for these specimens are

$$\sigma = \frac{FL}{A_0L_0}, \quad \varepsilon = \ln\left(\frac{L}{L_0}\right) \quad (11)$$

where F is the force measured by the load cell of the testing machine, and L_0 and A_0 are the initial length and cross-section area of the specimen, respectively. The current length of the specimen L is determined from the displacement measurements. Since the repeatability of the tests was very good, only one representative curve is depicted in Figure 3.8 for each direction. The curves are terminated at the average failure strain obtained between duplicate tests.

For the three in-plane directions (0° , 45° and 90°), the curves obtained with $h_0/D_0 = 1$ and $h_0/D_0 = 1.5$ specimens are similar until a logarithmic strain of $\varepsilon \approx 0.2$. Then, for the specimen with $h_0/D_0 = 1.5$, the buckling observed experimentally leads to a decrease in stress level as seen from the stress-strain curves in Figure 3.8 (a). Due to this instability, only the tests performed on the specimen with $h_0/D_0 = 1$ will be analysed further. The flow stress in the 45° loading direction is found lower than in the 0° and 90° directions, in a similar way as in the uniaxial tensile tests. However, in contrast to what is observed for uniaxial tension conditions, the flow stress in the 90° direction is found slightly higher than in the 0° direction. The strain hardening is also found to be higher in the normal direction (ND) than in the in-plane directions, while the strain to failure is significantly reduced. Also, as depicted in Figure 3.8 (b)

the yielding in the different in-plane directions of loading is somewhat different compared with the uniaxial tensile tests. In the study of Pedersen et al. (2011), it was found that the stress-strain curves from the uniaxial tension test in the 0° direction coincided with that from the compression test through the normal direction (ND) of the plate. This is in some conflict with the results found here, where the stress level is higher in the normal direction (ND) compression test. It should be kept in mind that friction can play an important role in the material response since uniaxial compression loading conditions may not be fulfilled when the plastic deformation becomes large.

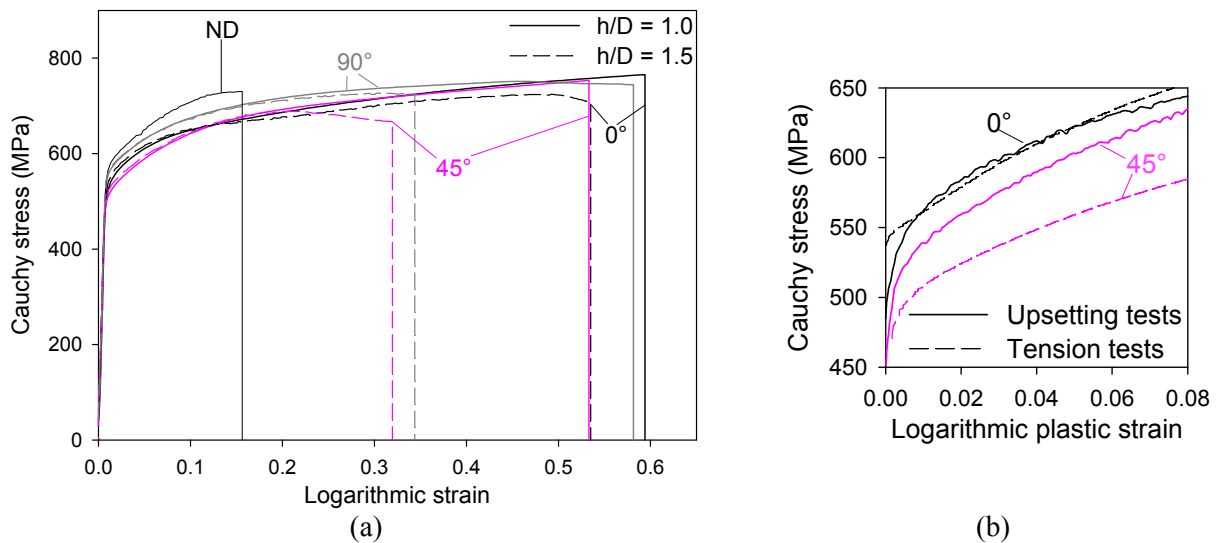


Figure 3.8. (a) Representative Cauchy stress-logarithmic strain curves for the compression tests on cylindrical specimens in the 0° , 45° and 90° in-plane directions and in ND. (b) Comparison between Cauchy stress-logarithmic plastic strain curves from tension and compression tests in the 0° and 45° directions plotted for small plastic strains.

As shown in Figure 3.9, the specimens fail along 45° planes under compressive loading. The fracture surfaces were flat but not always observable, since the specimens did not always split in two. The repeatability in terms of failure was compromised by friction and barrelling effects, so the specimens were arranged into different classes depending on the fracture mode. Some specimens failed abruptly across their whole height and the force dropped instantaneously to zero. In other experiments, the strain localization occurred on the edge of the specimen, and only small force drops were observed in the measured data. Finally, some specimens did not show any drop in the stress-strain curve, although they showed multiple fracture bands spread around the rim of the sample. Such fracture modes were the case for three out of five tests in the 45° direction, and for one out of six tests in the 90° direction. For this latter class of specimens it was not possible to identify the strain to failure, and consequently they are not used in the computation of the average failure strain.

Even though excluded from the study, it should be noted that the cylindrical specimens with $h_0/D_0 = 1.5$ and the cubic specimens also exhibited failure along 45° bands. The fracture surface of a specimen with $h_0/D_0 = 1.5$ is presented in Figure 3.10, where vertical white lines are traces due to the sliding of the two broken parts along each other. Due to this sliding, the observation of damage mechanism leading to failure is difficult. Moreover, only few specimens broke into two separate pieces.

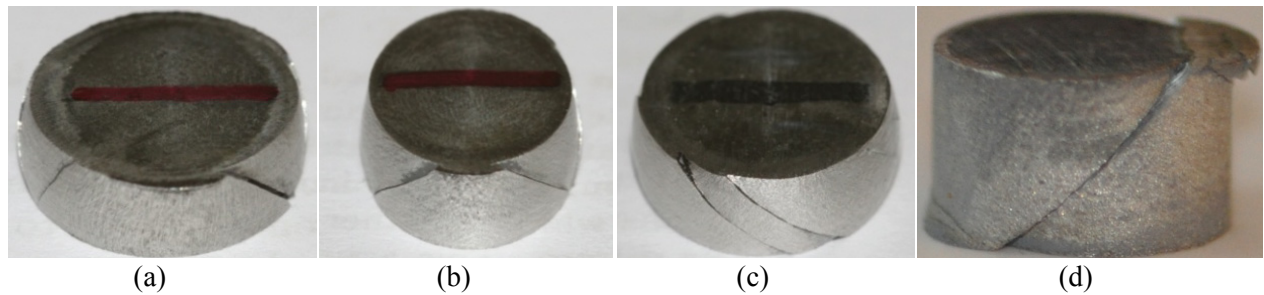


Figure 3.9. Failure modes observed for the compression tests in the (a) 0° , (b) 45° , (c) 90° in-plane directions and (d) in ND. The lines depicted on the top of the specimen (a), (b) and (c) represent ND.

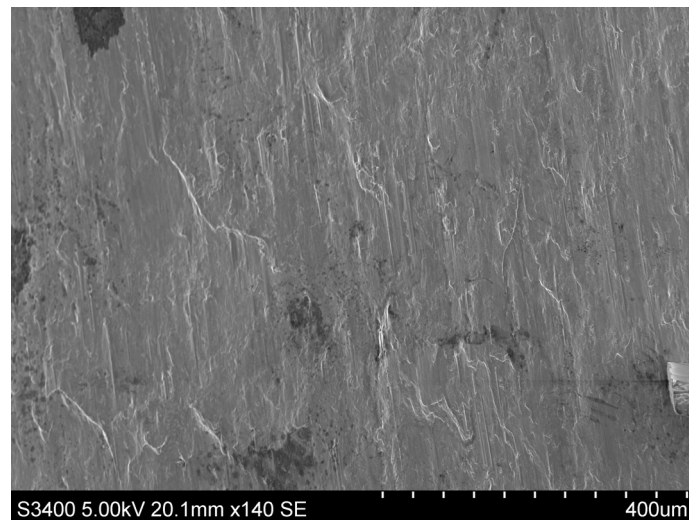


Figure 3.10. SEM picture of the fracture surface from a compression test with $h_0/D_0 = 1.5$ in the 45° in-plane direction.

For the specimens with $h_0/D_0 = 1$, the average values of the strains to failure ε_f are presented in Figure 3.11 as a function of the loading direction. The error bars represent the range of values obtained from duplicate tests and are seen to be quite significant. Given the scatter between duplicate tests and the exclusion of several of the tests, no precise conclusion can be drawn on the anisotropy of the strain to failure for compression tests in the in-plane directions. However, the strain to failure is found significantly lower for the tests performed in the normal direction (ND), compared to the in-plane directions.

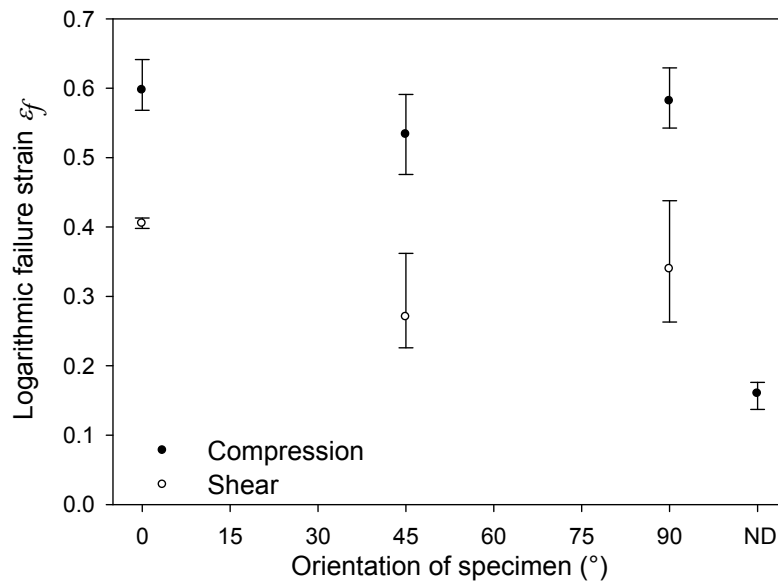


Figure 3.11. Average experimental failure strain versus specimen orientation for compression and shear tests. The error bars represent the range of failure strains from duplicate tests. The shear tests without DIC measurements and the compression tests not showing clear fracture are excluded.

3.5 Shear tests on butterfly specimens

To obtain a stress triaxiality close to zero, shear specimens of 2 mm thickness with geometry as shown in Figure 3.1 (e) were used (Gruben et al., 2011). The longitudinal axes of the spark-eroded specimens were oriented at 0°, 45° and 90° with respect to the rolling direction (RD). The specimens were bolted to the gripping system of the testing machine to allow for possible in-plane rotations of the specimen. The force in the load cell and the displacement of the cross-head of the testing machine were continuously recorded. Owing to the scatter in results, about 6–7 duplicate tests were performed for each direction, out of which 2–3 were instrumented using optical measurements. The same camera and digital image correlation (DIC) analysis as for the compression tests were used, providing displacement and strain fields of the observed specimen surface. This technique is particularly relevant in these tests, since the strains were found to be inhomogeneous over the gauge sections of the specimens and eventually strain localization occurred. One additional test was performed in the 0° direction using a high-speed camera running at a frame rate of 10 000Hz to observe the final stage of the test. This was done in an attempt to capture the localization of the strains leading to final failure in more detail.

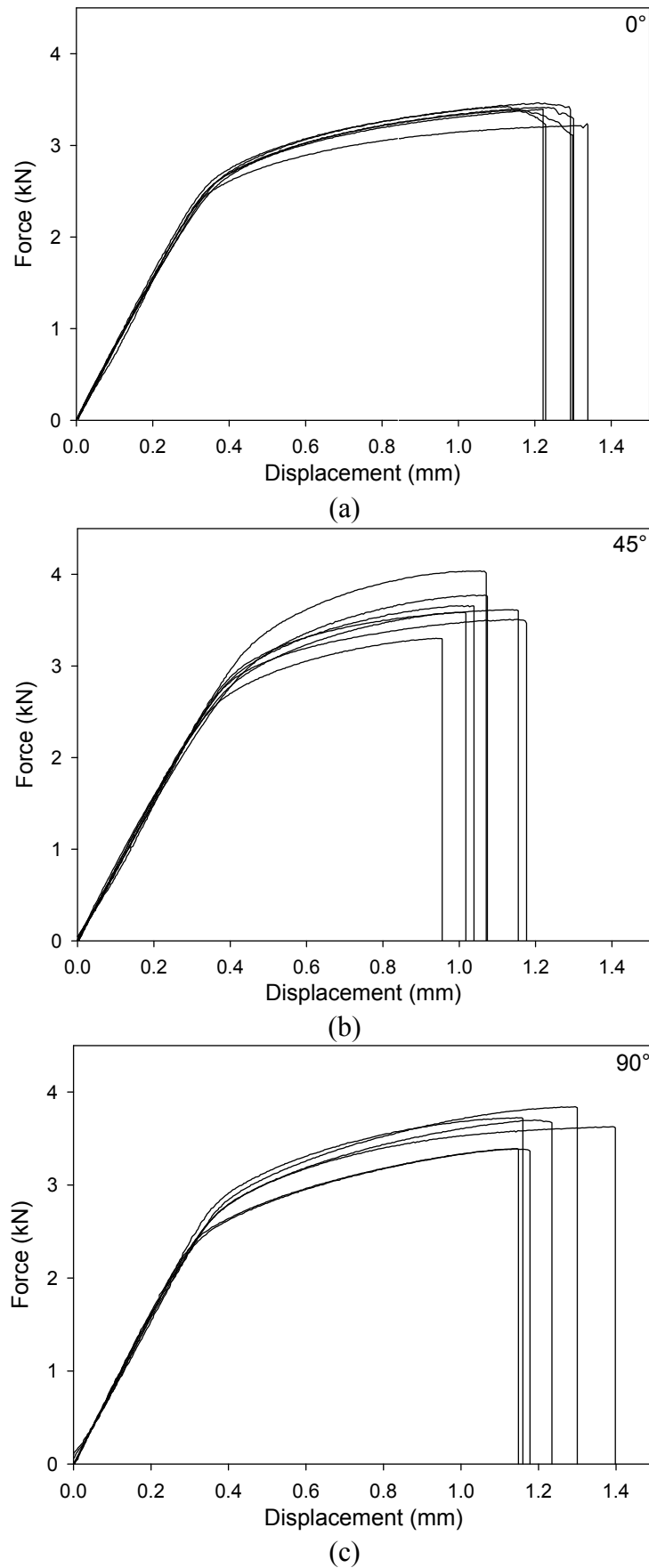


Figure 3.12. Force versus displacement for the shear tests on butterfly specimens in the (a) 0° , (b) 45° and (c) 90° in-plane directions.

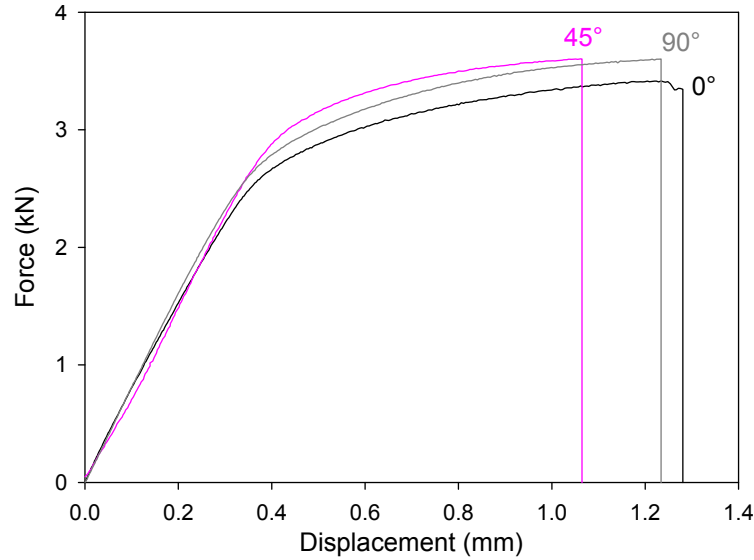


Figure 3.13. Representative force-displacement curves for the shear tests on butterfly specimens in the 0°, 45° and 90° in-plane directions.

Force versus displacement curves for duplicate shear tests in the 0°, 45° and 90° directions are shown in Figure 3.12, while representative force-displacement curves from the tests in the three directions are compared in Figure 3.13. Large scatter is observed in these tests (as also observed by Erice and Galvez, 2014). The force-displacement curves were corrected to account for the machine flexibility, but the remaining scatter in terms of load level is significant and reaches 18% of the maximum force level for the 45° loading direction. Several sources of error can be identified. A misalignment in the mounting of the specimen might lead to a scatter in the plastic behaviour. The tests were performed in two different laboratories (SIMLab and LMT-Cachan), and some sensitivity to the different gripping systems was observed (either bolted or clamped). The literature also proposes some microstructural reasons for the scatter. Rauch (1998) pointed out that shear tests in the +45° and -45° directions may show different behaviour. Since orthotropic behaviour of the material was assumed when machining the specimens, this possible effect was not considered. Nonetheless, Figure 3.13, which presents the representative force-displacement curves for each direction, indicates that the ductility is somewhat lower in the 45° direction than in the 0° and 90° directions. However, the rest of the study will only account for the shear tests performed in the 0° direction and no anisotropy will be considered for plasticity and failure under shear loading conditions.

For the shear tests, the strain field at the surface of the specimen was determined by use of DIC. The von Mises effective strain is adopted here for the shear tests

$$\varepsilon_{\text{eff}} = \frac{2}{\sqrt{3}} \sqrt{\varepsilon_1^2 + \varepsilon_2^2 + \varepsilon_1 \varepsilon_2} \quad (12)$$

where ε_1 and ε_2 are the principal logarithmic strains in the rolling plane of the plate. The maximum strains are found along a band slightly inclined from the axis of loading, as shown in Figure 3.14. The DIC analysis indicates that fracture occurs almost instantaneously along this band, since the propagation of the crack was not even captured at a frame rate of 10 000 Hz. The strain at failure ε_f is therefore defined as the average effective strain in the elements located along this shear band. The width of the band used for averaging was chosen equal to 0.6 mm and is represented by the white line on Figure 3.14. Figure 3.11 presents the average strain to failure as a function of the loading direction, and the error bars indicate the range of values from duplicate tests. Only the results from duplicate tests instrumented with DIC are included in Figure 3.11. As for the force-displacement curves, there is a large scatter in measured strain to failure between duplicate tests. In this respect, it should also be kept in mind that the results depend on the width of the zone chosen for averaging the failure strain. The choice of 0.6 mm was made to be able to take several elements into account while focusing on the area of strain localization.

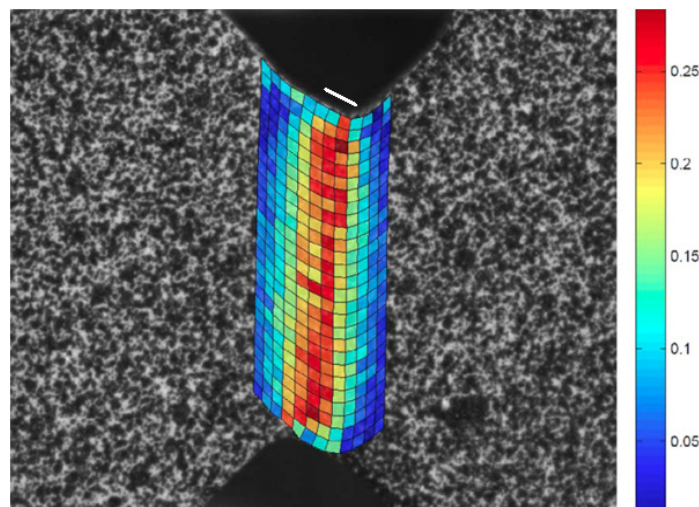


Figure 3.14. Effective strain field obtained by DIC for a shear test on butterfly specimen in the 45° in-plane direction (last image before failure).

Figure 3.15 presents micrographs of the failure surface obtained from a shear test performed in the 0° direction. For all directions, fracture occurred along a band inclined at approximately 10° with respect to the symmetry axis of the initial geometry (see Figure 3.15 (a)). However, since the specimens rotated somewhat during these tests, the orientation of the surface is aligned with the direction of the loading when fracture occurred. It can be seen from Figure 3.15 (a) that the fracture surface is slightly outside from the minimum cross section of the specimen. The flat and smooth surfaces (shown for the 0° loading direction in Figure 3.15 (b)) were similar in all directions of loading. However, dimples revealing ductile damage are

present in certain areas (see Figure 3.15 (c)) and grain boundaries are also visible (see Figure 3.15 (d)), suggesting intergranular failure.

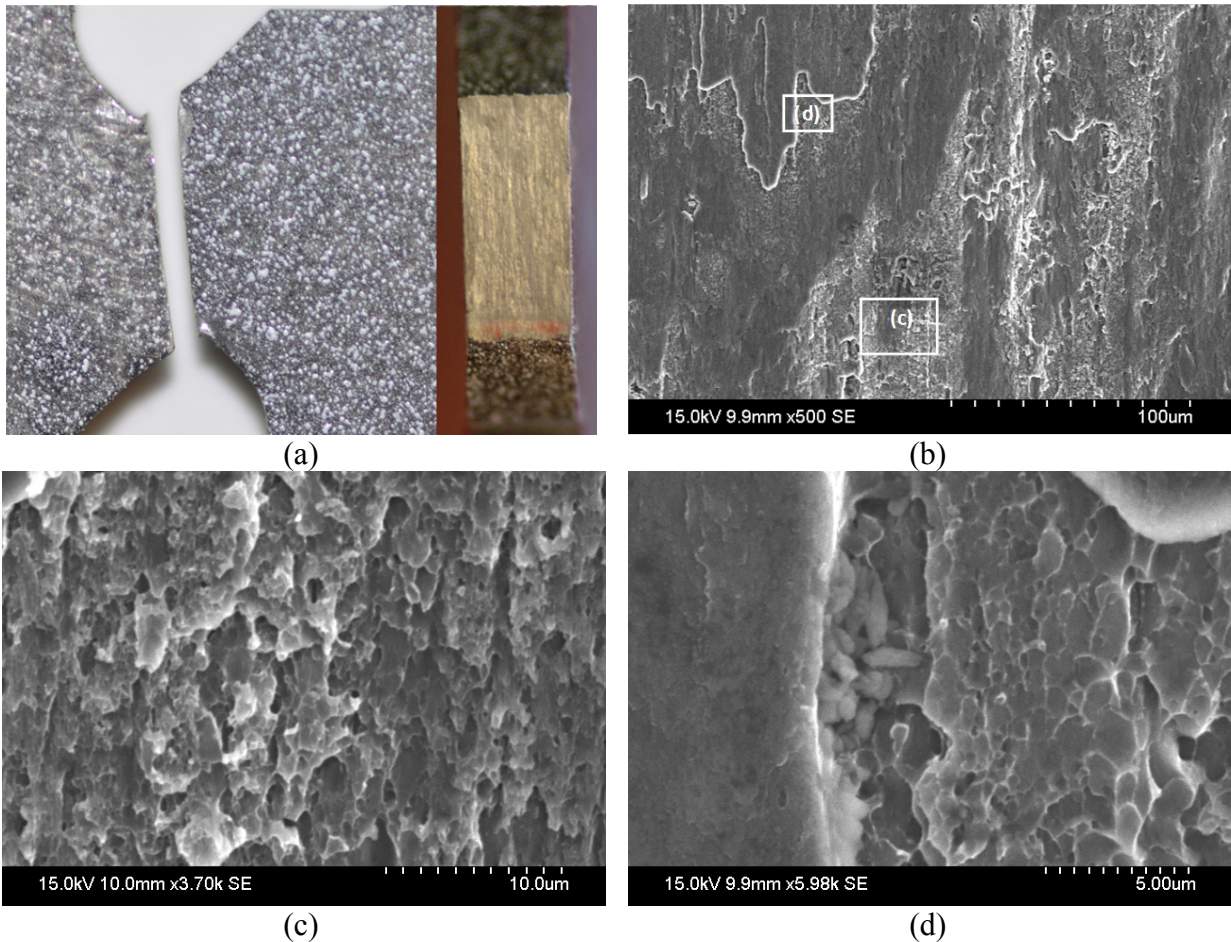


Figure 3.15. Fracture surface observed for a shear test on butterfly specimen in the 0° in-plane direction: (a) picture and (b)-(d) SEM micrographs.

3.6 Fracture surfaces and strain ratios

For both uniaxial tensile and compression tests in which shear failure occurred, the fracture surfaces were oriented at approximately 45° with respect to the loading direction, but not in a random manner. If one considers that the cross section of the specimen has an elliptic shape, Figure 3.16 shows two possible orientations (among infinitely many) of the 45° fracture surface with respect to the loading axis. In Figure 3.16 (a), the fracture surface is oriented at 45° to the loading direction and contains the semi-major axis of the ellipse, whereas in Figure 3.16 (b) it is also oriented at 45° to the loading direction but contains the semi-minor axis. Observations of the various fracture surfaces revealed that the latter case occurred consistently in uniaxial tension and preferentially in compression. A reasonable conclusion is that fracture surfaces are aligned with the orthotropic directions of the plate.

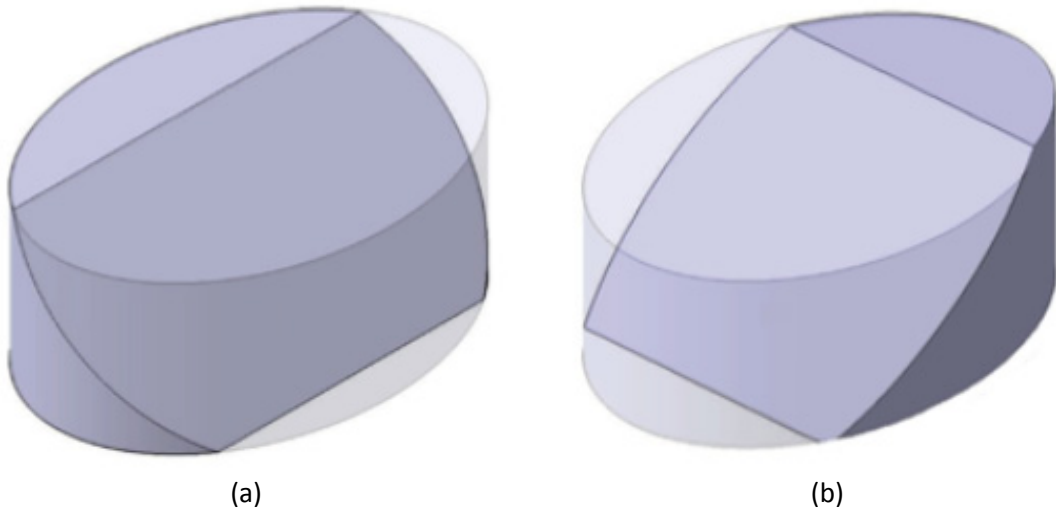


Figure 3.16. Schematic representation of two possible orientations of a 45° fracture surface on an elliptical cylinder. The surface contains (a) the semi-major and (b) the semi-minor axis of the ellipse.

The observation that the fracture surface orientation depends on the elliptical axis of the cylinder suggests that the localization process is related to the strain ratio R_α , defined for the loading direction α as

$$R_\alpha = \left. \frac{\dot{\varepsilon}_{TS}^p}{\dot{\varepsilon}_{ND}^p} \right|_\alpha \quad (13)$$

where $\dot{\varepsilon}_{TS}^p$ and $\dot{\varepsilon}_{ND}^p$ are the logarithmic plastic strain rates in the transverse direction of the specimen (TS) and in the normal direction (ND) of the plate, respectively. For the tests in the normal direction (ND), the strain ratio R_{ND} is defined as the ratio between $\dot{\varepsilon}_{RD}^p$ and $\dot{\varepsilon}_{TD}^p$, i.e. the logarithmic plastic strain rates in the rolling direction (RD) and in the transverse direction (TD) of the plate. Figure 3.17 presents the average experimental strain ratios and failure strains for the uniaxial tensile tests performed in the seven in-plane directions of the plate ($\alpha \in [0^\circ; 90^\circ]$) and in the normal direction (ND) of the plate. The value of R_α for each test was determined by averaging over the plastic regime, while the error bars represent the range of values from duplicate tests. It should, however, be noted that in the normal direction (ND), the strain ratio varied substantially within each test, and for this direction the average value was calculated after stabilization, which occurred around a plastic strain $\varepsilon^p \approx 0.05$. The strain ratios for the uniaxial compression tests are not presented since no continuous measurement of the diameter was performed during these tests. However, the elliptical fractured specimens for compression tests suggest that the strain ratios are similar in uniaxial tension and compression.

The directional variation of the fracture strain obtained from uniaxial tension tests on smooth specimens in the plane of the plate is found to be correlated to the directional variation of the strain ratio R_α . Figure 3.17 shows that a relatively low strain ratio implies a relatively low ductility and vice versa. Low values of the strain ratio imply a greater tendency of thinning of the plate than higher values. The fracture surface is oriented in such a way as to minimize its area, which also relates to the strain ratio.

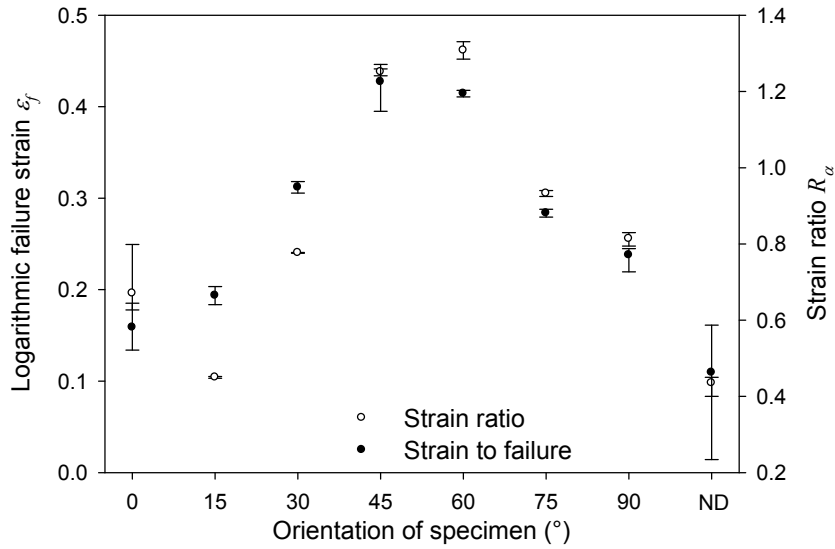


Figure 3.17. Experimental failure strain and strain ratio versus specimen orientation for tensile tests on smooth specimens. The error bars represent the range of failure strains from duplicate tests.

For tension tests in the 0° direction the strain ratio R_{0° is less than unity. The semi-minor axis of the ellipse is then parallel to the normal direction (ND), and the observed fracture surface, oriented at 45° to the loading direction, contains this axis, as shown in Figure 3.16 (b). In contrast, for the compression test in the same direction, the semi-minor axis of the ellipse is now parallel to the transverse direction of the specimen (TS) and, as depicted on Figure 3.9 (a), the fracture surface is oriented at 45° to the loading direction and contains this axis.

For the 45° loading direction, shear failure occurred only in compression. Then, as the strain ratio R_{45° is greater than unity and contrary to the 0° direction, the fracture surfaces, still oriented at 45° with the loading, contains the normal direction ND (see Figure 3.9 (b)).

The strain ratio R_{90° obtained for the tensile test in the 90° direction is very close to unity, and in this case fracture occurs on planes randomly located around the loading axis (see Figure 3.9 (c) for the compression test in the 90° direction). For the intermediate directions showing shear failure (15° , 30° and 70° with respect to the RD), the fracture surfaces are more

disrupted but are also globally oriented at 45° with respect to the loading direction and contain the semi-minor axis of the ellipse.

The tests performed in the normal direction (ND) of the plate show a lower strain to failure, but also a larger scatter than for the tests performed in the in-plane directions. The fracture surfaces, mainly orthogonal to the loading direction, show inter-granular failure. Here, grains with size of the same order as the width of the specimen can lead to premature failure. Also, the PFZs are preferentially oriented perpendicular to this loading direction, which may facilitate growth and coalescence of voids along planes orthogonal to the loading direction. These observations finally enable to assume that failure is facilitated when the PFZ concentration is high in the load-carrying plane (i.e. where the largest strains occur).

Chapter 4. Anisotropic plasticity model

4.1 Introduction

In this chapter, the constitutive model used to describe the elasto-plastic behaviour of the AA7075-T651 alloy is presented, followed by the calibration of the corresponding material parameters. Finally, the numerical models used to simulate the material tests performed in Chapter 3 are presented.

4.2 Constitutive model

A hypoelasto-plastic constitutive model based on the yield surface representation Yld2004-18p proposed by Barlat et al. (2005) is used to describe the anisotropic behaviour of the AA7075-T651 aluminium alloy. This yield surface was shown to be very efficient to describe the anisotropy of aluminium plates (Grytten et al., 2008) and due to the numerous experimental data available, the calibration of the anisotropy parameters is possible. The model accounts for isotropic elasticity, anisotropic yielding, associated plastic flow and isotropic strain hardening. The elastic strains are assumed small while the plastic strains may be finite. A corotational formulation is adopted to simplify the formulation of plastic anisotropy. The stress measure is realized in the unrotated configuration and expressed in a Cartesian coordinate system aligned with the principal directions of the orthotropic anisotropy. These axes are assumed to remain orthogonal during deformation.

The corotational Cauchy stress and corotational rate-of-deformation tensors are defined by (e.g. Belytschko et al., 2000)

$$\hat{\boldsymbol{\sigma}} = \mathbf{R}^T \cdot \boldsymbol{\sigma} \cdot \mathbf{R}, \quad \hat{\mathbf{d}} = \mathbf{R}^T \cdot \mathbf{d} \cdot \mathbf{R} \quad (14)$$

where $\boldsymbol{\sigma}$ is the Cauchy stress tensor, \mathbf{d} is the rate-of-deformation tensor and \mathbf{R} is the rotation tensor defined through the polar decomposition of the deformation gradient ($\mathbf{F} = \mathbf{R} \cdot \mathbf{U}$), where

\mathbf{U} is the right stretch tensor). The corotational rate-of-deformation tensor is decomposed into elastic and plastic parts

$$\hat{\mathbf{d}} = \hat{\mathbf{d}}^e + \hat{\mathbf{d}}^p \quad (15)$$

The linear hypoelastic formulation gives the relation between the rate of the corotational Cauchy stress and the elastic part of the corotational rate-of-deformation

$$\dot{\hat{\boldsymbol{\sigma}}} = \hat{\mathbf{C}}_{el} : \hat{\mathbf{d}}^e \quad (16)$$

where $\hat{\mathbf{C}}_{el}$ is the 4th order tensor of elastic moduli. As elastic isotropy is assumed, $\hat{\mathbf{C}}_{el}$ is uniquely defined by Young's modulus E and Poisson's ratio ν (a detailed expression is given in Appendix A).

The yield function is assumed convex and is written as

$$f(\hat{\boldsymbol{\sigma}}, \bar{p}) = \bar{\sigma}(\hat{\boldsymbol{\sigma}}) - \kappa(\bar{p}) \quad (17)$$

where $\bar{\sigma}$ is the equivalent stress, κ is the flow stress in uniaxial tension in the rolling direction and \bar{p} is the accumulated plastic strain. To model the anisotropy of the material, the equivalent stress defined by Barlat et al. (2005) is used

$$\bar{\sigma} = \left(\frac{1}{4}\phi\right)^{\frac{1}{m}} \quad (18)$$

where

$$\begin{aligned} \phi = \phi(\tilde{\mathbf{S}}', \tilde{\mathbf{S}}'') &= |\tilde{S}'_1 - \tilde{S}''_1|^m + |\tilde{S}'_1 - \tilde{S}''_2|^m + |\tilde{S}'_1 - \tilde{S}''_3|^m + |\tilde{S}'_2 - \tilde{S}''_1|^m + |\tilde{S}'_2 - \tilde{S}''_2|^m \\ &+ |\tilde{S}'_2 - \tilde{S}''_3|^m + |\tilde{S}'_3 - \tilde{S}''_1|^m + |\tilde{S}'_3 - \tilde{S}''_2|^m + |\tilde{S}'_3 - \tilde{S}''_3|^m \end{aligned} \quad (19)$$

The exponent m is used to determine the shape of the yield surface. In Eq.(19), $\tilde{\mathbf{S}}'$ and $\tilde{\mathbf{S}}''$ are collections of the principal values \tilde{S}'_i and \tilde{S}''_j of the tensors $\tilde{\mathbf{s}}'$ and $\tilde{\mathbf{s}}''$. These two last tensors are defined by linear transformations of the corotational Cauchy stress

$$\tilde{\mathbf{s}}' = \mathbf{C}' : \hat{\mathbf{s}} = \mathbf{C}' : \mathbf{T} : \hat{\boldsymbol{\sigma}}, \quad \tilde{\mathbf{s}}'' = \mathbf{C}'' : \hat{\mathbf{s}} = \mathbf{C}'' : \mathbf{T} : \hat{\boldsymbol{\sigma}} \quad (20)$$

where the 4th order tensor \mathbf{T} transforms the corotational Cauchy stress $\hat{\boldsymbol{\sigma}}$ into its deviatoric part $\hat{\mathbf{s}}$. The 4th order tensors \mathbf{C}' and \mathbf{C}'' contain the anisotropy weighting coefficients. For orthotropic symmetries, only 9 of these constants are non-trivial so that the tensors \mathbf{C}' and \mathbf{C}'' in Voigt notation read

$$\mathbf{C}' = \begin{bmatrix} 0 & -c'_{12} & -c'_{13} & 0 & 0 & 0 \\ -c'_{21} & 0 & -c'_{23} & 0 & 0 & 0 \\ -c'_{31} & -c'_{32} & 0 & 0 & 0 & 0 \\ 0 & 0 & 0 & c'_{44} & 0 & 0 \\ 0 & 0 & 0 & 0 & c'_{55} & 0 \\ 0 & 0 & 0 & 0 & 0 & c'_{66} \end{bmatrix}, \quad \mathbf{C}'' = \begin{bmatrix} 0 & -c''_{12} & -c''_{13} & 0 & 0 & 0 \\ -c''_{21} & 0 & -c''_{23} & 0 & 0 & 0 \\ -c''_{31} & -c''_{32} & 0 & 0 & 0 & 0 \\ 0 & 0 & 0 & c''_{44} & 0 & 0 \\ 0 & 0 & 0 & 0 & c''_{55} & 0 \\ 0 & 0 & 0 & 0 & 0 & c''_{66} \end{bmatrix} \quad (21)$$

and \mathbf{T} reads

$$\mathbf{T} = \frac{1}{3} \begin{bmatrix} 2 & -1 & -1 & 0 & 0 & 0 \\ -1 & 2 & -1 & 0 & 0 & 0 \\ -1 & -1 & 2 & 0 & 0 & 0 \\ 0 & 0 & 0 & 3 & 0 & 0 \\ 0 & 0 & 0 & 0 & 3 & 0 \\ 0 & 0 & 0 & 0 & 0 & 3 \end{bmatrix} \quad (22)$$

To obtain an isotropic version of this material model, all the coefficients of \mathbf{C}' and \mathbf{C}'' are set to unity. For more details on Yld2004-18p the reader is referred to Barlat et al. (2005). The evolution of the flow stress is defined by assuming isotropic hardening, using a Voce hardening rule

$$\kappa(\bar{p}) = \sigma_0 + Q(1 - \exp(-C\bar{p})) \quad (23)$$

where σ_0 , Q and C are material parameters. The evolution of the plastic part of the corotational rate-of-deformation tensor $\hat{\mathbf{d}}^p$ and the equivalent plastic strain-rate $\dot{\bar{p}}$ are defined by the normality of the yield surface

$$\hat{\mathbf{d}}^p = \dot{\lambda} \frac{\partial f}{\partial \hat{\mathbf{\sigma}}}, \quad \dot{\bar{p}} = -\dot{\lambda} \frac{\partial f}{\partial \kappa} = \dot{\lambda} \quad (24)$$

where $\dot{\lambda}$ is the plastic multiplier satisfying the usual loading-unloading conditions, written in Kuhn-Tucker form as

$$\dot{\lambda} \geq 0, \quad f \leq 0, \quad f\dot{\lambda} = 0 \quad (25)$$

This material model involves two elastic parameters E and ν , and 22 parameters for plasticity, namely σ_0 , Q , C , m , c'_{ij} and c''_{ij} .

4.3 Identification of the Yld2004-18p material constants

The three parameters of the isotropic hardening law σ_0 , Q and C are calibrated based on the tensile test in the rolling direction (RD) and the two elastic parameters E and ν are chosen equal to nominal values for aluminium (see Table 4.1). The plastic anisotropy of the material is taken into account with the 18 parameters in C' and C'' calibrated using the experimental results presented in Chapter 3.

4.3.1 The shape parameter m

The m parameter is not calibrated as the other parameters. Hosford (1972) and Hill (1979) showed that $m=8$ is reasonable for f.c.c. crystal structures. Since aluminium is studied here, $m=8$ was used in a first approach. Then, since the parameter m controls the shape of the yield surface, it was of interest to investigate its influence on the predicted behaviour of the different tests. Indeed, and as suggested by Barlat et al. (1991), the crystallographic texture and grain morphology of rolled aluminium plates could increase the exponent of the yield function compared to an isotropic microstructure, by changing the active slip systems during the plastic process. Then, a new set of anisotropic parameters was determined with $m=12$. The two identifications led to about the same residual in the least squares approach used in the calibration.

4.3.2 The anisotropy parameters

From a tension test on a smooth specimen in a given in-plane direction α , the yield stress and the strain in the transverse and normal directions are obtained. The flow stress ratio is defined as

$$r_\alpha = \frac{\sigma_\alpha}{\sigma_0} \quad (26)$$

Thus, σ_α is the flow stress in the direction α and σ_0 is the corresponding flow stress in the rolling direction (RD). The flow stress ratios were determined by use of the 0.2% proof stresses in the different directions before being adjusted by inverse identification using trial and error. By definition, the flow stress ratio represents a point on the yield surface and is equal to unity in the rolling direction (RD). Then, the strain ratio R_α defined in Eq.(13) is the ratio between $\dot{\epsilon}_{TS}^p$ and $\dot{\epsilon}_{ND}^p$, the logarithmic plastic strain rates in the transverse direction of the specimen (TS) and the normal direction (ND) of the plate. As plastic flow normal to the yield surface is assumed, the strain ratio determines the normal to the yield surface at a given stress state.

Figure 4.1 shows $\dot{\varepsilon}_{TS}^p$ versus $\dot{\varepsilon}_{ND}^p$ for tensile tests on smooth and notched tensile specimens in the 0° , 45° and 90° in-plane directions. The strain ratios are the slopes of the curves presented in Figure 4.1 (a) and are obtained by a least square fit of these curves to a linear function. Both the stress and the strain ratios provide relations between the parameters of the yield surface. Consequently, the seven in-plane tension tests on smooth specimen bring 14 constraints to the calibration of the anisotropic parameters.

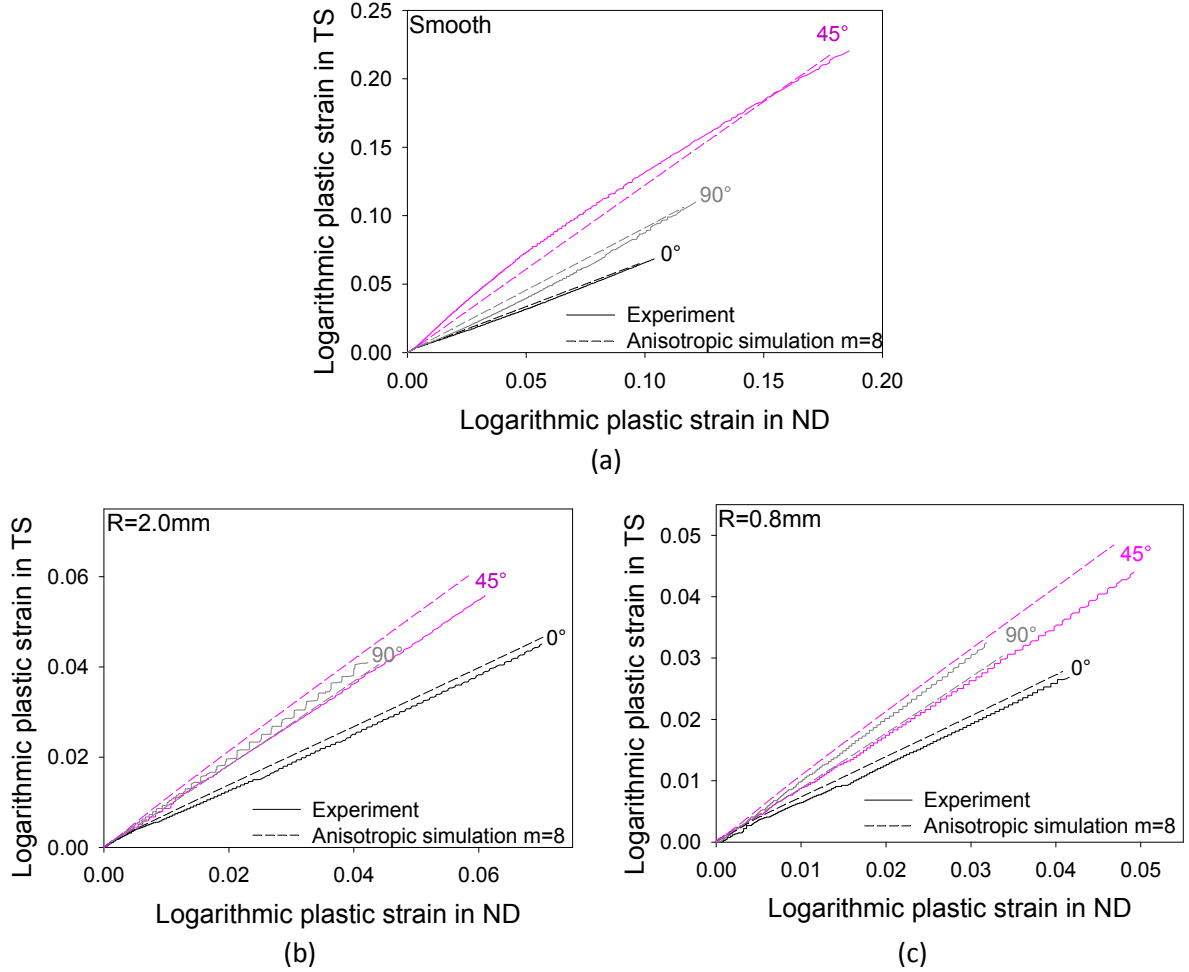


Figure 4.1. Experimental and predicted logarithmic strain in the transverse direction of the specimen (TS) versus logarithmic strain in the normal direction (ND) of the plate for (a) smooth specimens, (b) notched specimens with $R=2.0\text{mm}$ and (c) notched specimens with $R=0.8\text{mm}$, with the anisotropic model ($m=8$) calibrated for the AA7075-T651 alloy.

For the compression tests in the normal direction (ND), the strain and stress ratios are defined

$$R_{Biax} = \frac{\varepsilon_{TD}^p}{\varepsilon_{RD}^p}, \quad r_{Biax} = \frac{\sigma_C}{\sigma_0} \quad (27)$$

where ε_{RD}^p and ε_{TD}^p are the measured final strains in the rolling direction (RD) and transverse direction (TD) of the plate, respectively, and σ_C is the yield strength in compression (along

the normal direction (ND)). The compression tests performed in the normal direction (ND) give two additional constraints to the set of anisotropic parameters. It should be noted that due to the pressure insensitivity of the model, the yield function is symmetric in tension and compression. Consequently, the uniaxial compression in the normal direction (ND) is equivalent to equibiaxial tension in the plane of the plate. In the optimization, the compression data is used as a biaxial data point to find the anisotropic yield surface.

The calibration of the set of 18 anisotropic parameters was made in two steps. A first calibration was obtained by using the 16 experimental constraints (14 constraints from the uniaxial tension tests and two from uniaxial compression, as presented earlier). Then, numerical simulations of the different tests were run using the obtained values. The stress-strain curves of the tensile tests on smooth specimens in the seven different directions were found to be in good agreement with the experimental curves. In contrast, the shear tests on butterfly specimens aligned with the 0° direction of the plate showed a discrepancy of 23% on the force. The scatter observed between duplicate shear tests in Chapter 3 leads to conclude that the anisotropy of yielding in shear is not quantified in a reliable way. Consequently, the shear tests aligned with the 0° direction of the plate (showing the smallest scatter) will be considered for the calibration of the anisotropic yield surface. This choice implies that no anisotropy of yielding is expected in the numerical study of shear tests. The yield limits for the shear tests in the 0° and 90° directions were corrected and set as two new constraints. A second calibration of the set of 18 parameters is obtained combining seven tensile tests in the plane of the plate and one compression test in the short transverse direction (16 constraints), and two shear tests in the plane of the plate (two constraints). The resulting parameters obtained with $m=8$ and $m=12$ are presented in Table 4.1. Figure 4.2 compares the predicted and experimental flow stress ratios (a) and strain ratios (b). Those are found similar for $m=8$ and $m=12$, except for the 60° direction which exhibits a difference of 12% in the strain ratio. Then, the yield surfaces are illustrated in Figure 4.3. Several contours of each yield function are given in two different planes in stress space. As expected, the yield surface with $m=12$ is sharper than with $m=8$. An isotropic calibration of the parameters ($c'_{ij} = c''_{ij} = 1$) is also plotted in Figure 4.3 to show the influence of anisotropy.

Note that the uniaxial tensile test performed in the normal direction (ND) of the plate was not used for the calibration. The first reason is that these tests were performed much later than all the other tests and the calibration published in Fourmeau et al. (2011) was already satisfactory. The second reason is that these tests did not bring much improvement. Indeed, with the pressure independency of the yield function, uniaxial tension and uniaxial compression in the normal direction (ND) are assumed to be equivalent, yet their yield limits and strain ratios are similar.

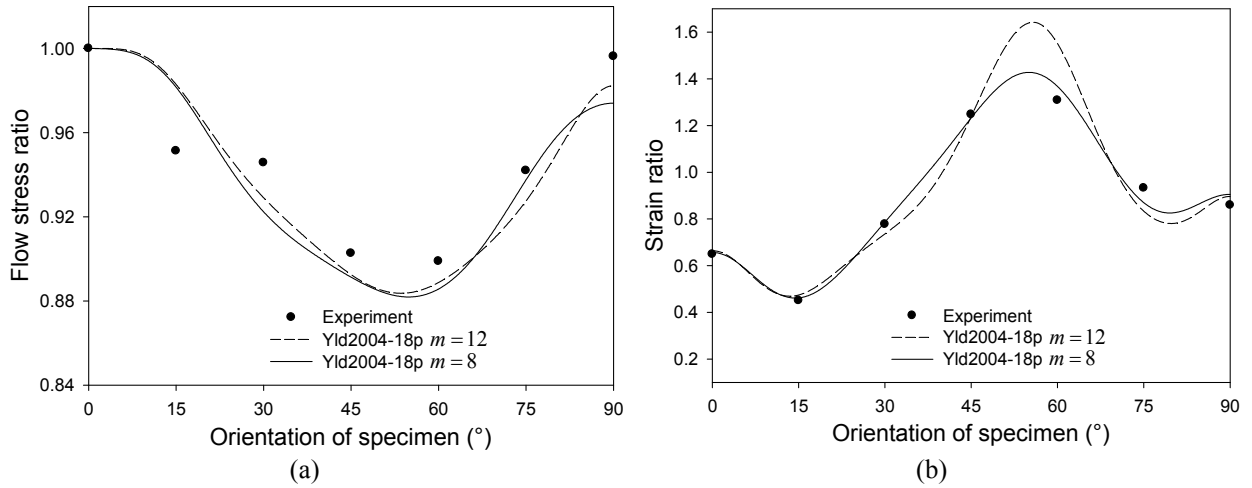


Figure 4.2. (a) Flow stress ratio and (b) strain ratio given by the Yld2004-18p model calibrated with $m=8$ and $m=12$ for the AA7075-T651 alloy.

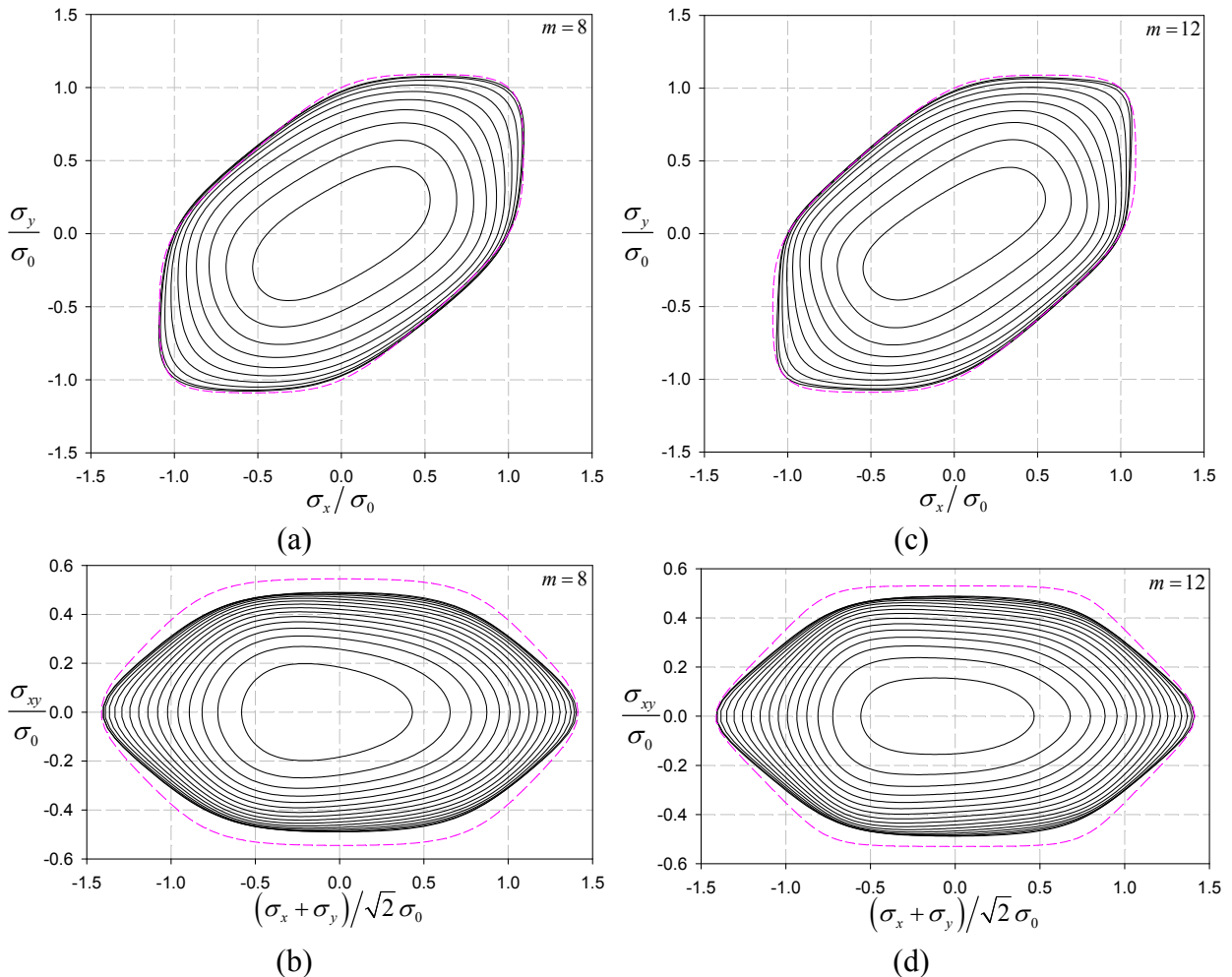


Figure 4.3. Illustration of yield surface given by the Yld2004-18p model calibrated with (a-b) $m=8$ and (c-d) $m=12$ for the AA7075-T651 alloy. The isotropic yield functions ($c'_{ij} = c''_{ij} = 1$) are plotted in dashed lines for comparison. The \underline{x} axis is aligned with RD, the \underline{y} axis with TD and the \underline{z} axis with ND.

Table 4.1. Material data for the model Yld2004-18p calibrated for the AA7075-T651 alloy.

	E (GPa)	ν	ρ (g/cm ³)	σ_0 (MPa)	Q (MPa)	C	K (GPa)	μ (GPa)	m
	70	0.3	2.7	538.8	177.24	12.58	58.334	26.924	8
	c'_{12}	c'_{13}	c'_{21}	c'_{23}	c'_{31}	c'_{32}	c'_{44}	c'_{55}	c'_{66}
$m=8$	0.157	0.696	-0.446	0.198	1.169	0.436	0.895	1	1
$m=12$	-0.066	0.101	-0.624	0.504	0.988	0.563	0.881	1	1
	c''_{12}	c''_{13}	c''_{21}	c''_{23}	c''_{31}	c''_{32}	c''_{44}	c''_{55}	c''_{66}
$m=8$	0.485	1.009	1.232	1.408	0.181	1.534	1.329	1	1
$m=12$	0.690	1.128	1.218	1.356	-0.055	1.495	1.290	1	1

4.4 Numerical procedures and finite element models

The constitutive relations described above were implemented as a user-defined material subroutine (see Grytten et al., 2008) in the non-linear finite element code LS-DYNA (LSTC, 2007). All tests presented in Chapter 3 were simulated using the explicit solver of LS-DYNA with 8-node fully integrated solid elements. To reduce the computational time, affected both by the element size and the number of elements, the mesh was only refined in the area exposed to large deformations and mass-scaling was applied. As boundary conditions, a function was applied to smoothly reach a constant velocity. The finite element geometries of the different specimens are shown in Figure 4.4, while the numbers and minimum size of the elements h_e are given in Table 4.2. Compression tests were performed with $h_0/D_0 = \{1, 1.5\}$ but only the results for $h_0/D_0 = 1$ will be presented for the reasons explained in Chapter 3. A friction coefficient $\gamma_f = 0.02$ was used between the lubricated platens and the cylindrical specimen loaded in compression. This value was found by trial and error: the friction coefficient was not found to influence yielding but only the behaviour at very large strains.

To characterize the local stress and strain fields in the test specimens up to incipient failure, the spatial distribution of the accumulated plastic strain \bar{p} and the stress triaxiality σ^* were determined from the simulations. It should be noted that since the tests are carried out for axisymmetric specimens of different shapes as well as shear specimens, the deviatoric stress state will differ significantly from one specimen to the other. However, to limit the investigation, the stress triaxiality was selected to represent the stress state. The accumulated plastic strain is defined by

$$\bar{p} = \int_0^t \frac{\hat{\boldsymbol{\sigma}} : \hat{\mathbf{d}}^p}{\bar{\sigma}} dt = \int_0^t \lambda dt \quad (28)$$

where $\bar{\sigma}$ is the equivalent stress defined by the Yld2004-18p yield function, and $\hat{\boldsymbol{\sigma}}$ and $\hat{\mathbf{d}}^p$ are the corotational Cauchy stress and plastic rate-of-deformation tensors, respectively (see Fourmeau et al. (2011) for details). The numerical fracture point is then defined at the instant of loading where fracture occurs experimentally. It is important to note that the accumulated plastic strain \bar{p} computed from the numerical simulations is different from the strain measured experimentally and these two strain measures should not be directly compared. Also, the choice to work with the accumulated plastic strain \bar{p} is supported by the analysis presented in Chapter 6. The stress triaxiality is here defined as

$$\sigma^* = \frac{I_1}{3\bar{\sigma}} \quad (29)$$

where $I_1 = \text{tr}(\hat{\boldsymbol{\sigma}})$ is the first invariant of the stress tensor $\hat{\boldsymbol{\sigma}}$ and plastic anisotropy is included by using the equivalent stress $\bar{\sigma}$ defined by the Yld2004-18p yield function. Note that in this definition of the stress triaxiality σ^* , the equivalent stress $\bar{\sigma}$ defined by the Yld2004-18p yield function have replaced the von Mises equivalent stress σ_{eq} used in Chapter 3. A more detailed presentation of the numerical results is given in Chapter 5.

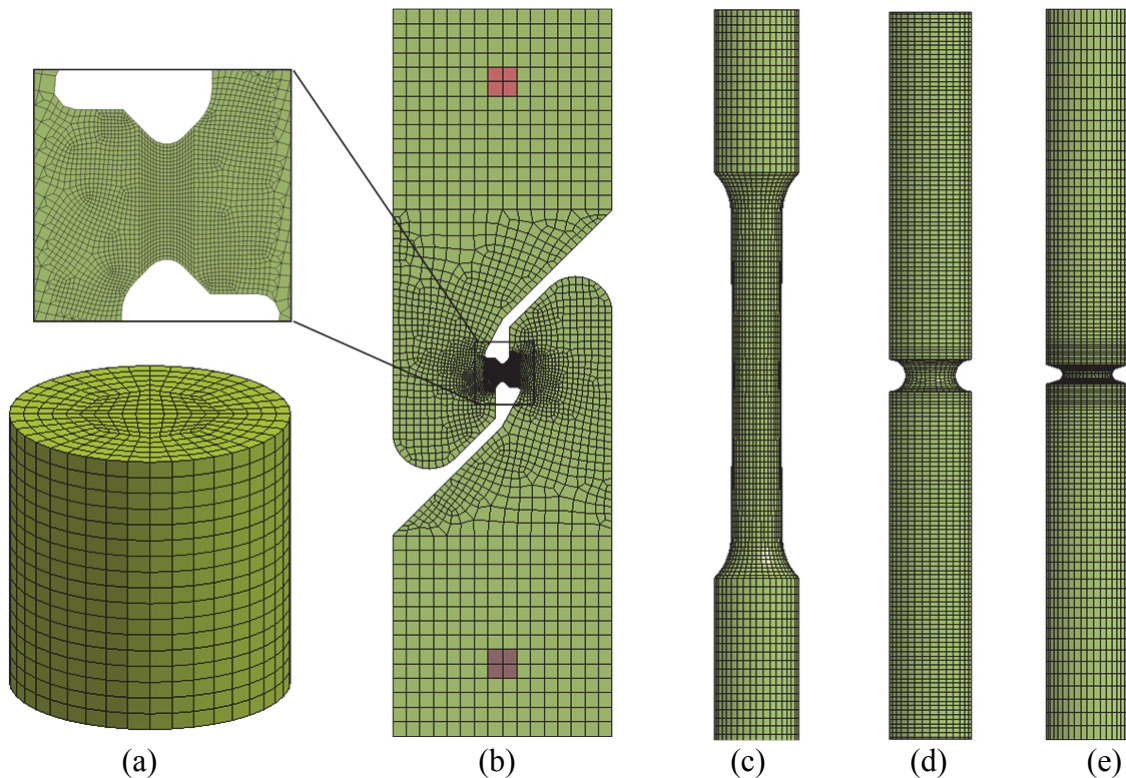


Figure 4.4. Finite element meshes of the specimens for the numerical simulations: (a) cylinder with $h_0/D_0=1$ for compression tests, (b) butterfly specimen for shear, (c) smooth axisymmetric specimen, (d) notched specimen with $R=2.0\text{mm}$ and (e) notched specimen with $R=0.8\text{mm}$ for tensile tests.

Table 4.2. Number and initial size of elements for each discretized specimen geometry.

	Compression	Butterfly	Smooth	Notch <i>R</i> = 2.0mm	Notch <i>R</i> = 0.8mm
Number of elements	30050	18628	36000	43136	57000
h_e (mm)	0.15	0.15	0.4	0.3	0.2

Chapter 5. Numerical analysis

5.1 Introduction

In this chapter, all the results obtained from the numerical simulations presented in the Chapter 4 are presented. Firstly, the numerical stress-strain curves are given and compared with the experimental curves. Then, the local stresses and the strain states in the elements where fracture occurred experimentally are analysed. Figure 5.1 shows these elements for each geometry of specimen.

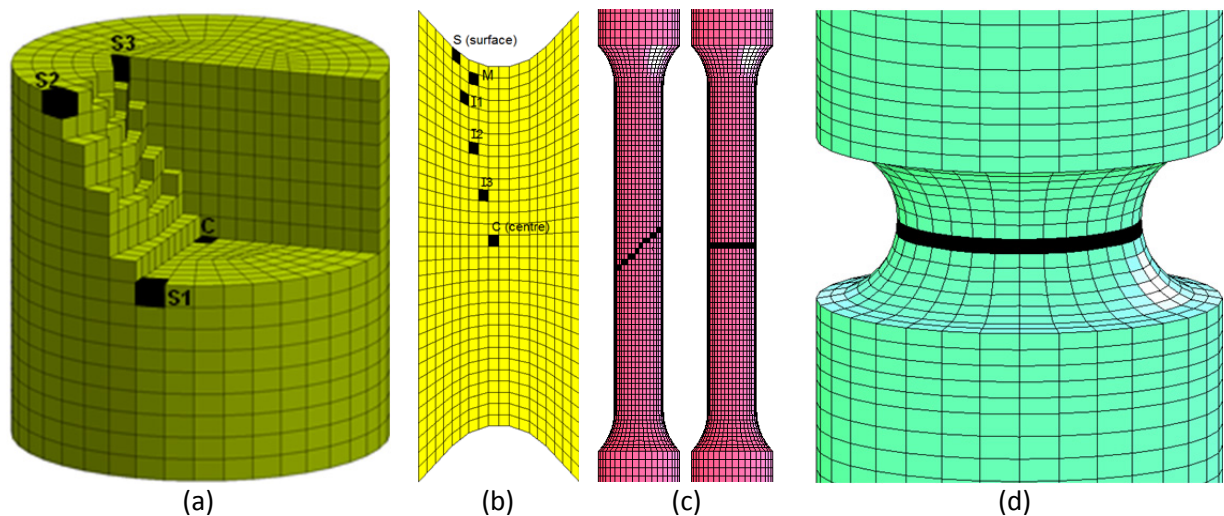


Figure 5.1. Part of the various discretized specimens shown in Figure 4.4 with black elements where fracture is experimentally observed (the two cases given in (c) correspond to two failure modes).

5.2 Macroscopic stress-strain curves

Numerical stress-strain curves from the various tests described in Chapter 4 are presented in Figure 5.2 to Figure 5.5 and compared with the experimental results. The stress and strain are computed in the same manner as for the experiments. Diameter reduction is used for tensile

tests, total elongation is used for compression tests and displacement of the upper bolt is used for the shear tests. Both the isotropic and anisotropic ($m=8$ and $m=12$) calibrations of the material model are used. The simulated stress-strain curves were found to be in good agreement with the experimental results for all the tests, validating the calibrated material model from a macroscopic point of view. The errors between experimental and numerical results are presented in Table 5.1. Note that only the shear test in the rolling direction is studied, following the discussions in Chapter 3 and Chapter 4.

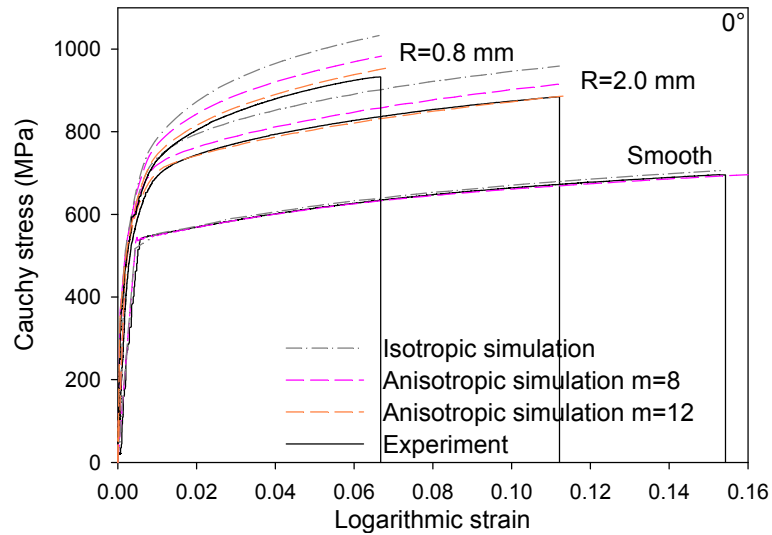
5.2.1 Isotropic version of Yld2004-18p

The numerical simulations were first run without including anisotropy. Thus, all the anisotropy parameters c'_{ij} and c''_{ij} were set equal to unity and the coefficient m was chosen equal to 8 and 12. In those cases, only the tests in the rolling direction are studied.

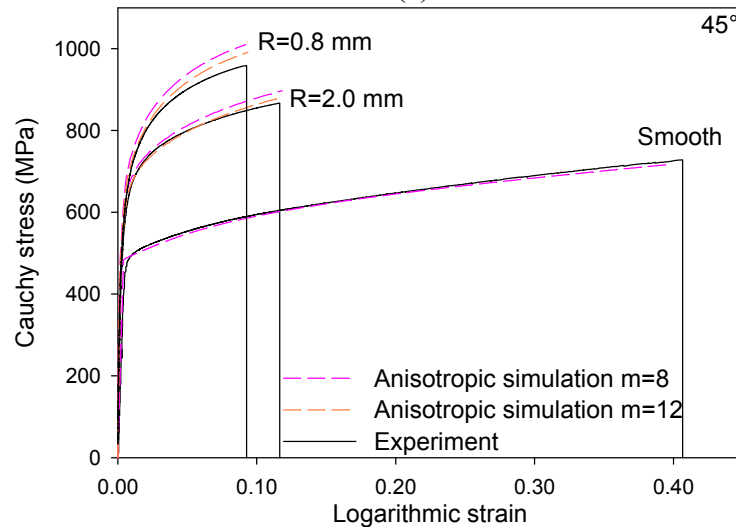
As the isotropic material model was calibrated using uniaxial tensile tests in the rolling direction, the simulation of this particular test is in good agreement with the experiment (see Figure 5.2 (a)). However, for both the tensile tests on notched specimens (Figure 5.2 (a)) and the shear tests (Figure 5.3), the numerical stress-strain curves (force-displacement curve for shear) clearly overestimate the experimental curves in the 0° direction. This behaviour has already been reported in several studies, see e.g. Wilson (2002) and Bai and Wierzbicki (2008), and has been explained by the effect of hydrostatic pressure. However, it may also be due to anisotropic effects which were not considered in those studies. Indeed, and as underlined in the introduction, effects of pressure sensitivity on the flow stress have been claimed for many materials among which aluminium alloys (see e.g. Spitzig and Richmond, 1984, Wilson, 2002, Bai and Wierzbicki, 2008). These former studies included pressure-dependence into the yield function, as determined by inverse identification, and obtained correct stress-strain curves for tensile test on both smooth and notched specimens. In our case, the calibration was done in the rolling direction, and this choice has a direct influence on the numerical results for the notched-specimen tests. In the following part, results are presented for simulations taking the anisotropy of the material into account.

Table 5.1. Error (in %) between experimental and numerical tests at 2% strain or 0.6mm displacement for the shear tests on butterfly specimens.

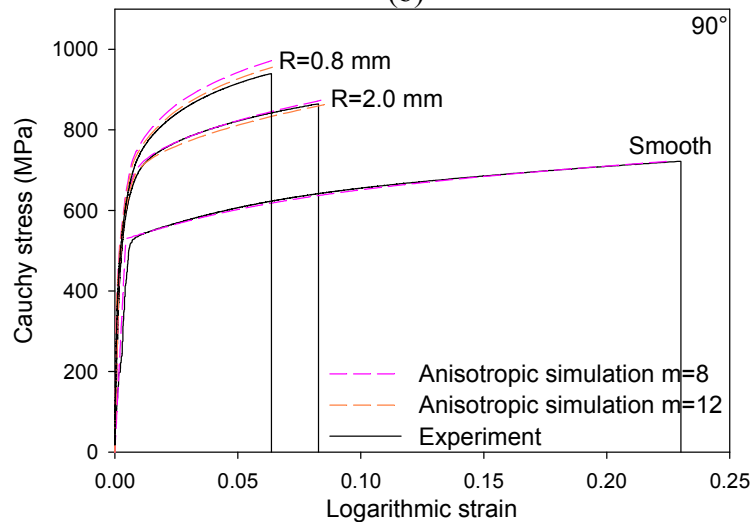
Shape parameter	$m=8$					$m=12$			
	Isotropic	0°	45°	90°	ND	Isotropic	0°	45°	90°
Notch $R=2.0\text{mm}$	6.28	2.15	1.20	0.20	-	6.28	1.61	0.56	0.83
Notch $R=0.8\text{mm}$	10.54	5.11	3.51	2.58	-	10.54	1.59	0.99	0.85
Cylinder $h_0/D_0=1$	2.81	2.81	9.21	7.56	7.42	-	-	-	-
Butterfly	10.85	0.10	-	5.98	-	-	-	-	-



(a)



(b)



(c)

Figure 5.2. Experimental and predicted Cauchy stress-logarithmic strain curves for tensile tests on smooth and notched specimen in the (a) 0° , (b) 45° and (c) 90° in-plane directions, with the anisotropic model ($m=8$ and $m=12$). Figure (a) also shows the prediction with the isotropic model.

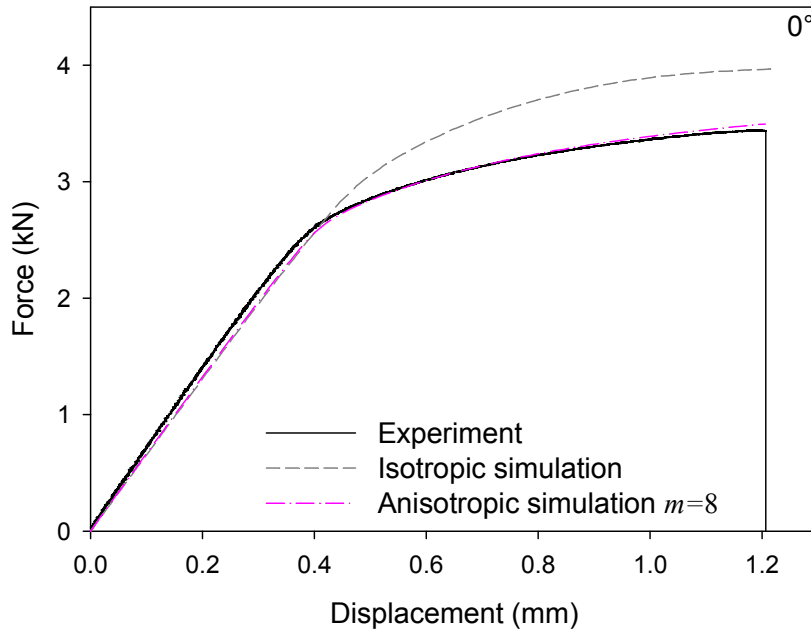


Figure 5.3. Experimental and predicted force-displacement curves for the shear test on a butterfly specimen in the 0° in-plane direction with the isotropic and anisotropic models ($m = 8$).

5.2.2 Anisotropic version of Yld2004-18p

Numerical simulations of the various material tests were run with the anisotropic version of the model with $m = 8$ and $m = 12$, and their associated parameters obtained in the calibration presented in Chapter 4. Results are presented for both values when differences were observed. Otherwise, only the calibration with $m = 8$ is used. Note that the uniaxial tension, shear and compression tests are not affected by the value of m , while the results for tensile tests on notched specimens are affected. For tensile tests on notched specimens, the strain ratios were not affected by the value of m , but the stress-strain curves with $m = 12$ are in general more accurate than those obtained with $m = 8$ (the maximum error in stress level decreases from 5% to 2%, see Table 5.1). This illustrates that the notch-strengthening effect is sensitive to the shape of the anisotropic yield surface.

As this model was calibrated using uniaxial tensile tests and shear tests, the simulations are in good agreement with these experimental results. Stress-strain curves for the tensile tests in seven different directions on smooth specimens are presented in Figure 5.4 (c), where they can be compared to the experimental data in Figure 5.4 (a). The error between experimental and numerical yield stresses is directly linked to the inaccuracy in the calibration of the material model (see Figure 4.2 (a)). The simulation error is small for all directions with a maximum of 3.5%. The simulated force-displacement curve for the shear tests is presented in Figure 5.3 for the 0° direction. As expected since the shear tests in the rolling direction was used to calibrate the anisotropic material model, the agreement between prediction and

experiments is better with the anisotropic than with the isotropic material model (see also Table 5.1). The stress-strain curves for tests on notched specimens in different directions and for the two notch root radii are presented in Figure 5.2. The overestimation observed with the isotropic model is considerably reduced with the anisotropic model (maximum values of the error are 5% of logarithmic strain with $m = 8$, see Table 5.1). One remarkable result is that the reduced effect of anisotropy on the stress-strain curves observed experimentally is reproduced with the anisotropic material model.

Concerning the strain ratios, numerical results are in good agreement with experiments for tensile tests on smooth specimens in the seven different directions. The logarithmic strain in the transverse direction of the specimen (TS) versus the logarithmic strain in the normal direction (ND) of the plate is presented in Figure 4.1 (a) for the 0° , 45° and 90° in-plane directions. For the tensile tests on notched specimens, the predicted strain ratios show more deviation (see Figure 4.1 (b) and (d)).

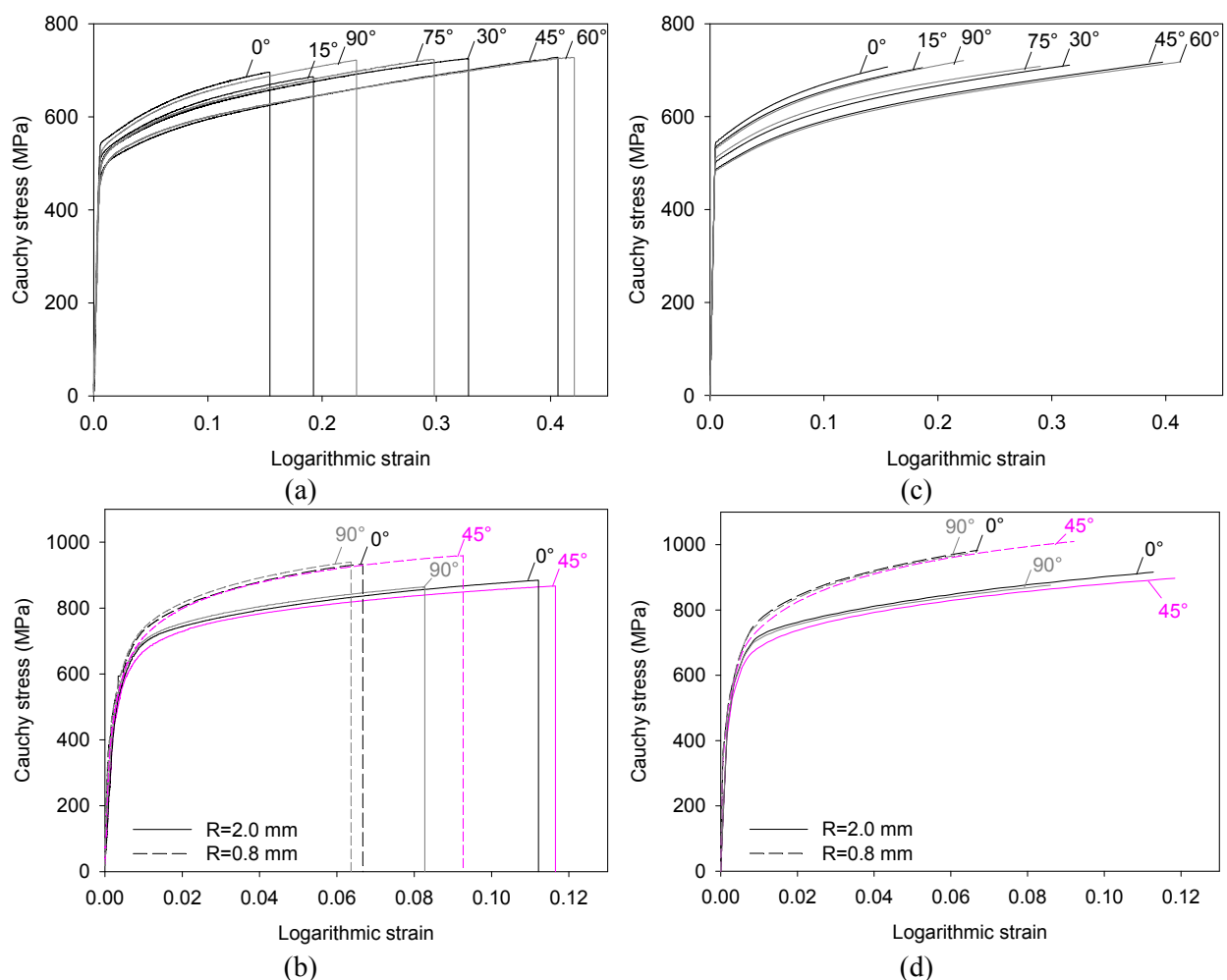


Figure 5.4. Representative experimental Cauchy stress-logarithmic strain curves for tensile tests on (a) smooth specimens and (b) notched specimens taken in different in-plane directions and (c)-(d) corresponding numerical predictions with the anisotropic model ($m = 8$).

Compression tests have also been simulated for the 0° , 45° , 90° in-plane directions and normal direction (ND) of the plate (Figure 5.5 (b)) and compared with experimental results in Figure 5.5 (a). Some deviations are seen between these simulations and the experimental results (see Table 5.1). One possible reason for this is believed to be the friction between the specimen and the rigid platens. Another possible reason is that the yield surface is insensitive to the pressure and is thus symmetric in uniaxial tension and uniaxial compression. Then, the experimental yield stress in uniaxial compression, not similar to the yield stress in uniaxial tension, cannot be predicted correctly with the chosen yield function. In addition, the deviation between predicted and experimental stress-strain curves is increasing with plastic strains and can reach 12% at a strain $\varepsilon = 0.6$ in the 0° direction for instance. This is due to the saturating plastic hardening law which was calibrated under uniaxial tension up to 16% strain (the failure strain in the 0° direction) and validated on the uniaxial tension test in the 45° direction up to strains of 45%. The use of a non-saturating hardening law or the calibration on compression tests could have enhanced the numerical predictions.

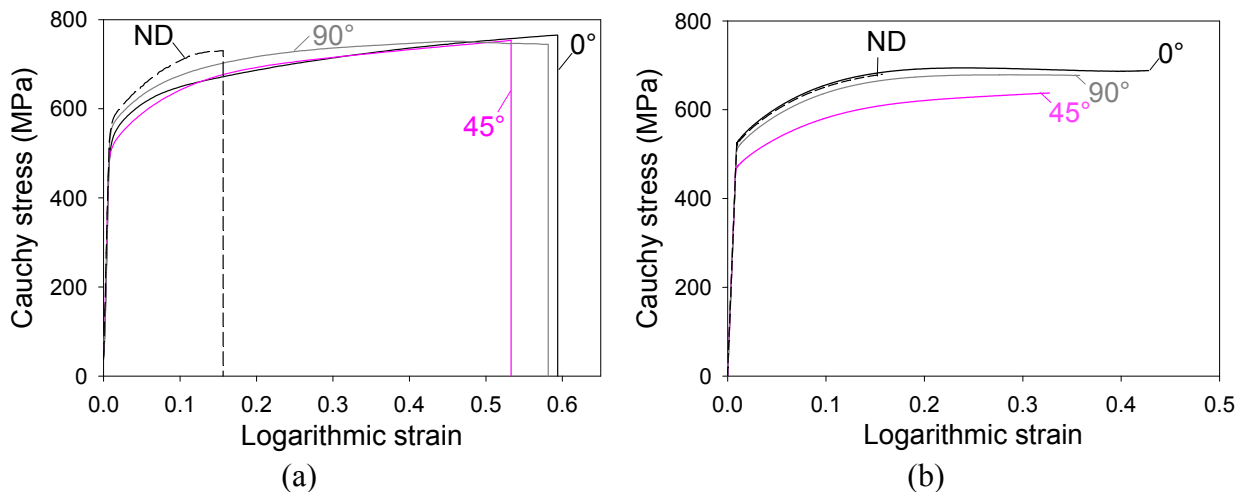


Figure 5.5. (a) Representative experimental Cauchy stress-logarithmic strain curves for compression tests on cylindrical specimens ($h_0/D_0=1$) in different directions of the plate and (b) corresponding numerical predictions with the anisotropic model ($m = 8$).

5.2.3 Influence of plastic anisotropy

It was found that the anisotropic material model provides a more accurate description of the notch-strengthening effect in the numerical simulations of the notched specimen tensile tests. The model is able to reproduce the experimental observations despite the assumptions of non-evolution of the anisotropy, incompressibility and pressure insensitivity.

To explain this observation, the normal coordinate stresses in the numerical simulations were extracted at the minimum cross section of the notched specimens. The shear stresses along the coordinate axes were found to be negligible compared to the normal stresses. Hence,

the longitudinal (LS) and transverse (TS) directions of the specimen and the normal direction (ND) of the plate can be considered as the principal axes of the stress tensor. Three steps of the loading must be distinguished. First, the loading is totally elastic and the behaviour of the material is isotropic. Second, plasticity starts at the root of the notch and propagates to the central part of the section. Third, the whole minimum section is plastified and the plastic flow continues until fracture. These three steps explain the better predictions of the notch-strengthening effect in the anisotropic simulations of the notched tensile tests:

- *1st step*: Figure 5.6 (a) shows the hydrostatic stress, deviatoric stress and stress triaxiality along the transverse axis of the specimen (TS) during elastic loading. The stresses are found to be heterogeneous in the minimum cross section. The boundary conditions at the root of the notch induce a stress state close to uniaxial tension in the loading direction (LS). In the central part, the notched geometry induces a multiaxial stress state. The major principal stress is along the direction of loading direction (LS) while the intermediate and minor principal stresses are the components orthogonal to the loading direction (TS and ND). The major and intermediate stresses are shown in Figure 5.6 (b) for the central element at the minimum cross section. The corresponding stress state decreases the value of the deviatoric stresses (which drive the plastic process) compared to the behaviour at the root of the notch.
- *2nd step* starts when the material at the root of the notch reaches the yield limit. This is represented by a cross in Figure 5.6 (b). With an anisotropic material model, the plastification does not occur simultaneously in the transverse direction of the specimen (TS) and the normal direction (ND) of the plate. This asymmetric plastic behaviour induces a non-equibiaxial stress state inside the remaining elastic central part of the minimum cross section. The stress path of the central element will differ from the isotropic case. Consequently, the yield surface will be reached in this element at a different location in stress space in the simulations with isotropic and anisotropic material models. This is represented by the points in Figure 5.6 (b), which also reveals that the stress values at yielding are lower for the anisotropic case. One explanation is that the deviatoric stresses increase slightly faster in the anisotropic case (see Figure 5.7 (a)). Consequently, yielding in the centre of the minimum cross section (and plasticity overall the cross section) is reached at an earlier stage of the loading in the anisotropic case.
- *3rd step* starts once the minimum cross section is totally plastified. As the yielding stress states are different for the isotropic and anisotropic cases, the plastic flow will also differ for the two cases. This is illustrated by Figure 5.7 (b), which shows that the hydrostatic stress increases at a lower rate in the anisotropic case.

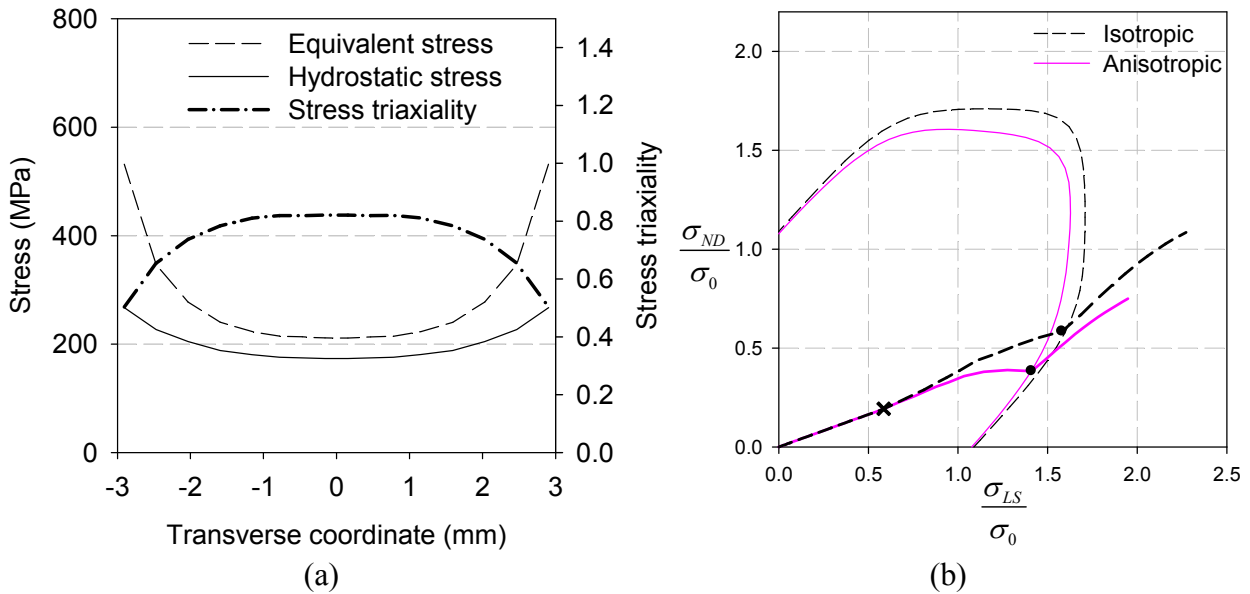


Figure 5.6. Predicted data from the tensile test on notched specimen ($R=2.0\text{mm}$) in the 0° direction using the anisotropic model ($m=8$): (a) equivalent stress, hydrostatic stress and stress triaxiality in the minimum cross section along the transverse direction of the specimen (TS) in the elastic domain and (b) yield loci with $\sigma_{TS}/\sigma_0 = 0.46$ and stress paths of the central element of the minimum cross section of the specimen. σ_{ND} denotes the normal stress in ND, σ_{LS} in LS and σ_{TS} in TS.

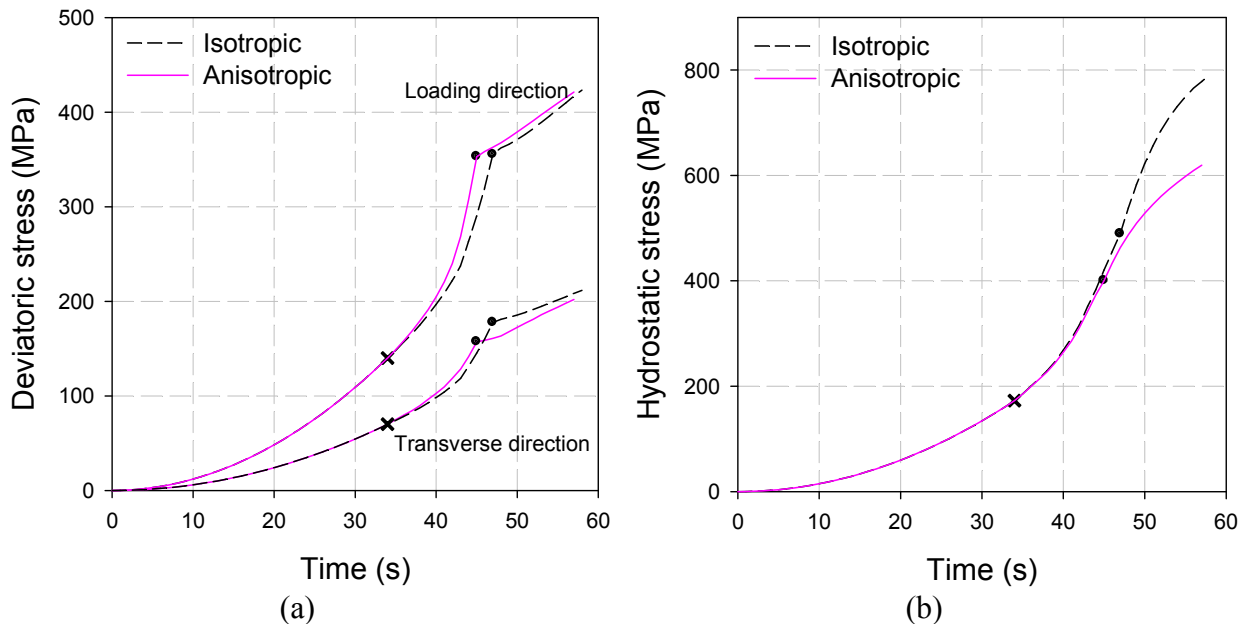


Figure 5.7. Predicted stresses in the centre of the minimum cross section of the notched specimen ($R=2.0\text{mm}$) for the tensile test in the 0° direction using the isotropic and anisotropic models ($m=8$): evolution until fracture of (a) the deviatoric stresses in LD and TD and (b) the hydrostatic stress.

5.3 Local stress and strain along fracture surface

To evaluate the stress and strain fields in the specimens, we consider the trajectories of accumulated plastic strain \bar{p} versus stress triaxiality σ^* from incipient plastic deformation to fracture for the finite elements defining the experimentally observed failure surface (cf. Figure 5.1). The envelopes of all trajectories and/or some selected trajectories are presented for the different tests (see Figure 5.8, Figure 5.10 and Figure 5.11). It is important to repeat here that the accumulated plastic strain \bar{p} computed from the numerical simulations is different from the strains measured experimentally and these different strain measures should not be directly compared. However, the difference between these measures has no influence on the discussion regarding the heterogeneity of the stress and strain fields and the impact of plastic anisotropy on the establishment of a failure criterion.

The results for the uniaxial tensile tests in the 0° , 45° and 90° directions are shown in Figure 5.8 (a). The trajectories of one of the surface elements and the element at the centre of the specimen correspond to the left and right parts of the envelope. Note that the elements considered to build the envelope depend on the loading direction and the corresponding failure mode. Thus, the elements marked in Figure 5.1 (c) left are used for the 0° and 90° directions, while the elements indicated in Figure 5.1 (c) right are used for the 45° direction. The upper part of the envelope is defined by the experimentally observed diameter reduction at fracture, i.e. fracture in the simulations is defined by the instant in the loading process where the predicted diameter reduction is equal to the measured diameter reduction at fracture in the experiments. The trajectories displayed in Figure 5.8 (a) show that the stress triaxiality increases from the initial value at the centre of the specimen, while it slightly decreases close to the surface. This change in stress triaxiality is due to necking of the specimens and is distinct at 45° while more limited for the two other directions. The envelopes for the different directions are similar for low plastic strains, especially at 0° and 90° , although the failure strain itself is quite different for these two directions. For the 45° direction the stress triaxiality at the centre of the specimen increases significantly with the accumulated plastic strain, since the large ductility in this direction allows for marked necking before fracture. The accumulated plastic strain at failure, \bar{p}_f , in the elements located in the critical cross section of the specimen is homogeneous when failure occurs at small plastic strains ($\bar{p}_f \in [0.156; 0.164]$ for the tensile test in the 0° direction), whereas a substantial variation is seen when the failure strain increases ($\bar{p}_f \in [0.336; 0.406]$ for the tensile test in the 45° direction). The maximum values of \bar{p}_f and σ^* at failure are reached at the centre of the specimens in all directions.

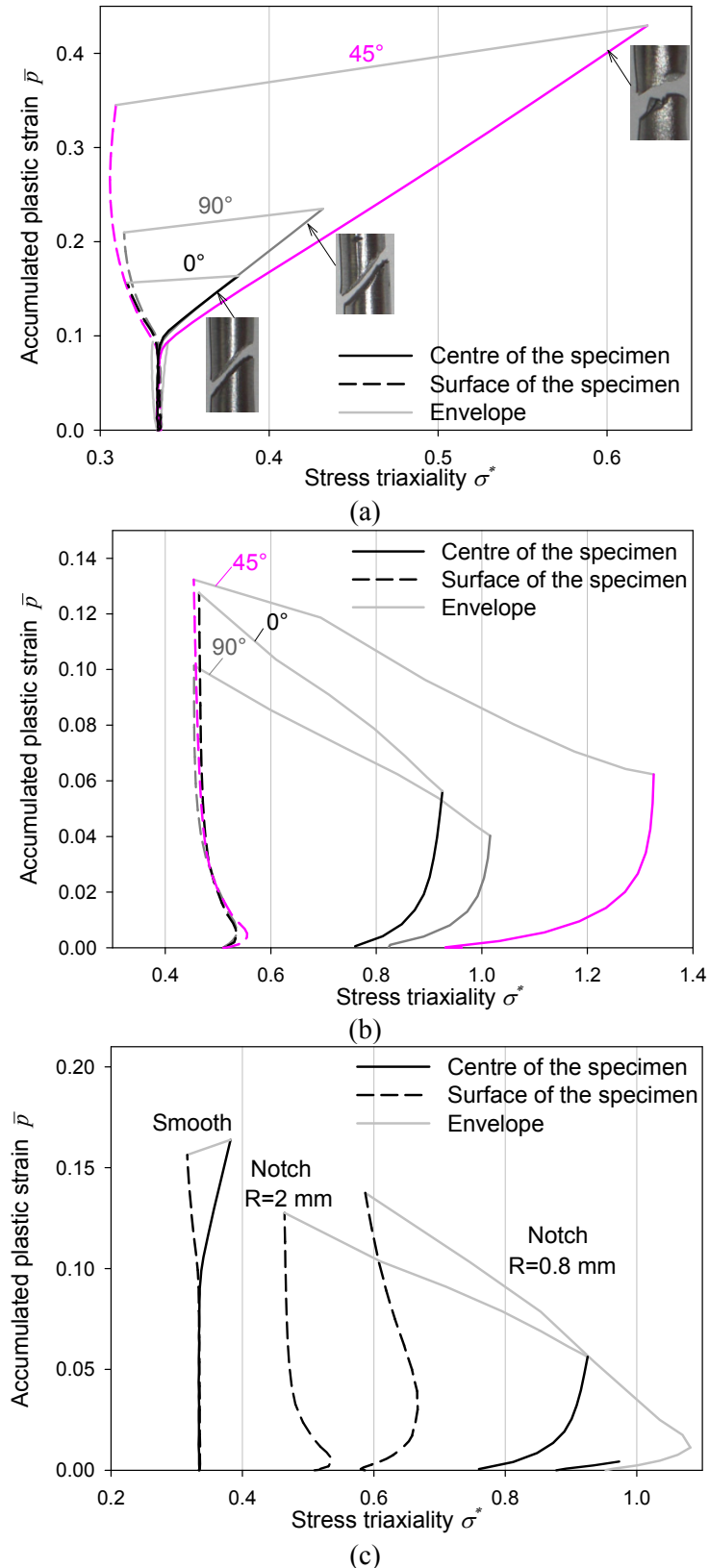


Figure 5.8. Envelopes of the trajectories of accumulated plastic strain versus stress triaxiality for elements depicted in black in Figure 5.1 for tensile tests in the 0°, 45° and 90° in-plane directions on (a) smooth specimens, (b) notched specimens ($R=2.0\text{mm}$) and (c) all tensile tests performed in the 0° direction. All trajectories are terminated at the loading corresponding to failure in the experiment.

The influence of anisotropy on the stress triaxiality is studied in Figure 5.8 (b), which presents the envelopes for the notched specimens with $R=2.0$ mm loaded in different directions. Figure 5.8 (b) further presents the results obtained with the smooth and notched specimens with the two radii $R=2.0$ mm and $R=0.8$ mm, loaded in the 0° direction, for comparison. The trajectories for the surface element, giving the minimum stress triaxiality, and the element in the centre of the specimen, not always giving the highest stress triaxiality, are shown. All other trajectories are comprised between these two lines. As explained by Fourmeau et al. (2011), the plastic flow initiates at the root of the notch and influences the stress state in the whole minimum cross section. Since this plastic flow is anisotropic, the stress state becomes non-axisymmetric and the stress triaxiality at the centre of the minimum cross section (at the initiation of plastic deformation) can be affected. In a similar way as for tests on smooth specimens, the stress triaxiality at the centre of the minimum cross section increases more for the 45° loading direction than for the other directions. Indeed, both the stress triaxiality and the accumulated plastic strain at failure are found to be highest for the 45° loading direction in the centre of the specimen. The accumulated plastic strains at failure are very different at the root of the notch and the centre of the minimum cross section, giving a considerably larger strain range than under uniaxial loading conditions (e.g. in the 0° direction, $\bar{p}_f \in [0.068; 0.127]$ for $R=2.0$ mm and $\bar{p}_f \in [0.004; 0.013]$ for $R=0.8$ mm, see Figure 5.8 (c)). Fracture occurs after a very small plastic straining at the centre of the minimum cross section (0.068 and 0.004 for notched specimens loaded in the 0° direction with $R=2.0$ mm and $R=0.8$ mm, respectively), while the strain at the surface of the specimen is much larger. In some cases, the centre was not the point of maximum stress triaxiality in the minimum cross section. This was the situation for the notched specimen with $R=0.8$ mm, where the trajectory of the central element was actually inside the envelope (see Figure 5.8 (c)). The envelope is in this case limited by the trajectory of an element located between the centre of the specimen and the root of the notch.

Another way to visualize the heterogeneities in the strain and stress fields is presented in Figure 5.9. Here the spatial distributions of the accumulated plastic strain and the stress triaxiality over the minimum cross section are depicted for the 0° direction at the global displacement corresponding to experimental failure. For the tensile test on smooth specimens (Figure 5.9 (a)) \bar{p} and σ^* are found rather homogeneous across the section. For the tensile tests on notched specimens (Figure 5.9 (b) and (c)) \bar{p} is the highest at the root of the notch, where σ^* is the lowest. Further, Figure 5.9 shows that the stress and strain fields are not axisymmetric due to anisotropy, and for the notched specimen with $R=0.8$ mm, σ^* is

maximum at the centre of the specimen. The latter observation was also made by El-Magd et al. (1997) and Børvik et al. (2003a) for steels.

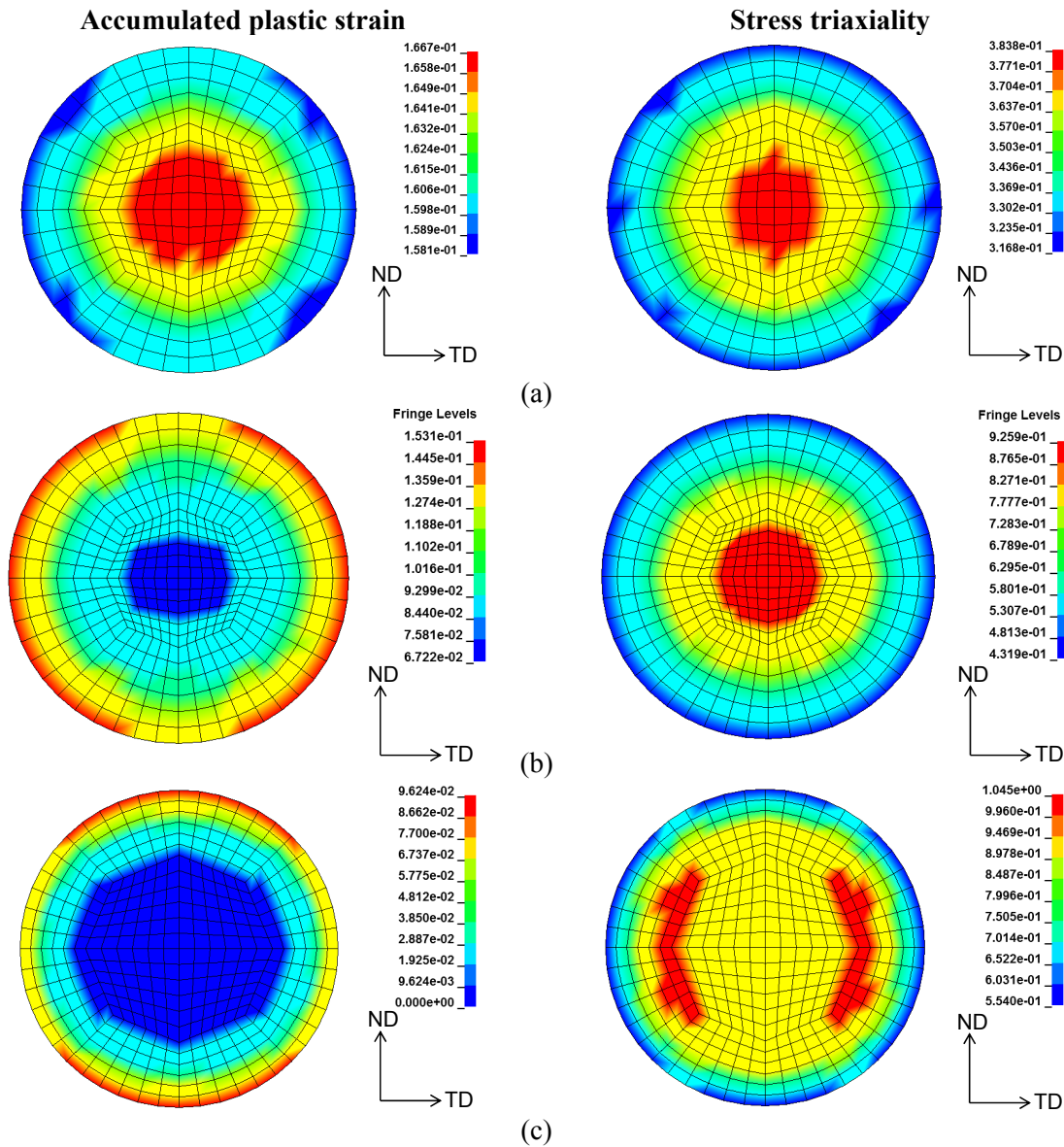


Figure 5.9. The distributions of accumulated plastic strain and stress triaxiality over the minimum cross section at the point of failure for tensile tests in the 0° in-plane direction on (a) smooth specimen, (b) notched specimen with $R=2.0$ mm and (c) notch specimen with $R=0.8$ mm.

The results for the compression test performed in the 0° in-plane direction are shown in Figure 5.10. Fracture is assumed in the simulation when the length of the specimen corresponds to the average length at fracture in duplicate experiments. The accumulated plastic strain and the stress triaxiality in the elements of the fracture surface are found very heterogeneous. The strong inhomogeneity in the accumulated plastic strain at fracture (e.g.

$\bar{p}_f \in [0.394; 0.789]$ in the 0° direction) makes the strains obtained from measurements of the global change in length of the specimen inaccurate and not representative for the real strains inside the specimen. Concerning the stress triaxiality, a highly compressive state of stress is found at the interface with the platen (point S2 in Figure 5.1 (c) and Figure 5.10), where friction effects are important, while a uniaxial compression stress state is only ensured at mid height on the surface of the cylinder (point S1). This reveals the importance of the barrelling effect. The inclined fracture surface contains the points with the maximum stress triaxiality. This suggests that under these negative stress triaxiality states, fracture preferentially occurs where the stress triaxiality is the highest. Note that the initial stress triaxiality is not even equal to the theoretical value of $-1/3$ in the entire specimen due to friction occurring also in the elastic regime.

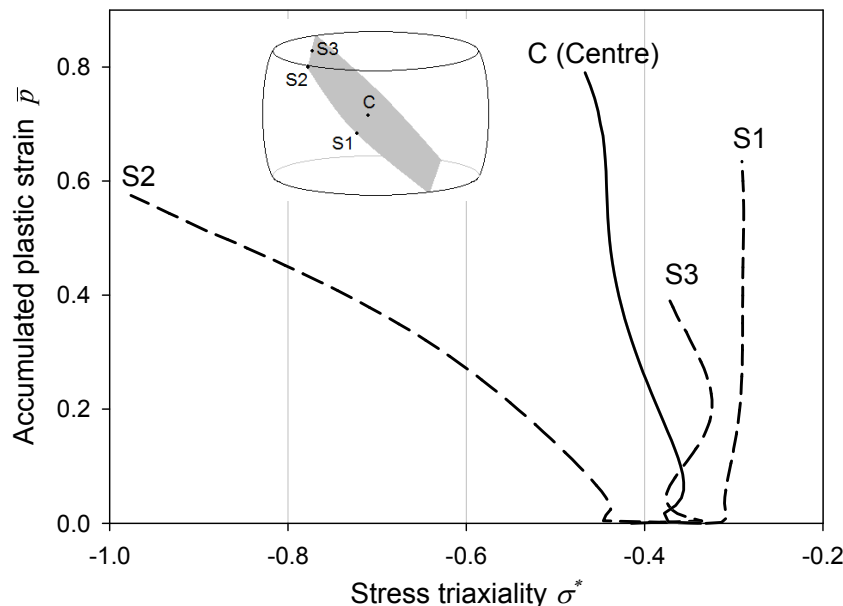


Figure 5.10. Trajectories of accumulated plastic strain versus stress triaxiality for elements depicted in black in Figure 5.1 (a) for the compression tests on cylinders with $h_0/D_0 = 1$ in the 0° in-plane direction. All trajectories are terminated at the displacement corresponding to failure in the experiment.

Figure 5.11 shows the results for the shear test in the 0° direction, revealing that the specimen experiences a complex loading history that deviates significantly from shear loading in some locations. Fracture was assumed when the central surface element C reached the experimentally obtained strain to failure. The rim element S and the element I1 (see Figure 5.1 (d) and Figure 5.11) experience stress triaxiality states deviating considerably from the theoretical value of zero. However, the elements located at the middle height of the shear band named I2, I3 and C experience a loading close to shear. The element at point M, which

corresponds to the maximum strain location, is also shown. This point is subjected to large plastic strains, but is not located on the fracture surface and is consequently not critical. The distribution of stress triaxiality and accumulated plastic strain in the shear specimen demonstrates that the minimum cross section is not subjected to a homogeneous shear stress. The influence of the direction of loading on the stress triaxiality field was found to be small.

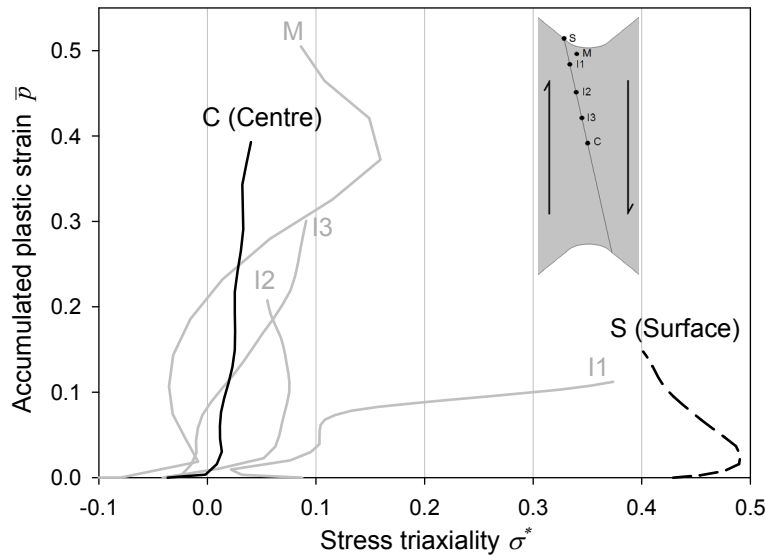


Figure 5.11. Trajectories of accumulated plastic strain versus stress triaxiality for elements depicted in black in Figure 5.1 (b) for the shear test in the 0° direction. All trajectories are terminated when the strain in the central surface element C corresponds to the failure strain determined in the DIC analysis.

5.4 Conclusions

It was found that Yld2004-18p provided an adequate description of the plastic anisotropy of the AA7075-T651 plate. Moreover, it was shown that plastic anisotropy is pivotal for an accurate prediction of the notch-strengthening effect. In particular it was shown that an isotropic yield function overestimates the stress level in the notched specimens. The shape of the anisotropic yield surface was revealed to significantly affect the prediction of the notched-specimen behaviour. These findings are important since notched specimens often are used to determine the fracture locus of materials, and in this context an accurate description of the stress state within the notch is essential. Also, the scatter in the results further enforces us to take the fracture strains at low stress triaxiality into account in a rather qualitative way.

A fracture locus giving the failure strain as a function of the stress triaxiality is a widely used way of representing the ductility of an isotropic material. It is usually constructed from experimentally obtained (global) failure strains and theoretical initial stress triaxiality values available for given specimen geometries. Figure 5.12 gives the experimental failure strains

obtained in Chapter 3 for the different tests in the different loading directions performed on specimens taken from the AA7075-T651 plate. It was assumed more prudent not to attribute a unique stress triaxiality value to each test. However, tests are ordered by increasing initial theoretical stress triaxiality. Figure 5.12 clearly shows that the usual representation of a “unique” fracture locus in terms of accumulated plastic strain versus stress triaxiality is not sufficient to describe the fracture behaviour for the AA7075-T651 alloy. This is expected since this kind of representation was first proposed for isotropic materials (e.g. McClintock, 1968; Rice and Tracey, 1969). To improve this representation, plastic anisotropy should be included. A possible route towards this aim is to include plastic anisotropy in Rice and Tracey’s analysis as done for instance by Benzerga et al. (2001) and in the Gurson model by Monchiet et al. (2008). In the analysis of Benzerga et al. (2001) both the accumulated plastic strain and the equivalent stress are simply replaced by the accumulated plastic strain and the equivalent stress associated to the anisotropic yield criterion used in the analysis. Recently, the effect of loading path on the fracture locus was examined theoretically by means of an axisymmetric void cell model by Benzerga et al. (2012). They found that the fracture loci under radial and non-radial loadings are quite distinct from each other. Under radial loadings, a unique fracture locus may be constructed for given initial values of microstructural variables. Under non-radial loadings, however, an infinite number of fracture loci in terms of failure strain versus average stress triaxiality and Lode parameter can be constructed. Thus, they claimed that the notion of a fracture locus is a “misnomer”. Moreover, as suggested by several researchers (e.g. Zhang et al., 2001; Nahshon and Hutchinson, 2008; Bai and Wierzbicki, 2008; Barsoum and Faleskog, 2011), the Lode parameter (as a function of the third invariant of the deviatoric stress tensor) seems to play an important role in the ductile fracture process.

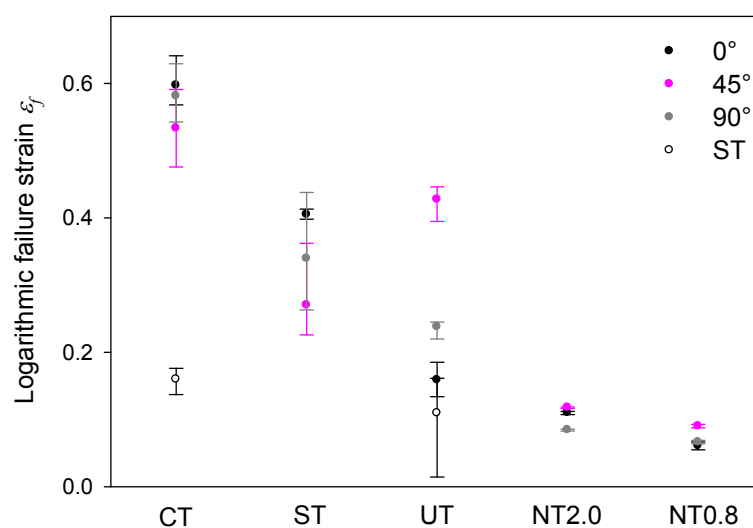


Figure 5.12. Average experimental strain to failure for the compression tests (CT), shear tests (ST), uniaxial tension tests (UT), notched tension tests with $R=2.0\text{mm}$ (NT2.0) and with $R=0.8\text{mm}$ (NT0.8). The error bars represent the range of failure strains from duplicate tests.

Based on the stress and strain field analysis, the presented study points out another difficulty in establishing a failure locus: the presence of several failure modes in addition to anisotropic plastic behaviour (see also Luo et al., 2012). For instance, for the uniaxial tension tests on smooth specimens, very different failure processes are observed (see Figure 3.4). Existing macroscopic failure models are not believed capable of capturing both the failure mode transition and the influence of the direction of loading. With respect to those observations, it might become necessary to include a description of the microstructure of the material and especially the distribution of the inclusions and the precipitate free zones (PFZs). The PFZs are the weakest zones in the material and are potential locations for strain localization and fracture initiation. As far as the AA7075-T651 aluminium alloy is concerned, the location of PFZs (related to the grain morphology) and the distribution of inclusions are both anisotropic.

Chapter 6. Analytical considerations

6.1 Introduction

In this chapter, two issues regarding failure are considered. First, the effect of anisotropic matrix behaviour is studied in the light of the analysis for void growth developed by Rice and Tracey (1969). Second, the usual localization criterion, given by Rice (1976), is analyzed with various constitutive characteristics among which shape of the yield surface, non-associativity and thermo-mechanical couplings.

6.2 Void growth approach for anisotropic materials

As discussed in Chapter 1, the void growth approach has for half a century been extensively used to describe the damage occurring in metals at the microstructural level, while subjected to plastic deformations. Nowadays, several stages of damage are usually distinguished: the nucleation of voids, their growth, and finally their coalescence leading to macroscopic failure. The earlier works concerned the growth of a single cylindrical void (McClintock, 1968) or a single spherical void (Rice and Tracey, 1969) inside an infinite rigid perfectly plastic medium. Later, Gurson (1977) studied a spherical void inside a finite rigid perfectly plastic spherical medium. Gurson's analysis was successively enriched by accounting for nucleation and coalescence of voids (Tvergaard and Needleman, 1984), but also by strain hardening (Gurson, 1977; Leblond, 1995), two populations of voids (Marini, 1985), void shape and distribution (Gologanu et al. 1993, 1994a), third invariant (Nahshon and Hutchinson, 2008) and plastic anisotropy (Monchiet et al., 2008). Gurson's analysis leads to an expression for the yield function resulting from a finite matrix containing a void. This development introduces the porosity since the matrix is of finite size. On the contrary, the Rice and Tracey analysis is performed inside an infinite medium and results only in the expression of the void growth rate. This expression does not give any influence of the void on the material behaviour and can be used as an uncoupled damage criterion. Regarding the present study of the AA7075-T651

alloy, no significant void growth was observed before failure for the tests performed in Chapter 3. Therefore, the influence of a void on the material behaviour can be neglected and for this reason, the Rice and Tracey (RT) analysis is relevant and will be further extended to an anisotropic material in the following. Inclusion of the anisotropy in the Gurson approach was studied by Benzerga and Besson (2001), while Monchiet et al. (2008) analysed the role of anisotropy both on the yield behaviour and the growth of voids.

6.2.1 Rice and Tracey analysis

Geometry and boundary conditions

As depicted in Figure 6.1, in the Rice and Tracey (RT) analysis, a spherical cavity of initial radius R_0 in an infinite medium is subjected to a multi-axial stress field Σ , obtained by imposing a strain rate field $\dot{\mathbf{E}}$ at the boundary of the body (i.e. at infinity). The fields inside the medium are denoted with small letters ($\mathbf{s}, \boldsymbol{\sigma}, \dot{\boldsymbol{\varepsilon}}$) while their values at infinity are denoted with capital letters ($\mathbf{S}, \Sigma, \dot{\mathbf{E}}$).

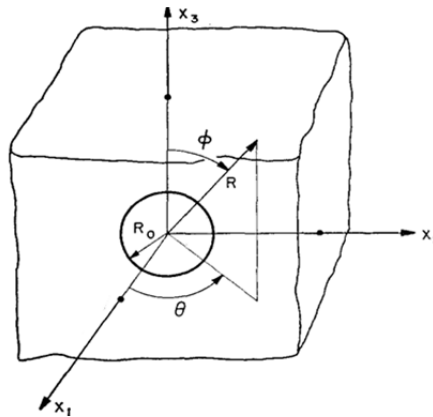


Figure 6.1. Geometry of a spherical void inside an infinite medium and coordinate system used by Rice and Tracey (1969).

The spherical coordinate system associated to this geometry is defined as

$$\underline{\mathbf{e}}_R = \begin{pmatrix} \sin \phi \cos \theta \\ \sin \phi \sin \theta \\ \cos \phi \end{pmatrix}_{(x_1, x_2, x_3)}, \quad \underline{\mathbf{e}}_\theta = \begin{pmatrix} -\sin \theta \\ \cos \theta \\ 0 \end{pmatrix}_{(x_1, x_2, x_3)}, \quad \underline{\mathbf{e}}_\phi = \begin{pmatrix} \cos \phi \cos \theta \\ \cos \phi \sin \theta \\ -\sin \phi \end{pmatrix}_{(x_1, x_2, x_3)} \quad (30)$$

Constitutive behaviour

The material of the medium is considered to be rigid perfectly plastic (i.e. no elastic strain and no plastic hardening) and the plastic flow is associated to a von Mises yield function defined as

$$f = \sigma_{eq} - \sigma_0 = 0 \quad \text{with} \quad \sigma_{eq} = \sqrt{\frac{3}{2} \mathbf{s} : \mathbf{s}} \quad (31)$$

where \mathbf{s} is the deviatoric stress, defined by $\mathbf{s} = \boldsymbol{\sigma} - \sigma_H \mathbf{I}$ with the hydrostatic stress $\sigma_H = \text{tr}(\boldsymbol{\sigma})/3$. Consequently, the deviatoric stress \mathbf{s} is directly linked to the strain rate $\dot{\boldsymbol{\epsilon}}$ according to

$$\mathbf{s} = \frac{2}{3} \frac{\sigma_0}{\dot{p}} \dot{\boldsymbol{\epsilon}} \quad (32)$$

where $\dot{p} = \sqrt{\frac{2}{3} \dot{\boldsymbol{\epsilon}} : \dot{\boldsymbol{\epsilon}}}$ is the energy conjugate equivalent strain rate.

Equilibrium

In the RT analysis, the weak form of the equilibrium equations is established from the internal work Q_i and external work Q_e

$$\begin{aligned} Q_i(\underline{\dot{u}}) &= \int_{V_m} \mathbf{s}(\dot{\boldsymbol{\epsilon}}) : \dot{\boldsymbol{\epsilon}} dV \\ Q_e(\underline{\dot{u}}) &= \int_{S_\infty} \boldsymbol{\Sigma} \cdot \underline{\mathbf{n}} \cdot \underline{\dot{u}} dS \end{aligned} \quad (33)$$

where $\mathbf{s}(\dot{\boldsymbol{\epsilon}})$ and $\dot{\boldsymbol{\epsilon}}$ are the deviatoric stress and strain rate fields inside the body and \mathbf{S} and $\boldsymbol{\Sigma}$ correspond to the deviatoric and total stress fields at infinity. V_m is the volume of the medium and fulfils $V = V_m + V_v$; V is the total volume and V_v is the volume of the void. S_∞ is the external surface of the medium located at infinity, $\underline{\mathbf{n}}$ is the normal vector to that surface, $\underline{\dot{u}}$ is the velocity field and $\dot{\boldsymbol{\epsilon}}$ is the associated strain rate field. The divergence theorem can be used to transform the two integrals presented in Eq.(33) and the weak form of the equilibrium equations is obtained through the minimization of the function

$$Q(\underline{\dot{u}}) = Q_i(\underline{\dot{u}}) - Q_e(\underline{\dot{u}}) = \int_V (\mathbf{s}(\dot{\boldsymbol{\epsilon}}) - \mathbf{S}) : \dot{\boldsymbol{\epsilon}} dV - \boldsymbol{\Sigma} \int_{S_v} \underline{\mathbf{n}} \cdot \underline{\dot{u}} dS \quad (34)$$

where S_v is the surface of the void.

Field(s)

Rice and Tracey selected a specific velocity field $\underline{\dot{u}}$ as

$$\underline{\dot{u}} = \dot{\mathbf{E}} \underline{\mathbf{x}} + D \underline{\dot{u}}^D + E \underline{\dot{u}}^E \quad (35)$$

where the factors D and E refer to the spherical and deviatoric expansion, respectively, $\dot{\mathbf{E}}$ is the strain rate field applied at infinity and $\underline{x} = R \underline{e}_R$ is the current coordinate. Rice and Tracey showed that the shape changing velocity field $\underline{\dot{u}}^E$ has no significant effect on the void growth rate at high stress triaxiality and is therefore neglected. The hydrostatic velocity field $\underline{\dot{u}}^D$ is radial and vanishes at infinity to respect the boundary condition. Thus, $\dot{\mathbf{E}}$ is the only quantity of Eq.(35) remaining at infinity. A convergence analysis additionally constrains the velocity field to fall off as R^{-2} , where R is the radius, see Figure 6.1. The selected velocity field and the corresponding strain rate field are

$$\underline{\dot{u}} = \dot{\mathbf{E}} \underline{x} + D \underline{\dot{u}}^D = \dot{\mathbf{E}} \underline{x} + D \dot{P} \left(\frac{R_0}{R} \right)^3 \underline{x} = \dot{\mathbf{E}} \underline{x} + D \dot{P} \lambda \underline{x} \quad \text{with} \quad \begin{cases} \dot{P} = \sqrt{\frac{2}{3} \dot{\mathbf{E}} : \dot{\mathbf{E}}} \\ \lambda = \left(\frac{R_0}{R} \right)^3 \end{cases} \quad (36)$$

$$\dot{\boldsymbol{\varepsilon}} = \dot{\mathbf{E}} + \dot{\boldsymbol{\varepsilon}}^D = \dot{\mathbf{E}} + D \dot{P} \lambda \mathbf{e}^D \quad \text{with} \quad \mathbf{e}^D = \mathbf{I} - 3 \underline{e}_R \otimes \underline{e}_R$$

where \dot{P} is the equivalent plastic strain rate at infinity. Note that the remote strain rate field $\dot{\mathbf{E}}$ is necessarily deviatoric since any hydrostatic component applied at infinity would bring an infinite change of volume. Also, this field induces a change of shape of the cavity.

Insertion of the chosen fields and constitutive behaviour into the equilibrium equation

Assuming that the remote deviatoric stress does not carry out any work on the surface involving the radial velocity field $\underline{\dot{u}}^D$ (i.e. RT split the deviatoric and hydrostatic contributions of the work), the minimization given in Eq.(34) reduces to

$$\int_V (\mathbf{s}(\dot{\boldsymbol{\varepsilon}}(D)) - \mathbf{S}) : \dot{\boldsymbol{\varepsilon}}^D dV = \Sigma_H \int_{S_v} \underline{n} \cdot \underline{\dot{u}} dS \quad (37)$$

where Σ_H is the hydrostatic stress at infinity. The solution of this equation will give an expression for D , which is the unknown of the problem. Inserting the field given in Eq.(36) and the constitutive behaviour given in Eq.(32) into the equilibrium given in Eq.(37) gives (details are skipped) leads to

$$\frac{1}{6\pi} \int_{\Omega} \left\{ \log \left(\sqrt{4D^2 - 4D\mu_{RT} + 1} + 2D - \mu_{RT} \right) - \log(1 - \mu_{RT}) \right. \\ \left. + \mu_{RT} \log \left(\frac{1}{2} \sqrt{4D^2 - 4D\mu_{RT} + 1} + \frac{1}{2} - D\mu_{RT} \right) \right\} d\Omega = \frac{\Sigma_H}{\sigma_0} \quad (38)$$

where $\mu_{RT} = \dot{E}_{RR} / \dot{P}$ (with $\dot{E}_{RR} = \underline{e}_R \cdot \dot{\mathbf{E}} \cdot \underline{e}_R$) is related to the third invariant of the strain tensor (see Rice and Tracey, 1969) and $d\Omega = \sin\phi d\phi d\theta$ denotes the solid angle. At this stage of the development RT assumed that D is large ($D \gg 1$) to get an analytical solution. Thus, the terms of order $1/D$ can be neglected and the terms involving D can be integrated over the unit sphere, giving

$$D = C \exp\left(\frac{3 \Sigma_H}{2 \sigma_0}\right) \quad (39)$$

where $C = \frac{1}{4} \exp\left[\frac{1}{4\pi} \int_{\Omega} (1 - \mu_{RT}) \log(1 - \mu_{RT}) d\Omega\right]$. Note that C is a function of μ_{RT} but is almost constant and can be approximated to its value for uniaxial tension loading conditions $C = 0.283$.

Averaged rate of growth

The average void growth rate \dot{R}_0 can be deduced from Eq.(39) taken at the void interface $R=R_0$. Only the radial expansion is accounted for, so the rate of displacement can be projected on \underline{e}_R and integrated over $d\Omega$

$$\dot{R}_0 = \int_{\Omega} \dot{E}_{RR} R_0 d\Omega + \int_{\Omega} D \dot{P} R_0 d\Omega \quad (40)$$

The integration of \dot{E}_{RR} over the unit sphere is equal to zero ($\dot{\mathbf{E}}$ is necessarily deviatoric), and D and R_0 do not depend on the angular variables, so the rate of void growth is found as

$$\frac{\dot{R}_0}{R_0} = 0.283 \dot{P} \exp\left(\frac{3 \Sigma_H}{2 \sigma_0}\right) \quad (41)$$

It should be recalled that this expression is obtained following several assumptions:

- No elasticity and no plastic hardening
- $D \gg 1$ (i.e. large stress triaxiality states)
- Influence of deviatoric stress field neglected
- Expansion of the void averaged as spherical

Otherwise, it should be noted that the macroscopic (and necessarily deviatoric) plastic strain rate is driving the radial expansion process, while the influence of the hydrostatic part of the loading appears in an additional exponential term.

6.2.2 Extension of the Rice and Tracey analysis for anisotropic matrix behaviour

The Rice and Tracey analysis is reconsidered here with an anisotropic yield function. The yield function expressed in Eq.(31) is now defined as a Hill yield function (1948)

$$f = \bar{\sigma} - \sigma_0 = 0 \quad \text{with} \quad \bar{\sigma} = \sqrt{\mathbf{s} : \mathbf{M} : \mathbf{s}} \quad (42)$$

where $\bar{\sigma}$ is the Hill equivalent stress replacing the von Mises equivalent stress σ_{eq} given in Eq.(31) and \mathbf{M} is the anisotropic matrix expressed as a diagonal matrix in a modified version of the Voigt notation as

$$\mathbf{M} = \text{diag} \left(\frac{-F+2H+2G}{9}, \frac{2F-H+2G}{9}, \frac{2F+2H-G}{9}, N, M, L \right), \quad \mathbf{s} = \begin{bmatrix} s_{11} \\ s_{22} \\ s_{33} \\ \sqrt{2}s_{23} \\ \sqrt{2}s_{31} \\ \sqrt{2}s_{12} \end{bmatrix} \quad (43)$$

where the six components F, G, H, L, M, N need to be calibrated and in case of purely isotropic behaviour, $F=G=H=1/2$ and $L=M=N=3$. With associative plasticity, the relation between stress and strain rate expressed in Eq.(32) becomes

$$\mathbf{s} = \frac{\sigma_0}{\dot{p}} \mathbf{M}^{-1} : \dot{\boldsymbol{\epsilon}} \quad (44)$$

where \mathbf{M}^{-1} is the inverse of the anisotropic diagonal matrix \mathbf{M} . The equivalent plastic strain rate, denoted \dot{p} , is energy conjugate to the Hill equivalent stress $\bar{\sigma}$. The fields are the same as in the original RT analysis (Eq.(36)) but the definition of equivalent plastic strain rate is different, viz.

$$\begin{aligned} \dot{\underline{u}} &= \dot{\mathbf{E}} \underline{x} + D\dot{\underline{u}}^D = \dot{\mathbf{E}} \underline{x} + D\dot{\bar{P}} \left(\frac{R_0}{R} \right)^3 \underline{x} = \dot{\mathbf{E}} \underline{x} + D\dot{\bar{P}} \lambda \underline{x} \quad \text{with} \quad \begin{cases} \dot{\bar{P}} = \sqrt{\dot{\mathbf{E}} : \mathbf{M}^{-1} : \dot{\mathbf{E}}} \\ \lambda = \left(\frac{R_0}{R} \right)^3 \end{cases} \\ \dot{\boldsymbol{\epsilon}} &= \dot{\mathbf{E}} + \dot{\boldsymbol{\epsilon}}^D = \dot{\mathbf{E}} + D\dot{\bar{P}} \lambda \mathbf{e}^D \quad \text{with} \quad \mathbf{e}^D = \mathbf{I} - 3\underline{\mathbf{e}}_R \otimes \underline{\mathbf{e}}_R \end{aligned} \quad (45)$$

The equilibrium equation to solve, given in Eq.(37) for isotropic material, remains unchanged for the anisotropic material. Nevertheless, the development of this equilibrium equation is altered by anisotropy in the following way

$$\begin{aligned} \frac{1}{6\pi} \int_{\Omega} h \left\{ \log \left(\sqrt{4(Dh)^2 - 4Dh\mu_{RT}^h + 1} + 2Dh - \mu_{RT}^h \right) - \log(1 - \mu_{RT}^h) \right. \\ \left. + \mu_{RT}^h \log \left(\frac{1}{2} \sqrt{4(Dh)^2 - 4Dh\mu_{RT}^h + 1} + \frac{1}{2} - Dh\mu_{RT}^h \right) \right\} d\Omega = \frac{\Sigma_H}{\sigma_0} \end{aligned} \quad (46)$$

where $h = \frac{1}{2} \sqrt{\mathbf{e}^D : \mathbf{M}^{-1} : \mathbf{e}^D}$ and $\mu_{RT}^h = \frac{1}{2h\bar{P}} \mathbf{e}^D : \mathbf{M}^{-1} : \dot{\mathbf{E}}$. The parameter h is a function of the anisotropy parameters, but also of the spherical coordinates and cannot be taken out of the integral. By assuming again that D is large, the previous equation can be simplified to

$$D = C^h \exp \left(\frac{3}{2h_{av}} \frac{\Sigma_H}{\sigma_0} \right) \quad (47)$$

where $C^h = \frac{1}{4} \exp \left[\frac{1}{4\pi h_{av}} \int_{\Omega} h \left\{ (1 - \mu_{RT}^h) \log(1 - \mu_{RT}^h) - (1 + \mu_{RT}^h) \log h \right\} d\Omega \right]$ and $h_{av} = \frac{1}{4\pi} \int_{\Omega} h d\Omega$ is the normalized parameter h averaged over the unit sphere. As in Rice and Tracey (1969), the average void growth rate can be expressed as

$$\frac{\dot{R}_0}{R_0} = C^h \dot{\bar{P}} \exp \left(\frac{3}{2h_{av}} \frac{\Sigma_H}{\sigma_0} \right) \quad (48)$$

The calibration of the anisotropic parameters of \mathbf{M} was done for the AA7075-T651 alloy and gave the values $F = H = 0.515$, $G = 0.485$, $N = 2.764$ and $L = M = 3$. For these specific values, $h_{av} = 1.0066$. A consequence is that the function C^h is not much affected by the anisotropy, which allows to express the average growth rate of a void as

$$\frac{\dot{R}_0}{R_0} = 0.283 \dot{\bar{P}} \exp \left(\frac{3}{2} \frac{\Sigma_H}{\sigma_0} \right) \quad (49)$$

where the only remaining difference with the original Rice and Tracey analysis (given in Eq.(41)) is the anisotropic definition of $\dot{\bar{P}}$. With the yield stress now equal to $\sigma_0 = \bar{\Sigma} = \sqrt{\mathbf{S} : \mathbf{M} : \mathbf{S}}$, the triaxiality $\sigma^* = \Sigma_H / \bar{\Sigma}$ also contains the plastic anisotropy.

6.2.3 Conclusions

This development enables to evaluate the influence of the plastic anisotropy on the expression of the void growth rate as obtained by Rice and Tracey (1969). In this study, this influence is found to be limited and with reasonable approximation, the solution of Rice and Tracey (1969) is still valid but with a different definition of the equivalent plastic strain rate and triaxiality

ratio. This analysis suggests that the failure locus, usually expressed for isotropic materials in the $(\varepsilon_f = \sqrt{\frac{2}{3}} \boldsymbol{\varepsilon}^p : \boldsymbol{\varepsilon}^p \Big|_f, \sigma^* = \sigma_H / \sqrt{\frac{3}{2}} \mathbf{s} : \mathbf{s})$ space, should be represented in the “anisotropic space” when the material is anisotropic: $(\varepsilon_f = \sqrt{\boldsymbol{\varepsilon}^p : \mathbf{M}^{-1} : \boldsymbol{\varepsilon}^p} \Big|_f, \sigma^* = \sigma_H / \sqrt{\mathbf{s} : \mathbf{M} : \mathbf{s}})$. This is consistent with the definitions of the accumulated plastic strain and stress triaxiality used in the anisotropic plasticity model used in Chapter 5.

6.3 Localization criteria

Examples have been provided in Chapter 3 showing inclined fracture modes under uniaxial tension. In this chapter the conditions for localization are considered. We adopt a general set of rate-independent constitutive relations, and derive conditions for strain localization to occur. Rudnicki and Rice (1975) adopted the viewpoint that the macroscopic constitutive relations may permit homogeneous deformation of an initially uniform material to give way to an incipient non-uniform deformation field, concentrated within a localized band but uniform outside it. This approach will be developed in the following with the associated conditions solved. But before this, the constitutive framework we have in mind will be presented in the fully thermo-mechanical context, as thermal effects may play an important role in the localization process.

6.3.1 General constitutive framework

It is now well established that features of the behaviour of materials that may lead to localization are mostly mechanisms linked with softening: this may be strain softening (plasticity, damage and other phenomena), thermal softening, geometrical softening (as in single crystals for instance) and even strain-rate softening (dynamic strain ageing and consecutive negative strain-rate sensitivity observed through the Portevin-Le Châtelier phenomenon). Another source of localization is non-symmetry of the inelastic behaviour as observed in non-associative behaviour (non-Schmidt effects, friction and dilatancy effects), but also in the inclusion of thermo-mechanical couplings. Some of these effects will be underlined in the following of this work. The coming section introduces indeed the set of constitutive equations that incorporate these effects.

Thermodynamic framework

The thermodynamic framework with infinitesimal strains is presented with more details in Appendix B for thermo-elastic behaviour of various materials. The main ingredients of the framework are summed up below

<ul style="list-style-type: none"> • Internal variables : $\{\boldsymbol{\varepsilon}, \zeta_i, T\}$ • Associated driving forces : $\{\boldsymbol{\sigma}, Z_i, s\}$ • Potential : $\psi(\boldsymbol{\varepsilon}, \zeta_i, T)$ • Yield function : $f(\boldsymbol{\sigma}, Z_i, T)$ • Plastic flow potential : $F(\boldsymbol{\sigma}, Z_i, T)$ • Evolution laws : $\dot{\zeta}_i = \dot{\lambda} \frac{\partial F}{\partial Z_i}$ • State laws : $\boldsymbol{\sigma} = \rho \frac{\partial \psi}{\partial \boldsymbol{\varepsilon}}, \quad Z_i = -\rho \frac{\partial \psi}{\partial \zeta_i}, \quad s = -\frac{\partial \psi}{\partial T}$ • Heat equation : $\rho c^{th} \dot{T} = r + k \Delta T + T \frac{\partial \boldsymbol{\sigma}}{\partial T} : \dot{\boldsymbol{\varepsilon}}^e + A_i^{th} \dot{\zeta}_i$ <p style="margin-top: 10px;">with $A_i^{th} = Z_i - T \frac{\partial Z_i}{\partial T}$</p>	(50)
--	------

where ρ is the density and c^{th} is the heat capacity. In the case of elasto-plastic behaviour with hardening and thermal softening, the adequate internal variables are chosen as

$$\zeta_i = \{\boldsymbol{\varepsilon}^p, \bar{p}\} \quad \text{and} \quad Z_i = \{\boldsymbol{\sigma}, -\kappa\} \quad (51)$$

and the potentials are defined by

$$\begin{aligned} \therefore \rho \psi(\boldsymbol{\varepsilon}, \boldsymbol{\varepsilon}^p, \bar{p}, T) &= \frac{1}{2} \mathbf{E}^i(T) : (\boldsymbol{\varepsilon} - \boldsymbol{\varepsilon}^p - \boldsymbol{\varepsilon}^{th}) : (\boldsymbol{\varepsilon} - \boldsymbol{\varepsilon}^p - \boldsymbol{\varepsilon}^{th}) + K^a(\bar{p}, T) \\ \therefore f &= f(\boldsymbol{\sigma}, \kappa^a, T) \quad \therefore F = F(\boldsymbol{\sigma}, \kappa^a, T) \end{aligned} \quad (52)$$

where $\mathbf{E}^i(T)$, given in detail in Appendix A, is the 4th order elastic tensor, $\boldsymbol{\varepsilon}^{th} = \alpha^{th}(T - T_0) \mathbf{I}$ is the thermal strain, $\alpha^{th}(T)$ is the thermal expansion coefficient and $K^a(\bar{p}, T)$ represents the plastic hardening. The state and evolution laws are

$$Z_i \equiv \begin{cases} \boldsymbol{\sigma} = \rho \frac{\partial \psi}{\partial \boldsymbol{\varepsilon}} = \mathbf{E}^i : (\boldsymbol{\varepsilon} - \boldsymbol{\varepsilon}^p - \boldsymbol{\varepsilon}^{th}) = \mathbf{E}^i : \boldsymbol{\varepsilon}^e \\ -\kappa^a = -\rho \frac{\partial \psi}{\partial \bar{p}} = -\frac{\partial K^a(\bar{p}, T)}{\partial \bar{p}} \end{cases} \quad \dot{\zeta}_i \equiv \begin{cases} \dot{\boldsymbol{\varepsilon}}^p = \dot{\lambda} \frac{\partial F}{\partial \boldsymbol{\sigma}} \\ \dot{\bar{p}} = -\dot{\lambda} \frac{\partial F}{\partial \kappa^a} \end{cases} \quad (53)$$

Isothermal tangent modulus \mathbf{H}^i

The isothermal tangent modulus relates the stress rate to the strain rate under isothermal conditions $\dot{T} = 0$. The constitutive behaviour obtained from the framework under these circumstances is given as

$$\begin{aligned}
 \dot{\boldsymbol{\sigma}} &= \mathbf{L}^i : \dot{\boldsymbol{\varepsilon}}, \quad \mathbf{L}^i = \begin{cases} \mathbf{E}^i & \text{if } f < 0 \text{ or } f = 0 \text{ and } \dot{f} < 0, \\ \mathbf{H}^i = \mathbf{E}^i - \frac{\boldsymbol{\alpha}^i \otimes \boldsymbol{\beta}^i}{H^i} & \text{if } f = 0 \text{ and } \dot{f} = 0, \end{cases} \\
 \therefore \boldsymbol{\alpha}^i &= \mathbf{E}^i : \frac{\partial f}{\partial \boldsymbol{\sigma}} \quad \therefore H^i = h^i + \boldsymbol{\alpha}^i : (\mathbf{E}^i)^{-1} : \boldsymbol{\beta}^i \\
 \therefore \boldsymbol{\beta}^i &= \frac{\partial F}{\partial \boldsymbol{\sigma}} : \mathbf{E}^i \quad \therefore h^i = -\frac{\partial f}{\partial \zeta_i} \frac{\partial F}{\partial Z_i}
 \end{aligned} \tag{54}$$

Note that under isothermal conditions and for the sake of clarity, the variables $\{\mathbf{E}^i, \boldsymbol{\alpha}^i, \boldsymbol{\beta}^i, h^i\}$ will be nominated $\{\mathbf{E}, \boldsymbol{\alpha}, \boldsymbol{\beta}, h\}$ and no dependency on the temperature will be accounted for.

Adiabatic tangent modulus \mathbf{H}^a

The adiabatic modulus relates the strain rate to the stress rate under adiabatic conditions. Under adiabatic conditions, one assumes the absence of external heat sources and conduction (no heat fluxes, $r = k = 0$) so that the evolution of the temperature (through the heat equation) becomes

$$\rho c^{th} \dot{T} = T \frac{\partial \boldsymbol{\sigma}}{\partial T} : \dot{\boldsymbol{\varepsilon}} + A_i^{th} \dot{\zeta}_i \quad \text{with} \quad A_i^{th} = \left\{ \mathbf{A}_{\varepsilon^p}^{th}, A_p^{th} \right\} = \left\{ \boldsymbol{\sigma} - T \frac{\partial \boldsymbol{\sigma}}{\partial T}, T \frac{\partial \kappa^a}{\partial T} - \kappa^a \right\} \tag{55}$$

Under adiabatic conditions, it is therefore possible to compute the rate of temperature. For the sake of simplicity, we neglect here the variations of thermo-elastic coefficients with respect to temperature. If needed, these variations can be incorporated. With this assumption we get

$$\frac{\partial \boldsymbol{\sigma}}{\partial T} = -\frac{\partial \mathbf{E}^i : \boldsymbol{\varepsilon}^{th}}{\partial T} = -\alpha^{th} \mathbf{E}^i : \mathbf{I} = -3\alpha^{th} K \mathbf{I} \tag{56}$$

Further, the plastic multiplier is obtained using the consistency condition enriched with the evolution laws (see Appendix B), and the following rate constitutive behaviour is established

$$\begin{aligned}
 \dot{\boldsymbol{\sigma}} &= \mathbf{L}^a : \dot{\boldsymbol{\varepsilon}}, \quad \mathbf{L}^a = \begin{cases} \mathbf{E}^a & \text{if } f < 0 \text{ or } f = 0 \text{ and } \dot{f} < 0, \\ \mathbf{H}^a = \mathbf{E}^a - \frac{\boldsymbol{\beta}^a \otimes \boldsymbol{\alpha}^a}{H_a} & \text{if } f = 0 \text{ and } \dot{f} = 0, \end{cases} \\
 \therefore \boldsymbol{\alpha}^a &= \boldsymbol{\alpha}^i + \frac{3KT\alpha^{th}}{\rho c^{th}} \left(6K\alpha^{th} \frac{\partial f}{\partial \boldsymbol{\sigma}} : \mathbf{I} - \frac{\partial f}{\partial \kappa^a} \frac{\partial \kappa^a}{\partial T} \right) \mathbf{I} \\
 \therefore \boldsymbol{\beta}^a &= \boldsymbol{\beta}^i + \frac{3K\alpha^{th}}{\rho c^{th}} \left((\boldsymbol{\sigma} + 3\alpha^{th} KT \mathbf{I}) : \frac{\partial F}{\partial \boldsymbol{\sigma}} + \left(\kappa^a - T \frac{\partial \kappa^a}{\partial T} \right) \frac{\partial F}{\partial \kappa^a} \right) \mathbf{I} \\
 \therefore \mathbf{E}^a &= \mathbf{E}^i + \frac{9(\alpha^{th} K)^2 T}{\rho c^{th}} \mathbf{I} \otimes \mathbf{I} \quad \therefore H_a = h^a + \boldsymbol{\alpha}^i : (\mathbf{E}^i)^{-1} : \boldsymbol{\beta}^i \\
 \therefore h^a &= h^i + \frac{A_i^{th}}{\rho c^{th}} \frac{\partial F}{\partial Z_i} \left(3K\alpha^{th} \frac{\partial f}{\partial \boldsymbol{\sigma}} : \mathbf{I} - \frac{\partial f}{\partial T} \right)
 \end{aligned} \tag{57}$$

Note that the product $\boldsymbol{\beta}^a \otimes \boldsymbol{\alpha}^a$ is not symmetric when the thermal coefficients are non-zero, even with associated plastic flow. Some additional details about the adiabatic 4th order elastic tensor \mathbf{E}^a are given in Appendix A. The only remaining unknown in the expressions for tensors $\boldsymbol{\alpha}^a$ and $\boldsymbol{\beta}^a$ is the yield function f , which will be particularized later.

Finite strains

When taking finite strains into account, some changes must be brought to the above presentation. For the sake of simplicity, this will be carried out here only under isothermal conditions. The rate-of-deformation tensor \mathbf{d} is decomposed into elastic and plastic parts

$$\mathbf{d} = \mathbf{d}^e + \mathbf{d}^p \quad (58)$$

where the elastic strains are assumed to be small and a linear hypoelastic formulation is adopted, i.e.

$$\boldsymbol{\sigma}^{\nabla J} = \mathbf{L}^J : \mathbf{d}, \quad \mathbf{L}^J = \begin{cases} \mathbf{E} & \text{if } f < 0 \text{ or } f = 0 \text{ and } \dot{f} < 0, \\ \mathbf{H}^J = \mathbf{E} - \frac{\boldsymbol{\alpha}^J \otimes \boldsymbol{\beta}^J}{H^J} & \text{if } f = 0 \text{ and } \dot{f} = 0, \end{cases} \quad (59)$$

where \mathbf{H}^J and \mathbf{E} are the 4th order tangent and elastic modulus tensors, respectively, f is the yield function and $\boldsymbol{\sigma}^{\nabla J}$ is the Jaumann stress rate defined by

$$\boldsymbol{\sigma}^{\nabla J} = \dot{\boldsymbol{\sigma}} + \boldsymbol{\sigma} \cdot \boldsymbol{\omega} - \boldsymbol{\omega} \cdot \boldsymbol{\sigma} \quad (60)$$

with $\boldsymbol{\omega}$ the spin, i.e. anti-symmetric part of the velocity gradient, while \mathbf{d} is its symmetric part. A particular property of the Jaumann stress rate is that for a first order positive homogeneous yield function f we have

$$\frac{\partial f}{\partial \boldsymbol{\sigma}} : \dot{\boldsymbol{\sigma}} = \frac{\partial f}{\partial \boldsymbol{\sigma}} : \boldsymbol{\sigma}^{\nabla J} \quad (61)$$

Consequently, the rate constitutive relations considered in Eq.(54) give the expression of the hardening modulus h through

$$\boldsymbol{\alpha}^J = \mathbf{E} : \frac{\partial f}{\partial \boldsymbol{\sigma}} = \boldsymbol{\alpha}, \quad \boldsymbol{\beta}^J = \frac{\partial F}{\partial \boldsymbol{\sigma}} : \mathbf{E} = \boldsymbol{\beta} \quad \text{and} \quad H^J = h + \boldsymbol{\alpha}^J : \mathbf{E}^{-1} : \boldsymbol{\beta}^J = H \quad (62)$$

6.3.2 Localization analysis for a homogeneous material

Localization Condition (LC) for infinitesimal strains

The usual viewpoint for addressing the localization phenomenon (see Rudnicki and Rice, 1976) considers that the macroscopic constitutive relations may permit the homogeneous deformation of an initially uniform material to give way to an incipient non-uniform deformation field, concentrated within a localized band but uniform outside it. A bifurcation approach is thus used to exhibit the conditions which allow this transition for an infinite block, from its initially uniform state to the non-uniform one containing a planar band as sketched in Figure 6.2. The rate constitutive laws given for the material are those developed earlier and we start with the isothermal situation.

Let's consider a homogenous medium M , in which strain localization could occur along a planar band B of normal \underline{n} , as depicted in Figure 6.2. If this localization is to happen, a jump in velocity gradient should appear at the interface between the rest of the block and the incipient band, even though the velocity is assumed to remain continuous. This compatibility requirement imposes

$$\left[\left[\frac{\partial \underline{v}}{\partial \underline{x}} \right] \right] = \frac{\partial \underline{v}}{\partial \underline{x}} \Big|_M - \frac{\partial \underline{v}}{\partial \underline{x}} \Big|_B = \underline{g} \otimes \underline{n} \quad (63)$$

where \underline{v} is the velocity vector, \underline{x} is the current position, \underline{n} is the normal vector to the band and \underline{g} defines the intensity of the discontinuity. The strain rate discontinuity is consequently

$$\left[\left[\dot{\underline{\epsilon}} \right] \right] = \dot{\underline{\epsilon}}_M - \dot{\underline{\epsilon}}_B = \frac{1}{2} (\underline{g} \otimes \underline{n} + \underline{n} \otimes \underline{g}) \quad (64)$$

Assuming Eq.(54) to be valid in the homogeneous medium and inside the band it follows that

$$\begin{cases} \dot{\underline{\sigma}}_M = \mathbf{L} : \dot{\underline{\epsilon}}_M \\ \dot{\underline{\sigma}}_B = \mathbf{L} : \dot{\underline{\epsilon}}_B \end{cases} \Rightarrow \left[\left[\dot{\underline{\sigma}} \right] \right] = \mathbf{L} : \left[\left[\dot{\underline{\epsilon}} \right] \right] \quad (65)$$

The other requirement is continuous equilibrium which corresponds to $\dot{\underline{\sigma}}_M \cdot \underline{n} = \dot{\underline{\sigma}}_B \cdot \underline{n}$ and consequently to

$$\left[\left[\dot{\underline{\sigma}} \right] \right] \cdot \underline{n} = \frac{1}{2} \mathbf{L} : (\underline{g} \otimes \underline{n} + \underline{n} \otimes \underline{g}) \cdot \underline{n} = \frac{1}{2} [\underline{n} \cdot \mathbf{L} \cdot \underline{n}] \cdot \underline{g} = \underline{0} \quad (66)$$

For localization to happen, Eq.(66) should have a non-zero solution \underline{g} , which corresponds to $\det(\underline{n} \cdot \underline{\mathbf{L}} \cdot \underline{n}) = 0$. The elastic tensor $\underline{\mathbf{E}}$ satisfies $\det(\underline{n} \cdot \underline{\mathbf{E}} \cdot \underline{n}) > 0$ (details in Appendix A), so the condition of localization (LC) reads

$$\det(\underline{n} \cdot \underline{\mathbf{H}} \cdot \underline{n}) = 0 \quad (67)$$

and corresponds to the loss of ellipticity condition. The equality sign is changed into < 0 if one considers plastic loading inside the band and elastic unloading outside it (Benallal and Comi, 1993).

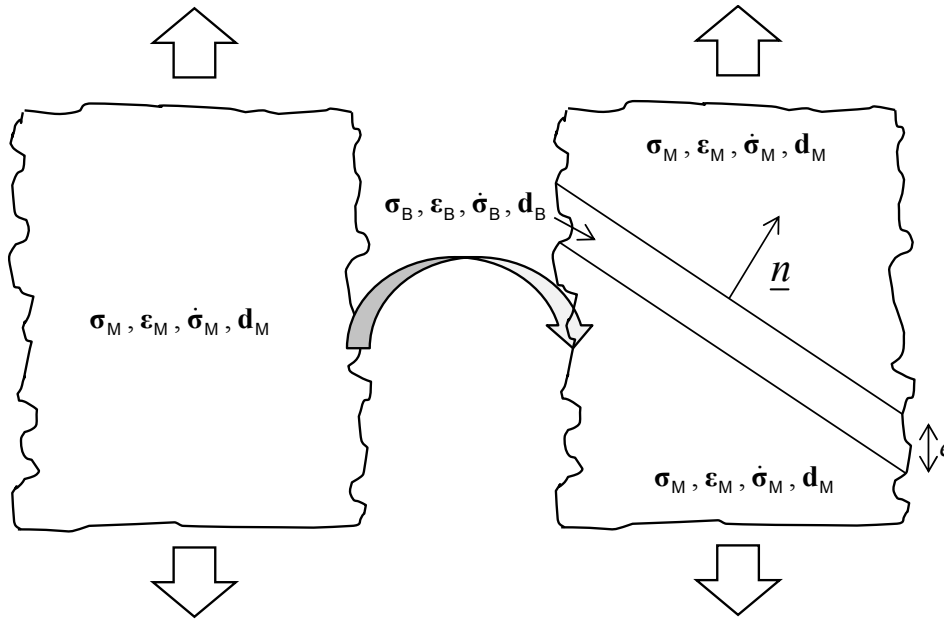


Figure 6.2. Schematic representation of a loaded homogeneous medium and localization along a planar band.

The acoustic tensor $\underline{n} \cdot \underline{\mathbf{H}} \cdot \underline{n}$ can be transformed into (details in Appendix A)

$$\underline{n} \cdot \underline{\mathbf{H}} \cdot \underline{n} = \underline{\mathbf{A}}^e \cdot \underline{\mathbf{B}}, \quad \begin{cases} \underline{\mathbf{A}}^e = \underline{n} \cdot \underline{\mathbf{E}} \cdot \underline{n} \\ \underline{\mathbf{B}} = \underline{\mathbf{I}} - \frac{1}{H} (\underline{\mathbf{A}}^e)^{-1} (\underline{n} \cdot \underline{\boldsymbol{\alpha}}) \otimes (\underline{\boldsymbol{\beta}} \cdot \underline{n}) \end{cases} \quad (68)$$

The multiplicative property of the determinant transforms the LC into $\det \underline{\mathbf{A}}^e \det \underline{\mathbf{B}} = 0$ and since $\det \underline{\mathbf{A}}^e$ is strictly positive (see Appendix A), the study reduces to solving $\det \underline{\mathbf{B}} = 0$. The tensor $\underline{\mathbf{B}}$ has two eigenvectors orthogonal to $\underline{n} \cdot \underline{\boldsymbol{\alpha}}$ and $\underline{\boldsymbol{\beta}} \cdot \underline{n}$ with corresponding eigenvalues $B_1 = B_2 = 1$ (Benallal and Comi, 1993) so

$$\det \underline{\mathbf{B}} = B_3, \quad B_3 = 1 - \frac{1}{H} (\underline{n} \cdot \underline{\boldsymbol{\alpha}}) \cdot (\underline{\mathbf{A}}^e)^{-1} \cdot (\underline{\boldsymbol{\beta}} \cdot \underline{n}) \quad (69)$$

The localization condition (LC) given in Eq.(67) then becomes

$$\det \mathbf{B} = 0 \Rightarrow H = (\underline{n} \cdot \underline{\alpha}) \cdot (\mathbf{A}^e)^{-1} \cdot (\underline{\beta} \cdot \underline{n}) \quad (70)$$

This last equation is the general LC with isotropic elasticity, without any assumption on the yield function and plastic flow, in a small strains framework. The geometrical method presented in Benallal and Comi (1993), also developed in Appendix C, is used here to get the six solutions for Eq.(70) which are H_k and H_{ij} with $(i, j, k) \in \{1, 2, 3\}$. The six associated solutions for the hardening modulus h (h_k and h_{ij}) can be computed using Eq.(54). From these six solutions the critical hardening modulus h_c , which is the maximum of the six last solutions, can be deduced.

Effects of thermo-mechanical couplings

The inclusion of thermal effects and thermo-mechanical couplings in the above analysis can be found in Benallal and Bigoni (2004). The localization condition reduces, with the notations adopted above, to the singularity of either the isothermal or the adiabatic tangent moduli. As these moduli have the general form adopted in the solution technique described above, it can also be applied to the thermo-mechanical case. It is not repeated here.

Effects of geometrical nonlinearities and finite strains

With the same requirements as in Eq.(64), we have

$$\llbracket \underline{\omega} \rrbracket = \frac{1}{2} (\underline{g} \otimes \underline{n} - \underline{n} \otimes \underline{g}) \quad (71)$$

and continuum equilibrium across the band (given in Eq.(66) for small strains) leads now to

$$\llbracket \underline{\dot{\sigma}} \rrbracket \cdot \underline{n} = \left[\mathbf{L} : \frac{1}{2} (\underline{g} \otimes \underline{n} + \underline{n} \otimes \underline{g}) - \underline{\sigma} \cdot \llbracket \underline{\omega} \rrbracket + \llbracket \underline{\omega} \rrbracket \cdot \underline{\sigma} \right] \cdot \underline{n} = \underline{0} \quad (72)$$

It follows after some manipulations that

$$\begin{cases} \underline{\sigma} \cdot \llbracket \underline{\omega} \rrbracket \cdot \underline{n} = \underline{\sigma} \cdot \frac{1}{2} (\underline{g} \otimes \underline{n} - \underline{n} \otimes \underline{g}) \cdot \underline{n} = \frac{1}{2} [\underline{\sigma} - \underline{\sigma} \cdot \underline{n} \otimes \underline{n}] \cdot \underline{g} \\ \llbracket \underline{\omega} \rrbracket \cdot \underline{\sigma} \cdot \underline{n} = \frac{1}{2} (\underline{g} \otimes \underline{n} - \underline{n} \otimes \underline{g}) \cdot \underline{\sigma} \cdot \underline{n} = \frac{1}{2} [\underline{n} \cdot \underline{\sigma} \cdot \underline{n} \mathbf{I} - \underline{n} \otimes \underline{n} \cdot \underline{\sigma}] \cdot \underline{g} \end{cases} \quad (73)$$

The condition for localization (given in Eq.(67) for small strains formulation) becomes with the Jaumann formulation (details in Appendix D)

$$\det(\underline{n} \cdot \mathbf{H} \cdot \underline{n} + \mathbf{A}^J) = 0 \quad (74)$$

$$\mathbf{A}^J = \frac{1}{2} [\underline{n} \cdot \boldsymbol{\sigma} \cdot \underline{n} \mathbf{I} + \boldsymbol{\sigma} \cdot \underline{n} \otimes \underline{n} - \underline{n} \otimes \underline{n} \cdot \boldsymbol{\sigma} - \boldsymbol{\sigma}]$$

where it is recalled that tangent modulus tensor \mathbf{H} is unchanged compared to the previous formulation. As in the infinitesimal case, six solutions for the hardening modulus h (h_k and h_{ij}) can be associated to the six solutions for H (H_k and H_{ij}). The critical hardening modulus h_c is again defined as the maximum of these six solutions. Note that the stress tensor $\boldsymbol{\sigma}$ is now directly involved in the localization condition.

6.3.3 Some applications

We consider here the non-quadratic and pressure-independent yield function (Hershey, 1954)

$$f = \left\{ \frac{1}{2} \left[(s_1 - s_2)^m + (s_2 - s_3)^m + (s_3 - s_1)^m \right] \right\}^{\frac{1}{m}} - \sigma_0 \quad (75)$$

where s_1, s_2, s_3 are the principal deviatoric stresses and the coefficient m is an even number that may give a non-quadratic yield function. Note that when $m = 2$, f corresponds to the von Mises yield function $f = \sqrt{3J_2} - \sigma_0$. Several constitutive models are built based on the Hershey yield function and listed in Table 6.1, where α_0 and β_0 are the pressure sensitivity terms related to the yield function and plastic flow potential, respectively, defined in Appendix F.

Table 6.1. Different cases studies for yield function, plastic flow and formulation.

	Associativity	Yield function f		Plastic flow F		Formulation	
		shape	pressure	shape	pressure	strains	thermal
CASE 1	yes	m	$\alpha_0 = 0$	m	$\beta_0 = 0$	small	isothermal
CASE 2	yes	m	$\alpha_0 \neq 0$	m	$\beta_0 = \alpha_0$	small	isothermal
CASE 2	no	m	$\alpha_0 \neq 0$	m	$\beta_0 = 0$	small	isothermal
CASE 3	no	m	$\alpha_0 = 0$	$n \neq m$	$\beta_0 = 0$	small	isothermal
CASE 4	yes	m	$\alpha_0 = 0$	m	$\beta_0 = 0$	Jaumann	isothermal
CASE 5	no	m	$\alpha_0 \neq 0$	m	$\beta_0 = 0$	Jaumann	isothermal
CASE 6	yes	m	$\alpha_0 = 0$	m	$\beta_0 = 0$	small	adiabatic

In some cases, the stress tensor intervenes in the result so the plastic behaviour is of importance. For the study of AA7075-T651 aluminium alloy, the Voce hardening law was

calibrated in Chapter 4. The yield condition was written $f = \sigma_{eq} - \kappa(\bar{p})$ and the Voce hardening law was given as

$$\kappa(\bar{p}) = \sigma_0 + Q(1 - \exp(-C\bar{p})) \quad (76)$$

with the values of σ_0 , Q and C calibrated for the AA7075-T651 alloy presented in Table 4.1.

CASE 1: Hershey yield function - associative plastic flow

With the Hershey yield function and associative plastic flow, the six solutions of hardening moduli (h_k and h_{ij}) normalized with the shear modulus μ , are presented in Figure 6.3 (a) for $m = 16$, and the critical hardening modulus h_c is the maximum of the six values. Note that the curves obtained are symmetric with respect to the Lode parameter $\mu_L = 0$, corresponding to shear conditions, and that $h_c = \max(h_k; h_{ij}) = h_{13}$ (details in Appendix F). Figure 6.3 (b) presents the critical normalized hardening modulus h_c , with different values of the shape parameter m .

With associated and pressure-independent flow rule, the critical hardening moduli h_c is always negative, whatever the Lode parameter μ_L and shape parameter m are. This means that with a strictly increasing hardening law and without any softening mechanism, the material will not localize. However, it is noted here that a larger shape parameter m promotes localization by increasing the value of h_c for all Lode parameters different than the particular values $\mu_L = \{-1; 0; 1\}$. Also, the critical hardening modulus depends here on the Lode parameter, not on the stress triaxiality.

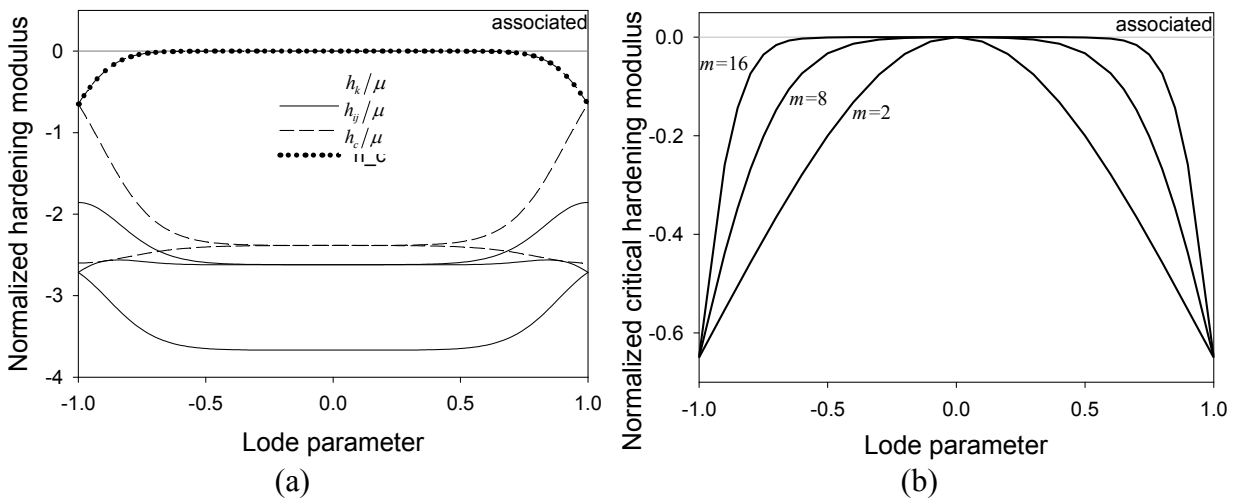


Figure 6.3. Normalized hardening moduli with a Hershey yield function and associative plastic flow: (a) six moduli h_{ij}/μ and h_k/μ for $m = 16$ and (b) critical h_c/μ for $m = \{2; 8; 16\}$.

CASE 2: Hershey yield function with pressure dependency - associative plastic flow

The Hershey yield function is now enriched with a pressure dependency term f_0 in the following way

$$f(\bar{\sigma}, \theta_L, \sigma_H) = \left\{ \frac{1}{2} \left[(s_1 - s_2)^m + (s_2 - s_3)^m + (s_3 - s_1)^m \right] \right\}^{\frac{1}{m}} + f_0 \sigma_H - \sigma_0 \quad (77)$$

so that the gradient of f is not deviatoric anymore and its trace is proportional to f_0 . A realistic pressure sensitive term $f_0 = 0.015$ is obtained by assuming a different of 1% between the yield stress under uniaxial tension and compression (more details are given in Appendix F). Figure 6.4 shows the critical normalized hardening modulus with $m=2$ and $m=16$ for this realistic pressure dependency and compare it with pressure independent yielding ($f_0=0$). It is observed that the pressure dependency decreases the value of the critical hardening modulus in the range $\mu_L \in [-0.5, 0.5]$. Also, the curve is slightly shifted towards the positive Lode parameters and is not symmetric with respect to $\mu_L=0$. The shift occurs towards negative Lode parameters for negative value of f_0 .

The LC is modified with a linear pressure dependency of the yield surface, but is still independent of the stress triaxiality state. With a non-linear dependence of the function f to σ_H (as e.g. in the Gurson's yield function), the stress triaxiality ratio would intervene in the expression of h_c and the condition for localization would explicitly appear as a function of the Lode parameter and the stress triaxiality. This would be in agreement with the studies on the Lode and triaxiality influence on failure mentioned in the Chapter 1, and needs to be investigated further.

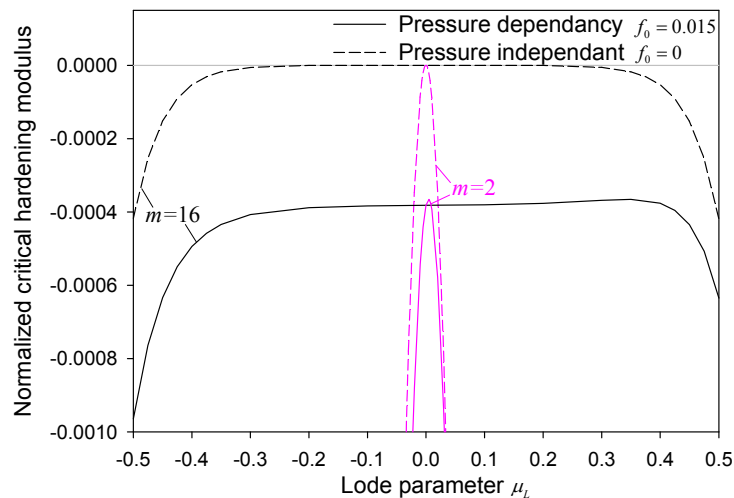


Figure 6.4. Normalized critical hardening moduli with associative plastic flow, pressure dependent term $f_0 = \{0, 0.015\}$ and $m = \{2, 16\}$.

CASE 3: Pressure dependent Hershey yield function - non-associative Hershey plastic flow

As described in the introduction, non-associative plastic flow is, besides softening, a way to promote localization. Non-associativity can be obtained by using a plastic flow potential slightly different from the yield function. The assumption of pressure-independent yielding and plastic flow is relevant for metallic materials. However, as discussed in Chapter 5, an isotropic model solely based on deviatoric stresses is not always perfectly predictive for high stress triaxiality states. Thus, in our case, a pressure dependent yield function is a reasonable alternative. The same realistic term $f_0 = 0.015$ as in CASE 2 is used to obtain the curves presented in Figure 6.5, where the associative and pressure independent model (CASE 1) is given for the sake of comparison. Note that in both cases the plastic flow is isochoric. Figure 6.5 exhibits that with non-associative plastic flow, the critical hardening modulus can be positive for some values of the Lode parameter. With the positive term $f_0 = 0.015$, the range of positive h_c is shifted towards $\mu_L = -1$. The curve obtained with a negative values $-f_0$ (not presented here) is the symmetric of the curve for f_0 with respect to the axes $\mu_L = 0$. Again, a shaper yield surface is observed to promote localization for a wider range of Lode parameter. The maximum value of the critical hardening modulus with $m = 16$, reached at $\mu_L = -0.34$, is $h_c = 1.25$ MPa. This value is low and shows that the influence of reasonable non associativity is quantitatively small but offers a possible localization of strains with a strictly increasing hardening like the Voce hardening law. However, for $\mu_L = -1$ corresponding to uniaxial tension, the effect of the non-associativity is negligible and the critical hardening modulus remains negative.

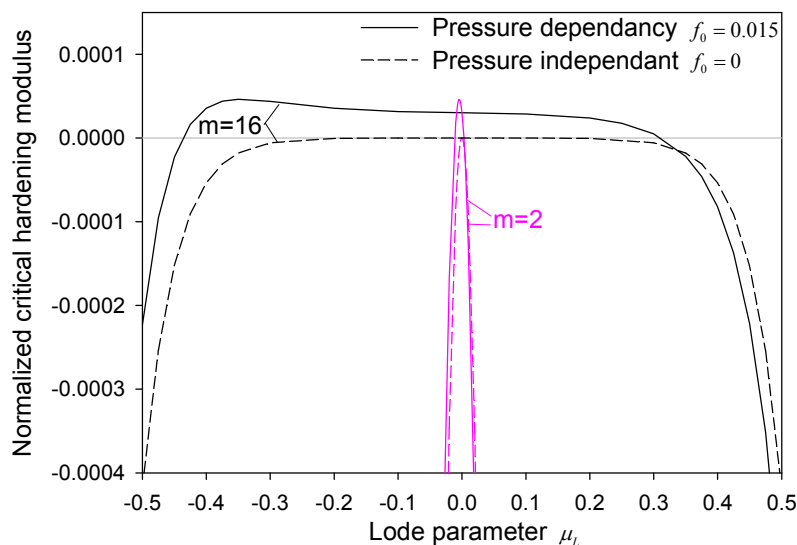


Figure 6.5. Normalized critical hardening moduli with non-associated plastic flow (pressure-dependent yield function) for $f_0 = \{0, 0.015\}$ and $m = \{2, 16\}$.

CASE 4: Hershey yield function - non-associative Hershey plastic flow (different shape parameter)

The plastic flow potential is now based on the Hershey yield function and only its shape parameter is changed from m to n . Then, the tensors α and β are still pressure-insensitive and β corresponds to the tensor α with parameter m replaced by n . Indeed, this attempt of non-associativity only gives an “average” of the curves obtained with associativity for different values of m .

CASE 5: Hershey yield function - associative plastic flow – Jaumann formulation

The CASE 1 is now presented with large strain formulation in Figure 6.6, at the yield stress level ($\sigma_{eq} = \sigma_0 = 538.8$ MPa) and exhibits that the critical hardening modulus is positive for a range of the Lode parameter symmetric around $\mu_L = 0$. This range is again larger for a higher shape parameter m . Also, the maximum value of the critical hardening modulus with $m = 16$, reached for $\mu_L = 0$, is $h_c = 2.32$ MPa. This value is of the same order as the value obtained with non-associative plastic flow.

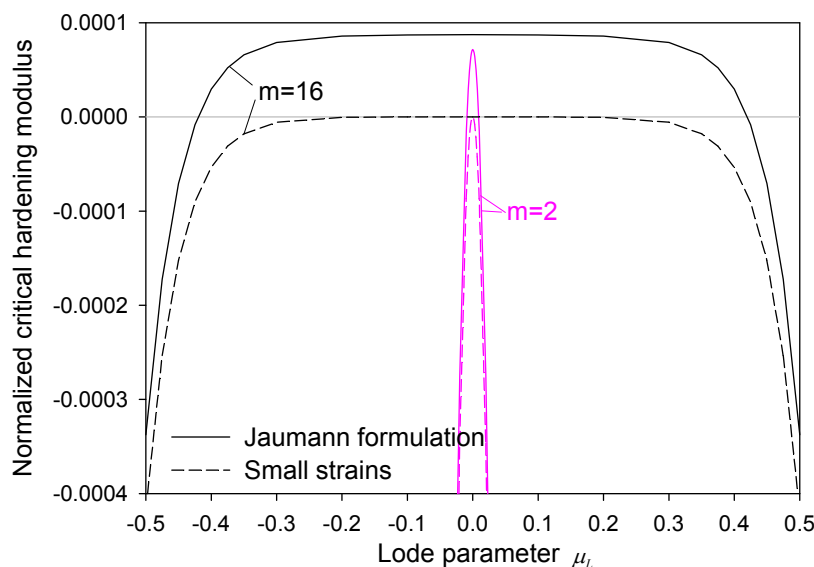


Figure 6.6. Normalized critical hardening modulus with Jaumann formulation for associated plastic flow with $m = \{2, 16\}$.

CASE 6: Hershey yield function - associative plastic flow – Thermal softening

The CASE 1 is now developed under adiabatic conditions, i.e. enriched by the temperature influence. As with the large strain formulation, the plastic behaviour of the AA7075-T651 alloy have an influence on the result and the stress is again taken at yielding so

$\sigma_{eq} = \sigma_0 = 538.8 \text{ MPa}$. A linear dependency of the temperature T is chosen for the elasto-plastic parameters such as the plastic hardening κ and the isothermal elastic tensor \mathbf{E}^i , i.e.

$$\begin{cases} \mathbf{E}^i = \frac{T_m - T}{T_m - T_r} \mathbf{E} \\ \kappa(\bar{p}, T) = \kappa(\bar{p}) \frac{T_m - T}{T_m - T_r} \end{cases} \quad (78)$$

where T_r is the reference temperature and T_m the melting temperature. The value of the material parameters related to thermal behaviour are $\rho = 2810 \text{ kg}\cdot\text{m}^{-3}$, $T_m = 903 \text{ K}$, $\alpha^{th} = 23.1 \cdot 10^{-6} \text{ K}^{-1}$ and $c^{th} = 897 \text{ J}\cdot\text{kg}^{-1}\cdot\text{K}^{-1}$. The normalized critical hardening modulus is presented for the adiabatic formulation in Figure 6.7, using the small strain formulation. At the reference temperature T_r , the curve for h_c is almost similar to the curve under isothermal conditions. This indicates that the adiabatic influence is negligible compared to the influence of non-associativity or Jaumann formulation. However, the temperature T has an effect and tend to increase h_c significantly for the extreme values of the Lode parameters $\mu_L = \{-1; 1\}$. Even though the critical hardening modulus h_c remains negative, localization may occur owing to the thermal softening.

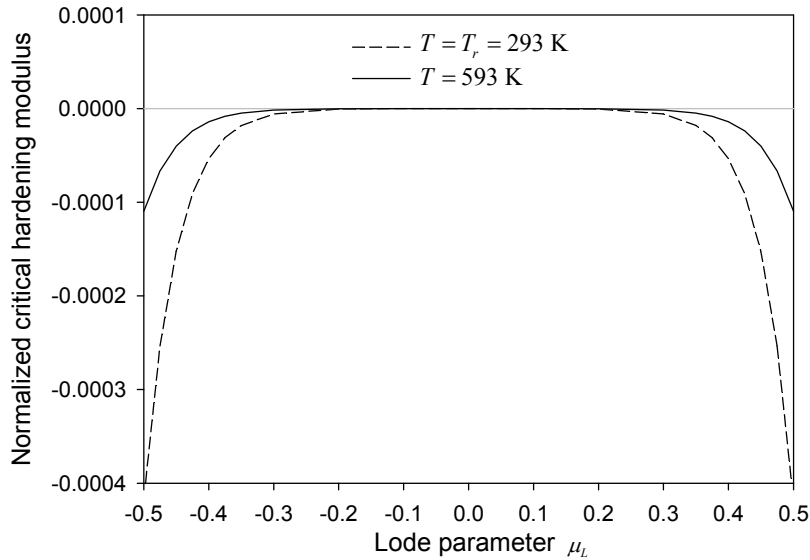


Figure 6.7. Normalized critical hardening modulus with adiabatic formulation and $T = \{293, 593 \text{ K}\}$ for associative plastic flow and $m = 16$.

6.3.4 Conclusions

This analysis has led to the expressions of the critical hardening modulus h_c as defined by the condition for localization of strains, for several constitutive characteristics. The main conclusions from this study are given below

- The critical hardening modulus was always expressed as a function of the Lode parameter and no dependence to the other stress invariants (i.e. stress triaxiality ratio) was obtained. However, by introducing a non-linear dependency of the yield function to the hydrostatic stress, h_c becomes a function of both the Lode parameter and the stress triaxiality.
- For the small strain formulation with associative plastic flow, h_c is negative for all Lode parameters μ_L . The maximum value ($h_c = 0$) is reached for $\mu_L = 0$ and the minima are reached for $\mu_L = \{-1; 1\}$.
- The shape parameter of the yield function m modifies the shape of the curves for h_c between the values $\mu_L = \{-1; 0; 1\}$. The localization condition is ensured at higher h_c with a sharper yield surface.
- The non-associative plastic flow and the large strain formulation increase the value of h_c in a similar manner, so h_c becomes positive for a certain range of the Lode parameter around the value $\mu_L = 0$. This range increases as the shape parameter m increases.
- The thermo-mechanical couplings only have an influence if the material parameters depend on the temperature and may increase h_c around the extreme values $\mu_L = \{-1; 1\}$. However, with no dependence to T (yet adiabatic conditions), the critical hardening modulus is unchanged.
- Whatever the constitutive equations, h_c is always negative under uniaxial tension loading condition ($\mu_L = -1$).

These analytical developments indicate that the localization theory with enriched formulations (non-associativity or large strains) can increase the critical hardening modulus h_c but a more extensive study (with anisotropy or small perturbation, see Chapter 9 for further outlooks) is necessary to obtain results corresponding to experimental observations (positive hardening modulus when localization occurs under uniaxial tension for instance).

Chapter 7. Anisotropic failure criterion

7.1 Introduction

This chapter presents the formulation and calibration of an anisotropic version (AECL) of the phenomenological extended Cockcroft-Latham (ECL) failure criterion originally presented by Gruben et al. (2012). Numerical simulations of the material tests performed experimentally (presented in Chapter 3 and already simulated with anisotropic plasticity in Chapter 4) are carried out using the uncoupled AECL criterion to evaluate its predictive capability.

7.2 Extended Cockcroft–Latham (ECL) criterion

Various failure criteria are used to model the failure of ductile metallic material. A very simple approach is to impose a critical plastic strain. Somewhat more elaborated criteria are based on the plastic work. For instance, the Cockcroft-Latham (CL) criterion (Cockcroft and Latham, 1968) is based on the “plastic work” computed from the positive part of the maximum principal stress. Another possibility is to compute the “plastic work” from the maximum shear stress, when shear is believed to be the dominating failure mechanism (integral-based Tresca, IT). An extended version of the Cockcroft-Latham criterion, denoted the ECL criterion, presented by Gruben et al. (2012), takes into account contributions from both the maximum principal stress and the maximum shear stress in computing the damage evolution. A slightly modified version of the ECL criterion will be studied here.

Formulation

In the modified version of the ECL criterion, the evolution of the damage variable D is defined by

$$\dot{D} = \left\langle \frac{\phi \hat{\sigma}_I + (1 - \phi)(\hat{\sigma}_I - \hat{\sigma}_{III})}{S_0} \right\rangle^{s_0} \dot{\bar{p}} \quad (79)$$

where $\langle x \rangle = \max(x, 0)$, $\hat{\sigma}_I \geq \hat{\sigma}_{II} \geq \hat{\sigma}_{III}$ are the ordered principal values of the corotational Cauchy stress tensor $\hat{\boldsymbol{\sigma}}$, and $S_0 > 0$, $s_0 > 0$ and $0 \leq \phi \leq 1$ are constants identified from available experimental data. Failure occurs when the variable D reaches a critical value $D_C = 1$, i.e. damage is not coupled to the constitutive relation in this study. The ECL criterion represents a weighting of two failure criteria, obtained by using specific values of the parameters;

- When $s_0 = 1$ and $\phi = 1$, the ECL criterion transforms into the Cockcroft-Latham (CL) criterion, as a “plastic work”-based criterion

$$\dot{D} = \frac{\langle \hat{\sigma}_I \rangle}{S_0} \dot{\bar{p}} \Rightarrow D_C = \frac{1}{S_0} \int_0^{\bar{p}_f} \langle \hat{\sigma}_I \rangle d\bar{p} \quad (80)$$

where \bar{p}_f is the accumulated plastic strain at fracture. This criterion is often calibrated through the Cockcroft-Latham parameter $W_C = D_C S_0$, which is the critical “plastic work”.

- When $s_0 = 1$ and $\phi = 0$, the ECL criterion transforms into an Integral-based Tresca (IT) criterion and involves the maximum shear stress through

$$\dot{D} = \frac{\langle \hat{\sigma}_I - \hat{\sigma}_{III} \rangle}{S_0} \dot{\bar{p}} \Rightarrow D_C = \frac{1}{S_0} \int_0^{\bar{p}_f} \langle \hat{\sigma}_I - \hat{\sigma}_{III} \rangle d\bar{p} \quad (81)$$

Coupled versus uncoupled damage

Naturally, the question of coupling appeared as soon as a damage variable was introduced. For the AA7075-T651 alloy, the observation of fracture surfaces (see Chapter 3) does not exhibit evidence of large plastic damage (such as large void growth for instance), and the stress-strain curves do not exhibit any softening. The inter-granular failure reveals that a damage process is occurring at the PFZs along grain boundaries, but the volume fraction concerned (i.e. the volume fraction of PFZs) is so low that no macroscopic softening is observed. Thus, the damage does not influence substantially the material behaviour. In terms of modeling, this means that the damage may not need to be coupled to the constitutive behaviour of the material. For that reason and in a first attempt, an uncoupled damage modeling approach was chosen. Then, the damage variable formulation should not be misinterpreted: the aim of the study is only to show the capability of a failure criterion (e.g. predictive capability for other stress states than those used in the calibration). Another consequence of the uncoupled approach is that the critical damage is not a material parameter and was chosen equal to unity ($D_C = 1$).

7.3 Anisotropic extended Cockcroft–Latham (AECL) criterion

Formulation

The anisotropy of failure for the AA7075-T651 alloy is exhibited in Figure 7.1, which presents the experimental critical “plastic work”, $W_C = \int_0^{p_f} \langle \hat{\sigma}_I \rangle dp$, as a function of the loading direction for the uniaxial tensile tests. This anisotropy can be taken into account in the ECL criterion through a factor depending on the direction of the loading. The equivalent plastic strain rate $\dot{\bar{p}}$ is modified following the work presented by Dunand and Mohr (2011). A new equivalent plastic strain rate is defined as

$$\dot{\bar{p}}_A = s_A \dot{\bar{p}} \quad (82)$$

where

$$s_A = \sqrt{\mathbf{n}^f : \mathbf{P} : \mathbf{n}^f}, \quad \mathbf{n}^f = \frac{\partial f / \partial \hat{\boldsymbol{\sigma}}}{\|\partial f / \partial \hat{\boldsymbol{\sigma}}\|} \quad (83)$$

in which $\|\mathbf{x}\| = \sqrt{\mathbf{x} : \mathbf{x}}$ and the unit tensor \mathbf{n}^f gives the direction of the plastic flow. The 4th order tensor \mathbf{P} is defined in Voigt form as

$$\mathbf{P} = \text{diag}(P_1, P_2, P_3, P_4, P_5, P_6) \quad (84)$$

The parameters of \mathbf{P} are non-negative and describe the anisotropy of the material with respect to failure. This anisotropy is embedded into $\dot{\bar{p}}_A$ through the factor s_A . It is noted that $\dot{\bar{p}}$ through its definition already accounts for the plastic anisotropy of the material. Then, the damage evolution transforms into

$$\dot{D} = s_A \left\langle \frac{\phi \hat{\sigma}_I + (1-\phi)(\hat{\sigma}_I - \hat{\sigma}_{III})}{S_0} \right\rangle^{s_0} \dot{\bar{p}} \quad (85)$$

This criterion is denoted the AECL criterion for short. Another version of the AECL could be stress-based by defining the damage and the scaling factor in the following way

$$\dot{D} = s_{A\sigma} \left\langle \frac{\phi \hat{\sigma}_I + (1-\phi)(\hat{\sigma}_I - \hat{\sigma}_{III})}{S_0} \right\rangle^{s_0} \dot{\bar{p}}, \quad s_{A\sigma} = \frac{\sqrt{\hat{\boldsymbol{\sigma}} : \mathbf{P} : \hat{\boldsymbol{\sigma}}}}{\sqrt{\hat{\boldsymbol{\sigma}} : \hat{\boldsymbol{\sigma}}}} \quad (86)$$

This stress-based AECL criterion will be evaluated and compared with the strain-based AECL criterion in the following section.

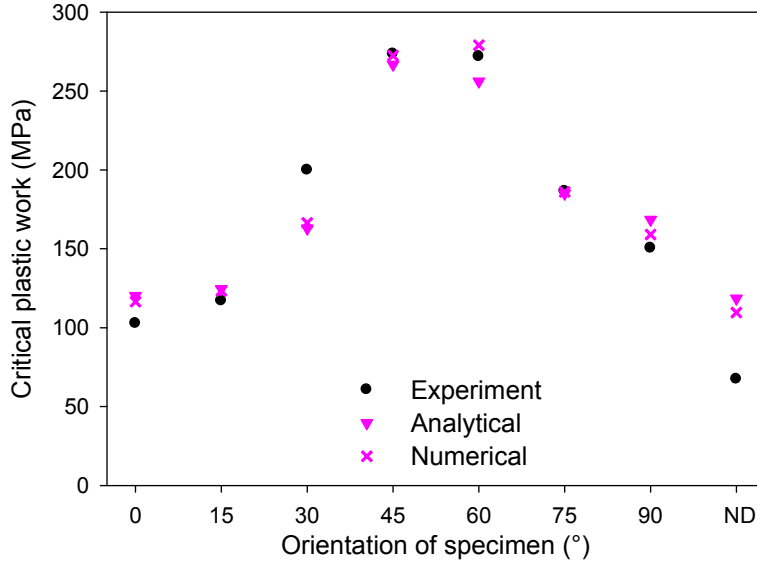


Figure 7.1. Critical “plastic work” versus loading direction for tensile tests on smooth specimens for the AA7075-T651 alloy.

Calibration of the AECL criterion

Firstly, the parameters of the ECL criterion are calibrated using different tests in the 0° direction. Then, the anisotropy parameters of the AECL criterion are calibrated using the uniaxial tests in different loading directions. The calibration of the parameters of the ECL criterion is not straight forward, since no usual test enables to isolate S_0 , s_0 and ϕ . The tests selected to do the calibration are the uniaxial tensile test and the shear test performed in the 0° direction. The tensile tests performed on notched specimens are not used for the calibration, since the stress state they provide is inhomogeneous. Then, to simplify the identification procedure, a choice is made to set the parameter $s_0 = 1$. The following method is used to calibrate the parameters S_0 and ϕ (given in Table 7.1).

- The uniaxial tensile tests performed in the 0° direction enable to calibrate the parameter S_0 since $\hat{\sigma}_{II} = \hat{\sigma}_{III} = 0$ we get

$$\langle \phi \hat{\sigma}_I + (1-\phi)(\hat{\sigma}_I - \hat{\sigma}_{III}) \rangle = \hat{\sigma}_I \Rightarrow D_C = \frac{1}{S_0} \underbrace{\int_0^{\bar{p}_{J0^\circ}} \hat{\sigma}_I d\bar{p}}_{W_{C0^\circ}} = 1 \quad (87)$$

$$\Rightarrow S_0 = W_{C0^\circ}$$

Thus, a representative experimental Cauchy stress-plastic strain curve from the tensile tests on smooth specimen in the 0° direction is used to compute W_{C0° and deduce the value of S_0 .

- The shear tests performed in the 0° direction enable to calibrate the parameter ϕ , assuming $\hat{\sigma}_I = \hat{\sigma}_{12} = -\hat{\sigma}_{III}, \hat{\sigma}_{II} = 0$, we get

$$\begin{aligned} \langle \phi \hat{\sigma}_I + (1-\phi)(\hat{\sigma}_I - \hat{\sigma}_{III}) \rangle &= (2-\phi) \hat{\sigma}_{12} \Rightarrow D_C = \frac{(2-\phi)}{W_{C0^\circ}} \underbrace{\int_0^{\bar{p}_{fshear}} \hat{\sigma}_{12} d\bar{p}}_{W_{Cshear}} = 1 \\ \Rightarrow \phi &= 2 - \frac{W_{C0^\circ}}{W_{Cshear}} \end{aligned} \quad (88)$$

For the shear tests performed on the AA7075-T651 alloy, the only experimental data available are the force, the displacement and the strain field at the surface of the specimen, based on DIC measurements. The plastic strains and the principal stresses necessary to compute the “plastic work” are not accessible. Consequently, the “plastic work” is extracted from the numerical simulation at the central element of the butterfly specimen, where a stress state of shear is ensured. The value of the critical “plastic work” W_{Cshear} is obtained from the numerical simulation at the point where the predicted displacement reaches the displacement at failure obtained experimentally. Note that depending on the element chosen to extract the “plastic work”, the parameter ϕ may vary significantly. In the following, it should be kept in mind that this parameter might need to be readjusted if necessary. Note also that since the parameter $\phi \in [0;1]$, Eq.(88) implies the inequality $W_{Cshear} \leq W_{C0^\circ} \leq 2 W_{Cshear}$. This is inherent to the formulation of the damage variable D when $s_0 = 1$ and is fulfilled by the AA7075-T651 alloy. It remains to investigate if this inequality also applies to other materials.

For the AECL criterion, the calibration of the six anisotropy parameters P_i ($i=1,2,\dots,6$) is done using experimental data from the uniaxial tensile tests in different directions. The parameters P_1 , P_2 and P_4 can be calibrated from uniaxial tensile tests performed in the plane of the plate (seven in-plane directions from 0° to 90°), while the test in the normal direction (ND) of the plate enables to calibrate the parameter P_3 . The parameters P_5 and P_6 are left equal to unity in this study since no tests are available to calibrate them in a trivial manner. The calibration is performed using a least squares method based on experimental data averaged between duplicate tensile tests. For a uniaxial tension test performed in the direction α , the stress state is assumed to be perfectly uniaxial ($\hat{\sigma}_{II} = \hat{\sigma}_{III} = 0$) and the plastic strain rate components are computed from the experimental strain ratio to deduce the constant coefficient $s_A = s_{A\alpha}$. The failure condition reads

$$D_C = 1 = \frac{s_{A\alpha}}{s_0} \int_0^{\bar{p}_{f\alpha}} \hat{\sigma}_\alpha d\bar{p} \xrightarrow{s_0=1} W_{C0} = s_{A\alpha} W_{C\alpha} \quad (89)$$

The calibrated values are presented in Table 7.1 and the analytical predictions of the critical plastic work are plotted in Figure 7.1, where they also are compared to the experimental values. It is seen that the “plastic work” at failure obtained with the analytical calibration is in good agreement with the experimental values. The anisotropy parameters of the stress-based version of the AECL were calibrated in the same manner through $s_{A\sigma}$, but the residual from the least square method was found twice as large as the residual obtained with the strain-based formulation. Consequently, the strain-based formulation was kept as the better candidate for this material.

Table 7.1. Parameters of the AECL criterion calibrated for the AA7075-T651 alloy.

$S_0 = W_{C0^\circ}$ [MPa]	W_{Cshear} [MPa]	ϕ	P_1	P_2	P_3	P_4	P_5	P_6
102.64	84.23	0.781	0.759	0.134	0.902	0	1	1

7.4 Quasi-static tests at different stress triaxialities

Numerical simulations of all the tests were performed using the AECL criterion calibrated in Chapter 7.3 and the anisotropic plasticity relation (Yld2004-18p) calibrated in Chapter 4. Then, a parametric study was performed for all tests (except for the tensile tests on smooth specimens), to capture the influence of anisotropy on the failure strain and failure modes. To facilitate the description of the analysis, we will use the following denominations for the various combination of models (with $\phi=0.781$ and $m=12$):

- **A-A** : plastic anisotropy (Yld2004-18p) and anisotropic failure criterion (AECL)
- **I-A** : plastic isotropy ($c'_{ij} = c''_{ij} = 1$) and anisotropic failure criterion (AECL)
- **A-I** : plastic anisotropy (Yld2004-18p) and isotropic failure criterion (ECL)
- **I-I** : plastic isotropy ($c'_{ij} = c''_{ij} = 1$) and isotropic failure criterion (ECL)

Also, the influence of the parameter ϕ is studied by using $\phi=0$ and $\phi=1$ with the **A-A** model. Elements are eroded when the damage variable D reaches the critical value $D_c=1$. The first eroded element initiates a crack, which propagates towards final failure (i.e. specimen broken in two separate pieces) within several computation steps. The instant of failure (and strain at failure) is defined when the first element is eroded.

7.4.1 Numerical aspects

Mesh sensitivity for tensile tests on notched specimens

The influence of the minimum mesh size h_e was studied using three different element sizes: $h_e = 0.375$ mm, $h_e = 0.25$ mm and $h_e = 0.125$ mm (see Figure 7.2 for $R = 2.0$ mm). The simulations were performed with the **I-I** model. For the notch with $R = 0.8$ mm, as presented in Table 7.2, the largest mesh size $h_e = 0.375$ mm gives a different result than the two other finer meshes (7% of difference). The localization of strains in the minimum cross section is better captured with smaller elements. On the contrary, due to a smoother geometry and less localized strains, the strain to failure was almost not mesh size dependent with $R = 2.0$ mm. Also, no substantial influence of the mesh was observed on the failure modes. The rest of the study was therefore performed with the intermediate mesh size $h_e = 0.25$ mm to save computational time.

Table 7.2. Predicted failure strains for tensile tests on notched specimens (**I-I** model).

Geometry	Direction	Experiment	$h_e = 0.375$ mm	$h_e = 0.25$ mm	$h_e = 0.125$ mm
$R = 2.0$ mm	0°	0.110	0.120	0.120	0.121
$R = 0.8$ mm	0°	0.061	0.057	0.048	0.048

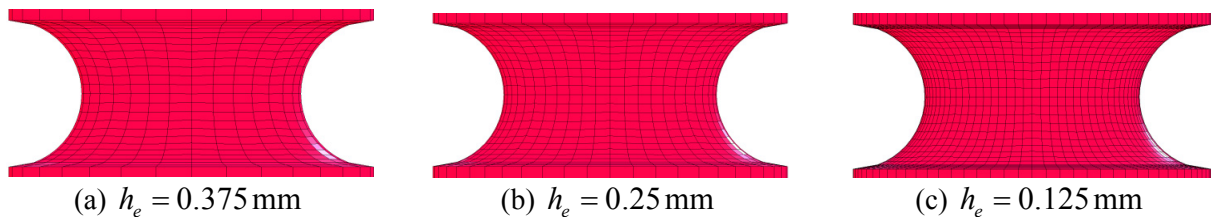


Figure 7.2. Meshes for notched specimens ($R = 2.0$ mm) with different mesh sizes h_e .

Friction coefficient γ_f for compression tests

In compression, the predicted stress softening, due to localization at large strains, and the failure strain are sensitive to the friction coefficient γ_f between the cylindrical specimen and the platens. The coefficient was optimized to make the predicted stress-strain curves fit the experimental curves. Table 7.3 shows that the predicted failure strain obtained with the **A-A** model in the 0° direction decreases as the values of γ_f (and thus the barrelling effect) increases. A friction coefficient $\gamma_f = 0.02$, found to be the most predictive for the 0° direction, was chosen for the rest of the study.

Table 7.3. Predicted failure strain for compression tests on cylinder $h_0/D_0 = 1$ (**A-A** model).

Geometry	Direction	Experiment	$\gamma_f = 0$	$\gamma_f = 0.005$	$\gamma_f = 0.01$	$\gamma_f = 0.02$	$\gamma_f = 0.05$
$h_0/D_0 = 1$	0°	0.597	0.757	0.710	0.667	0.610	0.525

7.4.2 Analysis of results

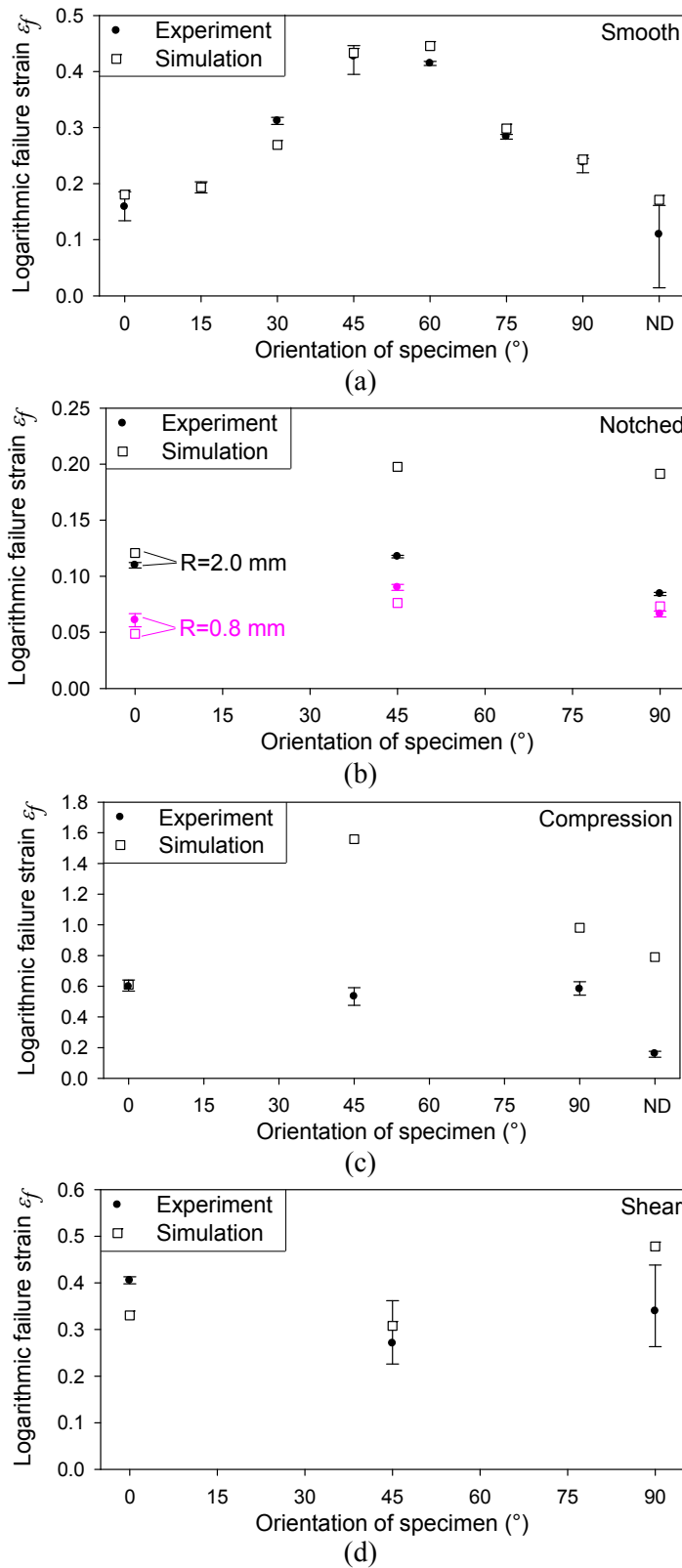


Figure 7.3. Failure strains obtained experimentally and in numerical simulations using the **A-A** model for (a) tensile tests on smooth specimens, (b) tensile tests on notched specimens, (c) compression tests on cylinder specimen with $h_0/D_0=1$ and (d) shear tests on butterfly specimens.

Failure strains

The predicted failure strains obtained with the **A-A** model are given in Figure 7.3 for all tests. The results obtained with the smooth specimen (used in the calibration of the AECL criterion) given in Figure 7.3 (a) are in good agreement with the experimental data, whereas the predictions for the notched specimens given in Figure 7.3 (b) are less accurate (especially for the notched specimens with $R=2.0\text{mm}$). For the compression tests, the results given in Figure 7.3 (c) are far from quantitatively correct, except in the 0° direction, which was used in the calibration of the friction coefficient γ_f . In addition, the anisotropy is not correctly predicted (i.e. lowest in-plane ductility in the 45° direction and a very low ductility in the normal direction ND). For the shear tests, the strains at failure given in Figure 7.3 (d) were extracted from the area used in the digital image correlation analysis. The failure strain in the 0° direction is 25% lower than the experimental value, but the anisotropy is qualitatively predicted (i.e. that the material is less ductile in the 45° direction).

Failure modes

The predicted failure modes obtained with the **A-A** model are shown for all tests from Figure 7.4 to Figure 7.7, exhibiting the spatial distribution of the damage variable on the various specimens.

For tensile tests on smooth specimens (see Figure 7.4), fracture occurs orthogonal to the specimen axis and is flat for all directions of loading except 45° . The 45° fracture surface observed experimentally (see Chapter 3) is not predicted. However, as depicted in Figure 7.4 (b), an inclination of the elements in the necking area and of the failure surface is observed for the 45° direction.

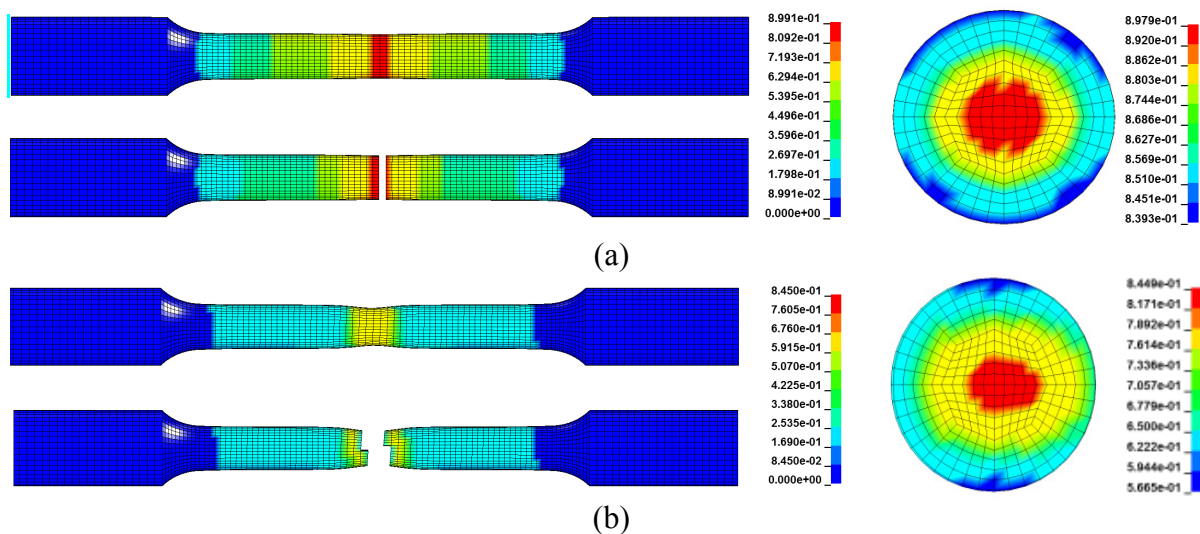


Figure 7.4. Spatial distributions of the damage variable obtained with the **A-A** model for smooth specimens loaded in the (a) 0° and (b) 45° in-plane directions before and after failure. The minimum cross section is shown just before failure.

For notched specimens with $R = 2.0$ mm (similar results were obtained for $R = 0.8$ mm and are therefore not presented) loaded in the 0° and 90° directions, failure occurs along a flat surface at the minimum cross section of the specimen (see Figure 7.5). On the contrary, for the 45° direction, the failure surface is disrupted and not located along the minimum cross section. Indeed, the first eroded elements are located outside the minimum cross section and the crack propagates along an inclined surface. To conclude, the predicted failure modes are not generally representative of the experimental observations. However, with a higher damage in the centre of the minimum cross section than at the borders observed for all tensile tests (see Figure 7.4 (b) right), one could expect to reproduce a cup-cone failure with a finer mesh (Gruben et al., 2013).

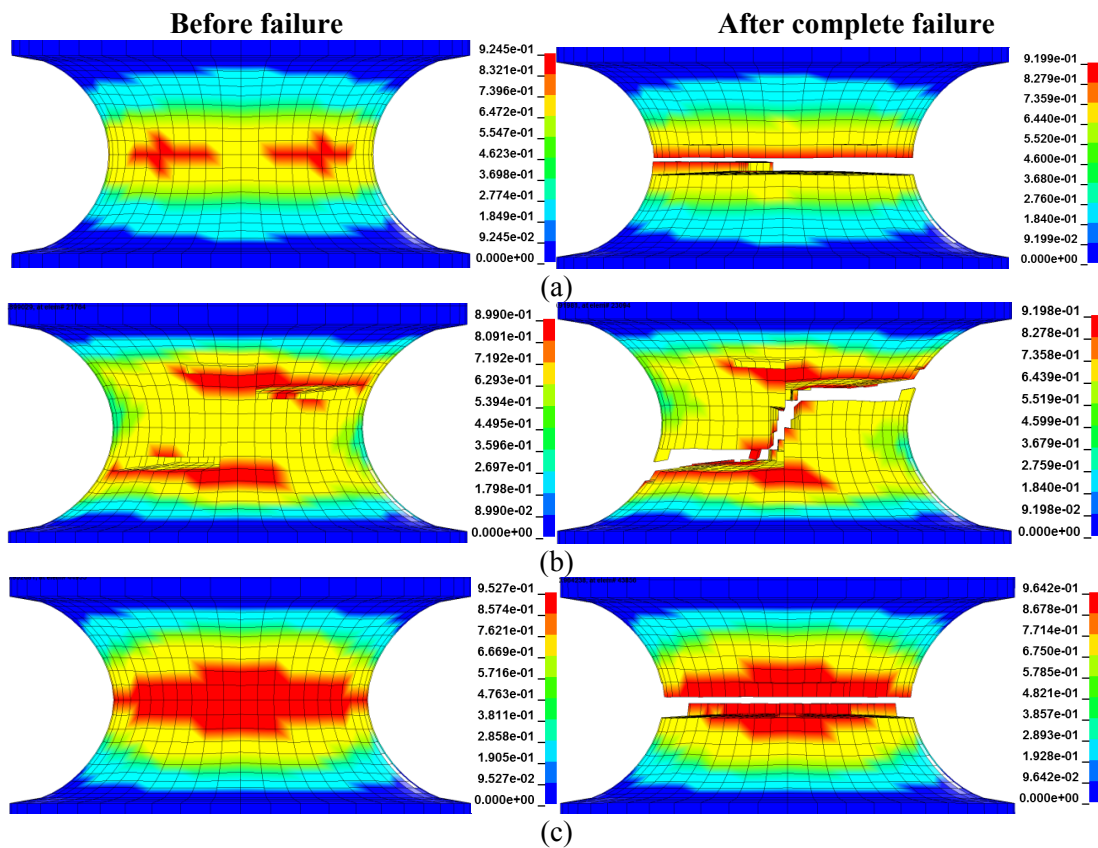


Figure 7.5. Spatial distributions of the damage variable obtained with the A-A model for notched specimens with $R = 2.0$ mm loaded in the (a) 0° , (b) 45° and (c) 90° in-plane directions.

For the compression tests (see Figure 7.6), bands of localized damage are located within the orthotropic planes, as observed experimentally in Chapter 3.4. Note that for the 45° and 90° directions, the specimens are plotted at a deformation much before failure, since the elements were too distorted at failure. For the 0° direction, the maximum damaged elements are located at the surface and mid-height of the cylinder, on the face aligned with the direction along which transverse strains are the largest (Figure 7.6 (a)). This is due to a strain ratio very

different from unity ($R_0 = 0.645$) which enhances the barrelling and promotes tensile stresses at mid-height of the specimen. Due to buckling in the 45° direction, the location of the maximum damage is displaced toward the contact surface but an inclined band of damage is still visible inside the specimen (Figure 7.6 (b)). With strain ratio close to unity, the 90° and the normal directions see a more limited barrelling. Then, the maximum damaged elements are located at mid-height, inside the specimens.

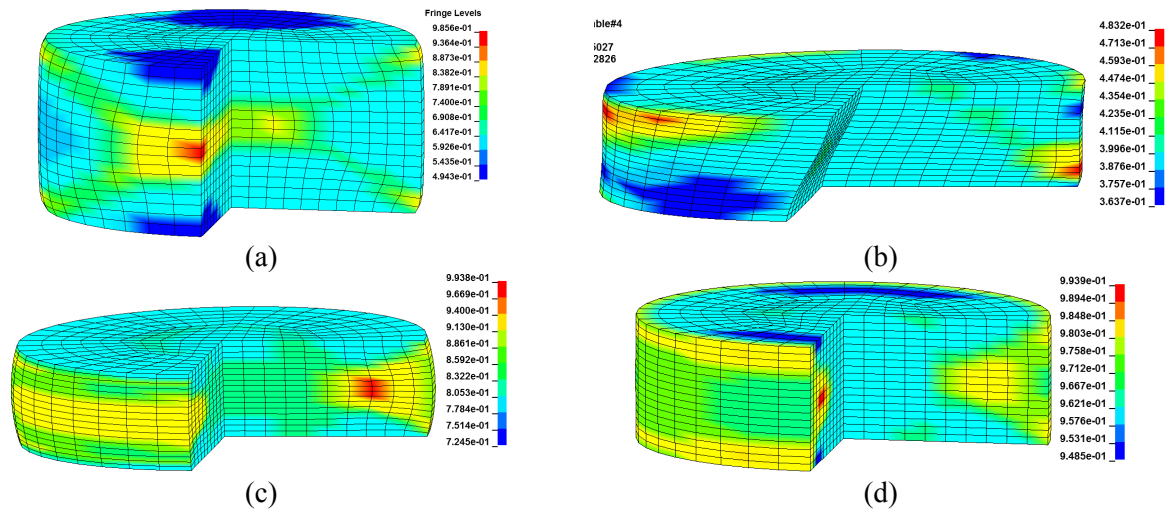


Figure 7.6. Spatial distributions of the damage variable obtained with the A-A model for cylindrical specimens with $h_0/D_0 = 1$ loaded in the (a) 0° , (b) 45° , (c) 90° in-plane directions and (d) in ND.

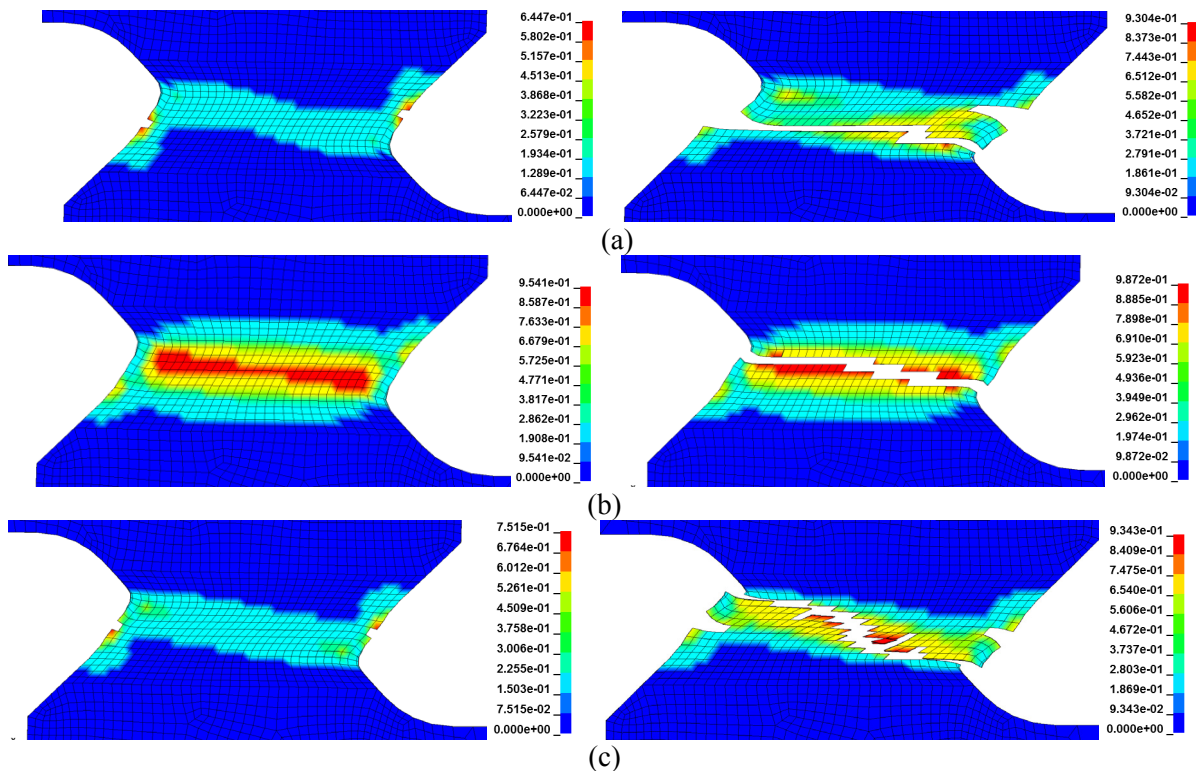


Figure 7.7. Spatial distribution of the damage variable obtained with the A-A model for butterfly specimens loaded in the (a) 0° , (b) 45° and (c) 90° in-plane directions.

For the three in-plane shear tests, the failure starts at the notch of the shear zone (see Figure 7.7). The resulting failure surface is flat for the 0° direction. On the contrary, the band where the damage is maximum is wider for the 45° direction and the resulting failure surface is more disrupted. Such disrupted failure surface was not observed experimentally.

Influence of anisotropy

Except for tensile tests on smooth specimen, numerical simulations were performed with the four different combinations of models presented in the beginning of Chapter 7.4 (**A-A**, **I-A**, **A-I** and **I-I**) to exhibit the influence of the anisotropy. The predicted failure strains are presented in Table 7.4.

Table 7.4. Predicted failure strain obtained for some of the tests with different models and parameters.

Geometry	Direction	Experiment	$\phi = 0.781$				$\phi = 0$	$\phi = 1$
			A-A	I-A	A-I	I-I	A-A	A-A
$R = 2.0\text{mm}$	0°	0.110	0.121	0.143	0.106	0.120	0.127	0.120
$R = 2.0\text{mm}$	90°	0.085	0.191	0.172	0.114	0.120	-	-
$R = 0.8\text{mm}$	0°	0.061	0.047	0.054	0.042	0.048	0.052	0.047
$h_0/D_0 = 1$	0°	0.597	0.610	0.821	0.565	0.684	0.193	1.162
Butterfly	0°	0.405	0.330	0.362	0.187	0.170	0.278	0.330

For the notched specimens loaded in the 0° direction, plastic isotropy increases the failure strain while isotropic failure decreases it. These opposite effects make the result with the **A-A** and **I-I** models very similar (difference of 1% for $R = 2.0\text{mm}$ and 2% for $R = 0.8\text{mm}$). This observation is valid for the two notch radii and for all directions except one case: in the 90° direction with $R = 2.0\text{mm}$, the plastic isotropy gives a lower failure strain with the anisotropic failure criterion (**I-A** model). This exception will be enlightened below. In general, the **A-A** model is not observed to be the most predictive model in terms of failure strain. For the four material models, failure always occurs in a flat manner for the 0° direction. On the contrary, for the 90° direction, an inclined failure surface is obtained with the **I-A** model, as previously observed for the 45° direction (Figure 7.5 (c)). Again, an unphysical response is responsible for the inclined surface and premature failure strain and helps understanding why the **I-A** model decreases the failure strain, contrary to what was expected and observed for the 0° direction.

For compression, the plastic isotropy increases the failure strain, while the isotropy of failure decreases it, as for the notched specimens. The difference between failure strains obtained with the **A-A** and **I-I** models is however larger (11%). This is due to a fundamental changes of the structural behaviour shown in Figure 7.8. With isotropic plasticity (**I-A** and **I-I**

models), the cylinder deforms in an axisymmetric manner and barrelling is limited. Then, as observed for 90° and normal directions with the **A-A** model, the maximum damage is located inside the specimen and no preferential plane exists. On the contrary, observations with the **A-I** model are not very different from results obtained with the **A-A** model (see Figure 7.6 (a)).

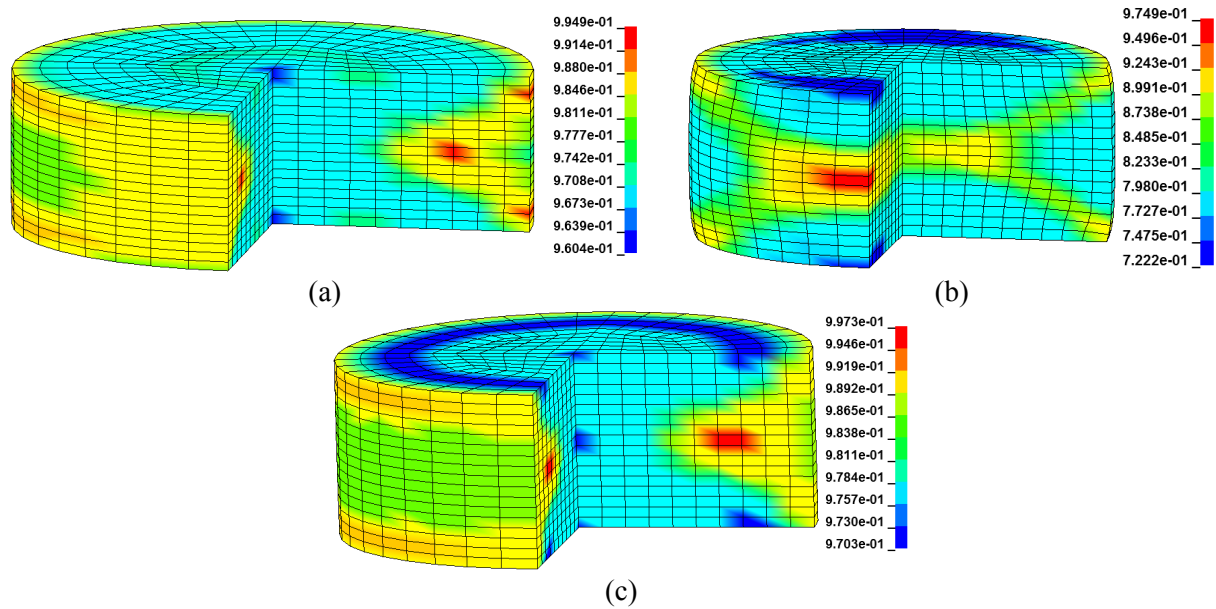


Figure 7.8. Spatial distributions of the damage variable for cylinder specimens with $h_0/D_0 = 1$ loaded in the 0° in-plane direction with the (a) **I-A** model, (b) **A-I** model and (c) **I-I** model.

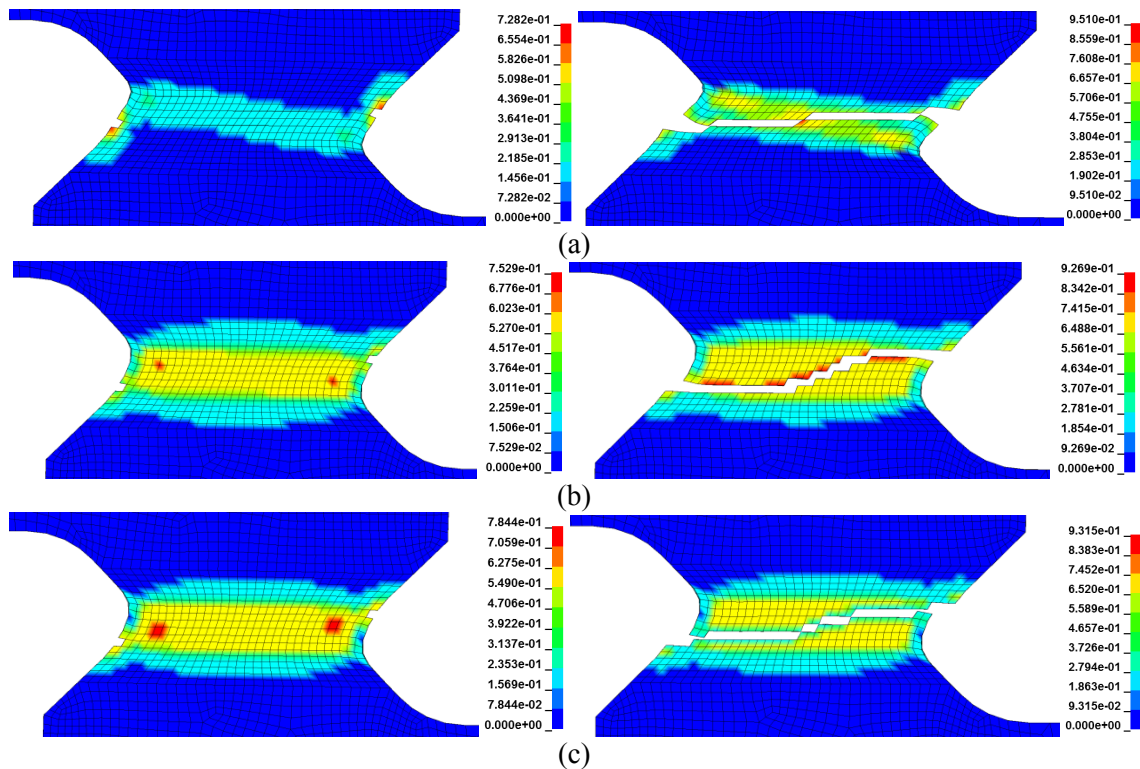


Figure 7.9. Spatial distributions of the damage variable for butterfly specimen loaded in the 0° in-plane direction with the (a) **I-A** model, (b) **A-I** model and (c) **I-I** model.

For shear, contrary to all other tests, the plastic anisotropy has only a small influence and makes the failure strain vary less than 10%. This is due to the calibration of the Yld2004-18p yield function performed with the shear tests in the 0° in-plane direction only, under the assumption of negligible anisotropy in shear (see Chapter 4). On the contrary, the anisotropy of the failure criterion has a strong influence, since the failure strain with the ECL criterion is approximately half that with the AECL criterion. This is a possible consequence of a large difference between failure strain under uniaxial tension in the 0° and 45° direction, handled by the AECL parameters P_i . As also shown in Figure 7.9, the failure mode (or band) obtained with the AECL criterion (**A-A** and **I-A** models) are more localized than with the ECL criterion (**A-I** and **I-I** models). This is a realistic effect of the AECL criterion.

Influence of the weighting parameter ϕ

Table 7.4 also give the failure strains obtained in the 0° direction with the **A-A** model for different ϕ parameters. For higher stress triaxiality states (notched specimens), the CL criterion ($\phi=1$) gives an earlier failure than the IT criterion ($\phi=0$). The principal stresses inside the notch are strictly positive so $\hat{\sigma}_I - \hat{\sigma}_{III} \leq \hat{\sigma}_I$. An increasing ϕ (i.e. giving more weight to the CL criterion) increases the damage evolution. With the **A-A** model, the difference in the failure strain between the two extreme values of ϕ is 5% for $R=2.0$ mm and 10% for $R=0.8$ mm. The failure modes are not significantly modified by the variation of the parameter ϕ .

On the contrary, for lower stress triaxiality states (shear and compression tests), the IT criterion ($\phi=0$) promotes failure compared with the CL criterion ($\phi=1$). This observation is inherent to the criterion and can be explained using the definition of the damage evolution. For shear loading conditions, the damage variable evolution is proportional to $(2-\phi)\hat{\sigma}_{12}$, so the larger the parameter ϕ , the slower the damage evolves. Also, the damage evolution is generated by the positive contributions of the maximum principal and shear stresses. Under uniaxial compression, which ideally implies $\hat{\sigma}_I = \hat{\sigma}_{II} = 0$ and $\hat{\sigma}_{III} < 0$, the damage will be similar to uniaxial tension $\phi=0$, while no damage evolution is envisaged for $\phi=1$. Thus, the predicted failure strain is increased by a factor of 5 by the CL criterion in the numerical simulations. The large overestimation of failure strains for all directions of loading (except 0° direction) suggests that, based on the available experimental and numerical data, the ϕ parameter might be overestimated.

Discussions and conclusions

An anisotropic yield function (Yld2004-18p) and an anisotropic failure criterion (AECL) were calibrated for the AA7075-T651 aluminium alloy, using uniaxial tensile tests, one shear test and one compression test. The calibrations of the isotropic versions of the yield function and the failure criterion (ECL) were performed on tests in the 0° direction. The 0° direction exhibits the highest yield limit and the lowest critical plastic work for all in-plane directions. Consequently, the plastic anisotropy decreases the predicted strength and the anisotropy of the failure criterion increases the predicted critical plastic work, compared with isotropic models.

The plastic anisotropy modifies the equivalent plastic strain rate. In addition, a side-effect of the plastic anisotropy is the loss of axisymmetry in stresses and strains in the tensile and compression tests, which eventually leads to a higher maximum shear stress $\hat{\sigma}_I - \hat{\sigma}_{III}$ (contrary to the maximum principal stress $\hat{\sigma}_I$ which is assumed to decrease). Thus, depending on the value of the weighting parameter ϕ of the failure criterion (controlling the relative importance of $\hat{\sigma}_I$ and $\hat{\sigma}_I - \hat{\sigma}_{III}$ in the damage evolution), the plastic anisotropy can either increase or decrease the failure strain. For tensile tests on notched specimens, it is generally observed that the plastic anisotropy decreases the failure strain. For shear tests, the plastic anisotropy (i.e. the variation between directions) is weak, due to the calibration of the yield function. However, as observed in the predicted force-displacement curves obtained in Chapter 4, the plastic anisotropy modifies the stresses and accumulated plastic strains and the failure strain predicted with anisotropic plasticity and isotropic plasticity differs.

The AECL criterion is not physically based and leads to quantitative discrepancies with experiments, observed for the notched tensile tests in our study. The maximum damage can sometimes be located outside the minimum cross section of the specimen, where fracture is expected and experimentally observed. This eventually leads to premature failure and disrupted failure surfaces. Another aspect of the AECL (and ECL) failure criterion is that the damage evolution is generated by the positive contributions of the maximum principal and shear stresses. This enlightens the importance of an accurate calibration of the weighting parameter ϕ , particularly for the lower stress triaxiality states. In this study, the shear tests in the 0° direction, used in the calibration of ϕ , have shown high scatter between duplicate tests. This experimental uncertainty for the shear tests irradiates on the global predictive capability of the AECL criterion.

Another issue here is the mesh size. Since the strain localization is often a precursor to fracture, a finer mesh capable of better describing the localization, could have changed some of the conclusions drawn here. One should also remember that these conclusions are drawn based on the anisotropy of the AA7075-T651 alloy. Other materials and calibration procedures might

change the influence of both plastic and fracture anisotropy. However, it is believed that the analyses presented here are valid and would only need adjustments. Finally, it should be noticed that this failure criterion is simple to calibrate, especially as it is based on tests already carried out for the calibration of the anisotropic yield surface.

Chapter 8. Structural impact of AA7075-T651 plates

8.1 Introduction

The aluminium alloy AA7075 is considered as one of the most important engineering aluminium alloys on the market today due to its high strength-to-density ratio (Hatch, 1984). Owing to this, the alloy is used in various industrial applications, such as aircraft bodies, automotive components or light-weight protective structures (e.g. Forrestal et al., 1992; Vlot, 1996; Gooch et al., 2007; Demir et al., 2008).

Børvik et al. (2010) carried out an experimental and numerical study to reveal the ballistic properties of the AA7075-T651 during impact generated loading conditions. They also investigated if simple isotropic constitutive relations and fracture criteria could be used in finite element simulations of high-strength aluminium components with a complex, non-recrystallized micro-structure subjected to structural impact. Here, the work by Børvik et al. (2010) is continued by introducing anisotropic plastic flow and anisotropic fracture in the numerical models. The main idea is to investigate to which extent an anisotropic material description will affect the ballistic properties, and to check if such an approach will improve the description of the fracture and fragmentation process in the numerical simulations. For completeness, some of the main experimental and numerical findings from Børvik et al. (2010) will first be repeated. Then anisotropic numerical models for the impact problem are introduced. Numerical simulations are finally carried out using both anisotropic and isotropic models, and the results are compared and discussed with regards to the experimental data.

8.2 Experimental and numerical results from Børvik et al. (2010)

Component tests using hardened steel projectiles (20 mm diameter, 197 g mass, 52 HRC) with blunt and ogival nose shapes (see Figure 8.1) were carried out in a compressed gas-gun

facility. The projectiles were mounted in a serrated sabot and launched at impact velocities just below and well above the ballistic limit velocity, i.e. the critical impact velocity, of the target. The sabot pieces were stopped by a sabot trap prior to impact. Target plates with dimension $600 \times 600 \text{ mm}^2$ and nominal thickness of 20 mm were clamped in a 500 mm diameter circular frame and tightened with 16 bolts. The penetration event was captured by a Photron Ultima APX-RS digital high-speed video camera operating at a constant framing rate of 50000 Hz. Initial and final velocities were measured using different laser-based optical devices (shown to be accurate to within 1-2 %), as well as by the high-speed camera system. Both initial and final target deformations were measured in-situ before and after each test. More details regarding the experimental set-up and the instrumentation used during testing can be found in Børvik et al. (2003b; 2010).

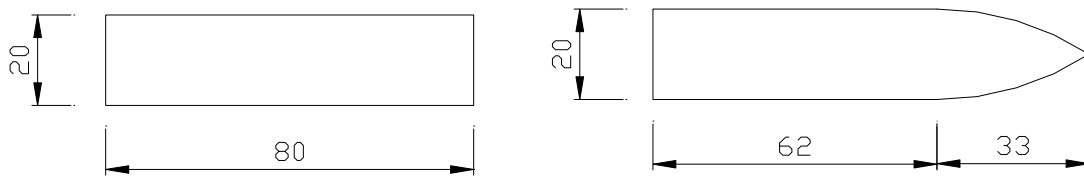


Figure 8.1. Geometry and dimensions (in mm) for blunt and ogival projectiles (Børvik et al., 2010).

Six impact tests with blunt and six impact tests with ogival projectiles were conducted for the 20 mm thick AA7075-T651 plates using the experimental equipment described above. All parameters were kept constant within each test series except for the impact velocity that varied between 180 m/s and 350 m/s. Initial (v_i) and residual (v_r) velocities of the projectile were measured in each test, and the results are plotted in Figure 8.2. Based on these measurements, the initial versus residual velocity curves were constructed. The ballistic limit velocities (v_{bl}) were taken as the lowest impact velocity within each test series, since they were found to be very close to the respective ballistic limits. The lines through the data points were determined based on a generalization of an analytical model originally proposed by Recht and Ipson (1963)

$$v_r = a(v_i^p - v_{bl}^p)^{1/p} \quad (90)$$

Where a and p may be considered as empirical constants and v_{bl} is the obtained ballistic limit. Both a and p were in this study fitted to the test data using the method of least squares. Figure 8.2 also gives experimentally obtained initial versus residual velocity curves for each projectile nose shape, together with the values of a and p . Even though some spread is seen in these plots, the agreement between the experimental data points and the Recht-Ipson model is in general good.

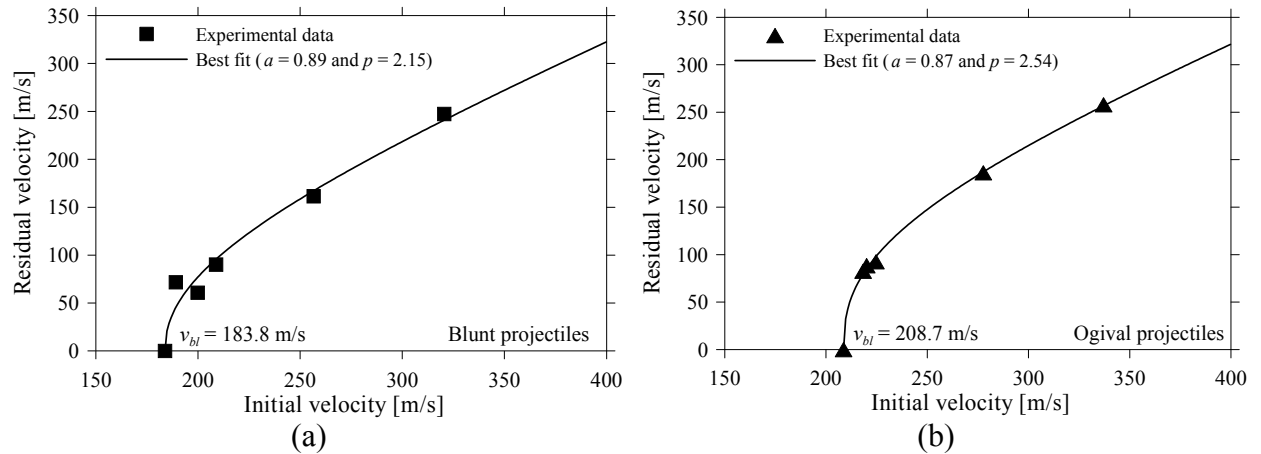


Figure 8.2. Initial versus residual velocity curves for 20 mm thick AA7075-T651 plates impacted by (a) blunt and (b) ogival projectiles (Børvik et al., 2010).

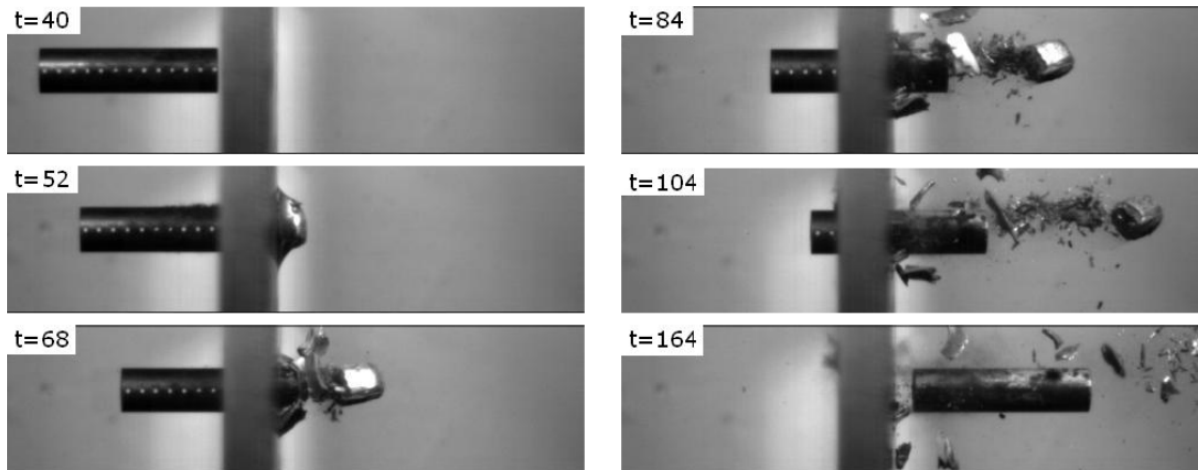


Figure 8.3. Perforation of the 20 mm thick AA7075-T651 target plate by a 20 mm diameter, 197 gram mass blunt nose projectile ($v_i = 199.8$ m/s, $v_r = 60.8$ m/s). The given times (in μ s) refer to the first image taken by the high-speed camera system (Børvik et al., 2010).

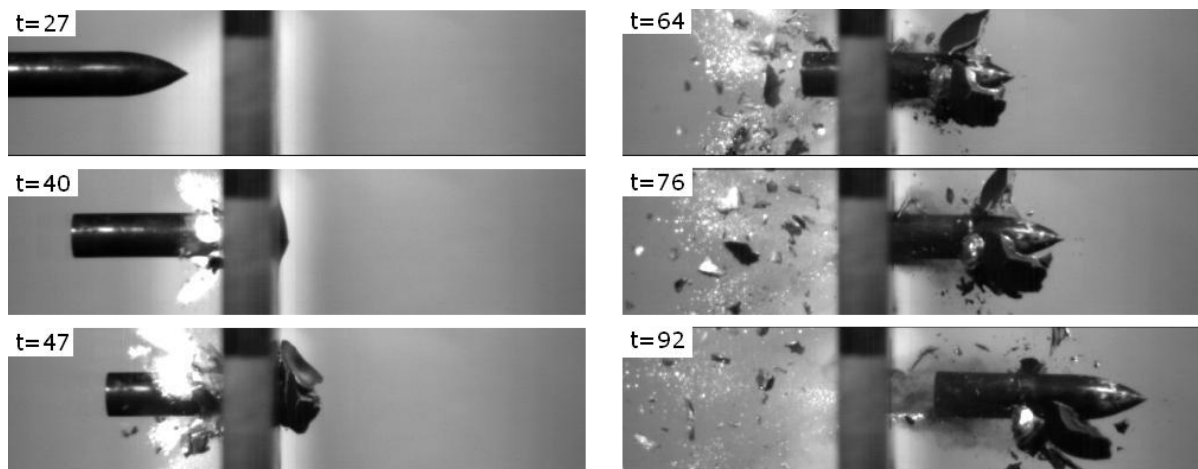


Figure 8.4. Perforation of the 20 mm thick AA7075-T651 target plate by a 20 mm diameter, 197 gram mass ogival nose projectile ($v_i = 277.7$ m/s, $v_r = 186.2$ m/s). The given times (in μ s) refer to the first image taken by the high-speed camera system (Børvik et al., 2010).

Figure 8.3 and Figure 8.4 show typical high-speed camera images of the perforation process for blunt and ogival projectiles, respectively. The perforation process is mainly due to plugging for blunt projectiles, and a plug with height approximately equal to the plate thickness is ejected from the target. In addition, fragmentation from the rear side of the target is seen due to the rather low ductility of the material. No fragments from the front side of the target are observed. For ogival projectile, the perforation process starts as ductile hole growth, which is the dominating fracture mode for pointed-nose projectiles impacting ductile materials. However, the perforation process quickly changes into fragmentation, and a large number of fragments are ejected from both sides of the target plate. The perforation process is found to be much more brittle than normally seen during perforation of ductile steel or aluminium alloys (see e.g. Børvik et al., 2004). The reason for this can be related to the complex microstructure of the AA7075-T651 alloy (see Chapter 2). This results in local variation in properties and strain localization to soft areas (PFZs), which may lead to inter-crystalline cracking, delamination and fragmentation during impact (Pedersen et al., 2011). It should finally be noticed that more energy is required to push material aside by ductile hole growth than shearing through the plate by localized plugging, which means that the ballistic limit velocity is higher for ogival than for blunt projectiles (see Figure 8.2). This has also been observed in similar tests on ductile steel plates by e.g. Børvik et al. (2002).

Numerical simulations of the impact tests were also performed by Børvik et al. (2010) in an attempt to predict the correct residual velocity and ballistic limit. All impact tests were analysed using the explicit solver of the non-linear finite element code LS-DYNA, and both 2D axisymmetric and 3D solid elements were used in the simulations. For 3D conditions, 8-node constant-stress solid elements with one integration point and stiffness-based hourglass control were applied. Contact was modelled using an eroding surface-to-surface algorithm available for SMP/MPP simulations. Independent of the projectile nose shape, a fixed element mesh was used. To save computational time, the 3D model was coarsened towards the fully clamped boundary using tetrahedral elements in a transition zone. The element size in the impact region was equal to $0.5 \times 0.5 \times 0.8 \text{ mm}^3$, giving 25 elements through the thickness, while only 7 elements were used over the target thickness in the global part of the plate. This resulted in about 330 000 elements and 850 000 nodes in the numerical model. An example of a solid element mesh used in 3D simulations is shown in Figure 8.5.

A thermoelastic-thermoviscoplastic constitutive model (the modified Johnson-Cook model) and a ductile fracture criterion (the Cockcroft-Latham criterion) were chosen by Børvik et al. (2010) in an attempt to model the target response. Thus, the constitutive behaviour and the fracture process of the material were assumed to be isotropic. To check the possible effect of anisotropy on the predictions, Børvik et al. used two different sets of material constants for the constitutive relation and fracture criterion in the simulations. The first set (Set 1) was

entirely based on uniaxial tensile tests in the rolling direction, while the second set (Set 2) was based on the uniaxial tension tests in the 45° direction. It is referred to Børvik et al. (2010) for more details regarding the various material tests, material models and the calibration of the different material parameter sets.

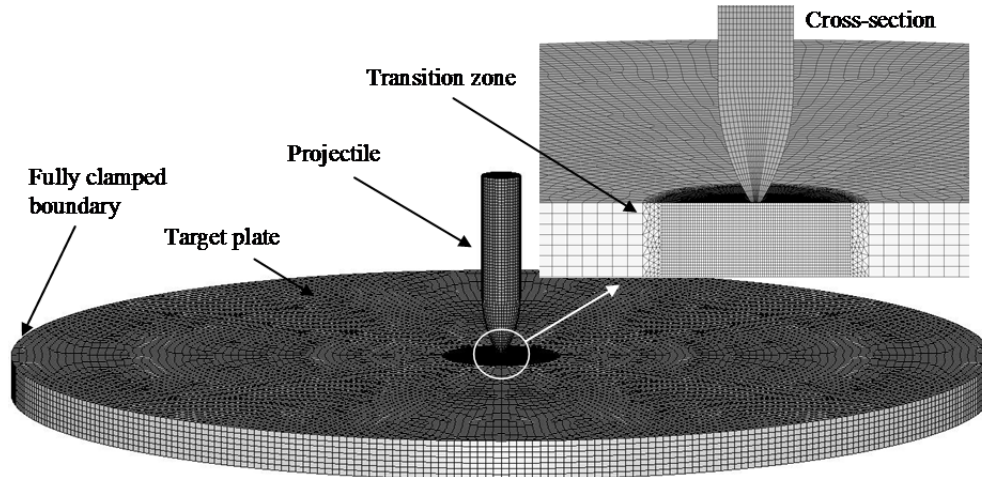


Figure 8.5. Mesh used in simulation of blunt and ogival projectile impact (Børvik et al., 2010).

Based on a number of simulations using these finite element models and the two different sets of material parameters, the initial versus residual velocity curves in Figure 8.6 were constructed. This figure shows that when the target is impacted by blunt projectiles, some spread in the initial versus residual velocity curves is obtained when the material constants are varied. For Set 1 an almost perfect fit to the experimental data was obtained, while for Set 2 the ballistic limit velocity was overestimated by 5%. For ogival projectiles the numerical results are less accurate. Set 1 gave an overestimation of the ballistic limit by about 30%, while the ballistic limit was slightly higher for Set 2 owing to the increased ductility of the material in the 45° direction.

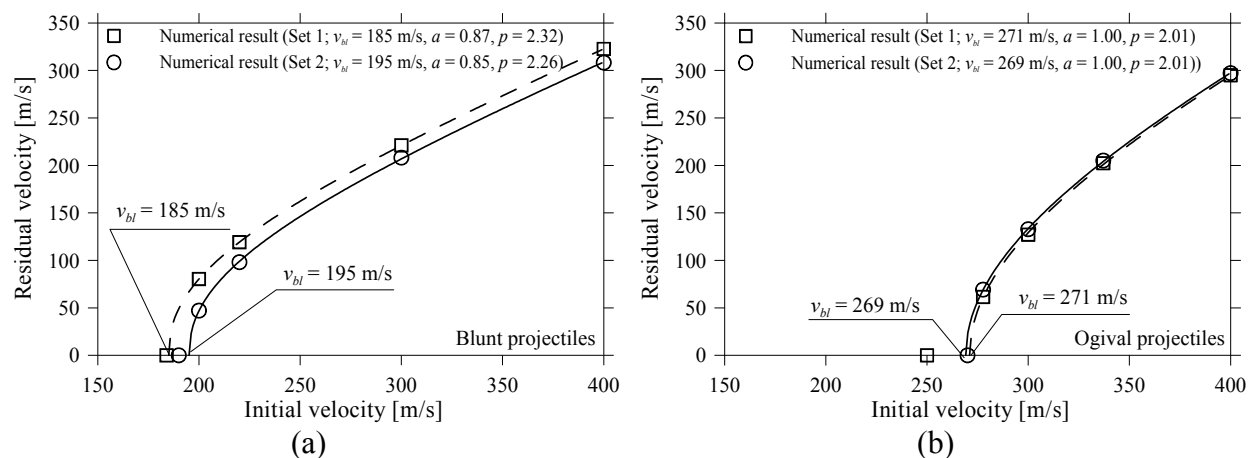


Figure 8.6. Predicted initial versus residual velocity curves for 20 mm thick AA7075-T651 plates by (a) blunt and (b) ogival projectiles using 3D constant-stress solid elements. The lines through the data points are best fits to the numerical results (Børvik et al., 2010).

Figure 8.7 shows some typical plots of the perforation process when 20 mm thick AA7075-T651 plates are perforated by blunt and ogival projectiles using material parameters obtained from the tension tests in the 0° direction (Set 1). The quasi-brittle behaviour seen experimentally (see Figure 8.3 and Figure 8.4) is partly captured in the simulation. Thus, the qualitative agreement between experimental tests and 3D simulations is good, even though there are some quantitative deviations. The reason for this seems to be that the FE models are not able to fully capture the quasi-brittle fracture behaviour of the alloy (i.e. the fragmentation and delamination process), especially during impact by ogival projectiles, and the predictions tend to overestimate the ballistic capacity of the target plates. In the following, the numerical simulations by Børvik et al. (2010) will be repeated using an anisotropic description of the material behaviour.

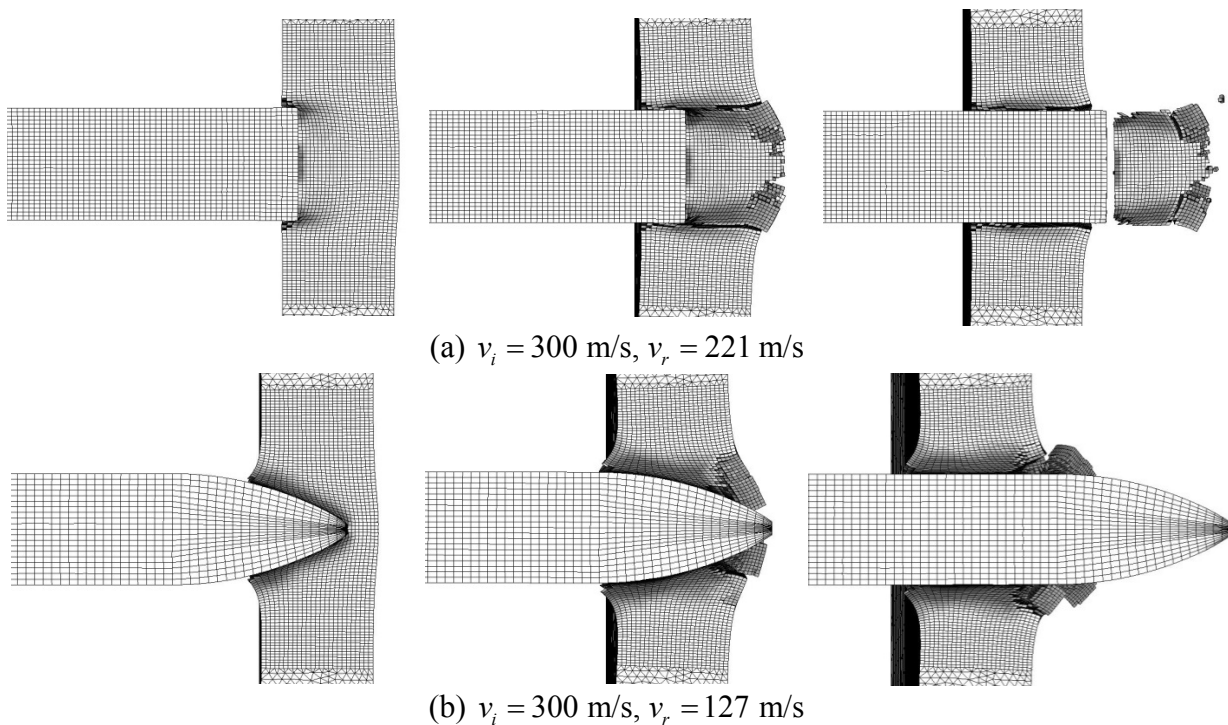


Figure 8.7. Perforation of 20 mm thick AA7075-T651 plates by (a) blunt and (b) ogival projectiles from simulations using 3D constant-stress solid elements and material parameters from Set 1. Plotted as fringe levels of accumulated plastic strain in the range 0 (light grey) to 0.5 (dark grey). The 3D model has been sliced through the centre to better show the perforation process (Børvik et al., 2010).

8.3 Anisotropic thermoelastic-thermoviscoplastic constitutive relations

Since the impact process described above implies high strain-rates and possibly induces adiabatic conditions, an anisotropic thermoelastic-thermoviscoplastic constitutive relation is required for the AA7075-T651 plate. The corotational Cauchy stress tensor and the

corotational rate-of-deformation tensor are given in Eq.(14) and Eq.(15) of Chapter 4.1, respectively. Their relation is given by

$$\dot{\hat{\boldsymbol{\sigma}}} = \hat{\mathbf{C}}_{el}^T(T) : \hat{\mathbf{d}}^e + \left[\frac{1}{E^T} \frac{\partial E^T}{\partial T} \hat{\boldsymbol{\sigma}} - 3K\alpha^{th} \mathbf{I} \right] \dot{T} \quad (91)$$

where $\hat{\mathbf{C}}_{el}^T$ is a 4th order isotropic tensor of thermo-elastic moduli and is defined by Poisson's ratio ν and Young's modulus $E^T = E^T(T)$ depending of the temperature T , given by

$$E^T(T) = \frac{T_m - T}{T_m - T_r} E \quad (92)$$

where E is Young's modulus at the reference temperature T_r and T_m is the melting temperature. A linear dependence of the temperature is chosen here. The dynamic yield function is defined as

$$f(\hat{\boldsymbol{\sigma}}, \bar{p}, \dot{\bar{p}}, T) = \bar{\sigma}(\hat{\boldsymbol{\sigma}}) - \kappa^T(\bar{p}, \dot{\bar{p}}, T) \quad (93)$$

where the equivalent stress $\bar{\sigma}$ is defined by the Yld2004-18p of Barlat et al. (2005) given by Eq.(18) to Eq.(22). The behaviour is elastic if $f < 0$, while plastic deformations occur for $f = 0$. Further, κ^T is the flow stress in uniaxial tension in the reference direction, now affected by the temperature and the strain rate, viz.

$$\begin{cases} \kappa^T(\bar{p}, \dot{\bar{p}}, T) = \kappa(\bar{p}) \left(\frac{T_m - T}{T_m - T_r} \right) \left(1 + \frac{\dot{\bar{p}}}{\dot{\bar{p}}_0} \right)^{C_0} \\ \kappa(\bar{p}) = \sigma_0 + Q(1 - \exp(-C\bar{p})) \end{cases} \quad (94)$$

The temperature rise caused by adiabatic heating is calculated as

$$\dot{T} = \frac{\beta^{th}}{\rho c^{th}} \hat{\boldsymbol{\sigma}} : \hat{\mathbf{d}}^p \quad (95)$$

where β^{th} is the Taylor-Quinney coefficient, defining the fraction of the plastic work converted into heat, ρ is the density and c^{th} is the specific heat of the material. Thermo-elastic coupling is neglected and c^{th} is assumed independent of the temperature. The calibration of the anisotropic yield function, the plastic hardening and the anisotropic fracture is the same as for the numerical simulations of the material tests presented in Chapter 4 and Chapter 6, and the parameters are given in Table 4.1 and Table 7.1. The thermal coefficients

and strain rate sensitivity parameters for the AA7075-T651 alloy are taken from Børvik et al. (2010), and these are given in Table 8.1. An elasto-plastic material model with linear hardening is used for the hardened steel projectiles (Børvik et al., 2001), and the material parameters are given in Table 8.2.

Table 8.1. Thermal and strain-rate parameters for the material model of the AA7075-T651.

\dot{p}_0 [1/s]	C_0	T_r [K]	T_m [K]	α^{th} [1/K]	c^{th} [J/kg/K]	β^{th}
0.0005	0.001	293	893	$23.1 \cdot 10^{-6}$	897	0.9

Table 8.2. Material data for the hardened steel projectile.

E [GPa]	ν	ρ [g/cm ³]	σ_0 [MPa]	E_t [GPa]
204	0.33	7.85	1900	15

As for the material tests presented in Chapter 7, the damage is not coupled to the constitutive behaviour in this study. This involves that the elements are eroded when the damage variable D reaches the critical value $D_c = 1$. Note that the fracture criterion only depends on the temperature and strain rate through the stress tensor.

8.4 Numerical results and discussion

To reveal the effects of an anisotropic material description on the ballistic properties of the AA7075-T651 alloy, numerical simulations with blunt and ogival projectiles were first performed using anisotropic plasticity (Yld2004-18p) and anisotropic fracture (AECL) (defined as the **A-A** model in Chapter 7). Except for the constitutive relation and the fracture criterion, the numerical models were identical to those used by Børvik et al. (2010). However, these differences make difficult a direct comparison between the results presented here and those by Børvik et al. (2010). A number of simulations were carried out for each nose shape, where the only variable was the initial impact velocity, and the residual velocity of the projectile was registered. The Recht-Ipson model in Eq.(90) was then fitted to the numerical data to obtain the ballistic limit curves and velocities.

Next, the four possible combinations of constitutive relation (anisotropic versus isotropic) and failure criterion (AECL versus ECL) were used in FE simulations of the ballistic impact problem. These models were defined as **A-A**, **I-A**, **A-I** and **I-I** in Chapter 7. The ballistic limit curves and velocities were not sought in this part of the study. Instead, simulations were run with constant impact velocity (one close to and one well above the ballistic limit) to see the direct influence of the different model combinations on the residual projectile velocity.

Note that all simulations discussed so far were run with $\phi=0.781$ and $m=12$. Therefore, two rather limited sensitivity studies were carried out at the end to investigate the effect of the weighting parameter ϕ in the AECL criterion and the effect of the shape of the yield surface controlled by m on the ballistic predictions.

8.4.1 Ballistic limit curves and velocities

Figure 8.8 shows predicted ballistic limit curves and velocities as obtained using the **A-A** model compared with the experimental results. The numerical predictions for blunt projectiles overestimate the residual velocities (giving conservative results), while for ogival projectiles they underestimate the residual velocities (giving non-conservative results). Compared to the experimental data, the ballistic limit velocity is underestimated by -7% for blunt projectiles, while it is overestimated by 23% for ogival projectiles (see also Figure 8.2). The predicted ballistic limits are somewhat lower, but still rather close, to those predicted by Børvik et al. (2010) using J_2 flow theory and an isotropic Cockcroft-Latham fracture criterion (see Figure 8.6). The deviation is -7% for the blunt projectile and -4% for the ogival projectile. However, at higher impact velocities, the ballistic limit curves seem to coincide with the experimental results (as also seen in a number of similar numerical studies). This clearly indicates that in order to study the effects of constitutive relation and fracture criterion in structural impact, the impact velocity should be close to the ballistic limit of the target material.

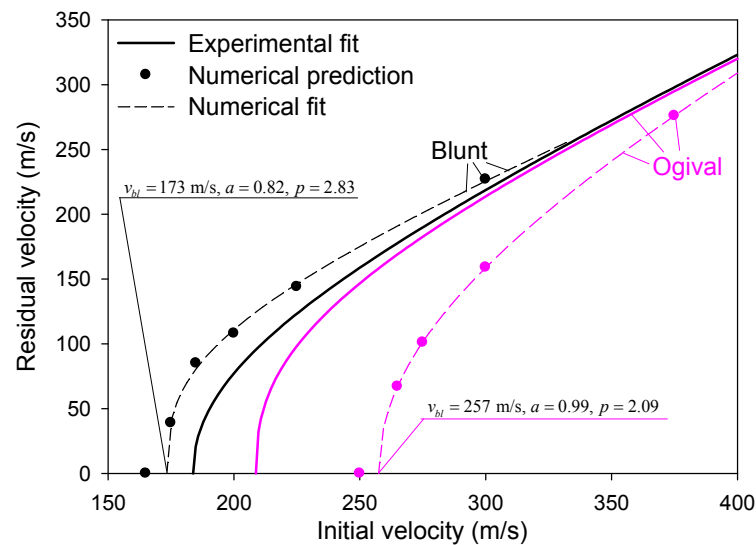


Figure 8.8. Experimental fits and predicted initial versus residual velocity curves and ballistic limits using the **A-A** model for 20 mm thick AA7075-T651 plates impacted by blunt and ogival projectiles.

Plots of the perforation process for blunt and ogival projectiles using the **A-A** model are given in Figure 8.9. If compared to the plots in Figure 8.7 from Børvik et al. (2010), the

perforation and fragmentation process are quite similar. However, the plug obtained with the **A-A** model and the blunt projectile is less damaged than the plug obtained by Børvik et al. (2010), and this seem more physical. Nevertheless, the main conclusion from this preliminary study is that the introduction of full anisotropic material properties in finite element simulations of structural impact does not significantly alter the ballistic properties for high-strength aluminium targets with a complex microstructure.

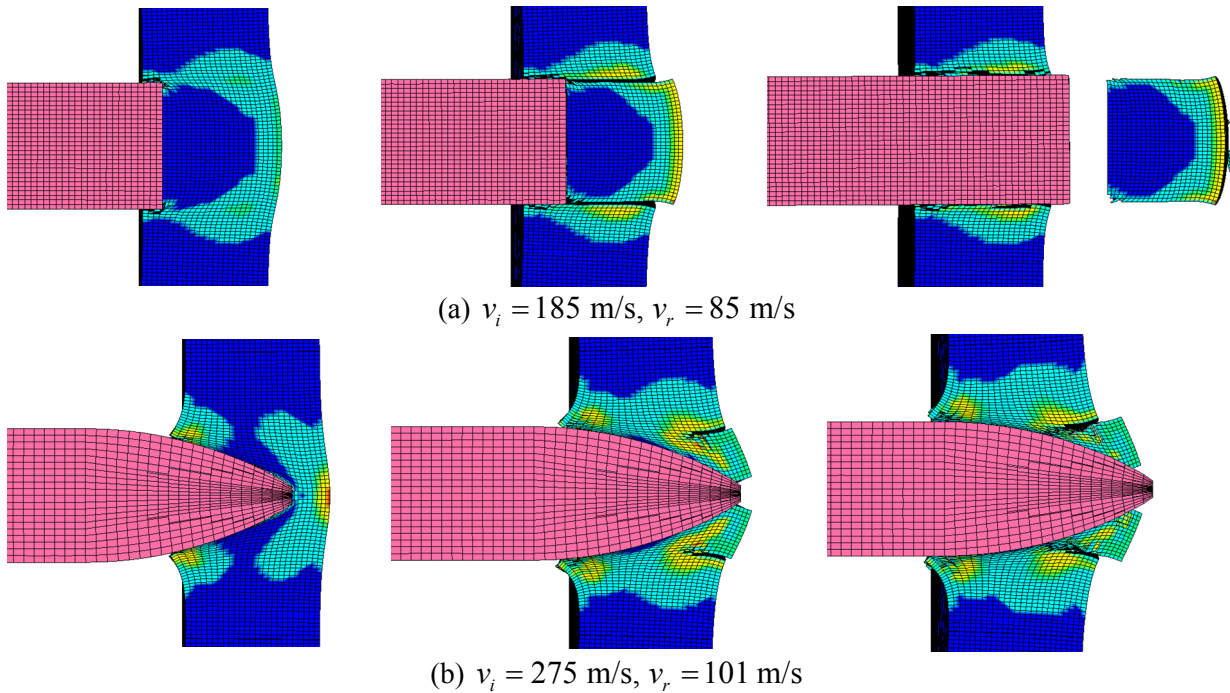


Figure 8.9. Perforation of the 20 mm thick AA7075-T651 plates by (a) blunt and (b) ogival projectiles from simulations using 3D constant-stress solid elements (**A-A** model). Fringe levels of the damage variable in the range 0 (dark blue) to 1 (red), sliced through the centre.

8.4.2 Anisotropy versus isotropy

Here, the four possible combinations of constitutive relation (**A-A**, **I-A**, **A-I** and **I-I** models) are used. Only two different impact velocities v_i were applied: one slightly higher than and one well above the ballistic limit for blunt and ogival projectiles, respectively. Interpreting the effect of anisotropy is a challenging task since the loadings during impact are very complex. For tensile tests on notched specimens, the influence of anisotropy was analysed using loading paths and yield loci (see Figure 5.6 (b)) but impact tests lead to much more heterogeneous stresses and strains than tensile tests on notched specimens. Thus, only general trends from these numerical results will be discussed. Predicted residual velocities v_r are presented in Table 8.3, while typical plots of the perforation process for blunt projectiles using the **A-A**, **I-A**, **A-I** and **I-I** models are shown in Figure 8.10.

Residual velocity

- *At high impact velocities:* for impact velocities well above the ballistic limits (300 m/s for blunt projectiles and 375 m/s for ogival projectiles), the predicted residual velocities are similar for all configurations. Thus, fully anisotropic and fully isotropic models give almost identical results (having a difference in residual velocity of only about 1% for both projectile types). However, as the impact velocities get closer to the ballistic limit (185 m/s for blunt projectiles and 275 m/s for ogival projectiles), the influence of anisotropy becomes more important and can vary with the impact velocity. Indeed, due to the strain-rate sensitivity and the temperature effect, the elements in the impacted area are subjected to stress states which may vary with v_i . Consequently, no systematic trend for the effect of anisotropic plasticity or anisotropic failure can be enlightened.
- *At impact velocities close to the ballistic limit:* for both projectiles, the plastic anisotropy decreases v_r , i.e. makes the target stronger. In contrast, the influence of the failure anisotropy is not so clear, since v_r is decreased for blunt projectiles and slightly increased for ogival projectiles when using the AECL criterion. The overall trend is that, at impact velocities close to the ballistic limit, the residual velocity is considerably reduced when introducing anisotropy both in the plastic flow and fracture (giving reduction of 20% for blunt projectiles and 13% for ogival projectiles between the **I-I** and the **A-A** models). A reduction in residual velocity gives an increase in ballistic limit. Thus, the perforation resistance of the target seems to increase by introducing anisotropic effects.

Table 8.3. Predicted residual velocity (in m/s) for impact of AA7075-T651 plates obtained with different constitutive relation and fracture criterion.

Geometry	Initial velocity v_i [m/s]	Fitted experimental residual velocity	$\phi=0.781$				$\phi=0$	$\phi=1$
			A-A	I-A	A-I	I-I	A-A	A-A
Blunt	300	218	227	226	232	230	233	219
Blunt	185	28	85	93	88	107	123	49
Ogival	375	295	276	271	282	279	345	271
Ogival	275	182	101	122	88	116	240	85

Failure modes

It is seen in Figure 8.10 that the fracture and fragmentation process is influenced by the anisotropy. By including anisotropy in the plastic flow and/or failure criterion (i.e. the **A-A**, **I-A** and **A-I** models), the failure process is not axisymmetric anymore (see Figure 8.10 (a)). This may lead to deviations of the plug and projectile during perforation. Also, with anisotropy in the fracture criterion (**A-A** and **I-A** models), the plug does not crack as it does for an isotropic criterion.

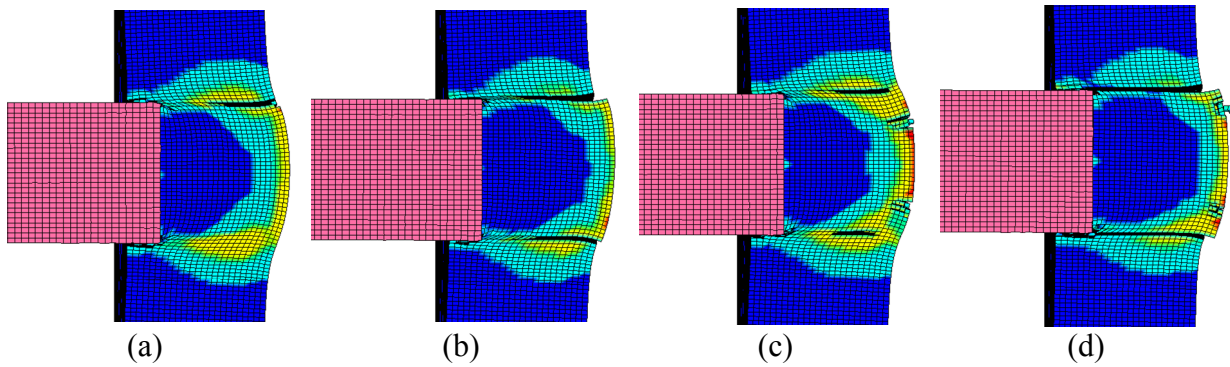


Figure 8.10. Plots of the perforation of 20 mm thick AA7075-T651 plates by blunt projectiles with $v_i = 175$ m/s using the (a) **A-A**, (b) **I-A**, (c) **A-I** and (d) **I-I** models.

8.4.3 Sensitivity study

Influence of the weighting parameter ϕ

So far, all simulations have been carried out using a constant weighting parameter ϕ in the fracture criterion. To investigate the effect of ϕ on the ballistic properties of the aluminium alloy, the simulations in Table 8.3 with the **A-A** model were rerun with two extreme values of ϕ (i.e. $\phi = 0$ and $\phi = 1$). Keep in mind that when $\phi = 0$, the AECL fracture criterion transforms into an anisotropic version of the integral-based Tresca criterion, while for $\phi = 1$ it turns into an anisotropic version of the Cockcroft-Latham criterion (see Chapter 6). The results from these simulations are given in Table 8.3.

A distinct increase in residual velocity is observed when $\phi = 0$, especially at impact velocities close to the ballistic limits. The obvious reason for this is that the integral-based Tresca criterion is much less sensitive to varying stress-states than the Cockcroft-Latham criterion (see Gruben et al., 2012). Thus, the influence of the ϕ parameter becomes very strong at shear-dominated stress-states. At higher impact velocities, the difference is only 6% between the two extreme values of ϕ for blunt projectiles, while for ogival projectiles the difference is 26%. This is somewhat counter-intuitive since blunt projectiles induce localised shear plugging of the plate in contrast to ductile hole enlargement for ogival projectiles. Indeed, the failure mode observed for blunt projectile starts with tensile damage at the bottom of the plate followed by shear bands in front of the projectile. However, the elements in contact with the nose of the ogival projectile are exposed to very large plastic deformations involving shear strains, and this causes a softening effect of the plate. Figure 8.11 shows some plots of the perforation process by blunt and ogival projectiles from typical simulations using the **A-A** model with $\phi = 0$ and $\phi = 1$. It is seen that the failure processes obtained with $\phi = 0$ are not realistic since all elements are eroded and almost no material is left in the plug or fragments

after perforation. On the contrary, with $\phi=1$, the elements subjected to tensile stresses intervenes more in the failure process, and a more realistic failure process is observed. Partial fragmentation as seen in is also detected when $\phi=1$. This is lacking when $\phi=0$.

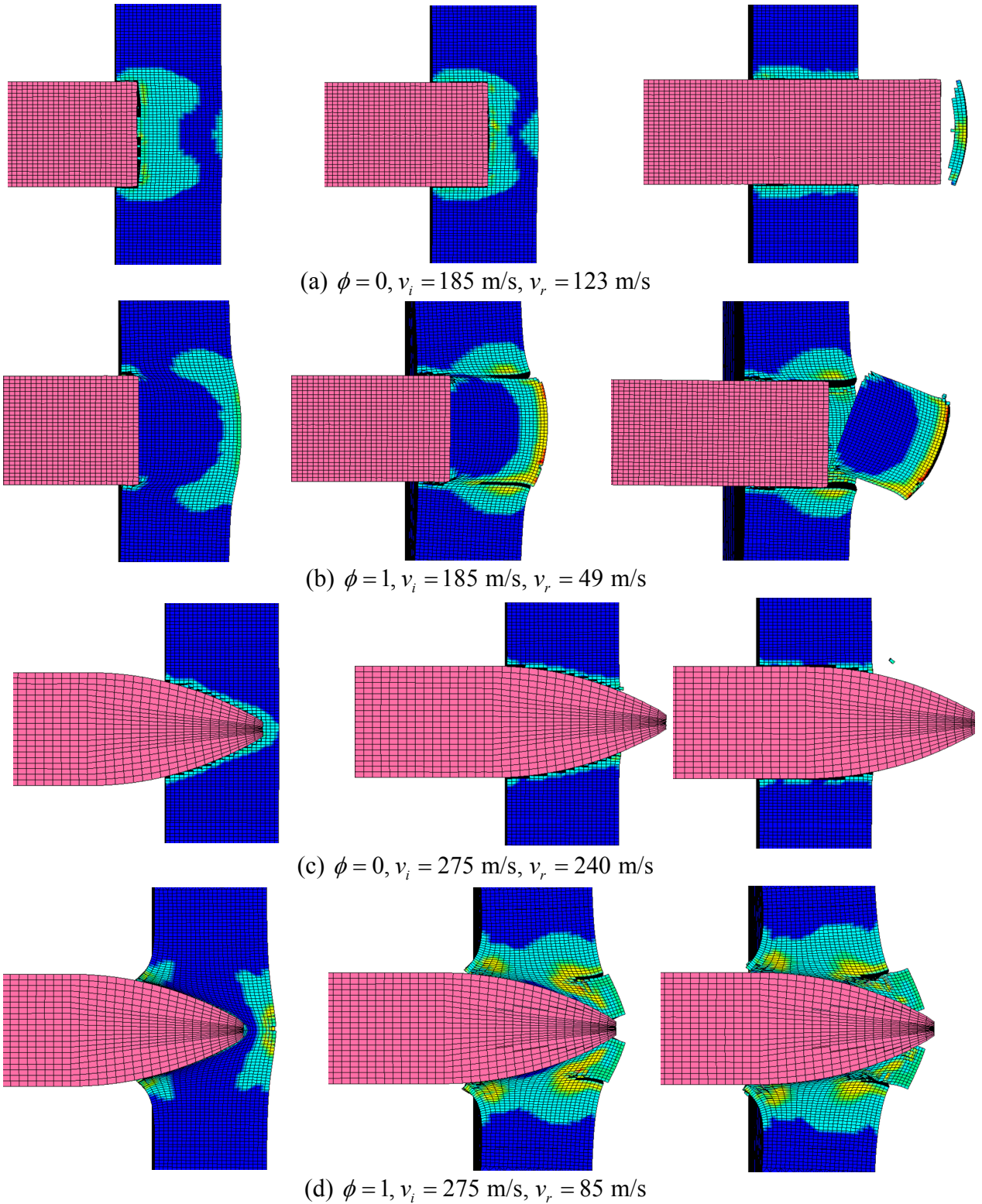


Figure 8.11. Plots of the perforation process by (a)-(b) blunt and (c)-(d) ogival projectiles from typical simulations using the **A-A** model where $\phi=0$ for (a)-(c) and $\phi=1$ (b)-(d).

In conclusion, when $\phi = 1$ the results are rather similar to those for $\phi = 0.781$ and close to the experimental value for blunt projectiles, while for ogival projectiles the ballistic limit is slightly overpredicted, giving non-conservative results. For $\phi = 0$ the results are unphysical due to the low prediction of the shear capacity of the material during impact.

Influence of the shape parameter m

The predicted results seem to differ somewhat from the results obtained by Børvik et al. (2010) using a thermoelastic-thermoviscoplastic constitutive model (the modified Johnson-Cook model and J_2 flow theory) and an isotropic fracture criterion (the Cockcroft-Latham model), also when applying the fully isotropic **I-I** model. One possible reason is that all simulations have been run with a high exponent ($m = 12$), while for J_2 flow theory $m = 2$. This exponent is used to determine the shape of the yield surface (see Chapter 4).

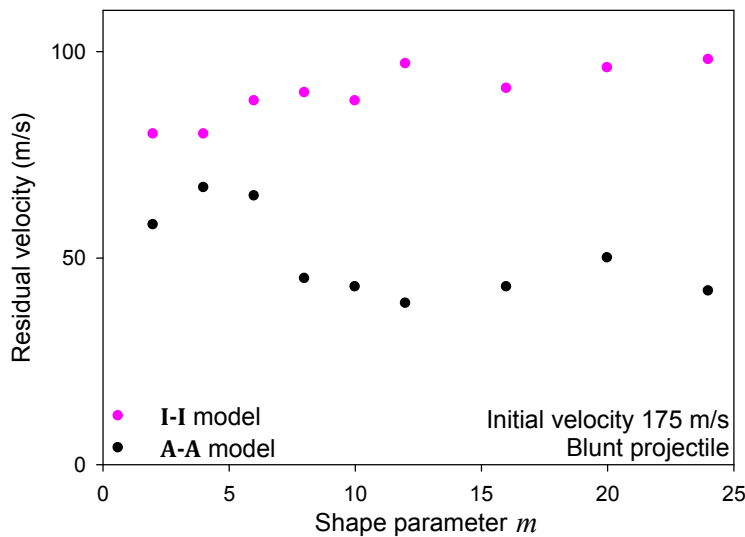


Figure 8.12. Predicted residual velocity curves for 20 mm thick AA7075-T651 plates impacted by blunt projectiles with initial velocity $v_i = 175$ m/s with different shape parameter m .

In order to investigate the effect of the shape of the yield surface on the perforation resistance of the material, a number of simulations using the **I-I** model and the **A-A** model were run using m as the only variable. The results from these simulations are plotted in Figure 8.12. For the **I-I** model, a rather steady increase in residual velocity is obtained with increasing m . Thus, the ballistic limit velocity of the target plate is reduced as the yield surface is sharpened. The reason is that a high exponent of the yield surface promotes strain localization. For the **A-A** model the results are more random. However, the general trend is that the residual velocity is reduced, i.e. making the ballistic limit increase, with increasing m . This suggests that the influence of anisotropy can be opposite and of the same order of magnitude as the influence of

the shape parameter. It is also interesting to note that for $m = 12$ the residual velocity using the **I-I** model reaches a local maximum and the **A-A** model a local minimum, maximizing the difference between the **I-I** and **A-A** models at this value of m . From Figure 8.12 it is in any case rather clear that the shape of the yield surface has an equally large (if not larger) effect on the predicted results as the introduction of anisotropy in the plastic flow and fracture. This somehow illustrates the complexity in the problem.

8.5 Conclusions

An anisotropic failure criterion based on the extended Cockcroft-Latham criterion has been proposed and used in numerical simulations of ballistic impacts against 20 mm thick plates of AA7075-T651. The criterion was calibrated based on uniaxial tensile and shear tests in the 0° direction, and evaluated through a number of simulations of various material tests in a similar way as for the anisotropic yield surface. In the numerical simulations of the ballistic impact problem, both blunt and ogival projectiles were applied, and the results were assessed against available experimental data.

The influence of anisotropy in the constitutive relation and fracture criterion is most important at impact velocity close to the ballistic limit velocity. Plastic anisotropy seems to decrease the perforation resistance of the plate, while the anisotropic failure criterion (AECL) affects the capacity of the plate in a different manner for blunt and ogival projectiles. This enlightens that the stress state, which is different for the two projectiles, plays a significant role in the perforation process. However, the overall observation from this study is that the residual velocity is considerably reduced when introducing anisotropy both in the plastic flow and fracture at impact velocities close to the ballistic limit. Also the fracture process itself is to some extent influenced by anisotropy. A reduction in residual velocity indicates an increase in ballistic limit. Thus, the plate gets stronger by introducing anisotropy. However, these conclusions may depend on how the isotropic criterion is calibrated. In this study, the isotropic criterion is calibrated based on tensile tests in the 0° direction, i.e. the material direction showing the lowest plastic work to failure.

The weighting parameter ϕ , giving the relative importance of the CL criterion (based on the first principal stress) and the IT criterion (based on the maximum shear stress), was found to have a significant influence on the predicted results. For impact velocities close to the ballistic limits of the target, the residual velocity could vary by as much as 60% for the extreme values of this parameter (i.e. $\phi = 0$ and $\phi = 1$). This means that the validity of the model strongly depends on the calibration of the weighting parameter ϕ and thus, on the quality of the shear test used in the calibration. Also the shape factor of the yield function m influences

the ballistic properties, and the general trend is that with the **A-A** model, the residual velocity is reduced with increasing m .

Several other factors may have a strong influence on the results in numerical simulations of ballistic impact (see e.g. Johnsen et al, 2013). Such factors may be the mesh size, the contact algorithm, the effect of friction, the coupled effect of temperature and strain rate on the flow stress, etc. The influence of anisotropy was admittedly not negligible, especially at impact velocities close to the ballistic limit, but it was not found larger than the influence of other factors. Taking anisotropy of plasticity and failure into account should be done in a wider optimization process of all parameters.

Finally, even though taking the anisotropy of plastic flow and failure into account was not found to significantly improve the numerical predictions, one should remember that the chosen anisotropic failure criterion has limitations. It was shown in Chapter 7 that the accuracy of this criterion was limited for shear dominated stress states and negative stress triaxialities. Even so, the main idea of this study was to investigate to what extent a simple anisotropic failure criterion could be used in a very complex problem like the impact and perforation of a high-strength aluminium alloy.

Chapter 9. Conclusions and further work

9.1 Conclusions

In this thesis, the anisotropic behaviour of the AA7075-T651 aluminium alloy in the form of 20 mm thick plates has been studied. Experiments were performed on several specimen geometries to quantify the anisotropy of plasticity and failure. In addition to microscopic observations of the virgin material, the failure surfaces were observed to identify the failure modes. An anisotropic yield function and an anisotropic failure criterion were calibrated and evaluated. Two analytical approaches for damage were examined with respect to the failure modes observed experimentally. Numerical simulations of impact on the AA7075-T651 plates were carried out and compared with experimental results obtained by Børvik et al. (2010). Finally, a first attempt of microstructural modeling of this alloy was proposed as further work with some preliminary results.

Experimental investigations

The AA7075-T651 aluminium alloy plates were observed with SEM and TEM, and were found to have some particular microstructural features:

- Pancake-shaped grains and a weak texture
- Inclusions distributed along the rolling direction of the plate
- Precipitate free zones (PFZs) of nanometer width

The PFZs, often considered as a pure aluminium zones inside a stronger matrix, were found to contain non-negligible amount of alloying elements in solid solution. This may have an influence on the plastic behaviour of these zones.

Material tests were carried out on the AA7075-T651 alloy at room temperature, under quasi-static conditions and until complete failure. Specimens were designed to expose the material to various stress states (e.g. initial stress triaxiality) and were machined in different

directions of the plate. Two classes of tests can be distinguished by their Lode parameter (third stress invariant). The axisymmetric geometries used for tensile tests on smooth and notched specimen and compression tests on cylindrical specimens give a Lode parameter $\mu_L = \pm 1$, while the shear tests performed on in-plane butterfly specimens give a Lode parameter $\mu_L = 0$. The failure surfaces were observed in a SEM when possible. The experimental results are summed up below.

- Tensile tests on smooth axisymmetric specimens were performed in seven different in-plane directions and in the normal direction (ND) of the plate (giving an initial stress triaxiality $\sigma^* = 1/3$). A marked anisotropy in yielding and plastic flow, and a large anisotropy in failure strain were observed. In in-plane uniaxial tension, the strain to failure varied strongly with the loading direction, in a similar way as the strain ratio. The ductility was low for low values of the strain ratio and vice versa. Failure occurred in a cup-and-cone mode in the directions with the highest ductility and in a shear mode in the directions with lowest ductility. An exception was found for the tests in the normal direction (ND), which failure strain was the lowest (with a large scatter between duplicate tests). These specimens exhibited a more disrupted failure surface with a tendency to flat areas following grain boundaries, orthogonal to the loading direction.
- Tensile tests on notched axisymmetric specimens of radius $R = 2.0\text{mm}$ and $R = 0.8\text{mm}$ were performed in the 0° , 45° and 90° in-plane directions of the plate. The strain to failure for the notched specimens was markedly reduced compared with the smooth specimens due to the increased levels of stress triaxiality. The fracture occurred in a cup-and-cone mode in all orientations and secondary cracks in the rolling plane were observed. The directional variation of the strain to failure was moderate.
- Shear tests were performed on butterfly specimens in the 0° , 45° and 90° in-plane directions of the plate to reach stress triaxiality states close to zero. The failure surface was flat and aligned with the direction of loading, and the DIC analysis indicated that fracture occurs almost instantaneously along the entire gauge length. The direction dependency of the strain to failure was moderate, but the results were compromised by the large scatter between duplicate tests. However, contrary to uniaxial tension, the ductility was observed lower in the 45° direction than in 0° and 90° directions. The finite element simulations demonstrated that only the middle part of the gauge section was subjected to pre-dominant shear loading, while close to the edges, complex, non-radial loadings were observed.
- Compression tests were performed on cylinder specimens in the 0° , 45° and 90° in-plane directions and in the normal direction (ND) of the plate, to reach negative stress

triaxialities. The variation in strain to failure with direction was moderate, but due to the lower stress triaxiality, strain to failure was consistently higher than in the corresponding uniaxial tension test. Also, as observed for tensile tests on smooth specimens, the ductility was found markedly lower in the normal direction of the plate. Despite the scatter in failure strain, systematic failure modes (localized along inclined bands) were observed.

- The tensile and compression tests in the normal direction (ND) of the plate exhibited low ductility, and the average strain to failure was similar, even if the overall stress triaxiality was very different. In the tension tests, the failure occurred in the rolling plane along the flat and elongated grain boundaries where precipitate free zones are located. The scatter was large, probably due to the small dimensions of the specimen compared to the grain size. In compression, failure occurred in a shear mode with a fracture surface inclined 45° to the loading axis.
- Owing to the plastic anisotropy, the cross section of the uniaxial tension and compression specimens deformed into an elliptic shape. In the cases where failure occurred in a shear mode, the orientation of the fracture surface was approximately 45° with the loading axis and contained either the semi-major axis or the semi-minor axis of the ellipse.

These experiments offer a large data base to build a representative constitutive model. However, although performed with care, the shear test results are difficult to include in the calibration of the model due to the large scatter between duplicate tests. It is believed that the geometry might be partly responsible for the scatter and other specimen should be envisaged. The behaviour under shear loading conditions (i.e. yielding and failure) was shown to be crucial for an accurate description of the material. Compression tests were initially performed on cylinders with $h_0/D_0=1.5$, but buckling implied large scatter in the failure strain. The use of cylinders with $h_0/D_0=1$ enabled to avoid the buckling effect, but the scatter in failure strain was not completely avoided. Specimens designed to limit the friction, responsible for barrelling of the specimens, can be used (Bai and Wierzbicki, 2004; Forrestal et al., 2013). Also, microscopic observations of the failure surfaces helped to identify the failure modes, while observations of interrupted tests could capture the physical mechanisms leading to final failure.

Modelling of plastic anisotropy

An elastic-plastic model including the Yld2004-18p anisotropic yield criterion proposed by Barlat et al. (2005), the associated flow rule and isotropic hardening was determined for the material, and numerical simulations were performed of all the material tests. It was found that

Yld2004-18p provided an adequate description of the plastic anisotropy of the AA7075-T651 material. Moreover, it was shown that plastic anisotropy is pivotal for an accurate prediction of the notch-strengthening effect. In particular it was shown that an isotropic yield function overestimated the stress level in the notched specimens, as also found by Wilson (2002). The shape of the anisotropic yield surface was revealed to significantly affect the prediction of the notched-specimen behaviour. These findings are important since notched specimens are often used to determine the fracture locus of materials, and in this context an accurate description of the stress state within the notch is essential.

Modelling of anisotropic failure

Void growth analysis

The Rice and Tracey (RT) analysis was developed with an anisotropic yield function. The analysis exhibited that the only non-negligible influence of anisotropy on the void growth lied on the equivalent plastic strain rate $\dot{\bar{p}}$ and in the stress triaxiality (defined from the anisotropic equivalent stress). This supports the idea that the plastic anisotropy is an important aspect of the behaviour to take into account when modeling failure. The failure locus for proportional loading situations should then be expressed in the space formed by the anisotropic equivalent strain at failure and stress triaxiality.

However, the void growth analyzed under the assumptions of RT (spherical void and growth) is not believed to be the most important failure mechanisms for the AA7075-T651. To overcome this issue, the analysis of void growth submitted to large shear deformations inside the PFZs can be envisaged. However, in that case, analytical solutions might be impossible to find and use of numerical tools may be required.

Localization analysis

The localization condition was solved to express the critical hardening modulus h_c for several constitutive relations. All softening mechanisms (sharper yield surface, non-associativity, finite strain formulation and thermal dependence of the parameters) tended to increase h_c , but no formulation was found to lead to a positive h_c for the Lode parameter $\mu_L = -1$ (i.e. generalized tension). Other softening mechanisms could be more extensively investigated to obtain better results. These applications have shown that this material seems to be very resistant to the localization in the case of axisymmetric extension or compression, but also under other stress states. To overcome these difficulties, Rice (1976), inspired by the Marciniak and Kuczynski approach in localized necking of sheets (Marciniak and Kuczynski, 1967), proposed a rigorous and three-dimensional analysis involving initial imperfections. As summarized in Yamamoto

(1978), the idea can be explained in the sense that a part of a material may have slightly different properties from the remaining portion and that continuing concentrated deformation within this inhomogeneity (imperfection) leads to failure at a strain smaller, than a value required for a perfectly homogeneous body. Both the localization band and the imperfection bands are taken in the form of planar bands. Also, in this approach, the material in the band is assumed to have slightly weaker properties within the imperfection than outside it. This imperfection may appear within the material by any process during plastic deformation (Rice, 1976), but is assumed to be present from the beginning (initial imperfection). For the AA7075-T651 alloy, the PFZs along grain boundaries can be interpreted as initial imperfections so this last formulation is a promising outlook and will be developed in further work.

Also, the localization condition obtained with a Hershey-type yield function (pressure-independent) was dependent on only one stress invariant, the Lode parameter. Yield surfaces with non-linear dependency to the hydrostatic stress, such as the Gurson's limit analysis for porous material, would offer the localization condition a dependency to the stress triaxiality ratio. It is believed that the resolution of the localization condition with an anisotropic constitutive behaviour could improve the results. However, efforts must be put into the formalism of the representative variables since only three stress invariants cannot represent the loading conditions anymore. To avoid this complexity, one outlook for the accomplishment of the localization analysis in the anisotropic context is the resolution of the localization condition implemented in a finite element code (Barsoum and Faleskog, 2011). This would allow solving the localisation condition with any constitutive behaviour without additional effort. Moreover, this would extend the resolution to non-homogeneous structures.

Anisotropic Extended Cockcroft-Latham criterion and ballistic application

An anisotropic version of the plastic work-based extended Cockcroft-Latham criterion (Gruben et al, 2012) was calibrated and evaluated for various loading conditions. Obtained failure strain and failure modes were compared to experimental observations. The predicted failure strains for tensile tests on smooth specimen (used in the calibration) were in good agreement with the experimental values for all directions. However, the failure modes were not predicted correctly. For tensile tests on notched specimens, the results were qualitatively correct, but the anisotropy was not correctly predicted and the results were only slightly enhanced compared with an isotropic model. Numerical simulations of the tests at low stress triaxiality (shear and compression tests) exhibited more realistic location for maximum damage than with an isotropic model, but the results in terms of failure strain were still inaccurate. Numerical simulations of the perforation of 20 mm thick AA7075-T651 plates by ogival and blunt projectiles were also performed. The effect of anisotropy was larger close to the ballistic limit

than for high impact velocities. The results were not qualitatively enhanced by the anisotropic model, but more realistic description of the failure was observed (such as the cracking along a preferential direction). Also, the influence of the anisotropy is not larger than the influence of other parameters such as the hardening law, the mesh size and the yield surface shape parameter m .

The weighting parameter ϕ , controlling the contribution of the Cockcroft-Latham (maximal principal stress) and Tresca-based (maximum shear stress) criteria, have an important influence on the predicted failure strain and thus on the residual velocity, particularly for shear dominated stress states. In our study, this parameter was calibrated on the shear test performed in the 0° direction of the plate. Unfortunately, the scatter obtained between duplicate shear tests gives an uncertainty in the value of the parameter ϕ . As also suggested in the outlooks for the experimental part, the repeatability of the shear tests could be enhanced by designing a more appropriate shear specimen.

Failure is predicted numerically by eroding elements, which is a rudimentary method since parts of the material mass are irreversibly lost. Recent hybrid numerical techniques were developed to replace element erosion with node splitting (www.impetus.com). This may lead to more realistic results in terms of failure modes.

9.2 Further work

One main conclusion from this study is that we have to go down in scale in order to fully understand and model the underlying mechanisms for the behaviour and fracture of complex alloys like the AA7075-T651. The anisotropy in the failure strains and the failure modes observed experimentally, under uniaxial tension for instance, is also found to be very important (see Chapter 3). Without being exhaustive, it is believed that what causes the anisotropic failure are the plastic anisotropy, the anisotropic grain morphology (and the PFZ distribution) and the anisotropic distribution of inclusions. It is believed that all microstructural ingredients are needed to predict this failure anisotropy. On the one hand, this implies the modelling of the precipitate free zones (PFZs) of nanometre size. On the other hand, if one wants to predict the macroscopic failure modes, a representative number of pancake-shaped grains should be modelled (at a millimetre scale). It is numerically challenging to cover six orders of magnitude with the finite element method, especially regarding the computational efficiency.

First attempt of microstructure modelling

A first approach was to model hexagonal grains and PFZs with one layer of solid elements in order to qualitatively observe the localization of strains. Hexagonal grains in 2D and grain

boundaries associated to each grain are represented. The grain and PFZ sizes are defined as L_G and L_{PFZ} , respectively, and each grain contains 882 elements. The number of elements through the thickness of the PFZ was found to have no significant influence and was fixed to two for the rest of the study. The ratio between the grain size and the PFZ size is then defined as $A_{G-PFZ} = L_G / L_{PFZ}$. In Chapter 2, the experimental ratio, defined as $a_{G-PFZ} = l_G / l_{PFZ}$, was found to lie within the range $a_{G-PFZ} \in [275; 6900]$. This physical ratio is very large and challenging to reproduce numerically. Consequently, numerical simulations were performed with $A_{G-PFZ} \ll a_{G-PFZ}$, but a parametrical study enabled to evaluate the sensitivity of the results to this ratio. Due to the poor aspect ratio of the elements inside the PFZs, fully-integrated elements with second-order accuracy (LSDYNA, 2007) were used to avoid shear locking. The thickness of the model (i.e. the thickness of all elements) was chosen of the same order as the in-plane dimensions of the elements. Also, due to the continuity between the mesh of the PFZs and the mesh of the grains, (which is a limitation imposed by the in-house grain generation tool used for this analysis), the number of element inside the grain is necessarily large. Consequently, only 16 grains were modelled in order to keep the computation time reasonable. The dimensions of the grains and PFZs are illustrated in Figure 9.1 (a).

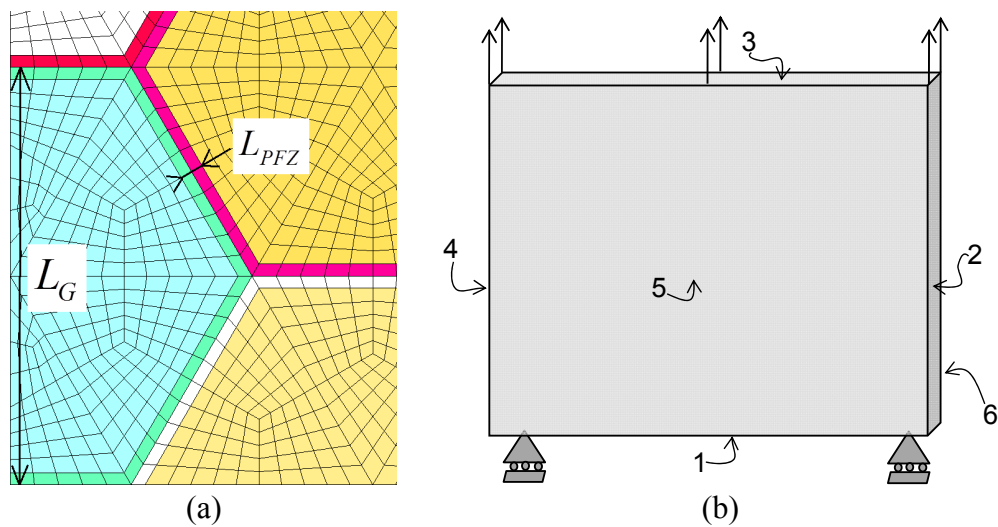


Figure 9.1. (a) Mesh for grain modelling with a length ratio $A_{G-PFZ} = L_G / L_{PFZ} = 20$ and (b) boundary conditions applied to the model.

The boundary conditions applied for uniaxial tension illustrated in Figure 9.1 (b) are

- displacement imposed in one direction to the node set (3), while no displacement along that direction is imposed to the opposite node set (1)
- planar constraint (parallelism) for the node sets (2) and (4), and (5) and (6), to allow displacements but avoid large normal distortions

The planar constraint was preferred to periodic boundary conditions because with only 1 element in the thickness of the model, the out-of plane displacements were unrealistically large. On the contrary, plain strain conditions lead to unrealistically high stress triaxiality. Grains are modelled with Yld2004-18p calibrated for the AA7075-T651 alloy (see Chapter 4) with same hardening law. The PFZs are assumed to have the same crystallographic orientation as the grains they belong to. Consequently, the yield function assigned to the half-thickness of a PFZ is the same as its neighbouring grain. However, as exhibited in Chapter 2, the PFZs present in the AA7075-T651 alloy are depleted of hardening precipitates and are composed of an aluminium matrix containing alloying elements in solid solution. This suggests that the behaviour of the PFZs is different from the inside of the grains. Typical yield stresses for low-strength aluminium alloys lie between 100–300 MPa, so the yielding stress of the PFZ (σ_{PFZ0}) is also chosen lower than the yielding stress of the AA7075-T651 alloy ($\sigma_0 = 538.81$ MPa). On the contrary, lower-strength aluminium alloys usually show higher values of hardening than high-strength aluminium, so the saturation stress of the PFZ is also chosen higher than for the AA7075-T651 alloy ($Q=177.24$ MPa). Moreover, the model of grains being regular (contrary to the real material), the localization of the plastic strains inside the PFZs is continuous through the model without obstacles, in an unrealistic manner. Then, if one wants a global yielding of the grains, the stress level in the PFZs should reach the yield stress of the grains. This could be accommodated by the fact that the strains inside the PFZs are highly constrained. Consequently, the gradient effects, stress triaxiality and a high concentration of dislocations may possibly harden the PFZs. The chosen material parameters for the PFZs are given in Table 9.1, while those of the grains are given in Table 4.1.

Table 9.1. Flow and hardening parameters of the material model Yld2004-18p for the PFZ.

σ_{PFZ0} [MPa]	Q_{PFZ} [MPa]	C_{PFZ}
100	616	1.81

Some results

The overall Cauchy stress and the overall logarithmic strain of the models can be computed from the displacement imposed and the total reaction force. Figure 9.2 (a) shows the stress-strain curves obtained from the model loaded in the 0° direction with ratio $A_{G-PFZ} = \{20,133\}$. Figure 9.2 (b) gives the maximum plastic strain at the instant when experimental failure strain is reached ($\varepsilon_f^0 = 0.159$ for the 0° direction and $\varepsilon_f^{45^\circ} = 0.427$ for the 45° direction). The plastic strain distributions presented in Figure 9.3 are obtained at these same failure instants. These plots show that with the chosen material parameters, the maximum plastic strains are located inside the PFZs for small strains and moves towards the grains for larger strains. Also, when this maximum is located inside the PFZs, the maximum strain seems to converge with

decreasing size of the PFZs. On the contrary, when located outside of the PFZs, the maximum strain is not markedly influenced by the PFZ size.

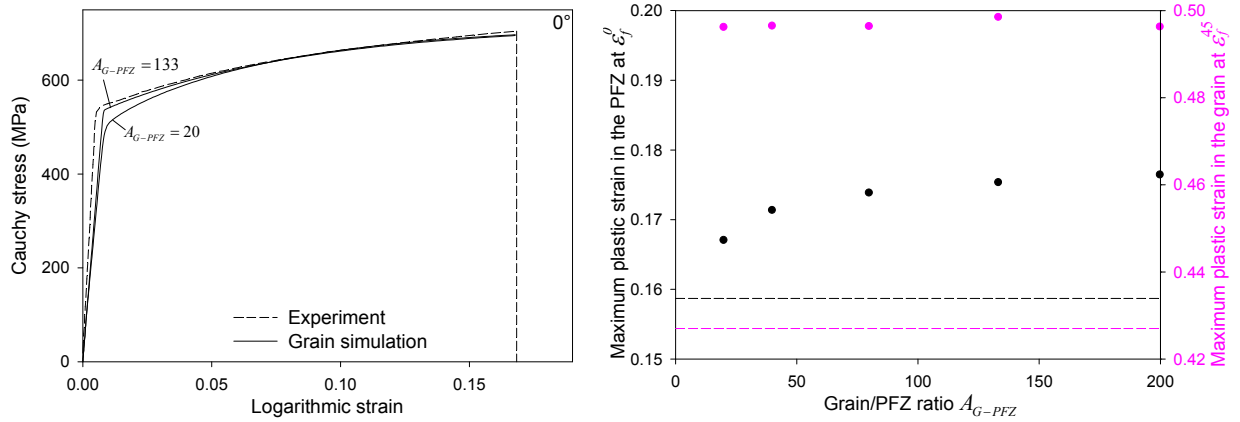


Figure 9.2. (a) Cauchy stress-true strain curves from microstructure simulations in the 0° direction with two different ratios A_{G-PFZ} (dashed line is the experimental curve) and (b) maximum plastic strain for different ratios A_{G-PFZ} for the 0° direction stopped at $\epsilon_f^{0^\circ} = 0.159$ (black) and for the 45° direction stopped at $\epsilon_f^{45^\circ} = 0.427$ (pink) (dashed lines give the macroscopic plastic strain for comparison).

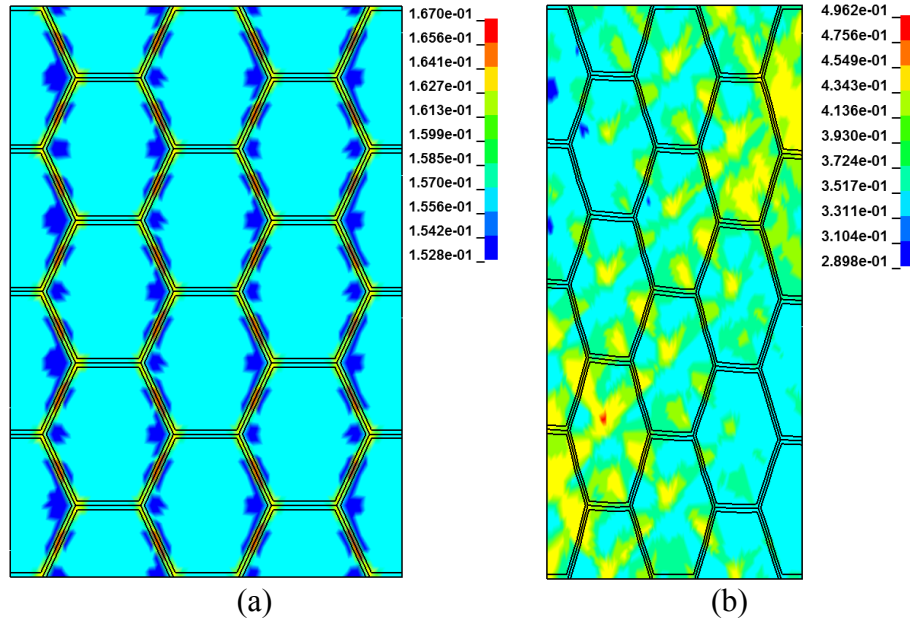


Figure 9.3. Plots of deformed grains modelled with $A_{G-PFZ} = L_G/L_{PFZ} = 20$ loaded in (a) the 0° direction and stopped at $\epsilon_f^{0^\circ} = 0.159$ and (b) the 45° direction and stopped at $\epsilon_f^{45^\circ} = 0.427$.

Taking into account the different orientations of the grains could enable to reproduce the incompatibility of the deformation between grains and introduce an additional source of heterogeneity. To that aim, crystal plasticity could be envisaged but this approach is computationally heavy. Another approach could be to use the yield functions Yld2004-18p

calibrated for the generic textures of rolled aluminium as shown by Saai et al. (2010) and to attribute them to a representative volume element (RVE) of grains. The PFZs being determinant for failure, a realistic representation of the pancake-shaped grains with sub-grains in a 3D model would enable obtaining different behaviour in the different directions. This is an affordable effort which is planned in the near future. In addition, choosing adapted failure criteria for the grain and for the PFZ would hopefully help to predict the correct macroscopic failure modes, but a larger amount of grains than presented here will be needed to be representative.

References

- Andreatta, F., Terryn, H., De Wit, J.H.W., 2003a. Effect of solution heat treatment on galvanic coupling between intermetallics and matrix in AA7075-T6. *Corrosion Science* 45 (8), 1733-1746.
- Andreatta, F., Lohrengel, M.M., Terryn, H., De Wit, J.H.W., 2003b. Electrochemical characterisation of aluminium AA7075-T6 and solution heat treated AA7075 using a micro capillary cell. *Electrochimica Acta* 48 (20-22), 3239-3247. *Electrochemistry in Molecular and Microscopic Dimensions*.
- Aretz, H., Hopperstad, O.S., Lademo, O.G., 2007. Yield function calibration for orthotropic sheet metals based on uniaxial and plane strain tensile tests. *Journal of Materials Processing Technology* 186 (1-3), 221-235.
- Arminjon, M., Bacroix, B., 1991. On plastic potentials for anisotropic metals and their derivation from the texture function. *Acta Mechanica* 88 (3), 219-243.
- Arminjon, M., Bacroix, B., Imbault, D., Raphanel, J.L., 1994. A fourth-order plastic potential for anisotropic metals and its analytical calculation from the texture function. *Acta Mechanica* 107 (1-4), 33-51.
- Bai, Y., Wierzbicki, T., 2008. A new metal plasticity and fracture with pressure and Lode dependence. *International Journal of Plasticity* 24 (6), 1071-1096.
- Bai, Y., Wierzbicki, T., 2010. Application of extended Mohr–Coulomb criterion to ductile fracture. *International Journal of Fracture* 161 (1), 1-20.
- Bao, Y., Wierzbicki, T., 2004. On fracture locus in the equivalent strain and stress triaxiality space. *International Journal of Mechanical Sciences* 46 (1), 81-98.
- Barlat, F., Lege, D., Brem, J.C., 1991. Six-component yield function for anisotropic materials. *International Journal of Plasticity* 7 (7), 693-712.
- Barlat, F., Chung, K., 1993. Anisotropic potentials for plastically deformation metals. *Modelling and Simulation in Materials Science and Engineering* 1 (4), 403-416.

- Barlat, F., Brem, J.C., Yoon, J.W., Chung, K., Dick, R.E., Lege, D.J., Pourboghrat, F., Choi, S.-H., Chu, E., 2003. Plane stress yield function for aluminum alloy sheets - Part 1: theory. *International Journal of Plasticity* 19 (9), 1297-1319.
- Barlat, F., Aretz, H., Yoon, J.W., Karabin, M.E., Brem, J.C., Dick, R.E., 2005. Linear transformation-based anisotropic yield functions. *International Journal of Plasticity* 21 (5), 1009-1039.
- Barsoum, I., Faleskog, J., 2007. Rupture mechanisms in combined tension and shear - experiments. *International Journal of Solids and Structures* 44 (6), 1768-1786.
- Barsoum, I., Faleskog, J., 2011. Micromechanical analysis on the influence of the Lode parameter on void growth and coalescence, *International Journal of Solids and Structures* 48 (6), 925-938.
- Belytschko, T., Liu, W.K., Moran, B., 2000. *Nonlinear Finite Elements for Continua and Structures*. John Wiley & Sons, Ltd., Chichester, England.
- Benallal, A., Comi, C., 1993. The role of deviatoric and volumetric non-associativities on strain localization. *Rend. Mat. Acc. Lincei* 9 (4), 279-290.
- Benallal, A., Bigoni, D., 2004. Effects of temperature and thermo-mechanical couplings on material instabilities and strain localization of inelastic materials. *Journal of Mechanics and Physics of Solids*, 52 (3), 725-753.
- Benallal, A., Berstad, T., Børvik, T., Hopperstad, O.S., Koutiri, I., Nogueira de Codes, R., 2008. An experimental and numerical investigation of the behaviour of AA5083 aluminium alloy in presence of the Portevin–Le Chatelier effect. *International Journal of Plasticity* 24 (10), 1916-1945.
- Benzerga, A., Besson, J., 2001. Plastic potentials for anisotropic porous solids. *European Journal of Mechanics A/Solids* 20 (3), 397-434.
- Benzerga, A., Surovik, D., Keralavarma, S.M., 2012. On the path-dependence of the fracture locus in ductile materials – Analysis. *International Journal of Plasticity* 37, 157-170.
- Bridgman, P.W., 1952. *Studies in large plastic flow and fracture: with special emphasis on the effects of hydrostatic pressure*. Harvard University Press, Cambridge, Mass.
- Bron, F., Besson, J., 2004. A yield function for anisotropic materials - Application to aluminum alloys. *International Journal of Plasticity* 20 (4-5), 937-963.
- Brownrigg, A., Spitzig, W.A, Richmond, O., Teirlinck, D., Embury, J.D., 1983. The influence of hydrostatic pressure on the flow stress and ductility of a spheroidized 1045 steel. *Acta Metallurgica* 31 (8), 1141-1150.
- Brünig, M., 1999. Numerical simulation of the large elastic-plastic deformation behavior of hydrostatic stress-sensitive solids. *International Journal of Plasticity* 15 (11), 1237-1264.

- Børvik, T., Hopperstad, O.S., Berstad, T., Langseth, M., 2001. A computational model of viscoplasticity and ductile damage for impact and penetration. *European Journal of Mechanics. A/Solids* 20 (5), 685-712.
- Børvik, T., Langseth, M., Hopperstad, O.S., Malo, K.A., 2002. Perforation of 12 mm thick steel plates by 20 mm diameter projectiles with blunt, hemispherical and conical noses, Part I: Experimental study. *International Journal of Impact Engineering* 27, 19-35.
- Børvik, T., Hopperstad, O.S., Berstad, T., 2003a. On the influence of stress triaxiality and strain rate on the behaviour of a structural steel. Part II. Numerical study. *European Journal of Mechanics A/Solids* 22 (1), 15-32.
- Børvik, T., Hopperstad, O.S., Langseth, M., Malo, K.A., 2003b. Effect of target thickness in blunt projectile penetration of Weldox 460 E steel plates. *International Journal of Impact Engineering* 28, 413-464.
- Børvik, T., Clausen, A.H., Hopperstad, O.S., Langseth, M., 2004. Perforation of AA5083-H116 aluminium plates with conical-nose steel projectiles – experimental study. *International Journal of Impact Engineering* 30 (4), 367-384.
- Børvik, T., Hopperstad, O.S., Pedersen, K.O., 2010. Quasi-brittle fracture during structural impact of AA7075-T651 aluminium plates. *International Journal of Impact Engineering* 37 (5), 537-551.
- Chen, Y., Pedersen, K.O., Clausen, A.H., Hopperstad, O.S., 2009. An experimental study on the dynamic fracture of extruded AA6xxx and AA7xxx aluminium alloys. *Materials Science and Engineering: A* 523 (1-2), 253-262.
- Choi, Y., Han, C.S., Lee, J.K., Wagoner, R.H., 2006. Modelling multiaxial deformation of planar anisotropic elasto-plastic materials, part I: Theory. *International Journal of Plasticity* 22 (9), 1745-1764.
- Chu, C.C., Needleman, A., 1980. Void nucleation effects in biaxially stretched sheets. *Journal of engineering materials and technology-transactions of the ASME* 102 (3), 249-256.
- Clausen, A.H., Børvik, T., Hopperstad, O.S., Benallal, A., 2004. Flow and fracture characteristics of aluminium alloy AA5083-H116 as function of strain rate, temperature and triaxiality. *Materials Science and Engineering: A* 364 (1-2), 260-272.
- Cockcroft, M.G., Latham, D.J., 1968. Ductility and the workability of metals. *Journal Institute of Metals* 96, 33-39.
- Darrieulat, M., Montheillet, F., 2003. A texture based continuum approach for predicting the plastic behaviour of rolled sheet. *International Journal of Plasticity* 19 (4), 517-546.
- Deschamps, A., Texier, G., Ringeval, S., Delfaut-Durut, L., 2009. Influence of cooling rate on the precipitation microstructure in a medium strength Al-Zn-Mg alloy. *Materials Science and Engineering: A* 501 (1-2), 133-139.

- Demir, T., Ubeyli, M., Yildirim, R.O., 2008. Investigation on the ballistic impact behavior of various alloys against 7.62mm armor piercing projectile. *Materials and Design* 29, 2009-2016.
- Dieter, G. E., 1988. *Mechanical Metallurgy*, SI ed., McGraw-Hill, Singapore.
- Dumont, D., Deschamps, A., Brechet, Y., 2004. A model for predicting fracture mode and toughness in 7000 series aluminium alloys. *Acta Materialia* 52 (9), 2529-2540.
- Dunand, M., Mohr, D., 2011. On the predictive capabilities of the shear modified Gurson and the modified Mohr-Coulomb fracture models over a wide range of stress triaxialities and Lode angles. *Journal of the Mechanics and Physics of Solids* 59 (7), 1374-1394.
- El-Magd, E., 1997. Influence of strain rate on ductility of metallic materials. *Steel Research* 68 (2), 67-71.
- Erice and Galvez, 2014. A coupled elastoplastic-damage constitutive model with Lode angle dependent failure criterion. *International Journal of Solids and Structures* 51, 93-110.
- Fagerholt, E., Dørum, C., Børvik, T., Laukli, H.I., Hopperstad, O.S., 2010. Experimental and numerical investigation of fracture in a cast aluminium alloy. *International Journal of Solids and Structures* 47 (24), 3352-3365.
- Forrestal, M.J., Luk, V.K., Rosenberg, Z., Brar, N.S., 1992. Penetration of 7075-T651 aluminum targets with ogival-nose projectiles. *International Journal of Solids and Structures* 29, 1729-1736.
- Forrestal, M.J., Børvik, T., Warren, T.L., Chen, W., 2013. Perforation of 6082-T651 Aluminum Plates with 7.62 mm APM2 Bullets at Normal and Oblique Impacts. Accepted for publication in *Experimental Mechanics* (DOI 10.1007/s11340-013-9817-3).
- Fourmeau, M., Børvik, T., Benallal, A., Lademo, O.G., Hopperstad, O.S., 2011. On the plastic anisotropy of an aluminium alloy and its influence on constrained multiaxial flow. *International Journal of Plasticity* 27 (12), 2005-2025. Special Issue In Honor of Nobutada Ohno.
- Fourmeau, M., Børvik, T., Benallal, A., Hopperstad, O.S., 2013. Anisotropic failure modes of high-strength aluminium alloy under various stress states. *International Journal of Plasticity* 48, 34-53.
- Freed, A.D., Sandor, B.I., 1985. The plastic compressibility of 7075-T651 aluminum-alloy plate. *Experimental Mechanics* 26 (2), 119-121.
- Gologanu, M., Leblond, J.B., Devaux, J., 1993. Approximate models for ductile metals containing nonspherical voids — case of axisymmetric prolate ellipsoidal cavities. *Journal of the Mechanics and Physics of Solids* 41 (11), 1723-1754.
- Gologanu, M., Leblond, J.-B., Devaux, J., 1994a. Approximate models for ductile metals containing nonspherical voids — case of axisymmetric oblate ellipsoidal cavities. *Journal of Engineering Materials and Technology* 116 (3), 290-297.

- Gologanu, M., Leblond, J.-B., Devaux, J., 1994b. Numerical and theoretical study of coalescence of cavities in periodically voided solids. *Computational Material Modelling* 42, 223-244.
- Gooch, W.A., Burkins, M.S., Squillacioti, R.J., 2007. Ballistic testing of commercial aluminum alloys and alternative processing techniques to increase the availability of aluminum armor. *Proceedings of the 23rd International Symposium on Ballistics*, Spain.
- Grytten, F., et al., 2008. Evaluation of identification methods for Yld2004-18p. *International Journal of Plasticity* 14 (18), 2248-2277.
- Gurson, A.L., 1977. Continuum theory of ductile rupture by void nucleation and growth. Part I : yield criteria and flow rules for porous ductile media. *Journal of Engineering Materials and Technology* 99 (1), 2-15.
- Gruben, G., Hopperstad, O.S., Børvik, T., 2012. Evaluation of uncoupled ductile fracture criteria for the dual-phase steel Docol 600DL. *International Journal of Mechanical Sciences* 62, 133-146.
- Gruben, G., Hopperstad, O.S., Børvik, T., 2013. Simulation of ductile crack propagation in dual phase steel. *International Journal of Fracture*, 180 (1), 1-22.
- Hahn, G., Rosenfield, A., 1975. Metallurgical factors affecting fracture toughness of aluminum alloys. *Metallurgical and Materials Transactions: A* 6 (4), 653-668.
- Hatch, J.E., 1984. *Aluminium: Properties and Physical Metallurgy*. American Society for Metals, Metals Park, Ohio.
- Hershey, A.V., 1954. The plasticity of an isotropic aggregate of anisotropic face centred cubic crystals. *Journal of Applied Mechanics*, 21, 241-249.
- Hill, R., 1948. A theory of the yielding and plastic flow of anisotropic metals. *Proceedings of the Royal Society of London. Series A, Mathematical and Physical Sciences* 193 (1033), 281-297.
- Hill, R., 1979. Theoretical plasticity of textured aggregates. *Mathematical Proceedings of the Cambridge Philosophical Society* 85 (1), 179-191.
- Hill, R., 1987. Constitutive dual potentials in classical plasticity. *Journal of the Mechanics and Physics of Solids* 35 (1), 22-33.
- Hill, R., 1990. Constitutive modelling of orthotropic plasticity in sheet metals. *Journal of the Mechanics and Physics of Solids* 38 (3), 405-417.
- Holmen, J.K., Johnsen, J., Jupp, S., Hopperstad, O.S., Børvik, T., 2013. Effects of heat treatment on the ballistic properties of AA6070 aluminium alloy. *International Journal of Impact Engineering* 57, 119-33.
- Hosford, W.F., 1972. A generalized isotropic yield criterion. *Journal of Applied Mechanics* 39 (2), 607-609.

- Hu, W., 2007. Constitutive modeling of orthotropic sheet metals by presenting hardening-induced anisotropy. *International Journal of Plasticity* 23 (4), 620-39.
- Johnsen, J., Holmen, J.K., Myhr, O.R., Hopperstad, O.S., Børvik, T., 2013. A nano-scale material model applied in finite element analysis of aluminium plates under impact loading. *Computational Materials Science* 79, 724-735.
- Jordon, J. B., Horstemeyer, M. F., Solanki, K., Bernard, J. D., J.T. Berry, J. T., Williams, T. N., 2009. Damage characterization and modeling of a 7075-T651 aluminum plate. *Material Sciences and Engineering: A* 527 (1-2), 169-178.
- Karafillis, A.P., Boyce, M.C., 1993. A general anisotropic yield criterion using bounds and a transformation weighting tensor. *Journal of Mechanics and Physics of Solids* 41 (12), 1859-1886.
- Khan, A.S., Liu, H., 2012. A new approach for ductile fracture prediction on Al 2024-T351 alloy. *International Journal of Plasticity* 35, 1-12.
- Kim, D., Barlat, F., Bouvier, S., Rabahallah, M., Balan, T., Chung, K., 2007. Non-quadratic anisotropic potential based on linear transformation of plastic strain rate. *International Journal of Plasticity* 23 (8), 1380–1399.
- Leacock, A.G., 2006. A mathematical description of orthotropy in sheet metals. *Journal of the Mechanics and Physics of Solids* 54 (2), 425–444.
- Leblond, J.-B., Perrin, G., Devaux, J., 1995. An improved Gurson-type model for hardenable ductile metals. *European Journal of Mechanics and Solids* 14 (4), 499-527.
- Lecarme, L., Tekoglu, C., Pardoën, T., 2011. Void growth and coalescence in ductile solids with stage III and stage IV strain hardening. *International Journal of Plasticity* 27 (8), 1203-1223.
- Lopes, A.B., Barlat, F., Gracio, J.J., Ferreira Duarte, J.F., Rauch, E.F., 2003. Effect of texture and microstructure on strain hardening anisotropy for aluminium deformed in uniaxial tension and simple shear. *International Journal of Plasticity* 19 (1), 1-22.
- LSTC, LS-DYNA Keyword User's Manual, Version 971, 2007. Livermore Software Technology Corporation, California.
- Luo, M., Dunand, M., Mohr, D., 2012. Experiments and modelling of anisotropic aluminium extrusions under multi-axial loading - Part II: Ductile fracture. *International Journal of Plasticity* 32-33, 36-58.
- Marciniak, Z., Kuczynski, K., 1967. Limit strains in the processes of stretch-forming sheet metal. *International Journal of Mechanical Sciences* 9 (9), 613-620.
- Marioara, C. D., Lefebvre, W. , Andersen, S. J., Friis, J., 2013. Atomic structure of hardening precipitates in an Al–Mg–Zn–Cu alloy determined by HAADF-STEM and first-principles calculations: relation to η -MgZn₂. *Journal of Materials Science* 48 (10), 3638-3651.

- Marini, B., Mudry, F., Pineau, A., 1985. Experimental study of cavity growth in ductile rupture. *Engineering Fracture Mechanics* 22 (6), 989-996.
- Marlaud, T., Deschamps, A., Bley, F., Lefebvre, W., Baroux, B., 2010. Influence of alloy composition and heat treatment on precipitate composition in Al-Zn-Mg-Cu alloys. *Acta Materialia* 58 (1), 248-260.
- McClintock, F.A., 1968. A criterion for ductile fracture by the growth of holes. *Journal of Applied Mechanics* 35 (2), 363-371.
- Monchiet, V., Cazacu, O., Charkaluk, E., Kondo, D., 2008. Macroscopic yield criteria for plastic anisotropic materials containing spheroidal voids. *International Journal of Plasticity* 24 (7), 1158-1189.
- Nahshon, K., Hutchinson, J.W., 2008. Modification of the Gurson Model for shear failure, *European Journal of Mechanics A/Solids* 27 (1), 1-17.
- Pardoën, T., Hutchinson, J.W., 2000. An extended model for void growth and coalescence. *Journal of the Mechanics and Physics of Solids* 48 (12), 2467-2512.
- Pardoën, T., Dumont, D., Deschamps, A., Brechet, Y., 2003. Grain boundary versus transgranular ductile failure. *Journal of the Mechanics and Physics of Solids* 51 (4), 637-665.
- Park, J.K., Ardell, A.J., 1988. Precipitate microstructure of peak-aged 7075 Al. *Scripta Metallurgica* 22 (7), 1115-1119.
- Pedersen, K.O., Børvik, T., Hopperstad, O.S., 2011. Fracture mechanisms of aluminium alloy AA7075-T651 under various loading conditions. *Material and Design* 32 (1), 97-107.
- Rauch, E.F., 1998. Plastic anisotropy of sheet metals determined by simple shear tests. *Material Sciences and Engineering: A* 241 (1-2), 179-183.
- Recht, R.F., Ipson, T.W., 1963. Ballistic perforation dynamics. *Journal for Applied Mechanics* 30, 384-390.
- Rice, J.R., Tracey, D.M., 1969. On the ductile enlargement of voids in triaxial stress fields. *Journal of Mechanics and Physics of Solids* 17 (3), 201-217.
- Rice, J.R., 1976. The localization of plastic deformation. *Theoretical and Applied Mechanics*, 1, 207-220
- Richmond, O., Spitzig, W.A., 1980. Pressure dependence and dilatancy of plastic flow. *Theoretical and Applied Mechanics* 15, 377-386.
- Rousselier, G., Barlat, F., Yoon, J.W., 2010. A novel approach for anisotropic hardening modelling. Part II: Anisotropic hardening in proportional and non-proportional loadings, application to initially isotropic material. *International Journal of Plasticity* 26 (7), 1029-1049.

- Rousselier, G., Luo, M., Mohr, D., 2012. Macroscopic plasticity modeling of anisotropic aluminum extrusions using a Reduced Texture Methodology. *International Journal of Plasticity* 30-31, 144-165.
- Rudnicki, J.W., Rice, J.R., 1975. Conditions for the localization of deformation in pressure-sensitive dilatant materials. *International Journal of Mechanics and Physics of Solids* 23,371-394.
- Saai, A., Dumoulin, S., Hopperstad, O.S., Lademo, O.-G., 2013. Simulation of yield surfaces for aluminium sheets with rolling and recrystallization textures. *Computational Materials Science* 67, 424-433.
- Soare, S., Barlat, F., 2010. Convex polynomial yield functions. *Journal of the Mechanics and Physics of Solids* 58 (11), 1804-1818.
- Spitzig, W.A., Richmond, O., 1984. The effect of pressure on the flow stress of metals. *Acta Metallurgica* 32 (3), 457-463.
- Steglich, D., Brocks, W., Heerens, J., Pardoen, T., 2008. Anisotropic ductile fracture of Al 2024 alloys. *Engineering Fracture Mechanics* 75 (12), 3692-3706.
- Stoughton, T.B., Yoon, J.W., 2009. Anisotropic hardening and non-associated flow in proportional loading of sheet metals. *International Journal of Plasticity* 25 (9), 1777–1817.
- Stoughton, T.B., Yoon, J.W., 2011. A new approach for failure criterion for sheet metals. *International Journal of Plasticity* 27 (3), 440-459.
- Teirlinck, D., Zok, F., Embury, J.D., Ashby, M.F., 1988. Fracture mechanism maps in stress space. *Acta Metallurgica* 36 (5), 1213-1228.
- Thomason, P.F., 1990. *Ductile fracture of metals*. Pergamon Press, Oxford.
- Tvergaard, V., Needleman, A., 1984. Analysis of the cup-cone fracture in a round tensile bar. *Acta Metallurgica* 32 (1), 157-169.
- Van Houtte, P., Mols, K., Van Bael, A., Aernoudt, E., 1989. Application of yield loci calculated from texture data. *Textures and Microstructures* 11, 23-39.
- Van Houtte, P., Van Bael, A., 2004. Convex plastic potentials of fourth and sixth rank for anisotropic materials. *International Journal of Plasticity* 20 (8-9), 1505-1524.
- Verhoeven, J. D., 1975. *Fundamentals of Physical Metallurgy*
- Vlot, A., 1996. Impact loading on fibre metal laminates. *International Journal of Impact Engineering* 18, 291-307
- Wierzbicki, T., Bao, Y., Lee, Y.W., Bai, Y., 2005. Calibration and evaluation of seven fracture models. *International Journal of Mechanical Sciences* 47 (4-5), 719-743.
- Wikipedia, http://en.wikipedia.org/wiki/7075_aluminium_alloy, [cited: 06-11-2013].

Wilson, C.D., 2002. A critical re-examination of classical metal plasticity. *Journal of Applied Mechanics* 69, 63-68.

Yamamoto, 1978. Conditions for shear localization in the ductile fracture of void-containing materials. *International Journal of Fracture*, 14 (4), 347-365.

Yerra, S. K., Tekoglu, C., Sheyvaerts, F., Delannay, L., Van Houtte, P., Pardoen, T., 2010. Void growth and coalescence in single crystals. *International Journal of Solids and Structures* 47 (7-8), 1016-1029.

Zhang, K.S., Bai, J.B., François, D., 2001. Numerical analysis of the influence of the Lode parameter on void growth, *International Journal of Solids and Structures* 38 (32-33), 5847-5856.

Appendix

A. Elastic 4th order tensor and related

Isothermal conditions

At room temperature, some elastic parameters are defined for convenience of the writing

$$K = \frac{3\lambda + 2\mu}{3}, \quad E = \frac{\mu(3\lambda + 2\mu)}{(\lambda + 2\mu)} = \frac{3\mu K}{\lambda + 2\mu}, \quad \nu = \frac{\lambda}{2(\lambda + \mu)} \quad (\text{A-96})$$

where (λ, μ) are the Lamé coefficients, K is the bulk modulus, E is the Young's modulus and ν the Poisson ratio. The Hooke tensor is defined by $\mathbf{E}^i = \mathbf{E} = 2\mu\mathbf{I}^{4S} + \lambda\mathbf{I} \otimes \mathbf{I}$, where $\mathbf{I}^{4S} = (\delta_{ik}\delta_{jl} + \delta_{il}\delta_{jk})/2$ is the symmetric part of the 4th order identity tensor. This gives with Voigt notations

$$\mathbf{E} = \begin{bmatrix} \lambda + 2\mu & \lambda & \lambda & 0 & 0 & 0 \\ \lambda & \lambda + 2\mu & \lambda & 0 & 0 & 0 \\ \lambda & \lambda & \lambda + 2\mu & 0 & 0 & 0 \\ 0 & 0 & 0 & \mu & 0 & 0 \\ 0 & 0 & 0 & 0 & \mu & 0 \\ 0 & 0 & 0 & 0 & 0 & \mu \end{bmatrix} \quad (\text{A-97})$$

The inverse of this tensor is $\mathbf{E}^{-1} = 1/2\mu\mathbf{I}^{4S} - \lambda/6\mu K\mathbf{I} \otimes \mathbf{I}$, i.e.

$$\mathbf{E}^{-1} = \frac{1}{3\mu K} \begin{bmatrix} \lambda + \mu & -\lambda/2 & -\lambda/2 & 0 & 0 & 0 \\ -\lambda/2 & \lambda + \mu & -\lambda/2 & 0 & 0 & 0 \\ -\lambda/2 & -\lambda/2 & \lambda + \mu & 0 & 0 & 0 \\ 0 & 0 & 0 & 3K & 0 & 0 \\ 0 & 0 & 0 & 0 & 3K & 0 \\ 0 & 0 & 0 & 0 & 0 & 3K \end{bmatrix} \quad (\text{A-98})$$

Two tensors of interest for the localiation analysis are

$$\begin{aligned}\therefore \mathbf{A}^e &= \underline{n} \cdot \mathbf{E} \cdot \underline{n} = \underline{n} \cdot (2\mu \mathbf{I}^{4S} + \lambda \mathbf{I} \otimes \mathbf{I}) \cdot \underline{n} \\ &= \mu \mathbf{I} + (\lambda + \mu) \underline{n} \otimes \underline{n}\end{aligned}\quad (\text{A-99})$$

$$\therefore (\mathbf{A}^e)^{-1} = \frac{1}{\mu} \mathbf{I} - \frac{\lambda + \mu}{\mu(\lambda + 2\mu)} \underline{n} \otimes \underline{n}$$

The determinant respect the following property

$$\det(\mathbf{A} + \underline{a} \otimes \underline{b}) = \det(\mathbf{A}) + \underline{b} \cdot \mathbf{A}^* \cdot \underline{a} \quad (\text{A-100})$$

where $\mathbf{A}^* = (\det \mathbf{A}) \mathbf{A}^{-1}$ is the transposed of the cofactor matrix of \mathbf{A} . This leads to

$$\begin{aligned}\therefore \det \mathbf{A}^e &= \det(\mu \mathbf{I} + (\lambda + \mu) \underline{n} \otimes \underline{n}) \\ &= \det(\mu \mathbf{I}) + (\lambda + \mu) \underline{n} \cdot (\mu \mathbf{I})^* \cdot \underline{n} \\ &= \det(\mu \mathbf{I}) + (\lambda + \mu) \underline{n} \cdot (\mu^2 \mathbf{I}) \cdot \underline{n} \\ &= \mu^2 (\lambda + 2\mu) \\ \therefore \det(\mathbf{A}^e)^{-1} &= \frac{1}{\det \mathbf{A}^e} = \frac{1}{\mu^2 (\lambda + 2\mu)}\end{aligned}\quad (\text{A-101})$$

Then, the term $\underline{n} \cdot \mathbf{H} \cdot \underline{n}$, containing the 4th order tangent tensor \mathbf{H} , can transform into

$$\begin{aligned}\underline{n} \cdot \mathbf{H} \cdot \underline{n} &= \underline{n} \cdot \mathbf{E} \cdot \underline{n} - \underline{n} \cdot \frac{\underline{\alpha} \otimes \underline{\beta}}{H} \cdot \underline{n} = \mathbf{A}^e - \frac{1}{H} (\underline{\alpha} \cdot \underline{n}) \otimes (\underline{\beta} \cdot \underline{n}) \\ \underline{n} \cdot \mathbf{H} \cdot \underline{n} &= \mathbf{A}^e \cdot \mathbf{B} \quad \text{with} \quad \begin{cases} \mathbf{A}^e = \underline{n} \cdot \mathbf{E} \cdot \underline{n} \\ \mathbf{B} = \mathbf{I} - \frac{1}{H} (\mathbf{A}^e)^{-1} \cdot (\underline{\alpha} \cdot \underline{n}) \otimes (\underline{\beta} \cdot \underline{n}) \end{cases}\end{aligned}\quad (\text{A-102})$$

Adiabatic conditions

The 4th order elastic tensor under adiabatic conditions is

$$\mathbf{E}^a = \mathbf{E}^i + \frac{9(\alpha^{th} K)^2 T}{\rho c} \mathbf{I} \otimes \mathbf{I} = 2\mu \mathbf{I}^{4S} + \lambda^a \mathbf{I} \otimes \mathbf{I} \quad \text{with} \quad \lambda^a = \lambda + \frac{9(\alpha^{th} K)^2 T}{\rho c} \quad (\text{A-103})$$

where $\mathbf{E}^i(T)$ is called the isothermal 4th order elastic tensor. The newly define Lamé coefficient $\lambda^a \geq \lambda$ contains the influence of adiabatic conditions on the elastic behaviour. Note

that consequently, the Young modulus E^a under adiabatic conditions is smaller than the isothermal E^i . Also, the following terms are of interest

$$\begin{aligned}
\therefore \mathbf{A}^{ae} &= \underline{n} \cdot \mathbf{E}^a \cdot \underline{n} = \mu \mathbf{I} + (\lambda^a + \mu) \underline{n} \otimes \underline{n} \\
\therefore (\mathbf{A}^{ae})^{-1} &= \frac{1}{\mu} \mathbf{I} - \frac{(\lambda^a + \mu)}{\mu(\lambda^a + 2\mu)} \underline{n} \otimes \underline{n} \\
\therefore \det(\mathbf{A}^{ae}) &= \mu^2 (\lambda^a + 2\mu)
\end{aligned} \tag{A-104}$$

B. Thermodynamic framework

We consider hereafter constitutive behaviour describing the thermo-inelastic behaviour of various materials. For small strains, this behaviour is defined by the free-energy potential per unit mass

$$\psi(\boldsymbol{\varepsilon}, \zeta_i, T) = e - Ts \tag{A-105}$$

where e is the internal energy, s is the specific entropy and T the temperature. $\boldsymbol{\varepsilon}$ is the total strain while ζ_i denotes a collection of internal variables (scalar, vector or second order tensor) describing all mechanisms governing inelastic deformation. The total strain $\boldsymbol{\varepsilon}$ is usually split into three components including the mechanical elastic strain $\boldsymbol{\varepsilon}^e$, the inelastic strain $\boldsymbol{\varepsilon}^p$ and the thermal strain $\boldsymbol{\varepsilon}^{th}$. A yield function $f(\boldsymbol{\sigma}, Z_i, T) \leq 0$ defines the range of reversibility (elastic process) and is defined by

$$\begin{cases} f(\boldsymbol{\sigma}, Z_i, T) < 0 & \text{reversible behaviour} \\ f(\boldsymbol{\sigma}, Z_i, T) = 0 & \text{irreversibility (inelastic process)} \end{cases} \tag{A-106}$$

During yielding and inelastic flow, the Prager's consistency holds, i.e.

$$\dot{f} = 0 \Leftrightarrow \frac{\partial f}{\partial \boldsymbol{\sigma}} \dot{\boldsymbol{\sigma}} + \frac{\partial f}{\partial Z_i} \dot{Z}_i + \frac{\partial f}{\partial T} \dot{T} = 0 \tag{A-107}$$

We note that f can, when necessary, be a function of the internal variables ζ_i instead or besides the driving forces Z_i . An inelastic potential $F = F(\boldsymbol{\sigma}, Z_i, T)$ may be introduced to define the evolution of the inelastic flow through normality rule as

$$\dot{\zeta}_i = \dot{\lambda} \frac{\partial F}{\partial Z_i} \tag{A-108}$$

where $\dot{\lambda} \geq 0$, called the plastic multiplier, must satisfy the Kuhn-Tucker condition $\dot{\lambda} f = 0$. In the case of $f = F$, the plastic flow is said to be associative. Note that the Prager's consistency condition given in Eq.(A-107) gives a mean to obtain this plastic multiplier. The first law of thermodynamic states the local *balance of energy* and can be expressed through the rate of specific internal energy of a system as

$$\rho \dot{e} = \boldsymbol{\sigma} : \dot{\boldsymbol{\varepsilon}} + r - \text{div}(q) \quad \text{where} \quad \begin{cases} q = -k \text{ grad}(T) \text{ is the heat flux} \\ r \text{ is the external heat sources} \end{cases} \quad (\text{A-109})$$

$$\Rightarrow \rho \dot{e} = \boldsymbol{\sigma} : \dot{\boldsymbol{\varepsilon}} + r + k \Delta T \quad \text{where the laplacien operator } \Delta = \text{div}(\text{grad})$$

where ρ is the mass density. The second law of thermodynamics expresses the *irreversibility* of the thermodynamic process and states that the intrinsic dissipation is never negative. This dissipation is not detailed here but leads to the *state laws*, giving the relations between the internal variables and their associated driving forces, the stress and the strain, and the entropy and the temperature, i.e.

$$-\boldsymbol{\sigma} = -\rho \frac{\partial \psi}{\partial \boldsymbol{\varepsilon}}, \quad Z_i = -\rho \frac{\partial \psi}{\partial \zeta_i}, \quad s = -\frac{\partial \psi}{\partial T} \quad (\text{A-110})$$

The relation between internal and free energy given in Eq.(A-105) can be developed to give another expression for the rate of specific internal energy of a system

$$\psi = e - Ts \Rightarrow \dot{e} = \dot{\psi} + \dot{T}s + T\dot{s} \quad \text{with} \quad \begin{cases} \dot{\psi} = \frac{\partial \psi}{\partial \boldsymbol{\varepsilon}} : \dot{\boldsymbol{\varepsilon}} + \frac{\partial \psi}{\partial \zeta_i} \dot{\zeta}_i + \frac{\partial \psi}{\partial T} \dot{T} \\ \dot{s} = -\frac{\partial \dot{\psi}}{\partial T} = -\frac{\partial^2 \psi}{\partial T \partial \boldsymbol{\varepsilon}} : \dot{\boldsymbol{\varepsilon}} - \frac{\partial^2 \psi}{\partial T \partial \zeta_i} \dot{\zeta}_i - \frac{\partial^2 \psi}{\partial^2 T} \dot{T} \\ \dot{T}s = -\frac{\partial \psi}{\partial T} \dot{T} \end{cases} \quad (\text{A-111})$$

$$\Rightarrow \rho \dot{e} = \boldsymbol{\sigma} : \dot{\boldsymbol{\varepsilon}} - T \frac{\partial \boldsymbol{\sigma}}{\partial T} : \dot{\boldsymbol{\varepsilon}} - Z_i \dot{\zeta}_i + T \frac{\partial Z_i}{\partial T} \dot{\zeta}_i + \rho c^{th} \dot{T} \quad \text{with} \quad c^{th} = -T \frac{\partial^2 \psi}{\partial^2 T}$$

Combining the specific internal energy given in Eq.(A-109) and Eq.(A-111) leads to a new version of the *balance equation* and to the so-called *heat equation* giving the evolution of temperature as

$$\boldsymbol{\sigma} : \dot{\boldsymbol{\varepsilon}} + r + k\Delta T = \boldsymbol{\sigma} : \dot{\boldsymbol{\varepsilon}} - T \frac{\partial \boldsymbol{\sigma}}{\partial T} : \dot{\boldsymbol{\varepsilon}} - Z_i \dot{\zeta}_i + T \frac{\partial Z_i}{\partial T} \dot{\zeta}_i + \rho c^{th} \dot{T} \quad (\text{A-112})$$

$$\Rightarrow \rho c^{th} \dot{T} = r + k\Delta T + T \frac{\partial \boldsymbol{\sigma}}{\partial T} : \dot{\boldsymbol{\varepsilon}}^e + A_i^{th} \dot{\zeta}_i \quad \text{with} \quad A_i^{th} = Z_i - T \frac{\partial Z_i}{\partial T}$$

C. Localization condition with infinitesimal strains - solutions

The localization condition (LC) is presented in the Chapter 6.3.2. Here, we aim at finding the critical hardening modulus which enables the localization and the orientation of the localization band given by the vector \underline{n} . The LC given in Eq.(69) and the expression of the hardening modulus h given in Eq.(54) can be combined to obtain the solution to localization in terms of h

$$H = \frac{1}{\mu} (\underline{n} \cdot \boldsymbol{\alpha}) \cdot (\boldsymbol{\beta} \cdot \underline{n}) - \frac{\lambda + \mu}{\mu(\lambda + 2\mu)} (\underline{n} \cdot \boldsymbol{\alpha} \cdot \underline{n}) (\underline{n} \cdot \boldsymbol{\beta} \cdot \underline{n}) \quad (\text{A-113})$$

$$\Rightarrow h = H - \frac{1}{2\mu} \left[\boldsymbol{\alpha} : \boldsymbol{\beta} - \frac{\lambda}{3K} \text{tr}(\boldsymbol{\alpha}) \text{tr}(\boldsymbol{\beta}) \right]$$

The geometrical method used to solve the LC is detailed in the following.

Geometrical method

In the LC, the deviatoric part of the stress state \mathbf{s} is involved only through the variables

$$\begin{cases} \Sigma = \underline{n} \cdot \mathbf{s} \cdot \underline{n} \\ T = (\mathbf{s} \cdot \underline{n}) \cdot (\mathbf{s} \cdot \underline{n}) \end{cases} \quad (\text{A-114})$$

Σ is the normal component of the stress vector in the direction \underline{n} and T is its magnitude. The vector \underline{n} being a unit vector ($n_1^2 + n_2^2 + n_3^2 = 1$), for a given stress \mathbf{s} (defined by its three principal values s_1, s_2, s_3), the variables Σ and T allow to compute the components of \underline{n} as

$$n_i^2 = \frac{T + s_i \Sigma + s_j s_k}{(s_i - s_j)(s_i - s_k)} \quad (\text{A-115})$$

where $(i, j, k) \in \{1, 2, 3\}$ are distinct values. Figure A-0.1 exhibits the admissible stress domain \mathbf{s} in the (Σ, T) space, defined by a triangle corresponding to the three conditions $0 \leq n_k \leq 1$, $k \in [1, 2, 3]$. This domain is just another representation (convenient for the calculations) of the

Mohr diagram usually defined in the (Σ, S) space, where $S = \sqrt{T - \Sigma^2}$ is the tangent component of \underline{s} . When $n_k = 1, n_i = n_j = 0$, the values of Σ and T are uniquely defined and correspond to the vertex \mathbf{p}_k , extremity of the domain \mathbf{s} . When $n_k = 0$, Eq.(A-115) can be interpreted as a straight line L_{ij} between the points \mathbf{p}_i and \mathbf{p}_j , border of the domain \mathbf{s} . To solve the problem of localization, the LC must be satisfied by the stress state \mathbf{s} . This corresponds to inserting the Eq.(A-115) \mathbf{s} into the LC given in Eq.(A-113) and brings a “stress-state-admissible” LC solution for H

$$H = \frac{1}{\mu} [\alpha_1 \beta_1 n_1^2 + \alpha_2 \beta_2 n_2^2 + \alpha_3 \beta_3 n_3^2] - \frac{\lambda + \mu}{\mu(\lambda + 2\mu)} [\alpha_1 n_1^2 + \alpha_2 n_2^2 + \alpha_3 n_3^2] [\beta_1 n_1^2 + \beta_2 n_2^2 + \beta_3 n_3^2] \quad (\text{A-116})$$

where α_k and β_k with $k \in \{1, 2, 3\}$ are the principal values of the tensors $\boldsymbol{\alpha}$ and $\boldsymbol{\beta}$. This equation is a second order polynomial function in Σ and T (through the expressions of n_k) and can be interpreted as a hyperbola curve \mathbf{c} in the (Σ, T) plane.

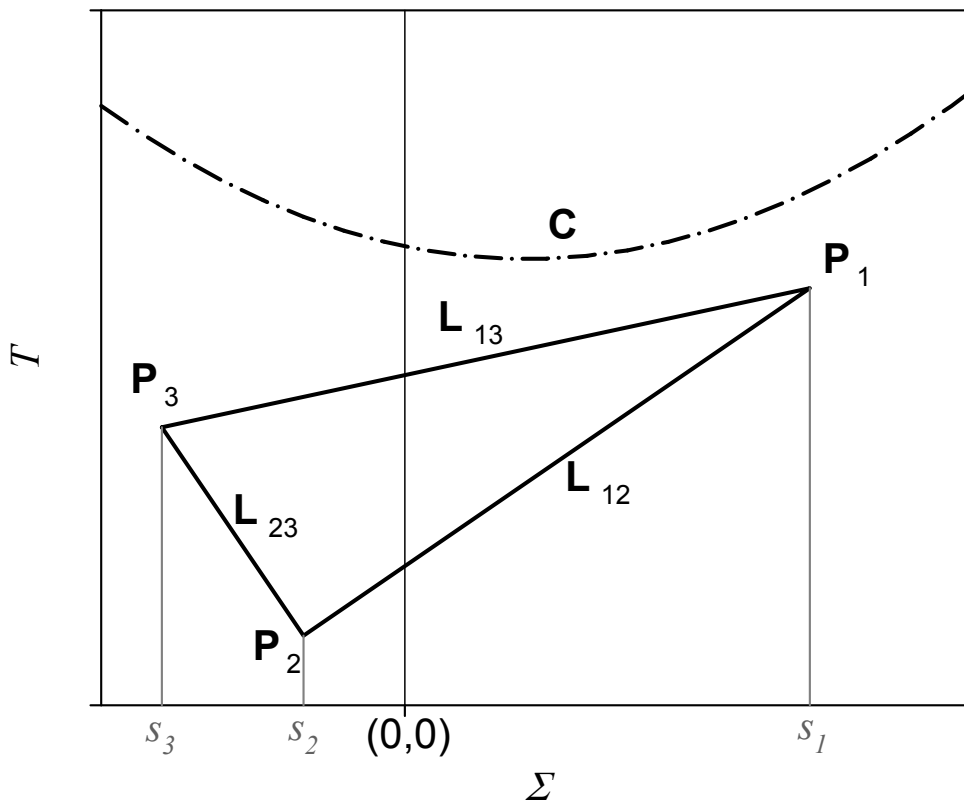


Figure A-0.1. Schematic geometrical interpretation of the localization condition in the (Σ, T) plane.

The resolution of the problem simplifies when the three principal deviatoric stresses are not distinct so three cases will be solved separately. The following presents the case with three distinct principal deviatoric stresses, the case with only two distinct principal deviatoric stresses and finally, the case with all principal stresses equal.

❖ The three principal values of \mathbf{s} are first considered distinct so that $S_{jk} = (s_i - s_j)(s_i - s_k) \neq 0$ and n_k is defined for every $k \in \{1, 2, 3\}$. The solution for H given in Eq.(A-116) comes from two configurations:

- H_k : \mathbf{c} reaches \mathbf{s} at one of its three vertices \mathbf{p}_k
- H_{ij} : \mathbf{c} is tangent to \mathbf{s} (i.e. to one of the sides \mathbf{l}_{ij}) and reaches \mathbf{s}

The first case (H_k) is solved directly using $n_k = 1, n_i = n_j = 0$. The three points \mathbf{p}_k are defined in the (Σ, T) plane by

$$\mathbf{p}_k : \begin{cases} n_i = n_j = 0 \\ n_k = 1 \end{cases} \Leftrightarrow \begin{cases} \Sigma = s_k \\ T = s_k^2 \end{cases} \quad (\text{A-117})$$

After several manipulations, the three corresponding values for H_k are found as

$$H_k = \frac{\alpha_k \beta_k}{\lambda + 2\mu} \quad (\text{A-118})$$

For the second case (H_{ij}), the following methodology must be followed (details i Appendix C)

- Step 1- Obtain explicitly the localization condition LC.
- Step 2- Write the tangency condition between \mathbf{s} and \mathbf{c} .
- Step 3- Write the belonging to \mathbf{s} through a contact condition CC and obtain.
- Step 4- Insure contact and tangency to define a unique solution Σ .
- Step 5- Insert the last solution Σ into LC to obtain the solution H_{ij} .
- Step 6- Insure that the solution Σ belongs to \mathbf{s} (i.e. lies between \mathbf{p}_i and \mathbf{p}_j)

Step 1 of the methodology gives

$$\mu H_{ij} = (\mathbf{a} \cdot \underline{n}) \cdot (\mathbf{b} \cdot \underline{n}) - \frac{\lambda + \mu}{\lambda + 2\mu} (\underline{n} \cdot \mathbf{a} \cdot \underline{n}) (\underline{n} \cdot \mathbf{b} \cdot \underline{n})$$

$$\mathbf{L}_{ij} : \begin{cases} n_i^2 = n \\ n_j^2 = 1 - n \\ n_k = 0 \end{cases} \Rightarrow \begin{cases} \underline{n} \cdot \boldsymbol{\sigma} \cdot \underline{n} = 0 \\ \underline{n} \cdot \mathbf{a} \cdot \underline{n} = (\alpha_i - \alpha_j)n + \alpha_j \\ \underline{n} \cdot \mathbf{b} \cdot \underline{n} = (\beta_i - \beta_j)n + \beta_j \end{cases} \quad (\text{A-119})$$

$$\text{and } \begin{cases} (\mathbf{a} \cdot \underline{n}) \cdot (\mathbf{b} \cdot \underline{n}) = (\alpha_i \beta_i - \alpha_j \beta_j)n + \alpha_j \beta_j \\ (\mathbf{a} \cdot \underline{n}) \cdot (\boldsymbol{\sigma} \cdot \underline{n}) = (\mathbf{b} \cdot \underline{n}) \cdot (\boldsymbol{\sigma} \cdot \underline{n}) = 0 \\ (\mathbf{a} \cdot \underline{n}) \cdot \boldsymbol{\sigma} \cdot (\mathbf{b} \cdot \underline{n}) = 0 \end{cases}$$

Step 1 finally gives a polynomial of second order

$$\mu H_{ij}(\Sigma, T) = h_{T^2} (s_i^2 \Sigma^2 + 2s_i \Sigma T + T^2) + h_{T^1} (s_i \Sigma + T) + h_{T^0}$$

$$\therefore h_{T^2} = -\frac{\lambda + \mu}{\lambda + 2\mu} \frac{(\alpha_i - \alpha_j)(\beta_i - \beta_j)}{[(s_i - s_j)(s_i - s_k)]^2}$$

$$\therefore h_{T^1} = \frac{(\alpha_i \beta_i - \alpha_j \beta_j) - \frac{\lambda + \mu}{\lambda + 2\mu} [\alpha_j (\beta_i - \beta_j) + (\alpha_i - \alpha_j) \beta_j]}{(s_i - s_j)(s_i - s_k)} + 2s_j s_k h_{T^2}$$

$$\therefore h_{T^0} = \frac{\mu}{\lambda + 2\mu} \alpha_j \beta_j + s_j s_k h_{T^1} - (s_j s_k)^2 h_{T^2}$$
(A-120)

Step 2, corresponding to the tangency between \mathbf{c} and the line \mathbf{L}_{ij} , gives

$$\mathbf{L}_{ij} : n_k = 0 \Rightarrow T + s_k \Sigma + s_i s_j = 0$$
(A-121)

$$\begin{cases} \frac{\partial \mathbf{c}}{\partial T} = \xi \frac{\partial \mathbf{L}_{ij}}{\partial T} \\ \frac{\partial \mathbf{c}}{\partial \Sigma} = \xi \frac{\partial \mathbf{L}_{ij}}{\partial \Sigma} \end{cases} \Rightarrow \begin{cases} \frac{\partial \mathbf{c}}{\partial T} = \xi \\ \frac{\partial \mathbf{c}}{\partial \Sigma} = \xi s_k \end{cases} \Leftrightarrow \frac{\partial \mathbf{c}}{\partial T} s_k = \frac{\partial \mathbf{c}}{\partial \Sigma}$$

Step 3 gives the contact between the curve \mathbf{c} and the line \mathbf{L}_{ij} through $n_k = 0$

$$T = -(s_k \Sigma + s_i s_j)$$
(A-122)

Step 4 gives

$$\left\{ \begin{array}{l} \frac{\partial \mathbf{C}}{\partial T} s_k = \frac{\partial \mathbf{C}}{\partial \Sigma} \\ T = -(s_k \Sigma + s_i s_j) \end{array} \right. \quad \text{with} \quad \left\{ \begin{array}{l} \frac{1}{\mu} \frac{\partial \mathbf{C}}{\partial T} = 2h_{T^2} (s_i \Sigma + T) + h_{T^1} \\ \frac{1}{\mu} \frac{\partial \mathbf{C}}{\partial \Sigma} = 2h_{T^2} s_i (s_i \Sigma + T) + s_i h_{T^1} \end{array} \right. \quad (\text{A-123})$$

$$\Rightarrow \Sigma = \frac{2h_{T^2} s_i s_j - h_{T^1}}{2h_{T^2} (s_i - s_k)}$$

Step 4 finally gives the solution for Σ

$$2\Sigma(\alpha_i - \alpha_j)(\beta_i - \beta_j) = \frac{\lambda + 2\mu}{\lambda + \mu} (s_i - s_j)(\alpha_i \beta_i - \alpha_j \beta_j) + (\alpha_i - \alpha_j)(s_j \beta_i - s_i \beta_j) + (\beta_i - \beta_j)(s_j \alpha_i - s_i \alpha_j) \quad (\text{A-124})$$

Step 5 leads to an explicit expression of LC

$$\left\{ \begin{array}{l} \mu H_{ij} = h_{T^2} (s_i^2 \Sigma^2 + 2s_i \Sigma T + T^2) + h_{T^1} (s_i \Sigma + T) + h_{T^0} \\ T = -(s_k \Sigma + s_i s_j) \end{array} \right. \quad (\text{A-125})$$

$$H_{ij} = h_2 \Sigma^2 + h_1 \Sigma + h_0 \quad \text{with} \quad \left\{ \begin{array}{l} h_2 = h_{T^2} (s_i - s_k)^2 \\ h_1 = (h_{T^1} - 2s_i s_j h_{T^2}) (s_i - s_k) \\ h_0 = h_{T^0} - s_i s_j h_{T^1} + (s_i s_j)^2 h_{T^2} \end{array} \right.$$

Combining Eq.(A-123) and Eq.(A-125) gives

$$H_{ij} = \frac{1}{16(\alpha_i - \alpha_j)(\beta_i - \beta_j)} \left\{ \frac{[\alpha_k (\beta_i - \beta_j) + (\alpha_i - \alpha_j) \beta_k]^2}{(\lambda + \mu)} - \frac{[\alpha_k (\beta_i - \beta_j) - (\alpha_i - \alpha_j) \beta_k]^2}{(\lambda + 2\mu)} \right\} + \frac{(\alpha_i - \alpha_j)(\beta_i - \beta_j)}{4\mu} \quad (\text{A-126})$$

Step 6 imposes that the variable Σ lies between s_i and s_j , $s_j \leq \Sigma \leq s_i$, which after several manipulations gives

$$-1 \leq B_{ij} \leq 1 \quad \text{with} \quad B_{ij} = \frac{1}{2} \frac{\lambda + 2\mu}{\lambda + \mu} \frac{\alpha_k (\beta_i - \beta_j) + (\alpha_i - \alpha_j) \beta_k}{(\alpha_i - \alpha_j)(\beta_i - \beta_j)} \quad (\text{A-127})$$

Admissible domains imposed by step 6 are given for the case studies in Appendix F. Then, the normal to the localization band associated to the solutions H_k and H_{ij} are given by

$$\begin{aligned} \therefore n_k &= 1 \\ \therefore n_{ij} &= \frac{(\lambda + 2\mu)}{(\lambda + \mu)} \frac{(\alpha_i \beta_i - \alpha_j \beta_j)}{2(\alpha_i - \alpha_j)(\beta_i - \beta_j)} - \left(\frac{\alpha_j}{2(\alpha_i - \alpha_j)} + \frac{\beta_j}{2(\beta_i - \beta_j)} \right) \end{aligned} \quad (\text{A-128})$$

❖ The case $S_{jk} = 0$ corresponds to a stress state with only two distinct principal values

$$\begin{cases} S_{23} = 0 \\ S_{12} = 0 \end{cases} \Leftrightarrow \begin{cases} s_1 = s_2 > s_3 \text{ (GC)} \\ s_1 > s_2 = s_3 \text{ (GT)} \end{cases} \quad (\text{A-129})$$

These situations can be graphically interpreted as the triangle of Figure A-0.1 reducing to two superimposed lines. The three points \mathbf{p}_k reduce to the two distinct points \mathbf{p}_1 and \mathbf{p}_3 (with $\mathbf{p}_2 \equiv \mathbf{p}_1$ for GC and $\mathbf{p}_2 \equiv \mathbf{p}_3$ for GT). Then, the first set of three solutions H_k reduces to two solutions H_1 and H_3 still defined by Eq.(A-118) (with $H_2 = H_1$ for GC and $H_2 = H_3$ for GT). Also, the three lines \mathbf{L}_{ij} reduce to \mathbf{L}_{13} only ($\mathbf{L}_{23} \equiv \mathbf{L}_{13}$ for GC and $\mathbf{L}_{12} \equiv \mathbf{L}_{13}$ for GT). This solution is still defined by Eq.(A-126). Finally, three solutions for hardening modulus h (h_1, h_3 and h_{13}) can be associated to the three solutions for H (H_1, H_3 and H_{13}).

❖ The case $S_{jk} = S_{ik} = 0$ corresponds to $s_1 = s_2 = s_3 = 0$ and therefore to hydrostatic state of stresses and can be easily handled on its own.

D. Localization condition with finite strains - formulation and solutions

Formulation

The function $\det(\underline{n} \cdot \mathbf{H} \cdot \underline{n} + \mathbf{A}^J)$ must be expressed. The term $\underline{n} \cdot \mathbf{H} \cdot \underline{n} + \mathbf{A}^J$ can be transformed with the methodology used in Appendix A

$$\begin{aligned} \underline{n} \cdot \mathbf{H} \cdot \underline{n} + \mathbf{A}^J &= \underline{n} \cdot \mathbf{E} \cdot \underline{n} - \underline{n} \cdot \frac{\boldsymbol{\alpha} \otimes \boldsymbol{\beta}}{H} \cdot \underline{n} + \mathbf{A}^J = \mathbf{A}^e + \mathbf{A}^J - \frac{1}{H} (\boldsymbol{\alpha} \cdot \underline{n}) \otimes (\boldsymbol{\beta} \cdot \underline{n}) \\ &= (\mathbf{A}^e + \mathbf{A}^J) \cdot \mathbf{B}^J \end{aligned} \quad (\text{A-130})$$

$$\text{with } \begin{cases} \mathbf{A}^J = \frac{1}{2} [(\underline{n} \cdot \boldsymbol{\sigma} \cdot \underline{n}) \mathbf{I} + \boldsymbol{\sigma} \cdot \underline{n} \otimes \underline{n} - \underline{n} \otimes \underline{n} \cdot \boldsymbol{\sigma} - \boldsymbol{\sigma}] \\ \mathbf{B}^J = \mathbf{I} - \frac{1}{H} (\mathbf{A}^e + \mathbf{A}^J)^{-1} \cdot (\boldsymbol{\alpha} \cdot \underline{n}) \otimes (\boldsymbol{\beta} \cdot \underline{n}) \end{cases}$$

Then, the determinant is

$$\det(\underline{n} \cdot \mathbf{H} \cdot \underline{n} + \mathbf{A}^J) = \det(\mathbf{A}^e + \mathbf{A}^J) \det \mathbf{B}^J \quad (\text{A-131})$$

Since \mathbf{A}^J is small compared to $(\mathbf{A}^e)^{-1}$, one can assume that $\det(\mathbf{A}^e + \mathbf{A}^J) > 0$. Therefore, as presented in Chapter 6.3.2, the second determinant of the right hand side of this last equation is

$$\begin{aligned} \det \mathbf{B}^J = B_3^J &= 1 - \frac{1}{H^J} (\underline{\alpha} \cdot \underline{n}) \cdot (\mathbf{A}^e + \mathbf{A}^J)^{-1} \cdot (\underline{\beta} \cdot \underline{n}) \\ \det \mathbf{B}^J = 0 &\Rightarrow H^J = (\underline{\alpha} \cdot \underline{n}) \cdot (\mathbf{A}^e + \mathbf{A}^J)^{-1} \cdot (\underline{\beta} \cdot \underline{n}) \end{aligned} \quad (\text{A-132})$$

with

$$(\mathbf{A}^e + \mathbf{A}^J)^{-1} = \left(\mathbf{A}^e \cdot \left(\mathbf{I} + (\mathbf{A}^e)^{-1} \cdot \mathbf{A}^J \right) \right)^{-1} = \left(\mathbf{I} + (\mathbf{A}^e)^{-1} \cdot \mathbf{A}^J \right)^{-1} \cdot (\mathbf{A}^e)^{-1} \quad (\text{A-133})$$

Since $(\mathbf{A}^e)^{-1} \cdot \mathbf{A}^J$ is small compared to \mathbf{I} , one can use the approximation given by Rice (1976): $(\mathbf{I} - \mathbf{M})^{-1} = \mathbf{I} + \mathbf{M} + \mathbf{M} \cdot \mathbf{M} + \dots$ when \mathbf{M} is small. A first order approximation gives

$$(\mathbf{A}^e + \mathbf{A}^J)^{-1} = (\mathbf{A}^e)^{-1} - (\mathbf{A}^e)^{-1} \cdot \mathbf{A}^J \cdot (\mathbf{A}^e)^{-1} \quad (\text{A-134})$$

The explicit expression of the second right-hand term is

$$\begin{aligned} (\mathbf{A}^e)^{-1} \cdot \mathbf{A}^J \cdot (\mathbf{A}^e)^{-1} &= \frac{1}{\mu} \frac{(\underline{n} \cdot \underline{\sigma} \cdot \underline{n})}{2\mu} \mathbf{I} - \frac{\lambda + \mu}{\mu(\lambda + 2\mu)} \frac{(\underline{n} \cdot \underline{\sigma} \cdot \underline{n})}{\mu} \underline{n} \otimes \underline{n} \\ &+ \frac{1}{2\mu^2} \left[\underline{\sigma} \cdot \underline{n} \otimes \underline{n} + \frac{\lambda}{(\lambda + 2\mu)} \underline{n} \otimes \underline{n} \cdot \underline{\sigma} - \underline{\sigma} \right] \end{aligned} \quad (\text{A-135})$$

The 4th order tensor given in Eq.(A-133) becomes

$$\begin{aligned} (\mathbf{A}^e + \mathbf{A}^J)^{-1} &= \frac{1}{\mu} \mathbf{I} \left[1 - \frac{(\underline{n} \cdot \underline{\sigma} \cdot \underline{n})}{2\mu} \right] - \frac{\lambda + \mu}{\mu(\lambda + 2\mu)} \underline{n} \otimes \underline{n} \left[1 - \frac{(\underline{n} \cdot \underline{\sigma} \cdot \underline{n})}{\mu} \right] \\ &- \frac{1}{2\mu^2} \left[\underline{\sigma} \cdot \underline{n} \otimes \underline{n} + \frac{\lambda}{(\lambda + 2\mu)} \underline{n} \otimes \underline{n} \cdot \underline{\sigma} - \underline{\sigma} \right] \end{aligned} \quad (\text{A-136})$$

The LC becomes then

$$H^J = \frac{1}{\mu} (\underline{\alpha} \cdot \underline{n}) \cdot (\underline{\beta} \cdot \underline{n}) \left[1 - \frac{\underline{n} \cdot \underline{\sigma} \cdot \underline{n}}{2\mu} \right] - \frac{\lambda + \mu}{\mu(\lambda + 2\mu)} (\underline{n} \cdot \underline{\alpha} \cdot \underline{n}) (\underline{n} \cdot \underline{\beta} \cdot \underline{n}) \left[1 - \frac{\underline{n} \cdot \underline{\sigma} \cdot \underline{n}}{\mu} \right] - \frac{1}{2\mu^2} \left[(\underline{n} \cdot \underline{\beta} \cdot \underline{n}) (\underline{\alpha} \cdot \underline{n}) \cdot (\underline{\sigma} \cdot \underline{n}) + \frac{\lambda \underline{n} \cdot \underline{\alpha} \cdot \underline{n}}{\lambda + 2\mu} (\underline{\sigma} \cdot \underline{n}) \cdot (\underline{\beta} \cdot \underline{n}) - (\underline{\alpha} \cdot \underline{n}) \cdot \underline{\sigma} \cdot (\underline{\beta} \cdot \underline{n}) \right] \quad (\text{A-137})$$

Analogically to Eq.(A-113), the LC becomes

$$H^J = H - \frac{1}{2\mu^2} \left[(\underline{n} \cdot \underline{\sigma} \cdot \underline{n}) (\underline{n} \cdot \underline{\alpha}) \cdot (\underline{\beta} \cdot \underline{n}) - \frac{2(\lambda + \mu)}{\lambda + 2\mu} (\underline{n} \cdot \underline{\sigma} \cdot \underline{n}) (\underline{n} \cdot \underline{\alpha} \cdot \underline{n}) (\underline{n} \cdot \underline{\beta} \cdot \underline{n}) + (\underline{n} \cdot \underline{\beta} \cdot \underline{n}) (\underline{n} \cdot \underline{\alpha}) \cdot (\underline{\sigma} \cdot \underline{n}) + \frac{\lambda}{\lambda + 2\mu} (\underline{n} \cdot \underline{\alpha} \cdot \underline{n}) (\underline{n} \cdot \underline{\sigma}) \cdot (\underline{\beta} \cdot \underline{n}) - (\underline{n} \cdot \underline{\alpha}) \cdot \underline{\sigma} \cdot (\underline{\beta} \cdot \underline{n}) \right] \quad (\text{A-138})$$

where H is the critical value found in Eq.(A-113). Note that with the large deformations formulation, the value of the critical modulus is a function of the stress state $\underline{\sigma}$. The methodology to solve the LC previously and detailed in Appendix C is again followed but the situation is now more complex and we assume that the stress is coaxial with the constitutive tensors $\underline{\alpha} \cdot \underline{n}$ and $\underline{\beta} \cdot \underline{n}$.

Geometrical method

The LC can be expressed in the (Σ, T) space with the vector \underline{n} still defined by Eq.(A-115).

The LC given in Eq.(A-116), now of third order since $(n_i^2)^3$ is involved, becomes

$$H^J = h_{\Sigma^3}^J \Sigma^3 + h_{\Sigma^2 T}^J \Sigma^2 T + h_{\Sigma T^2}^J \Sigma T^2 + h_{T^3}^J T^3 + h_{\Sigma^2}^J \Sigma^2 + h_{\Sigma T}^J \Sigma T + h_{T^2}^J T^2 + h_{\Sigma}^J \Sigma + h_T^J T + h_{T^0}^J \quad (\text{A-139})$$

❖ With three distinct principal deviatoric stresses, the two sets of three solutions coming from contact with \mathbf{p}_k and tangency with \mathbf{L}_{ij} must be considered again. The first set of three solutions

H_k ($n_k = 1$) reads now

$$\mathbf{p}_k : \begin{cases} \Sigma = \underline{n} \cdot \underline{\mathbf{s}} \cdot \underline{n} = s_k \\ T = \underline{s} \cdot \underline{s} = s_k^2 \\ n_k^2 = 1, n_i^2 = n_j^2 = 0 \end{cases} \Rightarrow \begin{cases} \underline{n} \cdot \underline{\sigma} \cdot \underline{n} = \sigma_k \\ \underline{n} \cdot \underline{\alpha} \cdot \underline{n} = \alpha_k \\ \underline{n} \cdot \underline{\beta} \cdot \underline{n} = \beta_k \end{cases} \quad \text{and} \quad \begin{cases} (\underline{\alpha} \cdot \underline{n}) \cdot (\underline{\beta} \cdot \underline{n}) = \alpha_k \beta_k \\ (\underline{\alpha} \cdot \underline{n}) \cdot (\underline{\sigma} \cdot \underline{n}) = \alpha_k \sigma_k \\ (\underline{\beta} \cdot \underline{n}) \cdot (\underline{\sigma} \cdot \underline{n}) = \beta_k \sigma_k \\ (\underline{\alpha} \cdot \underline{n}) \cdot \underline{\sigma} \cdot (\underline{\beta} \cdot \underline{n}) = \sigma_k \alpha_k \beta_k \end{cases} \quad (\text{A-140})$$

$$\Rightarrow H_k^J = H_k = \frac{\alpha_k \beta_k}{\lambda + 2\mu}$$

For the second set of solutions H_{ij} coming from the tangency with \mathbf{l}_{ij} , some useful expressions are given here

$$\mathbf{l}_{ij} : \begin{cases} n_i^2 = n \\ n_j^2 = 1 - n, \\ n_k = 0 \end{cases} \begin{cases} \underline{n} \cdot \underline{\sigma} \cdot \underline{n} = (\sigma_i - \sigma_j)n + \sigma_j \\ \underline{n} \cdot \underline{\alpha} \cdot \underline{n} = (\alpha_i - \alpha_j)n + \alpha_j, \\ \underline{n} \cdot \underline{\beta} \cdot \underline{n} = (\beta_i - \beta_j)n + \beta_j \end{cases}$$

$$\begin{cases} (\underline{\alpha} \cdot \underline{n}) \cdot (\underline{\beta} \cdot \underline{n}) = (\alpha_i \beta_i - \alpha_j \beta_j)n + \alpha_j \beta_j \\ (\underline{\alpha} \cdot \underline{n}) \cdot (\underline{\sigma} \cdot \underline{n}) = (\alpha_i \sigma_i - \alpha_j \sigma_j)n + \alpha_j \sigma_j \\ (\underline{\beta} \cdot \underline{n}) \cdot (\underline{\sigma} \cdot \underline{n}) = (\beta_i \sigma_i - \beta_j \sigma_j)n + \beta_j \sigma_j \\ (\underline{\alpha} \cdot \underline{n}) \cdot \underline{\sigma} \cdot (\underline{\beta} \cdot \underline{n}) = (\alpha_i \beta_i \sigma_i - \alpha_j \beta_j \sigma_j)n + \alpha_j \beta_j \sigma_j \end{cases} \quad (\text{A-141})$$

Step 1 finally gives a polynomial of third order

$$2\mu^2 H_{ij}^J(\Sigma, T) = h_{T^3}^J (s_i^3 \Sigma^3 + 3s_i^2 \Sigma^2 T + 3s_i \Sigma T^2 + T^3) \\ + h_{T^2}^J (s_i^2 \Sigma^2 + 2s_i \Sigma T + T^2) + h_{T^1}^J (s_i \Sigma + T) + h_{T^0}^J$$

$$\begin{cases} h_{T^3}^J = 2 \frac{\lambda + \mu (\alpha_i - \alpha_j)(\beta_i - \beta_j)}{\lambda + 2\mu (s_i - s_j)^2 (s_i - s_k)^3} \\ h_{T^2}^J = \frac{Z\alpha_j - W\alpha_i}{(s_i - s_j)(s_i - s_k)^2} (\beta_i - \beta_j) - 2\mu \frac{(\alpha_i - \alpha_j)(\beta_i - \beta_j)}{(s_i - s_j)^2 (s_i - s_k)^2} + 3s_j s_k h_{T^3}^J \\ h_{T^1}^J = \frac{\alpha_i - \frac{\lambda}{\lambda + 2\mu} \alpha_j}{(s_i - s_k)} (\beta_i - \beta_j) \\ \quad + 2\mu \frac{(\alpha_i \beta_i - \alpha_j \beta_j) - \frac{\lambda + \mu}{\lambda + 2\mu} (\alpha_j (\beta_i - \beta_j) + (\alpha_i - \alpha_j) \beta_j)}{(s_i - s_j)(s_i - s_k)} \\ \quad + 2s_j s_k h_{T^2}^J - 3(s_j s_k)^2 h_{T^3}^J \\ h_{T^0}^J = 2\mu \frac{\mu}{\lambda + 2\mu} \alpha_j \beta_j + s_j s_k h_{T^1}^J - (s_j s_k)^2 h_{T^2}^J + (s_j s_k)^3 h_{T^3}^J \end{cases} \quad (\text{A-142})$$

Steps 2 and 3 give the same tangency condition and contact condition as given in Appendix C. However, the derivatives of LC involved in TC are changed owing to the Jaumann formulation.

$$\begin{cases} \frac{\partial \mathbf{c}^J}{\partial T} s_k = \frac{\partial \mathbf{c}^J}{\partial \Sigma} \\ T = -(s_k \Sigma + s_i s_j) \end{cases},$$

$$\begin{cases} \frac{\partial \mathbf{c}^J}{\partial T} = 3h_{T^3}^J (s_i^2 \Sigma^2 + 2s_i \Sigma T + T^2) + 2h_{T^2}^J (s_i \Sigma + T) + h_{T^1}^J \\ \frac{\partial \mathbf{c}^J}{\partial \Sigma} = 3h_{T^3}^J s_i (s_i^2 \Sigma^2 + 2s_i \Sigma T + T^2) + 2h_{T^2}^J s_i (s_i \Sigma + T) + s_i h_{T^1}^J \end{cases}$$

(A-143)

$$\Rightarrow \varepsilon_{\Sigma^2} \Sigma^2 + \varepsilon_{\Sigma} \Sigma + \varepsilon_0 = 0$$

$$\begin{cases} \varepsilon_{\Sigma^2} = 3h_{T^3}^J (s_i - s_k)^3 \\ \varepsilon_{\Sigma} = 2(h_{T^2}^J - 3h_{T^3}^J s_i s_j)(s_i - s_k)^2 \\ \varepsilon_0 = (h_{T^1}^J - 2h_{T^2}^J s_i s_j + 3h_{T^3}^J (s_i s_j)^2)(s_i - s_k) \end{cases}$$

Step 4 is solution of a second order polynomial

$$\Sigma^J = \frac{-\varepsilon_{\Sigma} \pm \sqrt{\Delta}}{2\varepsilon_{\Sigma^2}} \quad \text{with} \quad \Delta = \varepsilon_{\Sigma}^2 - 4\varepsilon_{\Sigma^2} \varepsilon_0$$

(A-144)

Step 5 becomes

$$\begin{cases} 2\mu^2 H_{ij}^J = h_{T^3}^J (s_i^3 \Sigma^3 + 3s_i^2 \Sigma^2 T + 3s_i \Sigma T^2 + T^3) \\ \quad + h_{T^2}^J (s_i^2 \Sigma^2 + 2s_i \Sigma T + T^2) + h_{T^1}^J (s_i \Sigma + T) + h_{T^0}^J \\ T = -(s_k \Sigma + s_i s_j) \end{cases}$$

$$\Rightarrow H_{ij}^J = h_3^J \Sigma^3 + h_2^J \Sigma^2 + h_1^J \Sigma + h_0^J$$

(A-145)

$$\begin{cases} h_3^J = h_{T^3}^J (s_i - s_k)^3 \\ h_2^J = (h_{T^2}^J - 3(s_i s_j) h_{T^3}^J)(s_i - s_k)^2 \\ h_1^J = (h_{T^1}^J - 2(s_i s_j) h_{T^2}^J + 3(s_i s_j)^2 h_{T^3}^J)(s_i - s_k) \\ h_0^J = h_{T^0}^J - (s_i s_j) h_{T^1}^J + (s_i s_j)^2 h_{T^2}^J - (s_i s_j)^3 h_{T^3}^J \end{cases}$$

The expression of H_{ij}^J as a function of α_k and β_k is not given for sake of simplicity, and was only computed numerically.

E. Localization condition with adiabatic conditions - formulation

As a recall from Chapter 6.3.1, the rate constitutive behaviour under adiabatic conditions is

$$\dot{\boldsymbol{\sigma}} = \mathbf{L}^a : \dot{\boldsymbol{\varepsilon}}, \quad \mathbf{L}^a = \begin{cases} \mathbf{E}^a & \text{if } f < 0 \text{ or } f = 0 \text{ and } \dot{f} < 0, \\ \mathbf{H}^a = \mathbf{E}^a - \frac{\boldsymbol{\beta}^a \otimes \boldsymbol{\alpha}^a}{h^a + \frac{\partial f}{\partial \boldsymbol{\sigma}} : \mathbf{E}^i : \frac{\partial F}{\partial \boldsymbol{\sigma}}} & \text{if } f = 0 \text{ and } \dot{f} = 0, \end{cases}$$

$$\text{with } \begin{cases} \boldsymbol{\alpha}^a = \boldsymbol{\alpha}^i + \frac{3KT\alpha^{th}}{\rho c^{th}} \left(6K\alpha^{th} \frac{\partial f}{\partial \boldsymbol{\sigma}} : \mathbf{I} - \frac{\partial f}{\partial \kappa^a} \frac{\partial \kappa^a}{\partial T} \right) \mathbf{I} \\ \boldsymbol{\beta}^a = \boldsymbol{\beta}^i + \frac{3K\alpha^{th}}{\rho c^{th}} \left((\boldsymbol{\sigma} + 3KT\alpha^{th} \mathbf{I}) : \frac{\partial F}{\partial \boldsymbol{\sigma}} + \left(\kappa^a - T \frac{\partial \kappa^a}{\partial T} \right) \frac{\partial F}{\partial \kappa^a} \right) \mathbf{I} \end{cases} \quad (\text{A-146})$$

$$\text{with } \begin{cases} \mathbf{E}^a = \mathbf{E}^i + \frac{9(K\alpha^{th})^2}{\rho c^{th}} \mathbf{I} \otimes \mathbf{I} \\ h^a = h^i + \frac{A_i^{th}}{\rho c^{th}} \frac{\partial F}{\partial Z_i} \left(6K\alpha^{th} \frac{\partial f}{\partial \boldsymbol{\sigma}} : \mathbf{I} - \frac{\partial f}{\partial \kappa^a} \frac{\partial \kappa^a}{\partial T} \right) \end{cases}$$

Formulation

The localization condition $\det(\underline{\mathbf{n}} \cdot \mathbf{H}^a \cdot \underline{\mathbf{n}}) = 0$ can be transformed into

$$\underline{\mathbf{n}} \cdot \mathbf{H}^a \cdot \underline{\mathbf{n}} = \mathbf{A}^{ae} \cdot \mathbf{B}^a, \quad \begin{cases} \mathbf{A}^{ae} = \underline{\mathbf{n}} \cdot \mathbf{E}^a \cdot \underline{\mathbf{n}} \\ \mathbf{B}^a = \mathbf{I} - \frac{1}{H^a} (\mathbf{A}^{ae})^{-1} (\boldsymbol{\alpha}^a \cdot \underline{\mathbf{n}}) \otimes (\boldsymbol{\beta}^a \cdot \underline{\mathbf{n}}) \end{cases} \quad (\text{A-147})$$

The multiplicative property of the determinant transforms the localization condition (LC) into

$$\det \mathbf{A}^{ae} \det \mathbf{B}^a = 0 \quad (\text{A-148})$$

It is shown in Appendix A that $\det(\mathbf{A}^{ae})$ is strictly positive since the temperature T (and consequently λ^a) is positive. Therefore, as presented in Chapter 6.3.2, the second determinant of the left hand side of this last equation is

$$\det \mathbf{B}^a = B_3^a, \quad B_3^a = 1 - \frac{1}{H^a} (\boldsymbol{\alpha}^a \cdot \underline{\mathbf{n}}) \cdot (\mathbf{A}^{ae})^{-1} \cdot (\boldsymbol{\beta}^a \cdot \underline{\mathbf{n}})$$

$$\det \mathbf{B}^a = 0 \Rightarrow H^a = (\boldsymbol{\alpha}^a \cdot \underline{\mathbf{n}}) \cdot (\mathbf{A}^{ae})^{-1} \cdot (\boldsymbol{\beta}^a \cdot \underline{\mathbf{n}}) \quad (\text{A-149})$$

Analogically to Eq.(A-113), the LC becomes

$$H^a = \frac{1}{\mu} (\boldsymbol{\alpha}^a \cdot \underline{\mathbf{n}}) \cdot (\boldsymbol{\beta}^a \cdot \underline{\mathbf{n}}) - \frac{\lambda^a + \mu}{\mu(\lambda^a + 2\mu)} (\underline{\mathbf{n}} \cdot \boldsymbol{\alpha}^a \cdot \underline{\mathbf{n}}) (\underline{\mathbf{n}} \cdot \boldsymbol{\beta}^a \cdot \underline{\mathbf{n}}) \quad (\text{A-150})$$

F. Particular yield functions

Hershey yield function

The chosen Hershey yield function f can be expressed in the following way

$$\begin{cases} f(\mathbf{s}) = \left\{ \frac{1}{2} \left[(s_1 - s_2)^m + (s_2 - s_3)^m + (s_3 - s_1)^m \right] \right\}^{\frac{1}{m}} - \sigma_0 \\ s_1 = \frac{\sigma_{eq}}{3} (\sqrt{3}c_L - s_L), \quad s_2 = \frac{2\sigma_{eq}}{3} s_L, \quad s_3 = \frac{\sigma_{eq}}{3} (-\sqrt{3}c_L - s_L) \end{cases} \quad (\text{A-151})$$

$$\Rightarrow \begin{cases} f(\sigma_{eq}, \theta_L) = \frac{\sigma_{eq}}{3} [f'_L]^{\frac{1}{m}} - \sigma_0 \\ f'_L = \frac{3^{\frac{m}{2}}}{2} \left[(c_L - \sqrt{3}s_L)^m + (2c_L)^m + (c_L + \sqrt{3}s_L)^m \right] \end{cases}$$

with $c_L = \cos \theta_L$ and $s_L = \sin \theta_L$. Its derivative is then

$$\frac{\partial f}{\partial \boldsymbol{\sigma}} = \frac{\partial f}{\partial \sigma_{eq}} \frac{\partial \sigma_{eq}}{\partial \boldsymbol{\sigma}} + \frac{\partial f}{\partial \theta_L} \frac{\partial \theta_L}{\partial \boldsymbol{\sigma}} \quad (\text{A-152})$$

In particular,

$$\begin{cases} \frac{\partial f}{\partial \sigma_{eq}} = \frac{1}{3} [f'_L]^{\frac{1}{m}} & \left\{ \begin{array}{l} \frac{\partial f}{\partial \theta_L} = -\frac{\bar{\sigma}}{3} [f'_L]^{\frac{1}{m}-1} f''_L \\ \frac{\partial \sin(3\theta_L)}{\partial \boldsymbol{\sigma}} = \frac{\partial(-\xi)}{\partial \boldsymbol{\sigma}} \Rightarrow 3c_{3L} \frac{\partial \theta_L}{\partial \boldsymbol{\sigma}} = \frac{-27}{2} \left(\frac{s_{3L}}{3} \frac{\mathbf{s}}{\bar{\sigma}^2} + \frac{\mathbf{S}}{\bar{\sigma}^3} \right) \end{array} \right. \\ \frac{\partial \sigma_{eq}}{\partial \boldsymbol{\sigma}} = \frac{3}{2} \frac{\mathbf{s}}{\bar{\sigma}} & \\ \mathbf{S} = \frac{\partial J_3}{\partial \boldsymbol{\sigma}} = \mathbf{s} \cdot \mathbf{s} - \frac{\text{tr}(\mathbf{s} \cdot \mathbf{s})}{3} \mathbf{I} = \mathbf{s} \cdot \mathbf{s} - \frac{2\sigma_{eq}^2}{9} \mathbf{I} & \\ f''_L = \frac{3^{\frac{m}{2}}}{2} \left[(s_L + \sqrt{3}c_L)(c_L - \sqrt{3}s_L)^{2m-1} + 2^m s_L c_L^{2m-1} + (s_L - \sqrt{3}c_L)(c_L + \sqrt{3}s_L)^{2m-1} \right] & \end{cases} \quad (\text{A-153})$$

with $c_{3L} = \cos(3\theta_L)$ and $s_{3L} = \sin(3\theta_L)$. The normalized deviatoric stress tensor $\mathbf{N} = \mathbf{s}/\sigma_{eq}$ is defined

$$\begin{cases} \sum_{i=1}^3 N_i = 0 \\ \sum_{i=1}^3 N_i^2 = \frac{2}{3} \end{cases} \Rightarrow \mathbf{N} = \begin{bmatrix} \frac{-N + \sqrt{\frac{4}{3} - 3N^2}}{2} & 0 & 0 \\ 0 & N & 0 \\ 0 & 0 & \frac{-N - \sqrt{\frac{4}{3} - 3N^2}}{2} \end{bmatrix} \quad (\text{A-154})$$

where $N = \frac{2}{3}s_L$ is a picture of the Lode parameter in a similar way as in Benallal and Comi (1993), i.e.

$$N = \frac{2\mu_L}{3\sqrt{\mu_L^2 + 3}} \Leftrightarrow \theta_L = \arcsin\left(\frac{3}{2}N\right), \quad \mu_L = \frac{3\sqrt{3}N}{\sqrt{4 - 9N^2}} \quad (155)$$

Using $\mathbf{N}_2 = \mathbf{S}/\sigma_{eq}^2 = \mathbf{N} \cdot \mathbf{N} - \frac{2}{9}\mathbf{I}$ and gathering the four terms given in Eq.(A-153), the derivative of f is

$$\frac{\partial f}{\partial \boldsymbol{\sigma}} = \chi' \mathbf{N} + \chi'' \mathbf{N}_2 \quad \text{with} \quad \begin{cases} \chi' = \frac{f_L'^{\frac{1}{m}}}{2} \left[1 + t_{3L} \frac{f_L''}{f_L'} \right] \\ \chi'' = \frac{f_L'^{\frac{1}{m}}}{2} \left[\frac{3}{c_{3L}} \frac{f_L''}{f_L'} \right] \end{cases} \quad (\text{A-156})$$

with $t_{3L} = \tan(3\theta_L)$. The second order tensors \mathbf{N} , \mathbf{N}_2 (and consequently \mathbf{s} , \mathbf{S} and the derivative of f) are defined by the variable N , which is a picture of the Lode angle θ_L . The term $\boldsymbol{\alpha}$ becomes then

$$\boldsymbol{\alpha} = \mathbf{E} : \frac{\partial f}{\partial \boldsymbol{\sigma}} = \alpha' \mathbf{N} + \alpha'' \mathbf{N}_2 \quad \text{with} \quad \begin{cases} \alpha'(\theta_L, m) = 2\mu\chi' = \mu f_L'^{\frac{1}{m}} \left[1 + t_{3L} \frac{f_L''}{f_L'} \right] \\ \alpha''(\theta_L, m) = 2\mu\chi'' = \mu f_L'^{\frac{1}{m}} \left[\frac{3}{c_{3L}} \frac{f_L''}{f_L'} \right] \end{cases} \quad (\text{A-157})$$

The tensor $\boldsymbol{\alpha}$ is deviatoric, pressure-independent and independent of the equivalent stress σ_{eq} .

For the CASE 1, described in Chapter 6.3.2 (associative plastic flow), the localization condition LC is, as the tensor $\boldsymbol{\alpha}$, a function of the Lode angle θ_L only (i.e. μ_L and N). By combining the two sets of solutions (Eq.(A-118) and Eq.(A-126)) with the Eq.(A-113), the six hardening moduli h_k and h_{ij} are found for an associated model with pressure independent yield function

$$\begin{aligned}\therefore h_k &= \frac{\alpha_k^2}{\lambda + 2\mu} - \frac{1}{2\mu} \left[\frac{2}{27} \alpha'^2 + \frac{2}{3} \alpha''^2 + 2\alpha' \alpha'' (3N^3 - N) \right] \\ \therefore h_{ij} &= \frac{\alpha_k^2}{4(\lambda + \mu)} + \frac{\alpha_{i-j}^2}{4\mu} - \frac{1}{2\mu} \left[\frac{2}{27} \alpha'^2 + \frac{2}{3} \alpha''^2 + 2\alpha' \alpha'' (3N^3 - N) \right]\end{aligned}\quad (\text{A-158})$$

Hershey yield function with pressure-dependency

The previous yield function is now enriched by a pressure-dependence term f_0 so

$$f(\sigma_{eq}, \theta_L, \sigma_H) = \frac{\sigma_{eq}}{3} [f'_L]^{\frac{1}{m}} + f_0 \sigma_H - \sigma_0 \quad (\text{A-159})$$

The derivative of this yield function becomes

$$\begin{aligned}\frac{\partial f}{\partial \boldsymbol{\sigma}} &= \frac{\partial f}{\partial \sigma_H} \frac{\partial \sigma_H}{\partial \boldsymbol{\sigma}} + \frac{\partial f}{\partial \sigma_{eq}} \frac{\partial \sigma_{eq}}{\partial \boldsymbol{\sigma}} + \frac{\partial f}{\partial \theta_L} \frac{\partial \theta_L}{\partial \boldsymbol{\sigma}} \quad \text{with} \quad \frac{\partial \sigma_H}{\partial \boldsymbol{\sigma}} = \frac{1}{3} \mathbf{I} \\ \Rightarrow \frac{\partial f}{\partial \boldsymbol{\sigma}} &= \chi_0 \mathbf{I} + \chi' \mathbf{N} + \chi'' \mathbf{N}_2 \quad \text{with} \quad \chi_0 = \frac{f_0}{3}\end{aligned}\quad (\text{A-160})$$

Then the term $\boldsymbol{\alpha}$ becomes

$$\boldsymbol{\alpha} = \alpha_0 \mathbf{I} + \alpha' \mathbf{N} + \alpha'' \mathbf{N}_2 \quad \text{with} \quad \begin{cases} \alpha_0 = (2\mu + 3\lambda) \chi_0 = Kf_0 \\ \alpha'(\theta_L, m) = 2\mu \chi' = \mu f_L'^{\frac{1}{m}} \left[1 + t_{3L} \frac{f_L''}{f_L'} \right] \\ \alpha''(\theta_L, m) = 2\mu \chi'' = \mu f_L'^{\frac{1}{m}} \left[\frac{3}{c_{3L}} \frac{f_L''}{f_L'} \right] \end{cases} \quad (\text{A-161})$$

where α_0 is directly related to the pressure-dependence term f_0 .

Contrary to the CASE 1, the CASE 3 applies the non-associative plastic flow so $f \neq F$, $\boldsymbol{\alpha} \neq \boldsymbol{\beta}$ and the expression of $\boldsymbol{\alpha}$ and $\boldsymbol{\beta}$ are now stated

$$\begin{cases} \boldsymbol{\alpha} = \alpha' \mathbf{N} + \alpha'' \mathbf{N}_2 + \alpha_0 \mathbf{I} \\ \boldsymbol{\beta} = \alpha' \mathbf{N} + \alpha'' \mathbf{N}_2 \end{cases} \Rightarrow \begin{cases} \alpha_k = a_k + \alpha_0 \\ \beta_k = b_k = a_k \end{cases} \quad \text{with} \quad a_k = \alpha' N_k + \alpha'' \left(N_k^2 - \frac{2}{9} \right) \quad (\text{A-162})$$

With a Hershey-shaped pressure-independent plastic flow (non-associative), the solutions for hardening modulus h become

$$\begin{aligned}
\therefore h_k &= \frac{(a_k + \alpha_0)a_k}{\lambda + 2\mu} - \frac{1}{2\mu} \left[\frac{2}{27} \alpha'^2 + \frac{2}{3} \alpha''^2 + 2\alpha' \alpha'' (3N^3 - N) \right] \\
\therefore h_{ij} &= \frac{(\alpha_0 - a_k)^2}{4(\lambda + \mu)} + \frac{(a_i - a_j)^2}{4\mu} - \frac{\alpha_0^2}{4(\lambda + 2\mu)} \\
&\quad - \frac{1}{2\mu} \left[\frac{2}{27} \alpha'^2 + \frac{2}{3} \alpha''^2 + 2\alpha' \alpha'' (3N^3 - N) \right]
\end{aligned} \tag{A-163}$$

A value of f_0 can be computed for the AA7075-T651

$$\begin{cases} \sigma_T & \text{yielding under uniaxial tension (UT)} \\ \sigma_C = (1 + d_{TC}) \sigma_T & \text{yielding under uniaxial compression (UC)} \end{cases}$$

$$f \Rightarrow \begin{cases} \sigma_T \left(1 + \frac{f_0}{3} \right) = \sigma_0 \\ \sigma_C \left(1 - \frac{f_0}{3} \right) = \sigma_0 \end{cases} \Rightarrow \begin{cases} \sigma_T = \frac{2 + d_{TC}}{2 + 2d_{TC}} \sigma_0 \\ f_0 = \frac{3d_{TC}}{2 + d_{TC}} \end{cases} \xrightarrow{d_{TC}=0.01} \begin{cases} f_0 = 0.015 \\ \alpha_0 = 870 \text{ MPa} \end{cases} \tag{A-164}$$

where d_{TC} , the percentage of difference between σ_{YC} and σ_{YT} , is taken equal to 1% for a realistic (though imaginary) case.

Admissibility domains of H_{ij} for Hersey yield function

For the associated case (CASE 1), the admissibility of the solutions h_{ij} given in Appendix C simplifies, and intervals of admissibility are given by

$$-1 \leq \frac{\lambda + 2\mu}{\lambda + \mu} \frac{\alpha_k}{\alpha_{i-j}} \leq 1 \tag{A-165}$$

For non-associated case with a pressure-dependant flow stress for instance (CASE 3), the admissibility of the solutions h_{ij} becomes

$$-1 \leq \frac{\lambda + 2\mu}{2(\lambda + \mu)} \frac{(\alpha_k + \beta_k)}{\alpha_{i-j}} \leq 1 \tag{A-166}$$

The three functions B_{ij} are given in Figure A-0.2 for a Lode parameter $\mu_L \in [-1; 1]$, with the Hershey yield function with $m = \{2; 16\}$ and for associated plastic flow (CASE 1: $\alpha_0 = 0$) and non-associated plastic flow (CASE 3: $\alpha_0 \neq 0$)

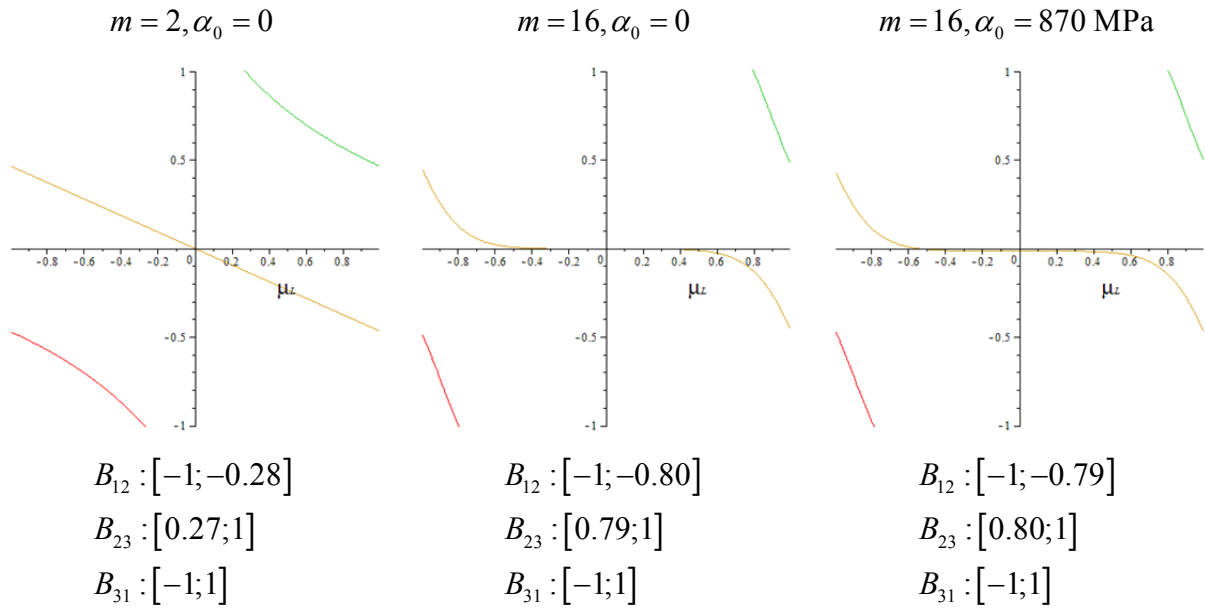


Figure A-0.2. Graphs for B_{12} (red), B_{23} (green) and B_{31} (yellow) as functions of the Lode parameter and admissible domains.

**DEPARTMENT OF STRUCTURAL ENGINEERING
NORWEGIAN UNIVERSITY OF SCIENCE AND TECHNOLOGY**

N-7491 TRONDHEIM, NORWAY
Telephone: +47 73 59 47 00 Telefax: +47 73 59 47 01

"Reliability Analysis of Structural Systems using Nonlinear Finite Element Methods",
C. A. Holm, 1990:23, ISBN 82-7119-178-0.

"Uniform Stratified Flow Interaction with a Submerged Horizontal Cylinder",
Ø. Arntsen, 1990:32, ISBN 82-7119-188-8.

"Large Displacement Analysis of Flexible and Rigid Systems Considering Displacement-Dependent Loads and Nonlinear Constraints",
K. M. Mathisen, 1990:33, ISBN 82-7119-189-6.

"Solid Mechanics and Material Models including Large Deformations",
E. Levold, 1990:56, ISBN 82-7119-214-0, ISSN 0802-3271.

"Inelastic Deformation Capacity of Flexurally-Loaded Aluminium Alloy Structures",
T. Welo, 1990:62, ISBN 82-7119-220-5, ISSN 0802-3271.

"Visualization of Results from Mechanical Engineering Analysis",
K. Aamnes, 1990:63, ISBN 82-7119-221-3, ISSN 0802-3271.

"Object-Oriented Product Modeling for Structural Design",
S. I. Dale, 1991:6, ISBN 82-7119-258-2, ISSN 0802-3271.

"Parallel Techniques for Solving Finite Element Problems on Transputer Networks",
T. H. Hansen, 1991:19, ISBN 82-7119-273-6, ISSN 0802-3271.

"Statistical Description and Estimation of Ocean Drift Ice Environments",
R. Korsnes, 1991:24, ISBN 82-7119-278-7, ISSN 0802-3271.

"Properties of concrete related to fatigue damage: with emphasis on high strength concrete",
G. Petkovic, 1991:35, ISBN 82-7119-290-6, ISSN 0802-3271.

"Turbidity Current Modelling",
B. Brørs, 1991:38, ISBN 82-7119-293-0, ISSN 0802-3271.

"Zero-Slump Concrete: Rheology, Degree of Compaction and Strength. Effects of Fillers as Part Cement- Replacement",
C. Sørensen, 1992:8, ISBN 82-7119-357-0, ISSN 0802-3271.

"Nonlinear Analysis of Reinforced Concrete Structures Exposed to Transient Loading",
K. V. Høiseth, 1992:15, ISBN 82-7119-364-3, ISSN 0802-3271.

"Finite Element Formulations and Solution Algorithms for Buckling and Collapse Analysis of Thin Shells",
R. O. Bjærum, 1992:30, ISBN 82-7119-380-5, ISSN 0802-3271.

"Response Statistics of Nonlinear Dynamic Systems",
J. M. Johnsen, 1992:42, ISBN 82-7119-393-7, ISSN 0802-3271.

"Digital Models in Engineering. A Study on why and how engineers build and operate digital models for decision support",
J. Høyte, 1992:75, ISBN 82-7119-429-1, ISSN 0802-3271.

- "Sparse Solution of Finite Element Equations",
A. C. Damhaug, 1992:76, ISBN 82-7119-430-5, ISSN 0802-3271.
- "Some Aspects of Floating Ice Related to Sea Surface Operations in the Barents Sea",
S. Løset, 1992:95, ISBN 82-7119-452-6, ISSN 0802-3271.
- "Modelling of Cyclic Plasticity with Application to Steel and Aluminium Structures",
O. S. Hopperstad, 1993:7, ISBN 82-7119-461-5, ISSN 0802-3271.
- "The Free Formulation: Linear Theory and Extensions with Applications to Tetrahedral Elements with Rotational Freedoms",
G. Skeie, 1993:17, ISBN 82-7119-472-0, ISSN 0802-3271.
- "Høyfast betongs motstand mot piggdekkslitasje. Analyse av resultater fra prøving i Veisliter'n",
T. Tveter, 1993:62, ISBN 82-7119-522-0, ISSN 0802-3271.
- "A Nonlinear Finite Element Based on Free Formulation Theory for Analysis of Sandwich Structures",
O. Aamlid, 1993:72, ISBN 82-7119-534-4, ISSN 0802-3271.
- "The Effect of Curing Temperature and Silica Fume on Chloride Migration and Pore Structure of High Strength Concrete",
C. J. Hauck, 1993:90, ISBN 82-7119-553-0, ISSN 0802-3271.
- "Failure of Concrete under Compressive Strain Gradients",
G. Markeset, 1993:110, ISBN 82-7119-575-1, ISSN 0802-3271.
- "An experimental study of internal tidal amphidromes in Vestfjorden",
J. H. Nilsen, 1994:39, ISBN 82-7119-640-5, ISSN 0802-3271.
- "Structural analysis of oil wells with emphasis on conductor design",
H. Larsen, 1994:46, ISBN 82-7119-648-0, ISSN 0802-3271.
- "Adaptive methods for non-linear finite element analysis of shell structures",
K. M. Okstad, 1994:66, ISBN 82-7119-670-7, ISSN 0802-3271.
- "On constitutive modelling in nonlinear analysis of concrete structures",
O. Fyrileiv, 1994:115, ISBN 82-7119-725-8, ISSN 0802-3271.
- "Fluctuating wind load and response of a line-like engineering structure with emphasis on motion-induced wind forces",
J. Bogunovic Jakobsen, 1995:62, ISBN 82-7119-809-2, ISSN 0802-3271.
- "An experimental study of beam-columns subjected to combined torsion, bending and axial actions",
A. Aalberg, 1995:66, ISBN 82-7119-813-0, ISSN 0802-3271.
- "Scaling and cracking in unsealed freeze/thaw testing of Portland cement and silica fume concretes",
S. Jacobsen, 1995:101, ISBN 82-7119-851-3, ISSN 0802-3271.
- "Damping of water waves by submerged vegetation. A case study of laminaria hyperborea",
A. M. Dubi, 1995:108, ISBN 82-7119-859-9, ISSN 0802-3271.
- "The dynamics of a slope current in the Barents Sea",
Sheng Li, 1995:109, ISBN 82-7119-860-2, ISSN 0802-3271.
- "Modellering av delmaterialenes betydning for betongens konsistens",
Ernst Mørtzell, 1996:12, ISBN 82-7119-894-7, ISSN 0802-3271.

- "Bending of thin-walled aluminium extrusions",
Birgit Søvik Opheim, 1996:60, ISBN 82-7119-947-1, ISSN 0802-3271.
- "Material modelling of aluminium for crashworthiness analysis",
Torodd Berstad, 1996:89, ISBN 82-7119-980-3, ISSN 0802-3271.
- "Estimation of structural parameters from response measurements on submerged floating tunnels",
Rolf Magne Larssen, 1996:119, ISBN 82-471-0014-2, ISSN 0802-3271.
- "Numerical modelling of plain and reinforced concrete by damage mechanics",
Mario A. Polanco-Loria, 1997:20, ISBN 82-471-0049-5, ISSN 0802-3271.
- "Nonlinear random vibrations - numerical analysis by path integration methods",
Vibeke Moe, 1997:26, ISBN 82-471-0056-8, ISSN 0802-3271.
- "Numerical prediction of vortex-induced vibration by the finite element method",
Joar Martin Dalheim, 1997:63, ISBN 82-471-0096-7, ISSN 0802-3271.
- "Time domain calculations of buffeting response for wind sensitive structures",
Ketil Aas-Jakobsen, 1997:148, ISBN 82-471-0189-0, ISSN 0802-3271.
- "A numerical study of flow about fixed and flexibly mounted circular cylinders",
Trond Stokka Meling, 1998:48, ISBN 82-471-0244-7, ISSN 0802-3271.
- "Estimation of chloride penetration into concrete bridges in coastal areas",
Per Egil Steen, 1998:89, ISBN 82-471-0290-0, ISSN 0802-3271.
- "Stress-resultant material models for reinforced concrete plates and shells",
Jan Arve Øverli, 1998:95, ISBN 82-471-0297-8, ISSN 0802-3271.
- "Chloride binding in concrete. Effect of surrounding environment and concrete composition",
Claus Kenneth Larsen, 1998:101, ISBN 82-471-0337-0, ISSN 0802-3271.
- "Rotational capacity of aluminium alloy beams",
Lars A. Moen, 1999:1, ISBN 82-471-0365-6, ISSN 0802-3271.
- "Stretch Bending of Aluminium Extrusions",
Arild H. Clausen, 1999:29, ISBN 82-471-0396-6, ISSN 0802-3271.
- "Aluminium and Steel Beams under Concentrated Loading",
Tore Tryland, 1999:30, ISBN 82-471-0397-4, ISSN 0802-3271.
- "Engineering Models of Elastoplasticity and Fracture for Aluminium Alloys",
Odd-Geir Lademo, 1999:39, ISBN 82-471-0406-7, ISSN 0802-3271.
- "Kapazität og duktilitet av dybelforbindelser i trekonstruksjoner",
Jan Siem, 1999:46, ISBN 82-471-0414-8, ISSN 0802-3271.
- "Etablering av distribuert ingeniørarbeid; Teknologiske og organisatoriske erfaringer fra en norsk ingeniørbedrift",
Lars Line, 1999:52, ISBN 82-471-0420-2, ISSN 0802-3271.
- "Estimation of Earthquake-Induced Response",
Símon Ólafsson, 1999:73, ISBN 82-471-0443-1, ISSN 0802-3271.
- "Coastal Concrete Bridges: Moisture State, Chloride Permeability and Aging Effects"

Ragnhild Holen Relling, 1999:74, ISBN 82-471-0445-8, ISSN 0802-3271.

”Capacity Assessment of Titanium Pipes Subjected to Bending and External Pressure”,
Arve Bjørset, 1999:100, ISBN 82-471-0473-3, ISSN 0802-3271.

“Validation of Numerical Collapse Behaviour of Thin-Walled Corrugated Panels”,
Håvar Ilstad, 1999:101, ISBN 82-471-0474-1, ISSN 0802-3271.

“Strength and Ductility of Welded Structures in Aluminium Alloys”,
Mirosław Matusiak, 1999:113, ISBN 82-471-0487-3, ISSN 0802-3271.

“Thermal Dilation and Autogenous Deformation as Driving Forces to Self-Induced Stresses in High Performance Concrete”,
Øyvind Bjøntegaard, 1999:121, ISBN 82-7984-002-8, ISSN 0802-3271.

“Some Aspects of Ski Base Sliding Friction and Ski Base Structure”,
Dag Anders Moldestad, 1999:137, ISBN 82-7984-019-2, ISSN 0802-3271.

"Electrode reactions and corrosion resistance for steel in mortar and concrete",
Roy Antonsen, 2000:10, ISBN 82-7984-030-3, ISSN 0802-3271.

"Hydro-Physical Conditions in Kelp Forests and the Effect on Wave Damping and Dune Erosion. A case study on Laminaria Hyperborea",
Stig Magnar Løvås, 2000:28, ISBN 82-7984-050-8, ISSN 0802-3271.

"Random Vibration and the Path Integral Method",
Christian Skaug, 2000:39, ISBN 82-7984-061-3, ISSN 0802-3271.

"Buckling and geometrical nonlinear beam-type analyses of timber structures",
Trond Even Eggen, 2000:56, ISBN 82-7984-081-8, ISSN 0802-3271.

”Structural Crashworthiness of Aluminium Foam-Based Components”,
Arve Grønsund Hanssen, 2000:76, ISBN 82-7984-102-4, ISSN 0809-103X.

“Measurements and simulations of the consolidation in first-year sea ice ridges, and some aspects of mechanical behaviour”,
Knut V. Høyland, 2000:94, ISBN 82-7984-121-0, ISSN 0809-103X.

”Kinematics in Regular and Irregular Waves based on a Lagrangian Formulation”,
Svein Helge Gjørund, 2000:86, ISBN 82-7984-112-1, ISSN 0809-103X.

”Self-Induced Cracking Problems in Hardening Concrete Structures”,
Daniela Bosnjak, 2000:121, ISBN 82-7984-151-2, ISSN 0809-103X.

"Ballistic Penetration and Perforation of Steel Plates",
Tore Børvik, 2000:124, ISBN 82-7984-154-7, ISSN 0809-103X.

"Freeze-Thaw resistance of Concrete. Effect of: Curing Conditions, Moisture Exchange and Materials",
Terje Finnerup Rønning, 2001:14, ISBN 82-7984-165-2, ISSN 0809-103X

"Structural behaviour of post tensioned concrete structures. Flat slab. Slabs on ground",
Steinar Trygstad, 2001:52, ISBN 82-471-5314-9, ISSN 0809-103X.

"Slipforming of Vertical Concrete Structures. Friction between concrete and slipform panel",
Kjell Tore Fosså, 2001:61, ISBN 82-471-5325-4, ISSN 0809-103X.

"Some numerical methods for the simulation of laminar and turbulent incompressible flows", Jens Holmen, 2002:6, ISBN 82-471-5396-3, ISSN 0809-103X.

"Improved Fatigue Performance of Threaded Drillstring Connections by Cold Rolling", Steinar Kristoffersen, 2002:11, ISBN: 82-421-5402-1, ISSN 0809-103X.

"Deformations in Concrete Cantilever Bridges: Observations and Theoretical Modelling", Peter F. Takács, 2002:23, ISBN 82-471-5415-3, ISSN 0809-103X.

"Stiffened aluminium plates subjected to impact loading", Hilde Giæver Hildrum, 2002:69, ISBN 82-471-5467-6, ISSN 0809-103X.

"Full- and model scale study of wind effects on a medium-rise building in a built up area", Jónas Thór Snæbjörnsson, 2002:95, ISBN82-471-5495-1, ISSN 0809-103X.

"Evaluation of Concepts for Loading of Hydrocarbons in Ice-infested water", Arnor Jensen, 2002:114, ISBN 82-417-5506-0, ISSN 0809-103X.

"Numerical and Physical Modelling of Oil Spreading in Broken Ice", Janne K. Økland Gjosteen, 2002:130, ISBN 82-471-5523-0, ISSN 0809-103X.

"Diagnosis and protection of corroding steel in concrete", Franz Pruckner, 20002:140, ISBN 82-471-5555-4, ISSN 0809-103X.

"Tensile and Compressive Creep of Young Concrete: Testing and Modelling", Dawood Atrushi, 2003:17, ISBN 82-471-5565-6, ISSN 0809-103X.

"Rheology of Particle Suspensions. Fresh Concrete, Mortar and Cement Paste with Various Types of Lignosulfonates", Jon Elvar Wallevik, 2003:18, ISBN 82-471-5566-4, ISSN 0809-103X.

"Oblique Loading of Aluminium Crash Components", Aase Reyes, 2003:15, ISBN 82-471-5562-1, ISSN 0809-103X.

"Utilization of Ethiopian Natural Pozzolans", Surafel Ketema Desta, 2003:26, ISSN 82-471-5574-5, ISSN:0809-103X.

"Behaviour and strength prediction of reinforced concrete structures with discontinuity regions", Helge Brå, 2004:11, ISBN 82-471-6222-9, ISSN 1503-8181.

"High-strength steel plates subjected to projectile impact. An experimental and numerical study", Sumita Dey, 2004:38, ISBN 82-471-6282-2 (printed version), ISBN 82-471-6281-4 (electronic version), ISSN 1503-8181.

"Alkali-reactive and inert fillers in concrete. Rheology of fresh mixtures and expansive reactions." Bård M. Pedersen, 2004:92, ISBN 82-471-6401-9 (printed version), ISBN 82-471-6400-0 (electronic version), ISSN 1503-8181.

"On the Shear Capacity of Steel Girders with Large Web Openings". Nils Christian Hagen, 2005:9 ISBN 82-471-6878-2 (printed version), ISBN 82-471-6877-4 (electronic version), ISSN 1503-8181.

"Behaviour of aluminium extrusions subjected to axial loading". Østen Jensen, 2005:7, ISBN 82-471-6873-1 (printed version), ISBN 82-471-6872-3 (electronic version), ISSN 1503-8181.

”Thermal Aspects of corrosion of Steel in Concrete”.

Jan-Magnus Østvik, 2005:5, ISBN 82-471-6869-3 (printed version), ISBN 82-471-6868 (electronic version), ISSN 1503-8181.

”Mechanical and adaptive behaviour of bone in relation to hip replacement.” A study of bone remodelling and bone grafting.

Sébastien Muller, 2005:34, ISBN 82-471-6933-9 (printed version), ISBN 82-471-6932-0 (electronic version), ISSN 1503-8181.

“Analysis of geometrical nonlinearities with applications to timber structures”.

Lars Wollebæk, 2005:74, ISBN 82-471-7050-5 (printed version), ISBN 82-471-7019-1 (electronic version), ISSN 1503-8181.

“Pedestrian induced lateral vibrations of slender footbridges”.

Anders Rönquist, 2005:102, ISBN 82-471-7082-5 (printed version), ISBN 82-471-7081-7 (electronic version), ISSN 1503-8181.

“Initial Strength Development of Fly Ash and Limestone Blended Cements at Various Temperatures Predicted by Ultrasonic Pulse Velocity”.

Tom Ivar Fredvik, 2005:112, ISBN 82-471-7105-8 (printed version), ISBN 82-471-7103-1 (electronic version), ISSN 1503-8181.

“Behaviour and modelling of thin-walled cast components”.

Cato Dørum, 2005:128, ISBN 82-471-7140-6 (printed version), ISBN 82-471-7139-2 (electronic version), ISSN 1503-8181.

“Behaviour and modelling of selfpiercing riveted connections”.

Raffaele Porcaro, 2005:165, ISBN 82-471-7219-4 (printed version), ISBN 82-471-7218-6 (electronic version), ISSN 1503-8181.

”Behaviour and Modelling of Aluminium Plates subjected to Compressive Load”.

Lars Rønning, 2005:154, ISBN 82-471-7169-1 (printed version), ISBN 82-471-7195-3 (electronic version), ISSN 1503-8181.

”Bumper beam-longitudinal system subjected to offset impact loading”.

Satyanarayana Kokkula, 2005:193, ISBN 82-471-7280-1 (printed version), ISBN 82-471-7279-8 (electronic version), ISSN 1503-8181.

“Control of Chloride Penetration into Concrete Structures at Early Age”.

Guofei Liu, 2006:46, ISBN 82-471-7838-9 (printed version), ISBN 82-471-7837-0 (electronic version), ISSN 1503-8181.

“Modelling of Welded Thin-Walled Aluminium Structures”.

Ting Wang, 2006:78, ISBN 82-471-7907-5 (printed version), ISBN 82-471-7906-7 (electronic version), ISSN 1503-8181.

”Time-variant reliability of dynamic systems by importance sampling and probabilistic analysis of ice loads”.

Anna Ivanova Olsen, 2006:139, ISBN 82-471-8041-3 (printed version), ISBN 82-471-8040-5 (electronic version), ISSN 1503-8181.

“Fatigue life prediction of an aluminium alloy automotive component using finite element analysis of surface topography”.

Sigmund Kyrré Ås, 2006:25, ISBN 82-471-7791-9 (printed version), ISBN 82-471-7791-9 (electronic version), ISSN 1503-8181.

”Constitutive models of elastoplasticity and fracture for aluminium alloys under strain path change”, Dasharatha Achani, 2006:76, ISBN 82-471-7903-2 (printed version), ISBN 82-471-7902-4 (electronic version), ISSN 1503-8181.

“Simulations of 2D dynamic brittle fracture by the Element-free Galerkin method and linear fracture mechanics”, Tommy Karlsson, 2006:125, ISBN 82-471-8011-1 (printed version), ISBN 82-471-8010-3 (electronic version), ISSN 1503-8181.

“Penetration and Perforation of Granite Targets by Hard Projectiles”, Chong Chiang Seah, 2006:188, ISBN 82-471-8150-9 (printed version), ISBN 82-471-8149-5 (electronic version), ISSN 1503-8181.

“Deformations, strain capacity and cracking of concrete in plastic and early hardening phases”, Tor Arne Hammer, 2007:234, ISBN 978-82-471-5191-4 (printed version), ISBN 978-82-471-5207-2 (electronic version), ISSN 1503-8181.

“Crashworthiness of dual-phase high-strength steel: Material and Component behaviour”, Venkatapathi Tarigopula, 2007:230, ISBN 82-471-5076-4 (printed version), ISBN 82-471-5093-1 (electronic version), ISSN 1503-8181.

“Fibre reinforcement in load carrying concrete structures”, Åse Lyslo Døssland, 2008:50, ISBN 978-82-471-6910-0 (printed version), ISBN 978-82-471-6924-7 (electronic version), ISSN 1503-8181.

“Low-velocity penetration of aluminium plates”, Frode Grytten, 2008:46, ISBN 978-82-471-6826-4 (printed version), ISBN 978-82-471-6843-1 (electronic version), ISSN 1503-8181.

“Robustness studies of structures subjected to large deformations”, Ørjan Fyllingen, 2008:24, ISBN 978-82-471-6339-9 (printed version), ISBN 978-82-471-6342-9 (electronic version), ISSN 1503-8181.

“Constitutive modelling of morsellised bone”, Knut Birger Lunde, 2008:92, ISBN 978-82-471-7829-4 (printed version), ISBN 978-82-471-7832-4 (electronic version), ISSN 1503-8181.

“Experimental Investigations of Wind Loading on a Suspension Bridge Girder”, Bjørn Isaksen, 2008:131, ISBN 978-82-471-8656-5 (printed version), ISBN 978-82-471-8673-2 (electronic version), ISSN 1503-8181.

“Cracking Risk of Concrete Structures in The Hardening Phase”, Guomin Ji, 2008:198, ISBN 978-82-471-1079-9 (printed version), ISBN 978-82-471-1080-5 (electronic version), ISSN 1503-8181.

“Modelling and numerical analysis of the porcine and human mitral apparatus”, Victorien Emile Prot, 2008:249, ISBN 978-82-471-1192-5 (printed version), ISBN 978-82-471-1193-2 (electronic version), ISSN 1503-8181.

“Strength analysis of net structures”, Heidi Moe, 2009:48, ISBN 978-82-471-1468-1 (printed version), ISBN 978-82-471-1469-8 (electronic version), ISSN 1503-8181.

“Numerical analysis of ductile fracture in surface cracked shells”, Espen Berg, 2009:80, ISBN 978-82-471-1537-4 (printed version), ISBN 978-82-471-1538-1 (electronic version), ISSN 1503-8181.

“Subject specific finite element analysis of bone – for evaluation of the healing of a leg lengthening and evaluation of femoral stem design”,
Sune Hansborg Pettersen, 2009:99, ISBN 978-82-471-1579-4 (printed version), ISBN 978-82-471-1580-0 (electronic version), ISSN 1503-8181.

“Evaluation of fracture parameters for notched multi-layered structures”,
Lingyun Shang, 2009:137, ISBN 978-82-471-1662-3 (printed version), ISBN 978-82-471-1663-0 (electronic version), ISSN 1503-8181.

“Modelling of Dynamic Material Behaviour and Fracture of Aluminium Alloys for Structural Applications”
Yan Chen, 2009:69, ISBN 978-82-471-1515-2 (printed version), ISBN 978-82-471-1516-9 (electronic version), ISSN 1503-8181.

“Nanomechanics of polymer and composite particles”
Jianying He 2009:213, ISBN 978-82-471-1828-3 (printed version), ISBN 978-82-471-1829-0 (electronic version), ISSN 1503-8181.

“Mechanical properties of clear wood from Norway spruce”
Kristian Berbohm Dahl 2009:250, ISBN 978-82-471-1911-2 (printed version) ISBN 978-82-471-1912-9 (electronic version), ISSN 1503-8181.

“Modeling of the degradation of TiB₂ mechanical properties by residual stresses and liquid Al penetration along grain boundaries”
Micol Pezzotta 2009:254, ISBN 978-82-471-1923-5 (printed version) ISBN 978-82-471-1924-2 (electronic version) ISSN 1503-8181.

“Effect of welding residual stress on fracture”
Xiabo Ren 2010:77, ISBN 978-82-471-2115-3 (printed version) ISBN 978-82-471-2116-0 (electronic version), ISSN 1503-8181.

“Pan-based carbon fiber as anode material in cathodic protection system for concrete structures”
Mahdi Chini 2010:122, ISBN 978-82-471-2210-5 (printed version) ISBN 978-82-471-2213-6 (electronic version), ISSN 1503-8181.

“Structural Behaviour of deteriorated and retrofitted concrete structures”
Irina Vasililjeva Sæther 2010:171, ISBN 978-82-471-2315-7 (printed version) ISBN 978-82-471-2316-4 (electronic version) ISSN 1503-8181.

“Prediction of local snow loads on roofs”
Vivian Meløysund 2010:247, ISBN 978-82-471-2490-1 (printed version) ISBN 978-82-471-2491-8 (electronic version) ISSN 1503-8181.

“Behaviour and modelling of polymers for crash applications”
Virgile Delhaye 2010:251, ISBN 978-82-471-2501-4 (printed version) ISBN 978-82-471-2502-1 (electronic version) ISSN 1503-8181.

“Blended cement with reduced CO₂ emission – Utilizing the Fly Ash-Limestone Synergy”,
Klaartje De Weerd 2011:32, ISBN 978-82-471-2584-7 (printed version) ISBN 978-82-471-2584-4 (electronic version) ISSN 1503-8181.

“Chloride induced reinforcement corrosion in concrete” Concept of critical chloride content – methods and mechanisms.
Ueli Angst 2011:113, ISBN 978-82-471-2769-9 (printed version) ISBN 978-82-471-2763-6 (electronic version) ISSN 1503-8181.

“A thermo-electric-Mechanical study of the carbon anode and contact interface for Energy savings in the production of aluminium”.

Dag Herman Andersen 2011:157, ISBN 978-82-471-2859-6 (printed version) ISBN 978-82-471-2860-2 (electronic version) ISSN 1503-8181.

“Structural Capacity of Anchorage Ties in Masonry Veneer Walls Subjected to Earthquake. The implications of Eurocode 8 and Eurocode 6 on a typical Norwegian veneer wall.”

Ahmed Mohamed Yousry Hamed 2011:181, ISBN 978-82-471-2911-1 (printed version) ISBN 978-82-471-2912-8 (electronic ver.) ISSN 1503-8181.

“Work-hardening behaviour in age-hardenable Al-Zn-Mg(-Cu) alloys”.

Ida Westermann , 2011:247, ISBN 978-82-471-3056-8 (printed ver.) ISBN 978-82-471-3057-5 (electronic ver.) ISSN 1503-8181.

“Behaviour and modelling of selfpiercing riveted connections using aluminium rivets”.

Nguyen-Hieu Hoang, 2011:266, ISBN 978-82-471-3097-1 (printed ver.) ISBN 978-82-471-3099-5 (electronic ver.) ISSN 1503-8181.

“Fibre reinforced concrete”.

Sindre Sandbakk, 2011:297, ISBN 978-82-471-3167-1 (printed ver.) ISBN 978-82-471-3168-8 (electronic ver) ISSN 1503:8181.

“Dynamic behaviour of cablesupported bridges subjected to strong natural wind”.

Ole Andre Øiseth, 2011:315, ISBN 978-82-471-3209-8 (printed ver.) ISBN 978-82-471-3210-4 (electronic ver.) ISSN 1503-8181.

“Constitutive modeling of solargrade silicon materials”

Julien Cochard, 2011:307, ISBN 978-82-471-3189-3 (printed ver). ISBN 978-82-471-3190-9 (electronic ver.) ISSN 1503-8181.

“Constitutive behavior and fracture of shape memory alloys”

Jim Stian Olsen, 2012:57, ISBN 978-82-471-3382-8 (printed ver.) ISBN 978-82-471-3383-5 (electronic ver.) ISSN 1503-8181.

“Field measurements in mechanical testing using close-range photogrammetry and digital image analysis”

Egil Fagerholt, 2012:95, ISBN 978-82-471-3466-5 (printed ver.) ISBN 978-82-471-3467-2 (electronic ver.) ISSN 1503-8181.

“Towards a better understanding of the ultimate behaviour of lightweight aggregate concrete in compression and bending”.

Håvard Nedrelid, 2012:123, ISBN 978-82-471-3527-3 (printed ver.) ISBN 978-82-471-3528-0 (electronic ver.) ISSN 1503-8181.

“Numerical simulations of blood flow in the left side of the heart”

Sigrud Kaarstad Dahl, 2012:135, ISBN 978-82-471-3553-2 (printed ver.) ISBN 978-82-471-3555-6 (electronic ver.) ISSN 1503-8181.

“Moisture induced stresses in glulam”

Vanessa Angst-Nicollier, 2012:139, ISBN 978-82-471-3562-4 (printed ver.) ISBN 978-82-471-3563-1 (electronic ver.) ISSN 1503-8181.

“Biomechanical aspects of distraction osteogenesis”

Valentina La Russa, 2012:250, ISBN 978-82-471-3807-6 (printed ver.) ISBN 978-82-471-3808-3 (electronic ver.) ISSN 1503-8181.

“Ductile fracture in dual-phase steel. Theoretical, experimental and numerical study”
Gaute Gruben, 2012:257, ISBN 978-82-471-3822-9 (printed ver.) ISBN 978-82-471-3823-6 (electronic ver.) ISSN 1503-8181.

“Damping in Timber Structures”
Nathalie Labonnote, 2012:263, ISBN 978-82-471-3836-6 (printed ver.) ISBN 978-82-471-3837-3 (electronic ver.) ISSN 1503-8181.

“Biomechanical modeling of fetal veins: The umbilical vein and ductus venosus bifurcation”
Paul Roger Leinan, 2012:299, ISBN 978-82-471-3915-8 (printed ver.) ISBN 978-82-471-3916-5 (electronic ver.) ISSN 1503-8181.

“Large-Deformation behaviour of thermoplastics at various stress states”
Anne Serine Ognedal, 2012:298, ISBN 978-82-471-3913-4 (printed ver.) ISBN 978-82-471-3914-1 (electronic ver.) ISSN 1503-8181.

“Hardening accelerator for fly ash blended cement”
Kien Dinh Hoang, 2012:366, ISBN 978-82-471-4063-5 (printed ver.) ISBN 978-82-471-4064-2 (electronic ver.) ISSN 1503-8181.

“From molecular structure to mechanical properties”
Jianyang Wu, 2013:186, ISBN 978-82-471-4485-5 (printed ver.) ISBN 978-82-471-4486-2 (electronic ver.) ISSN 1503-8181.

“Experimental and numerical study of hybrid concrete structures”
Linn Grepstad Nes, 2013:259, ISBN 978-82-471-4644-6 (printed ver.) ISBN 978-82-471-4645-3 (electronic ver.) ISSN 1503-8181.

“Mechanics of ultra-thin multi crystalline silicon wafers”
Saber Saffar, 2013:199, ISBN 978-82-471-4511-1 (printed ver.) ISBN 978-82-471-4513-5 (electronic ver.) ISSN 1503-8181.

“Through process modelling of welded aluminium structures”
Anizahyati Alisibramulisi, 2013:325, ISBN 978-82-471-4788-7 (printed ver.) ISBN 978-82-471-4789-4 (electronic ver.) ISSN 1503-8181.

“Combined blast and fragment loading on steel plates”
Knut Gaarder Rakvåg, 2013:361, ISBN 978-82-471-4872-3 (printed ver.) ISBN 978-82-4873-0 (electronic ver.) ISSN 1503-8181.